

学位論文

**Understanding the enrichment of
heavy elements by the
chemodynamical evolution models of
dwarf galaxies**
(矮小銀河の化学力学進化モデルによ
る重元素の化学進化の理解)

平成29年12月 博士（理学）申請

東京大学大学院理学系研究科

天文学専攻

平居 悠

**Understanding the enrichment of
heavy elements by the
chemodynamical evolution models of
dwarf galaxies**
(矮小銀河の化学力学進化モデルによ
る重元素の化学進化の理解)

*A thesis submitted in fulfillment of the requirements
for the degree of Doctor of Philosophy*

in

The University of Tokyo

YUTAKA HIRAI

March 22, 2018

“The purpose of life is the investigation of the Sun, the Moon, and the heavens.”

Anaxagoras

Abstract

Understanding the enrichment of heavy elements in dwarf galaxies help us clarify the astrophysical sites of elements and evolutionary histories of the Local Group galaxies. Astronomical spectroscopic observations have shown that there are large star-to-star scatters in the abundances of elements synthesized by rapid neutron-capture process (r -process elements) in extremely metal-poor stars. On the other hand, the heaviest iron-peak element, Zn shows an increasing trend toward lower metallicity. These observational signatures preserve the information about the early stages of the formation of Local Group galaxies and astrophysical sites of heavy elements. According to the hierarchical structure formation scenario, the Milky Way halo is formed from the clustering of the smaller objects. The chemodynamical properties of the Local Group dwarf galaxies thus help us understand galaxy formation. However, the enrichment of heavy elements and their roles in the chemodynamical evolution of dwarf galaxies have not yet been clarified.

In this thesis, we performed a series of high-resolution N -body/smoothed particle hydrodynamics simulations of dwarf galaxies in isolated and cosmological initial conditions. We confirm that our simulations are consistent with the observed properties of the Local Group galaxies such as radial profiles, metallicity distribution, and mass-metallicity relation. We study the enrichment of r -process elements from neutron star mergers in dwarf galaxies. We find that neutron star mergers with merger times of 100 Myr can explain the observed r -process abundances ratios. This is because metallicity is not correlated with time ~ 300 Myr from the start of the simulation due to the low star formation efficiency in dwarf galaxies. In these galaxies, neutron star mergers with merger times less than 500 Myr can produce r -process elements in very metal-poor stars.

Star formation histories directly affect the abundances of r -process elements in metal-poor stars. We find that galaxies with dynamical times longer than 100 Myr reproduce the observed abundances of r -process elements. These galaxies have star formation rates less than 0.001 solar masses per year. On the other hand, the first neutron star merger appears at a higher metallicity in galaxies with a dynamical time shorter than typical neutron star merger times. The star formation rates of these galaxies are over 0.01 solar masses per year at around 100 Myr from the beginning of the simulation. These galaxies have lower scatters of r -process elements than those of the galaxies with longer dynamical times. We moreover find that the results are insensitive to the total mass of halos and merger times of neutron star mergers.

Enrichment of Zn in dwarf galaxies is also studied in this thesis. We take into account the yields of electron-capture supernovae, hypernovae, iron-core collapse supernovae, and type Ia supernovae in the simulations. We find that the ejecta from electron-capture supernovae contribute to forming extremely metal-poor stars with high Zn abundances. On the other hand, the scatters of the Zn to iron ratios seen at higher metallicity originate from the ejecta of type Ia supernovae. We also find that it

is difficult to reproduce the observed abundances without assuming the contribution from electron-capture supernovae.

The scatters of r -process elements mainly come from the inhomogeneity of the metals in the interstellar medium. We find that the scaling factor for metal diffusion larger than 0.01 is necessary to reproduce the observation of abundances of r -process elements and Zn in dwarf galaxies. This value is consistent with the value expected from turbulence theory and experiment. We also find that the timescale of metal mixing is less than 40 Myr. This timescale is shorter than that of typical dynamical times of dwarf galaxies.

To obtain the self-consistent picture for the formation of the Milky Way halo and satellite dwarf galaxies through the enrichment of heavy elements, we performed a series of cosmological zoom-in simulations of a galaxy. We computed the galaxy with a halo mass of 10^{10} solar masses at redshift 2 to resolve the scale of satellite dwarf galaxies. Most extremely metal-poor stars are formed before 1 Gyr from the beginning of the simulation. In the galaxy, there are star-to-star scatters of r -process elements in low metallicity. We find that r -process rich metal-poor stars are formed in halos with a total mass of $\sim 10^8$ solar masses and gas mass of $\sim 10^6$ solar masses.

In this thesis, we identify that neutron star mergers can be major astrophysical sites of r -process elements and electron-capture supernovae contribute to the enrichment of Zn in low metallicity. We demonstrate that abundances of heavy elements in metal-poor stars can be a nice tracer for the star formation histories and metal mixing in dwarf galaxies. From the cosmological simulations, we find that r -process rich stars are formed in the galaxy with a size similar to the ultra-faint dwarf galaxies. Our results demonstrate that the comparison with future high-resolution simulations that can resolve each star and observations of r -process elements in extremely metal-poor stars will be able to constrain the early chemodynamical evolution of the Local Group galaxies.

Acknowledgements

I would like to express my sincere gratitude to my supervisor, Toshitaka Kajino for his fruitful advice, endless patience, and continuous encouragement. I am very grateful to him for introducing me to the world of galactic chemodynamics. I also thank him for giving me many opportunities to present my research and introducing me many outstanding researchers.

I am deeply grateful to Yuhri Ishimaru¹ for continuous advice and fruitful discussion. Her works motivate me to do my research projects. I also thank her for giving me an opportunity to learn and discuss galactic chemical evolution with researchers and students at her laboratory. I would like to express my great pleasure working with her.

I am very grateful to Michiko Fujii for giving me suggestions to improve my work. I appreciate her very much for continuously giving me advice on the directions of my research project. I also thank her for introducing me and making connections to many researchers in astronomy.

I appreciate very much for Takayuki Saitoh for providing me the code, `ASURA` and giving me advice for extending the code. I learned a lot how to conduct large-scale numerical simulations from him. Fruitful discussion with him makes my works improve significantly.

I would like to thank Shinya Wanajo for fruitful discussions and providing me the nucleosynthesis yields. Collaboration with him makes us improve the understanding of the origin of elements in the Universe. I immensely appreciate Masaomi Tanaka for encouraging me to do this work. His advice motivates me to start new projects. I would like to thank Jun Hidaka for continuous advice from the beginning of this work. I appreciate Takuma Suda for providing me the latest version of SAGA database including the dataset of Local Group dwarf galaxies. I thank Yuichiro Sekiguchi, Nobuya Nishimura, and Aurora Simionescu for giving me insightful comments. I am grateful to Takashi Okamoto for fruitful discussions about galaxy formation.

People with many institutes gave me great insights. I would like to express gratitude to Junichiro Makino for giving me advice on prospects. I appreciate the referees of this thesis, Hideyuki Umeda, Takashi Onaka, Eiichiro Kokubo, Masashi Chiba, and Wako Aoki. I am deeply grateful to Yuzuru Yoshii and Toshikazu Shigeyama for giving me insightful suggestions. I also appreciate Nobuyuki Hasebe and Hiroshi Nagaoaka for encouraging me to do my projects. For galactic archaeology science, Miho Ishigaki, Kohei Hayashi, Hidetomo Homma, Daisuke Toyouchi, Takanobu Kiriara, and Tadafumi Matsuno gave me fruitful comments and suggestions. Seminars with Keiichi Wada, Motohiko Enoki, Masahiro Nagashima, Shigeki Inoue, Taira Oogi, and Hikari Shirakata enhance my knowledge of galaxy formation. I am grateful to Nicolas Prantzos, Patrick François, Simon Portegies Zwart, Diederik Kruijssen for hosting me for short stay and seminars in Europe. I thank Misa Aoki, Sachie

¹Deceased November 18, 2017

Tsukamoto, Nao Fukagawa, and Takuya Ojima for studying together about galactic chemical evolution.

I have conducted my research at Division of Theoretical Astronomy (DTA), National Astronomical Observatory of Japan (NAOJ) as a student of the University of Tokyo. People in these institutes have supported my daily research activities. I sincerely appreciate Kohji Tomisaka for giving me suggestions and supporting my works in DTA. I am grateful to Tomoya Takiwaki, Takashi Moriya, Takaya Nozawa, Hajime Sotani, and Masaki Yamaguchi for giving me insightful comments in daily discussions. I would like to thank Shota Shibagaki, Akimasa Kataoka, Masato Shirasaki, Kenneth Wong, Ke-Jung Chen, and Mariko Nomura for giving me advice for my works. I appreciate Shihoko Izumi, Hinako Fukushi, and Yuko Kimura for supporting my research activities. I thank Haruo Yoshida, Fumitaka Nakamura, Ken Osuga, Takashi Hamana, Tsuyoshi Inoue, Seiji Zenitani, Dai Yamazaki, Kengo Tomida, Masahiro Ogihara, Hiroyuki Takahashi, Tomohisa Kawashima, Takayoshi Kusune, Benjamin Wu, Keizo Fujimoto, Yasuhiro Hasegawa, Shun Furusawa, Akihiro Suzuki, Yasunori Hori, Takami Kuroda, Ko Nakamura, Yukari Ohtani, Jiang Jian, Yuta Asahina, Hirokazu Sasaki, Kanji Mori, Yudong Luo, Shian Izumida, Hiroshi Kobayashi, Takashi Shibata, Misako Tatsuuma, Shuri Oyamada, Kangrou Guo, Akihiko Fujii, and Katsuya Hashizume. I am also grateful to Grant J. Mathews, Roland Diehl, Colin A. Norman, Michael Richmond, Cemsinan Deliduman, Yamac Deliduman, Michael Famiano, A. Baha Balantekin, Shunji Nishimura, Tomoyuki Maruyama, Toshio Suzuki, and Takehito Hayakawa. Interactions with them have enhanced my works.

Finally, I sincerely appreciate my family for supporting my daily life for 27 years with great love.

This work was supported by JSPS KAKENHI Grant Number, 15J00548. This study was also supported by JSPS and CNRS under the Japan-France Research Cooperative Program. Numerical computations were carried out on Cray XC30 at Center for Computational Astrophysics, NAOJ. Numerical analyses were in part carried out on computers at Center for Computational Astrophysics, NAOJ.

Contents

Abstract	v
Acknowledgements	vii
1 Introduction	1
1.1 Astrophysical sites of elements	1
1.1.1 Solar system abundances	1
1.1.2 Nucleosynthesis	2
1.1.3 Astrophysical sites of heavy elements	4
1.1.3.1 Supernovae	4
1.1.3.2 Neutron star mergers	6
1.2 The Local Group galaxies	8
1.2.1 The observed Local Group Galaxies	8
1.2.2 Chemical abundances of Local Group dwarf galaxies	10
1.3 Formation and evolution of galaxies	14
1.3.1 Galaxy formation	14
1.3.2 Galactic chemical evolution	16
1.4 <i>N</i> -body / smoothed particle hydrodynamics code, ASURA	19
1.5 This thesis	21
2 Enrichment of <i>r</i>-process elements in dwarf spheroidal galaxies in the chemodynamical evolution models	25
2.1 Review: NSMs as a source of <i>r</i> -process elements	25
2.2 Method and models	28
2.2.1 Chemical enrichment process	28
2.2.2 NSM models	28
2.2.3 Definition of newly formed stars	29
2.2.4 Models of dSphs	30
2.3 Chemodynamical evolution of dSphs	32
2.3.1 Dynamical evolution of dSph models	32
2.3.2 Time variations of the SFRs	34
2.3.3 Metallicity distribution	35
2.4 Enrichment of <i>r</i> -process elements in dwarf spheroidal galaxies	37
2.4.1 Enrichment of <i>r</i> -process elements without metal mixing in SF region	37
2.4.2 Enrichment of <i>r</i> -process elements with metal mixing in SF region	40
2.4.3 The effect of SN feedback to the enrichment of <i>r</i> -process elements	42
2.4.4 Merger times of NSMs	46

2.4.5	The rate of NSMs	46
2.5	Summary	49
3	Early chemodynamical evolution of dwarf galaxies deduced from r-process elements	53
3.1	Review: Enrichment of r -process elements in dwarf galaxies and building blocks of the MW	53
3.2	Isolated dwarf galaxy models	55
3.3	Comparison with observed dwarf galaxies	57
3.3.1	Metallicity distribution functions	57
3.3.2	Mass–metallicity relation	58
3.3.3	α -element abundance	61
3.4	Enrichment of r -process elements	61
3.4.1	Effects of initial density of halos	61
3.4.2	Effects of total mass of halos	71
3.4.3	Merger times of NSMs	77
3.5	Implications to the formation of the MW halo	82
3.6	Summary	82
4	Enrichment of zinc in dwarf galaxies	85
4.1	Review: Astrophysical sites of Zn	85
4.2	Models	87
4.2.1	ECSN models	87
4.2.2	Nucleosynthesis yields of zinc	88
4.2.3	Metal mixing models	91
4.3	Chemodynamical evolution of dwarf galaxies	92
4.4	Enrichment of Zn	96
4.4.1	Enrichment of Zn at $[\text{Fe}/\text{H}] \lesssim -2.5$	96
4.4.2	Enrichment of Zn at $[\text{Fe}/\text{H}] \gtrsim -2.5$	98
4.4.3	Effects of ECSNe and HNe on the enrichment of Zn	101
4.5	Summary	105
5	Efficiency of metal mixing in dwarf galaxies	107
5.1	Review: Heavy elements as an indicator of metal mixing	107
5.2	Metal diffusion models	109
5.3	Results	109
5.4	Discussion	114
5.5	Summary	116
6	Enrichment of r-process elements in a cosmological context	117
6.1	Review: Enrichment of r -process elements and galaxy formation	117
6.2	Cosmological zoom-in simulations	118
6.3	Results	119
6.4	Discussion	125
6.5	Summary	125

7	Conclusions and future prospects	127
7.1	Conclusions	127
7.2	Future prospects	128
7.2.1	Multi-messenger astronomy	130
7.2.2	Star-by-star simulations	130
7.2.3	Connection between near and far fields	131
A	Parameter dependence	133
A.1	Radial profile	133
A.2	Time variations of the SFR and metallicity distribution	135
B	Dynamical friction	139
C	Effects of supernova yields of zinc and dependence on the resolution	143
C.1	Effects of supernova yields of zinc	143
C.2	Dependence on the resolution	145
	Bibliography	147

List of Figures

- | | | |
|-----|---|---|
| 1.1 | The solar isotopic abundances relative to silicon (Si) abundance as a function of mass numbers (Lodders, 2003). The Si abundance is set to be 10^6 | 2 |
| 1.2 | (a) Comparison of solar r -process abundance patterns with r -rich metal-poor stars (figure 7 of Sneden, Cowan, and Gallino, 2008). The solid light blue curves represent the scaled solar r -process abundance pattern (Simmerer et al., 2004), normalized by the Eu abundance. The abundances except for CS 22892-052 is shifted for comparison. (b) Difference of individual stars and solar r -process abundances. The dashed horizontal line denotes the zero offset. (c) Offset of average stellar abundance from the stellar model pattern of Arlandini et al. (1999). | 3 |
| 1.3 | The metallicity dependence on final fates of stars as a function of zero-age sequence mass (M_{ini} , figure 5 of Doherty et al., 2015). The dark-gray shaded, the light-grey, white, hatched, and gray regions denote the mass range of CO white dwarfs (WDs), CO(Ne) WDs, ONe WDs, ECSNe, and iron CCSNe, respectively. | 5 |
| 1.4 | The timeline of the multi-messenger observations of GW170817 (figure 2 of Abbott et al., 2017c). The observing facilities, instruments, and teams are listed at the beginning of the row. The solid circles denote representative observations. The vertical solid lines indicate the source was able to detect at least one instrument. The top left magnification inset shows that frequency of gravitational waves detected by LIGO-Hanford and LIGO-Livingston as a function of time. The top middle inset represents X-ray light curve. The top right inset denotes optical/near-infrared spectra observed by SALT (red curve, McCully et al., 2017; Buckley et al., 2018), ESO-NTT (green curve, Smartt et al., 2017), the SOAR 4m telescope (black curve, Nicholl et al., 2017), and ESO-VLT-XShooter (blue curve, Smartt et al., 2017). Bottom panels illustrate optical, X-ray, and radio images of the counterpart of GW170817. | 7 |
| 1.5 | The comparison with solar r -process abundance patterns and yields of r -process elements from NSMs (figure 4 of Wanajo et al., 2014, reproduced by permission of the AAS). The top panel represents r -process abundance pattern in the ejecta of $Y_e = 0.09$ (the red curve), 0.14 (the light green curve), 0.19 (the magenta curve), 0.24 (the brown curve), 0.34 (the blue curve), and 0.44 (the purple curve). The bottom panel compares solar r -process abundances (black circles), and mass-averaged yields (the red curve). | 9 |

- 1.6 SFHs of the LG dwarf galaxies (figure 11 of Weisz et al., 2014, reproduced by permission of the AAS). From left to right, panels show the MW satellites, M31 satellites, and field dwarf galaxies. The black solid curve shows the average SFH of all galaxies in each field. The gray shaded region shows the error of the average SFH. Colored curves show SFHs of each galaxy. 10
- 1.7 Stellar mass–metallicity relation for models and the LG dwarf galaxies. Black diamonds, triangles and squares with error bars are the observed value of the MW dSphs, M31 dSphs and the LG dIrrs, respectively (Kirby et al., 2013, K13). The sky-blue dot–dashed line represents the least square fitting of the samples of (Dekel and Woo, 2003, D03): $[\text{Fe}/\text{H}] \propto M_*^{0.40}$. The purple dashed line represents the least-square fitting of K13: $\langle [\text{Fe}/\text{H}] \rangle = (-1.69 \pm 0.04) + (0.30 \pm 0.02) \log (M_*/10^6 M_\odot)$ 11
- 1.8 (a) $[\text{Mg}/\text{Fe}]$ (b) $[\text{Ca}/\text{Fe}]$ as a function of $[\text{Fe}/\text{H}]$ (figure 11 of Tolstoy, Hill, and Tosi, 2009). Blue, green, orange, and purple plots represent α -element abundances in Fornax (Shetrone et al., 2003; Letarte, 2007), Sculptor (Shetrone et al., 2003; Geisler et al., 2005; Hill and DART Collaboration, 2012), Sagittarius (McWilliam and Smecker-Hane, 2005; Monaco et al., 2005; Sbordone et al., 2007), and Carina (Shetrone et al., 2003; Koch et al., 2008). Open and filled symbols respectively denote single-slit spectroscopy measurements and multi-object spectroscopy. The small gray squares show the α -element abundances of the disk and halo of the MW (Venn et al., 2004). 12
- 1.9 $[\text{Zn}/\text{Fe}]$ as a function of $[\text{Fe}/\text{H}]$ for the Milky Way (light gray points) and LG dwarf galaxies (colored points). Boötes I: Gilmore et al. (2013), Carina: Shetrone et al. (2003) and Venn et al. (2012), Comaberenices: Frebel et al. (2010), Draco: Shetrone, Côté, and Sargent (2001) and Cohen and Huang (2009), Fornax, Leo I: Shetrone et al. (2003), Reticulum II: Ji et al. (2016a), Sagittarius: Sbordone et al. (2007), Sculptor: Shetrone et al. (2003), Geisler et al. (2005), Simon et al. (2015), Skúladóttir et al. (2015), and Skúladóttir et al. (2017), Segue I: Frebel, Simon, and Kirby (2014), Sextans: Shetrone, Côté, and Sargent (2001) and Honda et al. (2011), Ursa Major II: Frebel et al. (2010), Ursa Minor: Shetrone, Côté, and Sargent (2001), Sadakane et al. (2004), and Cohen and Huang (2010). Error bars indicate the statistical as well as systematic errors given in each reference. All data are compiled using the SAGA database (Suda et al., 2008; Suda et al., 2011; Suda et al., 2017; Yamada et al., 2013). 13
- 1.10 $[\text{Ba}/\text{Fe}]$ as a function of $[\text{Fe}/\text{H}]$ (SAGA database, Suda et al., 2008; Suda et al., 2011; Suda et al., 2017; Yamada et al., 2013). Ba abundances are corrected to be $[\text{Ba}/\text{Eu}] = -0.89$ to remove the s -process contribution. Black, blue, and red plots respectively represent $[\text{Ba}/\text{Fe}]$ ratios in the MW, Reticulum II, and the other LG dwarf galaxies (Carina, Draco, Leo I, Sculptor, Ursa Minor, Boötes I, Leo IV, Ursa Major II, Comaberenices, and Sextans). 15

1.11	A galaxy within a halo in the simulation (figure 1 of Schaye et al., 2015). From blue to red, color shows gas temperature. The inset denote zoomed-in image of a galaxy formed in the simulation. . . .	17
1.12	Structure of this thesis.	22
2.1	Evolution of model s000. Upper panels: snapshots of slice gas density in log scale, between 10^{-4} cm^{-3} (blue) and 10^2 cm^{-3} (red). Lower panels: snapshots of stellar surface density with log scale, between $10^{-10} 10^{10} M_{\odot} \text{ kpc}^{-2}$ (black) and $10^{-3.5} 10^{10} M_{\odot} \text{ kpc}^{-2}$ (white).	33
2.2	Radial profiles of model s000 at $t = 0$ Gyr (green), 1 Gyr (blue), 5 Gyr (magenta), and 10 Gyr (red). (a) Radial dark matter density profile. (b) Radial gas density profile. (c) Radial stellar density profile. (d) Radial stellar velocity dispersion profile. Black dots are observed stellar velocity dispersion in the Fornax dSph (Walker et al., 2009).	34
2.3	The SFR as a function of time for our models. Red and magenta-dashed curves represent the SFR of models s000 and mExt, respectively. Blue and green-dashed histograms represent the observed SFR of the Fornax dSph (de Boer et al., 2012a) and the Sculptor dSph (de Boer et al., 2012b), respectively.	35
2.4	Metallicity distribution of model s000 (red curve), model s000 but $[\text{Fe}/\text{H}]$ is shifted to 0.5 dex taking into account the effect of SNe Ia (magenta-dashed curve), the observed value of the Fornax dSph (blue histogram) (Kirby et al., 2010), and the Sculptor dSph (green histogram) (Kirby et al., 2009; Kirby et al., 2010; Kirby and Cohen, 2012).	36
2.5	$[\text{Eu}/\text{Fe}]$ as a function of $[\text{Fe}/\text{H}]$ of model s000. Contour is the number of stars produced in our model, between 0 (purple) and 20 (red). Yellow curve is the median of model prediction. Dash-dotted curves are the first and third quartiles, respectively. Circles are the observed value of the Galactic halo stars (SAGA database, Suda et al., 2008; Suda et al., 2011; Yamada et al., 2013). Squares are the observed value of stars in Carina, Draco, Leo I, Sculptor, and Ursa Minor dSphs (SAGA database, Suda et al., 2017). Stars produced by our model are plotted within 0.5 kpc from the center of our model galaxies. . . .	38
2.6	(a) $[\text{Fe}/\text{H}]$ as a function of time from the start of the simulation of model s000. (b) $[\text{Eu}/\text{H}]$ as a function of time from the start of the simulation of model s000. Black circles are stars formed from gas particles, which are affected by one CCSN. Contour is the same as Figure 2.5.	39
2.7	$[\text{Eu}/\text{Fe}]$ as a function of $[\text{Fe}/\text{H}]$ of the model m000. Symbols are the same as Figure 2.5.	41
2.8	$[\text{Eu}/\text{Fe}]$ distribution of stars with $[\text{Fe}/\text{H}] < -2.0$ of our models (black histogram) and observation (red histogram: the Galactic halo stars, blue histogram: Carina, Draco, Leo I, Sculptor, and Ursa Minor dSphs). Data are compiled by SAGA database (Suda et al., 2008; Suda et al., 2011; Suda et al., 2017; Yamada et al., 2013). Left panel: plotted model is s000 (without metal mixing in SF region). Right panel: plotted model is m000 (with metal mixing in SF region). . . .	42

2.9	(a) Median [Eu/Fe] as a function of [Fe/H] produced by the different number of nearest neighbor particles (N_{ngb}). Solid curves are the median of model prediction and dashed curves are the first and third quartiles. Red curve represents mN16 ($N_{\text{ngb}} = 16$). Black curve represents m000 ($N_{\text{ngb}} = 32$). Green curve represents mN64 ($N_{\text{ngb}} = 64$). Blue curve represents s000 (without metal mixing in SF region). (b) Median [Eu/Fe] as a function of [Fe/H] produced by different initial number of particles (N). Red curve represents m014 ($N = 2^{14}$). Green curve represents m016 ($N = 2^{16}$). Blue curve represents m017 ($N = 2^{17}$). Sky blue curve represents m018 ($N = 2^{18}$). Black curve represents m000 ($N = 2^{19}$).	43
2.10	[Eu/Fe] as a function of [Fe/H] of model mExt ($M_{\text{tot}} = 7 \times 10^8 M_{\odot}$, $c_{\star} = 0.033$, $n_{\text{th}} = 0.1 \text{ cm}^{-3}$, $\epsilon_{\text{SN}} = 3 \times 10^{49} \text{ erg}$, and $t = 100 \text{ Myr}$). Symbols are the same as Figure 2.5.	45
2.11	[Eu/Fe] as a function of [Fe/H] with different merger times of NSMs. (a): mt10 ($t_{\text{NSM}} = 10 \text{ Myr}$). (b): mt500 ($t_{\text{NSM}} = 500 \text{ Myr}$). Symbols are the same as Figure 2.5.	47
2.12	[Fe/H] as a function of time of model m000. The horizontal axis is plotted from 600 Myr from the start of the simulation. Black curve is the average of the metallicity in each age. Contour is the same as Figure 2.5.	48
2.13	[Eu/Fe] as a function of time with different rate of NSMs. (a): mr0.001 ($f_{\text{NSM}} = 0.001$). (b): mr0.1 ($f_{\text{NSM}} = 0.1$). Symbols are the same as Figure 2.5.	50
3.1	Initial density profiles of dark matter particles. (a) Radial dark matter profiles of models with different initial densities. Red, green, blue, and orange curves represent models A, B, C, and D, respectively. (b) The same as those in (a) but for different total masses. Red, cyan, and magenta curves represent models A, E, and F, respectively. . . .	58
3.2	Stellar metallicity distribution functions at 14 Gyr. (a) MDFs of models with different initial densities. Red, green, blue, and orange curves represent models A, B, C, and D, respectively. (b) The same as those in (a) but for different total masses. Red, cyan, and magenta curves represent models A, E, and F, respectively.	59
3.3	Gas MDFs at 0.2 Gyr from the onset of SF. This time roughly corresponds to the time when the first NSM occurs. (a) Gas MDFs of models with different initial densities. Red, green, blue, and orange curves represent models A, B, C, and D, respectively. (b) The same as those in (a) but for different total masses. Red, cyan, and magenta curves represent models A, E, and F, respectively.	60

- 3.4 Stellar mass–metallicity relation for models and the LG dwarf galaxies. Large, colored dots stand for 0.4 dex shifted metallicity to account for lack of SNe Ia in models A (red filled circle), B (green filled circle), C (blue filled circle), D (orange inverted triangle), E (cyan filled square), and F (magenta filled square). Small colored dots stand for the same models, but their metallicity is not corrected. Black diamonds, triangles, and squares with error bars are the observed value of the MW dSphs, M31 dSphs, and the LG dIrrs, respectively (Kirby et al., 2013, K13). The sky-blue dot–dashed line represents the least square fitting of the samples of (Dekel and Woo, 2003, D03): $[\text{Fe}/\text{H}] \propto M_*^{0.40}$. The purple dashed line represents the least-square fitting of K13: $\langle [\text{Fe}/\text{H}] \rangle = (-1.69 \pm 0.04) + (0.30 \pm 0.02) \log (M_*/10^6 M_\odot)$. The green line represents the least-square fitting of models except for model D: $\langle [\text{Fe}/\text{H}] \rangle = (-1.93 \pm 0.05) + (0.50 \pm 0.04) \log (M_*/10^6 M_\odot)$. 62
- 3.5 $[\text{Mg}/\text{Fe}]$ as a function of $[\text{Fe}/\text{H}]$ for stars predicted by models after 1 Gyr evolution, i.e., before the onset of SNe Ia. The time of the onset of SF from the start of the simulation in models A, B, C, D, E, and F is 0.21, 0.06, 0.02, 0.02, 0.27, and 0.10 Gyr, respectively. We plot models A, B, C, and D, E, F from left to right in top and bottom panels, respectively. Gray scales are the number of stars predicted in our models, between 1 (black) and 100 (white). The small dots are the observed value of the MW halo stars. Red, blue, green, cyan, magenta, and orange dots are the observed value of Carina, Draco, Fornax, Leo I, Sculptor, and Ursa Minor dwarf galaxies, respectively. We compile all data in SAGA database (Suda et al., 2008; Suda et al., 2011; Suda et al., 2014; Yamada et al., 2013). 63
- 3.6 Standard deviation of stellar $[\text{Mg}/\text{Fe}]$ (σ) as a function of $[\text{Fe}/\text{H}]$ after 1 Gyr from the onset of SF. Red, green, blue, orange, cyan, and magenta curves represent models A, B, C, D, E, and F, respectively. 64
- 3.7 $[\text{Mg}/\text{Fe}]$ as a function of $[\text{Fe}/\text{H}]$ for gas computed by models at 1 Gyr from the onset of SF. We plot models A, B, C, and D, E, F from left to right in top and bottom panels, respectively. Contours are the mass fraction of gas. 65
- 3.8 SFRs as a function of time. Red, green, blue and orange curves show models A, B, C, and D, respectively. Vertical dotted lines show the time 1 Gyr after the formation of first stars in each model. These lines correspond to the time when Figure 3.10 is plotted. Vertical dotted lines of model C (blue), and D (orange) are overlapped. 67
- 3.9 The mean stellar $[\text{Fe}/\text{H}]$ as a function of time (solid curves). Red, green, blue and orange curves show models A, B, C, and D, respectively. Vertical lines are the dispersion of 2σ . We plot these lines when the number of stars is more than two. Around 0.1 Gyr, there is only one star in model C in each bin. Crosses indicate the value of $[\text{Fe}/\text{H}]_0$. Vertical dotted lines show the time 1 Gyr after the formation of first stars in each model. These lines correspond to the time when Figure 3.10 is plotted. Vertical dotted lines of model C (blue), and D (orange) are overlapped. 68

3.10	[Eu/Fe] as a function of [Fe/H] for stars predicted by models with different central density after 1 Gyr from the onset of SF. We plot models A to D from left to right. Gray scales are the number of stars predicted in our models, between 1 (black) and 10 (white). The small dots are the observed value of the MW halo stars (e.g., Roederer et al., 2014). Red, blue, green, cyan, magenta, and orange dots are the observed value of Carina (Shetrone et al., 2003; Lemasle et al., 2012; Venn et al., 2012), Draco (Shetrone, Côté, and Sargent, 2001; Cohen and Huang, 2009), Fornax (Lemasle et al., 2012), Leo I (Shetrone et al., 2003), Sculptor (Shetrone et al., 2003; Geisler et al., 2005) and Ursa Minor (Shetrone, Côté, and Sargent, 2001; Sadakane et al., 2004; Cohen and Huang, 2010) dwarf galaxies, respectively. All data are compiled in SAGA data base (Suda et al., 2008; Suda et al., 2011; Suda et al., 2014; Yamada et al., 2013).	70
3.11	Standard deviation of [Eu/Fe] (σ) as a function of [Fe/H] after 1 Gyr from the onset of SF. Red, green, blue, and orange curves represent models A, B, C, and D, respectively.	72
3.12	SFRs as a function of time. Red, cyan, and magenta curves show models A, E, and F, respectively. Vertical dotted lines show the time 1 Gyr after the formation of first stars in each model.	73
3.13	The mean stellar [Fe/H] as a function of time (solid curves). Red, cyan, and magenta curves show models A, E, and F, respectively. Symbols and lines are the same as in Figure 3.9.	74
3.14	[Eu/Fe] as a function of [Fe/H] for stars. From left to right, we plot models A, E, and F. We plot models in three left-hand panels at 1 Gyr after the onset of SF. We plot model F in the rightmost panel at 3 Gyr from the start of the simulation. Symbols are the same as in Figure 3.10.	76
3.15	Standard deviation of [Eu/Fe] (σ) as a function of [Fe/H] after 1 Gyr for models A, E, and 3 Gyr for model F from the onset of SF. Red, cyan and magenta curves represent models A, E, and F, respectively.	78
3.16	[Eu/Fe] as a function of [Fe/H] for stars produced by NSMs with a merger time of 10 Myr after 1 Gyr from the onset of SF. From left to right, we plot models A ₁₀ , B ₁₀ , C ₁₀ , and D ₁₀ . Symbols are the same as Figure 3.10.	79
3.17	[Eu/Fe] as a function of [Fe/H] for stars produced by NSMs with a merger time of 500 Myr after 1 Gyr from the onset of SF. From left to right, we plot models A ₅₀₀ , B ₅₀₀ , C ₅₀₀ , and D ₅₀₀ . Symbols are the same as Figure 3.10.	81
4.1	The IMF integrated yields of [Zn/Fe] as a function of metallicity. Blue circles, green squares, and red triangles connected with solid lines represent the IMF weighted yields of ECSNe, HNe, and CCSNe, respectively. The ECSN yields are taken from Wanajo et al. (2018). The HN and CCSN yields are taken from N13. The red dashed line shows the CCSN yields of CL04. Yields for $Z = 0$ are plotted at $\log_{10}(Z/Z_{\odot}) = -5.6$. We adopt $Z_{\odot} = 0.0134$ (Asplund et al., 2009).	90

4.2	Production factors of Zn isotopes. Blue circles, green squares, and red triangles connected with solid lines represent the production factors of ECSNe ($8.8 M_{\odot}$), HNe ($25 M_{\odot}$), and CCSNe ($15 M_{\odot}$) at the solar metallicity, respectively. Green and red dashed lines denote the production factors of HNe ($25 M_{\odot}$) and CCSNe ($15 M_{\odot}$) at $Z = 0$, respectively. Yields of isotopes are taken from (Wanajo et al., 2018) for ECSNe and N13 for HNe and CCSNe. The black dotted line indicates the production factor of 10 that is taken as the lower bound for each astrophysical site to be a main contributor of a given isotope (e.g., Woosley and Heger, 2007).	91
4.3	Time variations of SFRs in model G (red curve). The green line shows the SFH of the Sculptor dSph estimated from the color-magnitude diagram (de Boer et al., 2012b).	93
4.4	Predicted and observed metallicity distribution functions. The red histogram represents the metallicity distribution function of model G at 13.8 Gyr from the beginning of the simulation. The green dashed, and blue dash-dotted histograms show the observed metallicity distribution functions of the Sculptor and Leo I dSphs (Kirby et al., 2009; Kirby et al., 2010; Kirby and Cohen, 2012). All observed data are compiled using the SAGA database (Suda et al., 2017).	94
4.5	[Mg/Fe] as a function of [Fe/H] in model G. The color-coded stellar mass fractions are displayed in the logarithmic scale. The solid black curves show that the median values of computed data at each [Fe/H] bin. The dotted curves show the 5 % and 95 % significance levels. Gray dots represent the observed values for Sculptor dSph (Kirby et al., 2010). We plot observed values with internal errors of $\Delta[\text{Fe}/\text{H}] < 0.15$, $\Delta[\text{Mg}/\text{Fe}] < 0.30$ to be consistent with high resolution data (Hill et al. in prep) following Hill and DART Collaboration (2012).	95
4.6	Same as Figure 4.5, but for [Zn/Fe] as a function of [Fe/H] in model G. Black dots denote observed values of Sculptor dSph (Shetrone et al., 2003; Geisler et al., 2005; Simon et al., 2015; Skúladóttir et al., 2015; Skúladóttir et al., 2017). Typical error bars of the observation (Skúladóttir et al., 2017) are shown in the top right corner of the figure. The red points show the average values of [Zn/Fe] in the MW halo stars (Saito et al., 2009). The vertical error bars on red points indicate the difference between the maximum and minimum values of [Zn/Fe] in each metallicity bin. The horizontal bars on red points represent the range of [Fe/H] in each bin.	97
4.7	(a) [Fe/H] and (b) [Zn/Fe] as a function of time in model G. The color-coded stellar mass fractions are displayed in the logarithmic scale.	99
4.8	Same as Figure 4.6 but for (a) model H and (b) model I. Model H adopts the metallicity dependent mass range of ECSN progenitors computed by the stellar evolution model in Poelarends (2007). Model I assumes that stars from 8.5 to $9.0 M_{\odot}$ become ECSNe in all the metallicity range.	100

4.9	Standard deviations (σ) of [Mg/Fe] (the red solid curve) and [Zn/Fe] (the blue dotted curve) as a function of [Fe/H] in model G.	101
4.10	Same as Figure 4.6 but for the models without ECSNe. Panels (a) and (b) represent the models with $f_{\text{HN}} = 0.5$ and 0.05 (models J and K, respectively).	103
4.11	Same as Figure 4.6 but for the models without HNe. Panels (a) and (b) represent models L and M, respectively.	104
5.1	Stellar [Mg/Fe] as a function of [Fe/H]. Panels (a), (b), (c), (d), and (e) represent the results of models d1000, d0100, d0010, d0001, and d0000, respectively. Panel (f) represents observational data. The red hatched area shows the region that there are no stars with Mg. Color contours show computed stellar abundances in the logarithm of a mass fraction in each grid. The black dots represent the observed abundances of the MW. The colored dots represent the observed abundances of the LG dwarf galaxies (green: Carina, blue: Draco, purple: Leo I, magenta: Sculptor, ocher: Ursa Minor, orange: Boötes I, dark green: Leo IV, grass green: Ursa Major II, sky-blue: Coma Berenices, red-purple: Sextans, and red: Reticulum II). We compile all observed data using the SAGA database (Suda et al., 2008; Suda et al., 2011; Suda et al., 2014; Yamada et al., 2013).	111
5.2	Stellar [Ba/Fe] as a function of [Fe/H]. Panels (a), (b), (c), (d), and (e) represent the results of models d1000, d0100, d0010, d0001, and d0000, respectively. Panel (f) represents observational data. The red hatched area shows the region in which there are no stars with Ba in dSphs except for the Reticulum II UFD. The symbols are the same as in Figure 5.1. We correct the observational value of [Ba/Eu] to be -0.89 for all stars with $[\text{Fe}/\text{H}] > -2.75$. We compile all observed data using the SAGA database (Suda et al., 2008; Suda et al., 2011; Suda et al., 2014; Yamada et al., 2013).	112
5.3	Same as Figure 4.6 but for the different efficiencies of metal mixing. Panels (a) and (b) show models d0010 ($C_d = 0.001$) and d1000 ($C_d = 0.1$), respectively.	113
6.1	Stellar and gas surface density at $z = 2.0$. Top left panel shows face-on view of stellar surface density. Top right panel shows face-on view of gas surface density. Bottom left panel shows edge-on view of stellar surface density. Bottom right panel shows edge-on view of gas surface density. From black to white, the color scale denotes surface density from $10^{1.0}$ to $10^{3.8} M_{\odot} \text{pc}^{-2}$	120
6.2	Time variations of SFRs. The SFRs are plotted within 30 kpc from the center of the galaxy. The black curve denotes the total SFR. Colored curves represent formation rates of stars with different metallicities. Red, green, blue, and orange curves denote formation rates of stars with $-1 < [\text{Fe}/\text{H}] \leq 0$, $-2 < [\text{Fe}/\text{H}] \leq -1$, $-3 < [\text{Fe}/\text{H}] \leq -2$, and $[\text{Fe}/\text{H}] \leq -3$, respectively.	121

6.3	Metallicity distribution of the halo. We plot the metallicity distribution within 30 kpc from the galactic center and 1 kpc above the galactic disk.	122
6.4	[Mg/Fe] as a function of [Fe/H] within 30 kpc from the center of the galaxy. The color scale is the same as in Figure 4.6.	123
6.5	[Eu/Fe] as a function of [Fe/H] within 30 kpc from the center of the galaxy. The color scale is the same as in Figure 4.6.	124
7.1	The scenario proposed in this thesis.	129
A.1	Radial profiles of models of different parameters at $t = 5.0$ Gyr. Red triangles, green diamonds, blue pentagons, and magenta hexagons represent model s000, sn10 ($n_{\text{th}} = 10 \text{ cm}^{-3}$), c050s ($c_{\star} = 0.5$), and se01 ($\epsilon_{\text{SN}} = 10^{50} \text{ erg}$), respectively. (a): Radial dark matter density profile. (b): Radial gas density profile. (c): Radial stellar density profile. (d): Radial velocity dispersion profile.	134
A.2	The SFR as a function of time for our models. Red curve, green dashed curve, blue short-dashed curve, and magenta dotted curve represent models s000, sn10 ($n_{\text{th}} = 10 \text{ cm}^{-3}$), sc50 ($c_{\star} = 0.5$), and se01 ($\epsilon_{\text{SN}} = 10^{50} \text{ erg}$), respectively. The black histogram and black-dotted histogram represent the observed SFR of the Fornax dSph (de Boer et al., 2012a) and the Sculptor dSph (de Boer et al., 2012b), respectively.	136
A.3	Metallicity distribution of our models. The black histogram and black-dotted histogram are observed metallicity distribution of the Fornax dSph (Kirby et al., 2010) and the Sculptor dSph (Kirby et al., 2009; Kirby et al., 2010; Kirby and Cohen, 2012), respectively. Red curve, green dashed curve, blue dashed-dotted curve, and magenta dashed-dotted-dotted curve represent s000, sn10 ($n_{\text{th}} = 10 \text{ cm}^{-3}$), sc50 ($c_{\star} = 0.5$), and se01 ($\epsilon_{\text{SN}} = 10^{50} \text{ erg}$), respectively.	137
B.1	Radial density profiles of dark matter (black), gas (red) and stars (blue) at 13.8 Gyr from the beginning of the simulation. Solid and dashed curves denote the model G and Q. Both curves are mostly overlapped.	141
B.2	Time variations of SFRs in model G (blue) and Q (red).	142
C.1	Comparison of the [Zn/Fe] evolution for the models assuming different SN yields. Model G (red curves) adopts the nucleosynthesis yield of N13. Model N (blue curves) adopts the yield of CL04. Solid curves show the median values. Dotted curves indicate the 5 % and 95 % significance levels at each [Fe/H] bin.	144
C.2	Same as Figure C.1 but for models with different resolution. Red, green, and blue curves represent models G ($N = 2^{18}$), O ($N = 2^{17}$), and P ($N = 2^{16}$), respectively.	145

List of Tables

1.1	Parameters of baryon physics.	21
2.1	Parameters of the initial condition.	30
2.2	List of models discussed in this chapter.	31
2.3	Mass of metal mixing region.	44
2.4	List of yields.	49
3.1	List of our models discussed in this chapter.	56
3.2	Final properties of our models. From left to right the columns show model name, stellar mass, median metallicity, and standard deviation of MDF.	59
4.1	The mass ranges of ECSN progenitors.	88
4.2	Yields of Fe and Zn of each type of SN.	89
4.3	List of models discussed in this chapter.	92
5.1	Adopted value of the scaling factor for metal diffusion.	109
A.1	List of models.	134
B.1	List of models discussed in Appendix B.	140
C.1	List of models discussed in Appendix C.	143

List of Abbreviations

CCSN	C ore- C ollapse S upernova
CCSNe	C ore- C ollapse S upernovae
dIrr	d warf I rregular galaxy
DISPH	D ensity I ndependent S moothed P article H ydrodynamics
dSph	d warf S pheroidal galaxy
FAST	F ully A synchronous S plit T ime-integrator
GMC	G iant M olecular C louds
GRB	G amma R ay B urst
HN	H ypernova
HNe	H ypernovae
IMF	I nitial M ass F unction
ISM	I nter S tellar M edium
LG	L ocal G roup
MDF	M etallicity D istribution F unction
MW	M ilky W ay
NSM	N eutron S tar M erger
SF	S tar F ormation
SFE	S tar F ormation E fficiency
SFH	S tar F ormation H istory
SFR	S tar F ormation R ate
SN	S upernova
SNe Ia	T ype Ia S upernovae
SNe	S upernovae
SPH	S moothed P article H ydrodynamics
SSP	S ingle S tellar P opulation
UFD	U ltra- F aint D warf galaxy
WD	W hite D warf

Physical Constants

Boltzmann constant	$k_B = 1.381 \times 10^{-16} \text{ erg K}^{-1}$
Gravitational constant	$G = 6.672 \times 10^{-8} \text{ dyn cm}^2 \text{ g}^{-2}$
Parsec	$\text{pc} = 3.085 \times 10^{18} \text{ cm}$
Solar mass	$M_\odot = 1.989 \times 10^{33} \text{ g}$
Baryon density	$\Omega_b = 0.0484$
Dark energy density	$\Omega_\Lambda = 0.692$
Total matter density	$\Omega_m = 0.308$
Hubble constant	$H_0 = 67.8 \text{ km s}^{-1}$
Matter power spectrum	$\sigma = 0.815 \text{ km s}^{-1}$
Tilted scalar spectral index	$n_s = 0.968$

List of Symbols

A	The mass number of nucleus	
c_\star	Dimensionless star formation efficiency parameter	
f_b	Baryon fraction	
f_{NSM}	Number fraction of neutron star mergers	
f_{poll}	Metal pollution factor	
m_{DM}	Mass of one dark matter particle	M_\odot
m_{gas}	Mass of one gas particle	M_\odot
m_\star	Mass of one star particle	M_\odot
M_{DM}	Dark matter halo mass	M_\odot
M_{gas}	Total gas mass	M_\odot
M_{mix}	Gas mass used for metal mixing	M_\odot
M_{poll}	Gas mass polluted by supernovae	M_\odot
M_{sw}	Gas mass swept up by a supernova	M_\odot
M_{tot}	Total halo mass	M_\odot
M_\star	Stellar mass	M_\odot
N_{ngb}	Number of nearest neighbor particles	
N_{SN}	Number of supernovae	
N_\star	Number of stars	
n_{th}	Threshold density for star formation	cm^{-3}
q	Energy density	erg cm^{-3}
r_c	Core radius	kpc
r_{max}	Initial outer radius	kpc
t_β	Timescale of β -decay	s
t_{dyn}	Dynamical time	Myr
t_{mix}	Timescale of metal mixing	Myr
t_n	Timescale of neutron-capture	s
t_{NSM}	Neutron star merger time	Myr
T_{th}	Threshold temperature for star formation	K
U	Internal energy	erg
Y_e	Electron fraction	
Z	Metallicity	
z	Redshift	
α	^4He	
ϵ_{SN}	supernova explosion energy	erg
ρ	Central density	
τ	Expansion timescale	ms

Dedicated to my family

Chapter 1

Introduction

Understanding the enrichment of heavy elements in galaxies helps us clarify the astrophysical sites of elements and chemodynamical evolution of galaxies. At the time of the big-bang, the Universe consists of hydrogen, helium, and lithium. Explosive events such as supernovae (SNe) and neutron star mergers (NSMs) distribute heavy elements to the interstellar medium (ISM). Stars are formed from the gas containing these elements. Abundances of heavy elements in stars, therefore, reflect the astrophysical sites of these elements and star formation histories (SFHs) in galaxies.

Dwarf galaxies are the ideal sites to study enrichment of heavy elements. According to the hierarchical structure formation scenario, galaxies are formed from clustering of smaller systems (e.g., White and Rees, 1978; Blumenthal et al., 1984; Springel et al., 2008). Dwarf galaxies would be survivors from the early stages of galaxy formation. In the Local Group (LG), over 100 dwarf galaxies are observed (e.g., McConnachie, 2012). These galaxies with resolved stellar populations give us clues to understand the astrophysical sites of heavy elements and chemodynamical evolution of galaxies.

In this thesis, we focus on the enrichment of elements synthesized by the rapid neutron-capture process (*r*-process elements) and zinc (Zn) in dwarf galaxies. These elements show characteristic features in the chemical abundances of metal-poor stars. In this chapter, we review the astrophysical sites of elements, observed LG galaxies, formation and evolution of galaxies.

1.1 Astrophysical sites of elements

1.1.1 Solar system abundances

The solar system abundances give us information of the astrophysical sites of elements. The chemical compositions of the Sun can be determined by the absorption lines in the solar photosphere or CI chondrites (e.g., Asplund et al., 2009). Figure 1.1 shows the solar system isotopic abundances determined by CI chondrites (Lodders, 2003). As shown in this figure, the abundances exponentially decline to mass number, $A \sim 100$ and constant after that. There is the strong peak at $A = 56$ because the ^{56}Fe nucleus is the most stable nucleus among all isotopes. The peaks at $A = 80, 130, 196$ and $A = 90, 138, 208$ are due to the *r*-process and the slow neutron-capture process (*s*-process), respectively. These peaks come from the magic number ($N = 50, 82, 126$) of the nucleus.

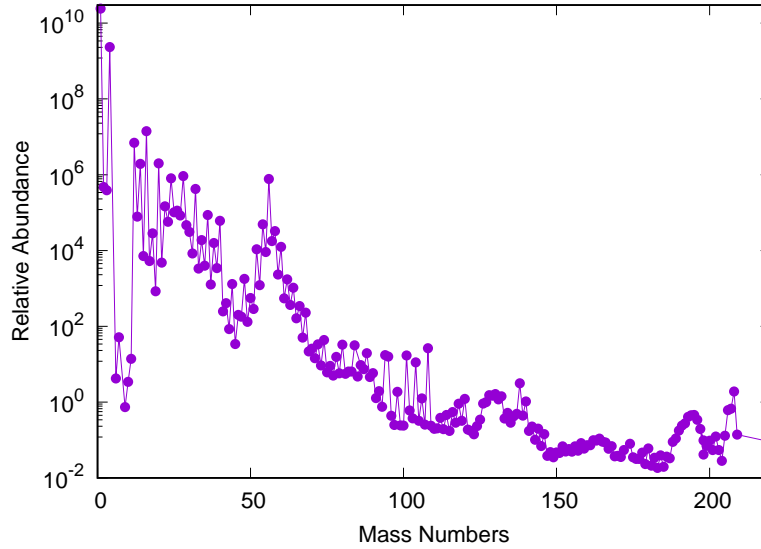


FIGURE 1.1: The solar isotopic abundances relative to silicon (Si) abundance as a function of mass numbers (Lodders, 2003). The Si abundance is set to be 10^6 .

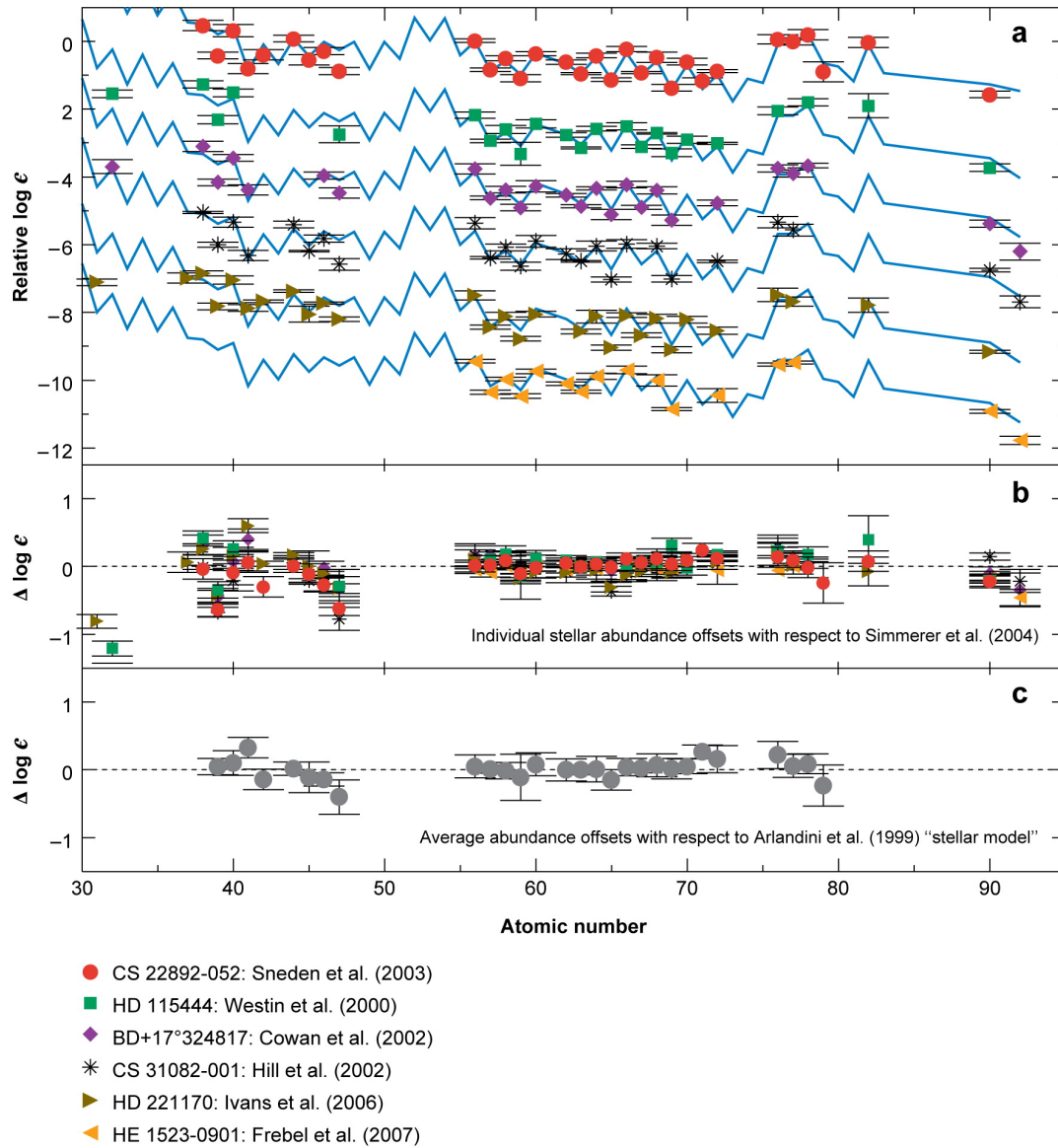
The solar system abundance patterns of r -process elements match those of metal-poor stars (e.g., Sneden, Cowan, and Gallino, 2008). Figure 1.2 compares the abundance patterns of r -process elements in the Sun and metal-poor stars. According to this figure, elements from $50 \leq A < 90$ exactly matches the solar system abundance pattern in metal-poor stars. Lighter and heavier r -process elements show small variations. This result indicates that these elements from $50 \leq A < 90$ are formed with the same pattern throughout the evolutionary history of galaxies.

1.1.2 Nucleosynthesis

Synthesis of elements in the Universe has three paths: big bang, stellar nucleosynthesis, and destruction of a nucleus by a cosmic ray. Elements from H to Li are synthesized by big-bang. No stable isotopes in the mass number of 5 and 6 prevent forming heavier elements except for ${}^7\text{Li}$. Destruction of a nucleus by cosmic ray synthesize small kinds of elements such as Be and B.

Heavier elements are synthesized in the stars. Stellar nucleosynthesis was systematically studied in Burbidge et al. (1957) and Cameron (1957). Major burning stages in stars synthesize elements from He to Fe. The proton-proton chain and CNO cycle in hydrogen burning convert four ${}^1\text{H}$ to ${}^4\text{He}$ (α). Later stages of stellar evolution have He, C, O, ... burning stages. These burning stages synthesize elements up to iron-peak elements. However, it is difficult to synthesize isotopes heavier than ${}^{56}\text{Fe}$ because the binding energy of a nucleus is maximum around this mass number.

Elements heavier than iron-peak are mainly synthesized by the capture of neutrons (n). The neutron-capture processes are divided into two processes. If the timescale




 Sneden C, et al. 2008.
Annu. Rev. Astron. Astrophys. 46:241–88

FIGURE 1.2: (a) Comparison of solar r -process abundance patterns with r -rich metal-poor stars (figure 7 of Sneden, Cowan, and Gallino, 2008). The solid light blue curves represent the scaled solar r -process abundance pattern (Simmerer et al., 2004), normalized by the Eu abundance. The abundances except for CS 22892-052 is shifted for comparison. (b) Difference of individual stars and solar r -process abundances. The dashed horizontal line denotes the zero offset. (c) Offset of average stellar abundance from the stellar model pattern of Arlandini et al. (1999).

of β -decay (t_β) is shorter than the timescale of neutron-capture (t_n), elements are synthesized along with the stable isotopes (s -process). The s -process cannot synthesize isotopes heavier than ^{209}Bi , which is the most stable isotope.

The other neutron-capture process, the r -process occurs when $t_\beta \gg t_n$. Nucleosynthesis in the r -process occurs along with the nuclear limit lines. For the r -process, the neutron-rich environment is required. Kratz et al. (1993) showed that the number density of neutron should be $\sim 10^{20} - 10^{30} \text{ cm}^{-3}$ for the r -process to reproduce the solar abundances of r -process elements. The electron fraction (Y_e) indicates the proton-to-neutron ratio. If $Y_e < 0.5$, the number of neutrons is larger than that of protons. Wanajo (2013) showed that the condition to synthesize elements beyond the third peak ($A \sim 196$) is $Y_e < 0.2$ if the asymptotic entropy (S) is less than $100 k_B \text{ nucleon}^{-1}$, where k_B is the Boltzmann constant. High entropy environment is also suitable for the r -process. Since S is proportional to T^3/ρ , where T is the temperature, and ρ is the density, high entropy means that the density is low at a given temperature. This leads to be more difficult to synthesize seed nuclei through the reaction: $\alpha + \alpha + n \rightarrow {}^9\text{Be}$. As a result, the number of neutron per one seed nuclei becomes high. In the case of $S > 100 k_B \text{ nucleon}^{-1}$, the condition to synthesize elements heavier than third peak is $(S/230 k_B \text{ nucleon}^{-1})/((Y_e/0.4)(\tau/20\text{ms})) > 1$, where τ is the expansion timescale of the ejecta (Wanajo, 2013). The astrophysical sites of the r -process should satisfy these conditions.

1.1.3 Astrophysical sites of heavy elements

1.1.3.1 Supernovae

Massive stars explode as core-collapse supernovae (CCSNe) at the end of their life. The final fates of stars depend on the metallicity. Figure 1.3 shows final fates of stars. Stars within mass range between $8-10 M_\odot$ develop oxygen-neon-magnesium core by C-burning. In these stars, low reaction thresholds of Ne and Mg increase electron Fermi energy and electron capture triggers the gravitational collapse. These stars explode as electron capture supernovae (ECSNe). Wanajo, Janka, and Müller (2011) estimated that the upper limit of the rate of ECSNe is $\sim 4\%$ of all CCSNe.

Stars more massive than $10 M_\odot$ explode as iron CCSNe. When the core of the star reaches nuclear statistical equilibrium at $T \sim 10^{10} \text{ K}$, the dissociation of Fe-group nuclei to α particles and a growing number of free nucleons (e.g. Janka, Melson, and Summa, 2016). This causes the core collapse. The iron CCSNe are a major source of heavy elements from carbon through zinc (e.g., Woosley and Weaver, 1995; Nomoto, Kobayashi, and Tominaga, 2013).

Some fractions of stars more massive than $20 M_\odot$ explode with kinetic energy ~ 1 dex higher than that of normal CCSNe. These SNe are called hypernovae (HNe). HNe are thought to be associated with long gamma-ray bursts (GRBs). Observations of long GRBs suggest that the rate of HNe is fewer than 1 % of all type Ib/c SNe (Podsiadlowski et al., 2004b; Guetta and Della Valle, 2007). HNe can be sources of iron-peak elements (e.g., Umeda and Nomoto, 2002; Umeda and Nomoto, 2005;

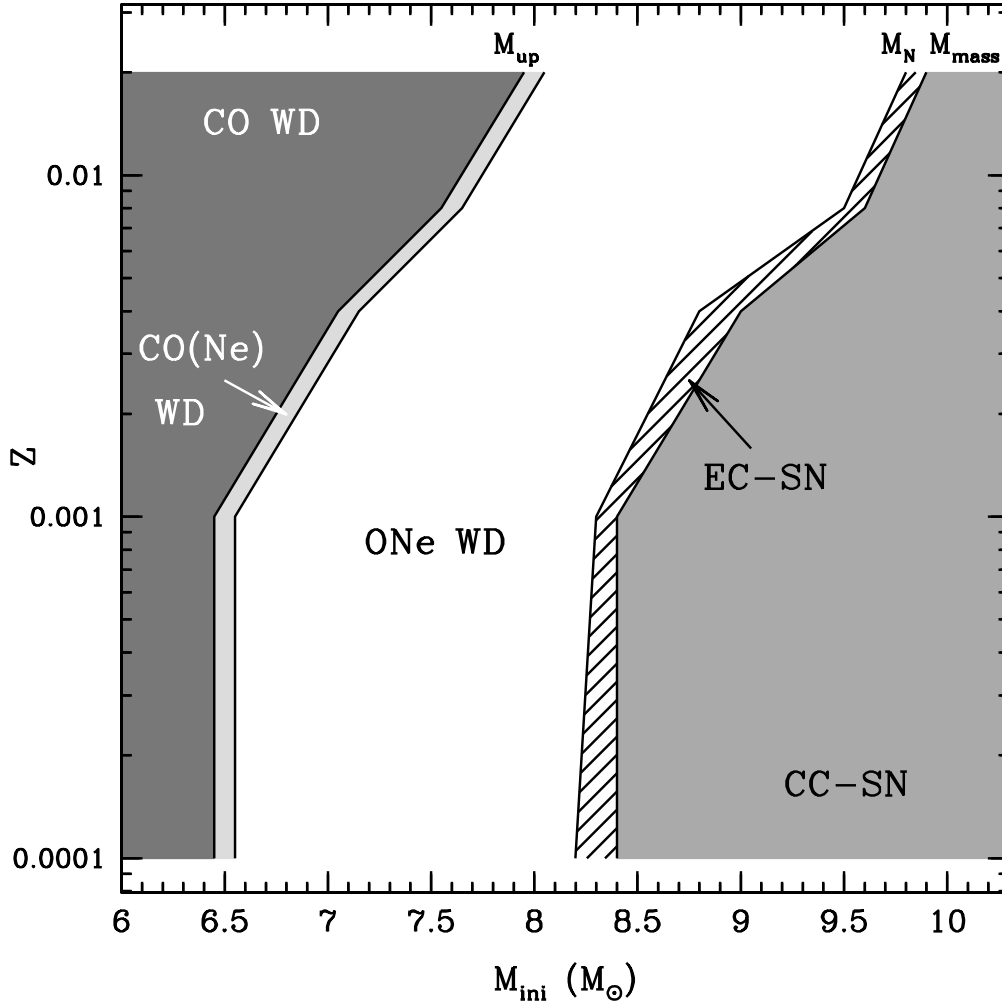


FIGURE 1.3: The metallicity dependence on final fates of stars as a function of zero-age sequence mass (M_{ini} , figure 5 of Doherty et al., 2015). The dark-gray shaded, the light-grey, white, hatched, and gray regions denote the mass range of CO white dwarfs (WDs), CO(Ne) WDs, ONe WDs, ECSNe, and iron CCSNe, respectively.

Kobayashi et al., 2006; Tominaga, Umeda, and Nomoto, 2007). The outward Si-burning region compared to normal iron CCSNe produce higher $[(\text{Zn}, \text{Co}, \text{V})/\text{Fe}]^1$, and smaller $[(\text{Mn}, \text{Cr})/\text{Fe}]$ ratios (Umeda and Nomoto, 2005).

CCSNe have long been regarded as astrophysical sites of r -process elements (e.g., Burbidge et al., 1957; Hillebrandt, Nomoto, and Wolff, 1984; Sumiyoshi et al., 2001; Wanajo et al., 2003). The r -process was thought to occur in the prompt explosion after the bounce. Recent numerical simulations, however, show that such explosion does not occur. According to the recent simulations, neutrino-heating plays an important role in the explosion of CCSNe (Janka et al., 2012). The neutrino-heating increases Y_e in SNe. Wanajo (2013) showed that the value of Y_e is typically larger than 0.4. The entropy is also not enough to synthesize r -process elements to the third peak. In models with proto-neutron star mass of $1.4 M_\odot$, the entropy is $130 k_B \text{ nucleon}^{-1}$ at 10 s after the bounce. They show that the mass of proto-neutron stars should be larger than $2.0 M_\odot$, which is too massive compared to the typical mass of neutron stars. These results suggest that CCSNe are not the suitable site for the r -process. SNe from strongly magnetized and rapidly rotating progenitors currently are the only possibility to synthesize r -process elements to the third peak (Winteler et al., 2012; Nishimura, Takiwaki, and Thielemann, 2015; Shibagaki et al., 2016). These types of SNe would have low Y_e environment which is suitable for the r -process.

1.1.3.2 Neutron star mergers

NSMs can be other major sites for the enrichment of heavy elements (e.g., Thielemann et al., 2017). Observed binary pulsars are one of the indirect evidence of the existence of NSMs. In the Milky Way (MW), there are at least four binary pulsars that merge within the Hubble time (Lorimer, 2008). Short GRBs are also thought to be associated with NSMs (e.g., Fernández and Metzger, 2016). Using these signatures, the rate of NSMs is estimated to be $1000_{-990}^{+9000} \text{ Gpc}^{-3} \text{ yr}^{-1}$ (Abadie et al., 2010b).

The first event of NSM (GW170817) is detected on August 17, 2017. Advanced LIGO/Virgo reported that two neutron stars with the total mass of $2.74 M_\odot$ are merged at the distance of 40 Mpc from the Earth (Abbott et al., 2017b). The rate of NSMs estimated from this observation is $1540_{-1220}^{+3200} \text{ Gpc}^{-3} \text{ yr}^{-1}$. After the detection of gravitational waves, the counterpart of GW170817 is detected in multi-messenger (gamma-ray, X-ray, ultraviolet, optical, infrared, and radio) observations (Abbott et al., 2017c; Abbott et al., 2017a; Goldstein et al., 2017; Savchenko et al., 2017; Soares-Santos et al., 2017; Cowperthwaite et al., 2017; Nicholl et al., 2017; Chornock et al., 2017; Margutti et al., 2017; Alexander et al., 2017; Valenti et al., 2017; Haggard et al., 2017; Tanvir et al., 2017; Díaz et al., 2017; McCully et al., 2017; Arcavi et al., 2017b; Lipunov et al., 2017; Kim et al., 2017; Arcavi et al., 2017a; Pian et al., 2017; Troja et al., 2017; Smartt et al., 2017; Utsumi et al., 2017; Li et al., 2018). Figure 1.4 shows timelines of the multi-messenger observations of GW170817. The short GRB, GRB 170817A is observed after 1.74 s after the detection of the gravitational waves (Abbott et al., 2017a). This observation confirms that NSMs are progenitors of short GRBs.

¹ $[A/B] = \log_{10}(N_A/N_B) - \log_{10}(N_A/N_B)_\odot$, where N_A and N_B are the number of the elements A and B, respectively.

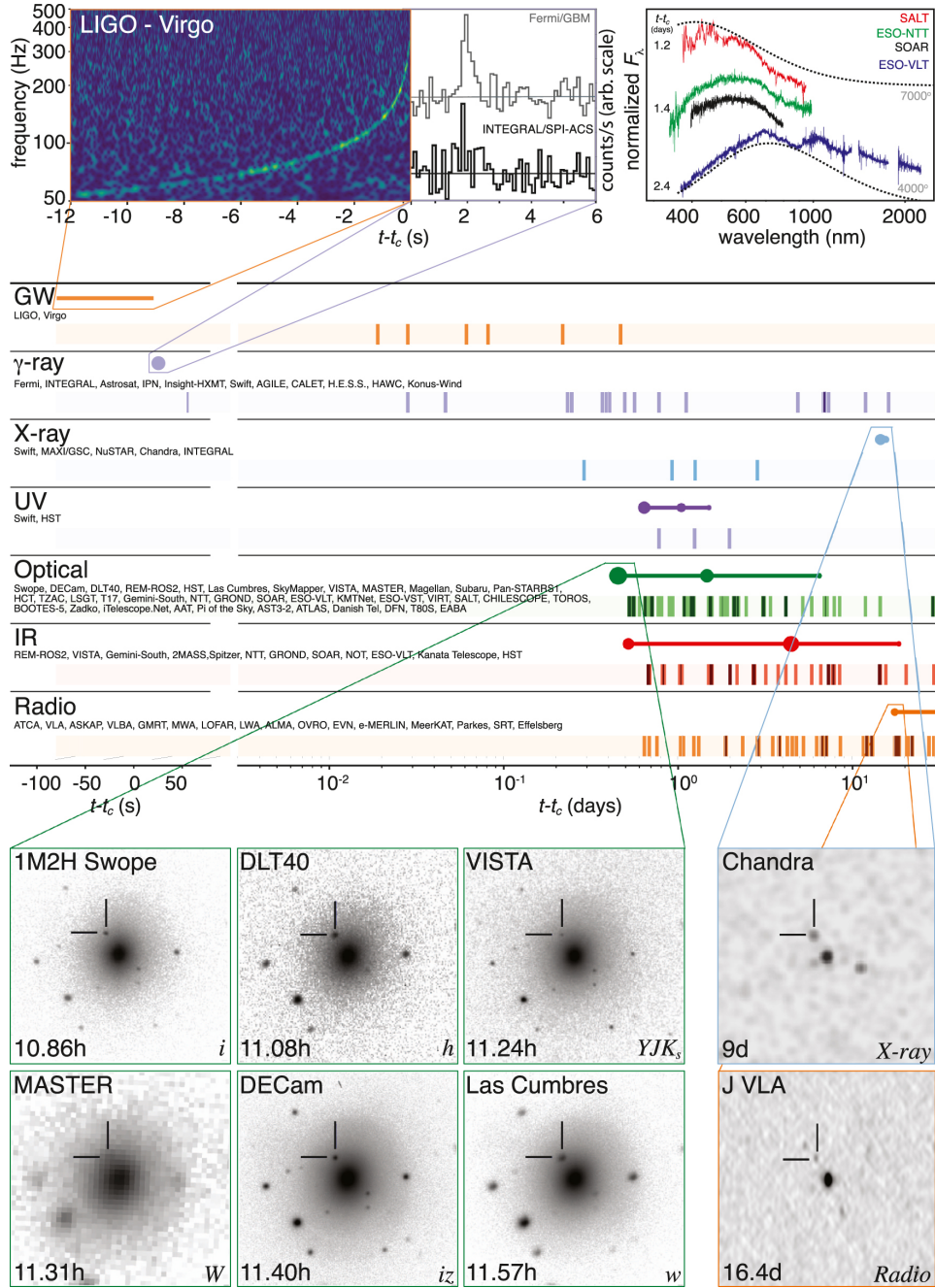


FIGURE 1.4: The timeline of the multi-messenger observations of GW170817 (figure 2 of Abbott et al., 2017c). The observing facilities, instruments, and teams are listed at the beginning of the row. The solid circles denote representative observations. The vertical solid lines indicate the source was able to detect at least one instrument. The top left magnification inset shows that frequency of gravitational waves detected by LIGO-Hanford and LIGO-Livingston as a function of time. The top middle inset represents X-ray light curve. The top right inset denotes optical/near-infrared spectra observed by SALT (red curve, McCully et al., 2017; Buckley et al., 2018), ESO-NTT (green curve, Smartt et al., 2017), the SOAR 4m telescope (black curve, Nicholl et al., 2017), and ESO-VLT-XShooter (blue curve, Smartt et al., 2017). Bottom panels illustrate optical, X-ray, and radio images of the counterpart of GW170817.

The optical counterpart, kilonova AT2017gfo is also observed after the detection of GW170817 (e.g., Smartt et al., 2017; Utsumi et al., 2017). At the early stages of the afterglow (< 2 days), the blue optical component is dominated. After this phase, the color of AT2017gfo becomes rapidly redder. This light curve is apparently different from those of SNe. Tanaka et al. (2017) performed radiative transfer simulations of the kilonova. They found that the emission is powered by the ejecta of $0.03 M_{\odot}$ which contain lanthanide elements. This is the first direct observed evidence that NSMs produce r -process elements.

Nucleosynthesis studies have shown that NSMs can synthesize r -process elements with $A \geq 110$ (e.g., Thielemann et al., 2017). Dynamical ejecta from NSMs produce materials with $Y_e < 0.1$. This ejecta is suitable for synthesizing the heavy r -process elements. However, it is not enough to explain the universality of r -process elements between the solar r -process pattern and r -process rich metal-poor stars (Snedden, Cowan, and Gallino, 2008). Newtonian simulations of NSMs showed only heavier r -process elements ($A \gtrsim 110$) are synthesized. There is no observed evidence that there are stars which have only heavy r -process elements. Recent simulations with general relativity and neutrino transport showed shock heated ejecta have relatively higher Y_e ($0.1 < Y_e < 0.4$, Wanajo et al., 2014). Wanajo et al. (2014) showed that NSMs can synthesize r -process elements in the range $90 \lesssim A \lesssim 240$ (Figure 1.5). This result suggests that NSMs are the promising sources of r -process elements in the Universe.

1.2 The Local Group galaxies

1.2.1 The observed Local Group Galaxies

The LG consists of over 100 galaxies including the MW (McConnachie, 2012). These galaxies are located within 3 Mpc from the Sun. Because they are close to the Earth, it is possible to resolve stellar populations of several galaxies in the LG. The observations of chemodynamical properties of the LG galaxies help us understand the formation and evolution of the LG galaxies.

SFHs in the LG galaxies can be estimated from color-magnitude diagrams. Weisz et al. (2014) showed that the LG dwarf galaxies have various SFHs (Figure 1.6). Their results suggested that average SFHs in dwarf spheroidal galaxies (dSphs) exponentially decline with a timescale of ~ 5 Gyr. For dwarf irregulars (dIrrs), transition dwarfs, and dwarf ellipticals, SFHs are characterized by the combination of an exponentially declining SFH with timescales of 3–4 Gyr for lookback ages > 10 –12 Gyr ago and a constant SFH after that. They also suggest that lower mass galaxies tend to stop the star formation (SF) in the early phase.

The detailed observations of the individual galaxy in the LG show that characteristic features in each galaxy. The intermediate age (1–10 Gyr) stellar populations are dominated in Fornax dSph (de Boer et al., 2012a). It also has a radial age gradient. Younger and more metal-rich populations are dominated in its central region. For Sculptor dSph, a stellar population is dominated by old and metal-poor stars (de Boer et al., 2012b). Its SFH has a peak at 13 – 14 Gyr ago and ends the SF at 7 Gyr ago. Carina dSph has episodic SFHs (e.g., de Boer et al., 2014). This would be triggered

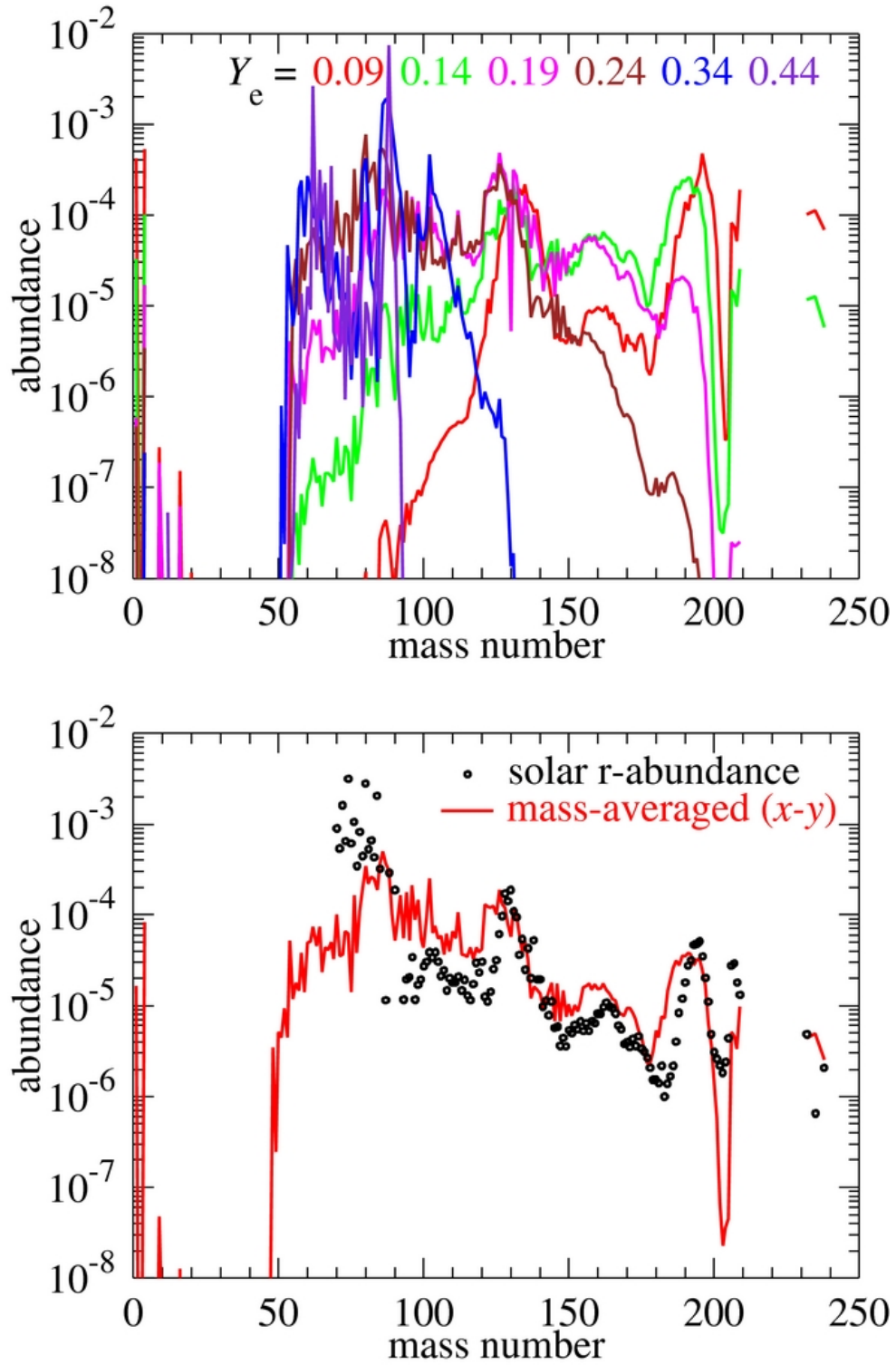


FIGURE 1.5: The comparison with solar r -process abundance patterns and yields of r -process elements from NSMs (figure 4 of Wanajo et al., 2014, reproduced by permission of the AAS). The top panel represents r -process abundance pattern in the ejecta of $Y_e = 0.09$ (the red curve), 0.14 (the light green curve), 0.19 (the magenta curve), 0.24 (the brown curve), 0.34 (the blue curve), and 0.44 (the purple curve). The bottom panel compares solar r -process abundances (black circles), and mass-averaged yields (the red curve).

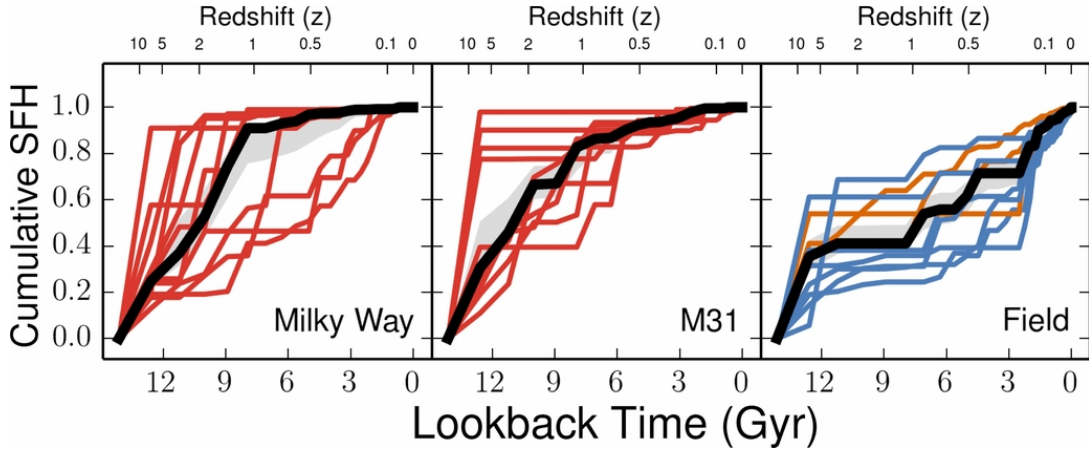


FIGURE 1.6: SFHs of the LG dwarf galaxies (figure 11 of Weisz et al., 2014, reproduced by permission of the AAS). From left to right, panels show the MW satellites, M31 satellites, and field dwarf galaxies. The black solid curve shows the average SFH of all galaxies in each field. The gray shaded region shows the error of the average SFH. Colored curves show SFHs of each galaxy.

by the interaction with the MW (Piatek et al., 2003) or gas infall (Lemasle et al., 2012).

1.2.2 Chemical abundances of Local Group dwarf galaxies

The chemical abundances of metal-poor stars in LG dwarf galaxies provide us an imprint of evolutionary histories of galaxies. Metallicity distribution functions (MDFs) are one of the fundamental indicators for the chemical evolution of galaxies. Metallicity in LG dwarf galaxies has been measured by the empirical relation between the Ca II infrared triplet and $[\text{Fe}/\text{H}]$, calibrated based on metallicities of globular clusters. Helmi et al. (2006) found that MDFs in Sculptor, Sextans, Fornax, and Carina dSphs lack stars with $[\text{Fe}/\text{H}] \lesssim -3$. Their results shed light on the question, where the extremely metal-poor (EMP) stars (stars with $[\text{Fe}/\text{H}] < -3$) in the MW halo are formed. On the other hand, Starkenburg et al. (2010) showed that the widely-used linear empirical calibration of Ca II infrared triplet strongly deviate from their revised calibration at $[\text{Fe}/\text{H}] < -2$. EMP stars currently have been found in classical dSphs with median and high resolution spectroscopy (e.g., Frebel, Kirby, and Simon, 2010; Tafelmeyer et al., 2010; Starkenburg et al., 2013). In addition, Kirby et al. (2008) found 15 EMP stars in seven UFDs. Norris et al. (2008) reported that there is a star with $[\text{Fe}/\text{H}] = -3.4$ in Boötes I UFD. These observations of EMP stars support the hierarchical structure formation scenario from Lambda (Λ) cold dark matter (CDM) cosmology. According to this scenario, dwarf galaxies dissolve to form the MW halo.

Average metallicity of galaxies correlates with their mass. The mass-metallicity relation of galaxies can be understood by the deepness of the gravitational potential well. More massive galaxies have deeper gravitational potential well and retain more gas and metals (Dekel and Silk, 1986). Dekel and Woo (2003) predicted that

metallicity (Z) and stellar mass (M_*) correlates with $Z \propto M_*^{0.4}$ by their analysis of the relation between SN feedback and mass of galaxies. They found that this relation fits well with the observed mass-metallicity relation in LG dwarf galaxies. Kirby et al. (2013) measured metallicities of red-giants in 15 MW dSphs, seven LG dIrrs, and 13 M31 dSphs (Figure 1.7). They found that the mass-metallicity relation roughly continues from galaxies with $M_* = 10^{3.5}$ to $10^{12} M_\odot$. The derived relation using their sample ($M_* < 10^9 M_\odot$) is $Z \propto M_*^{0.30 \pm 0.02}$. They also found that both dSphs and dIrrs follow the same mass-metallicity relation. Although each galaxy has different evolutionary history, all galaxies including LG galaxies lie in the same relation of mass and metallicity.

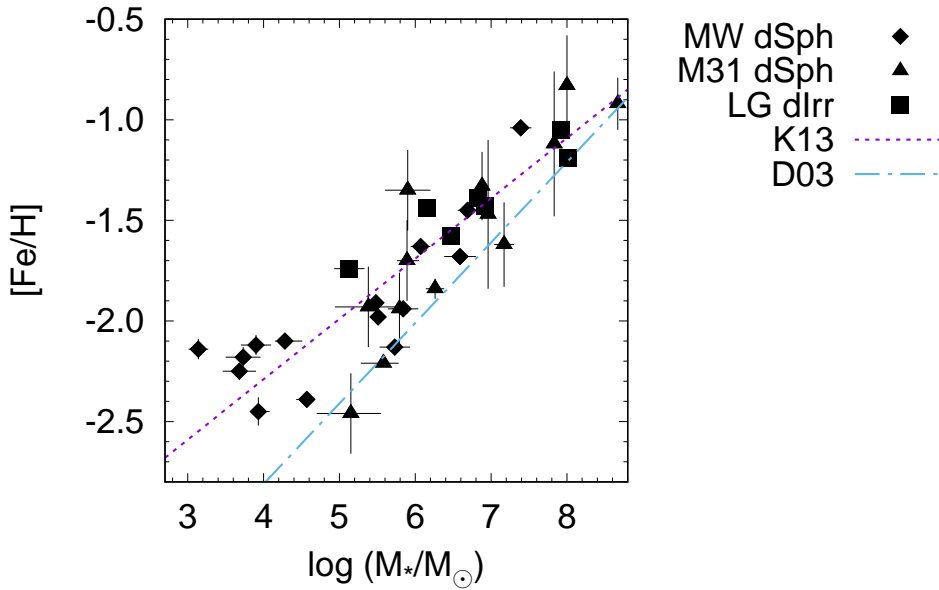
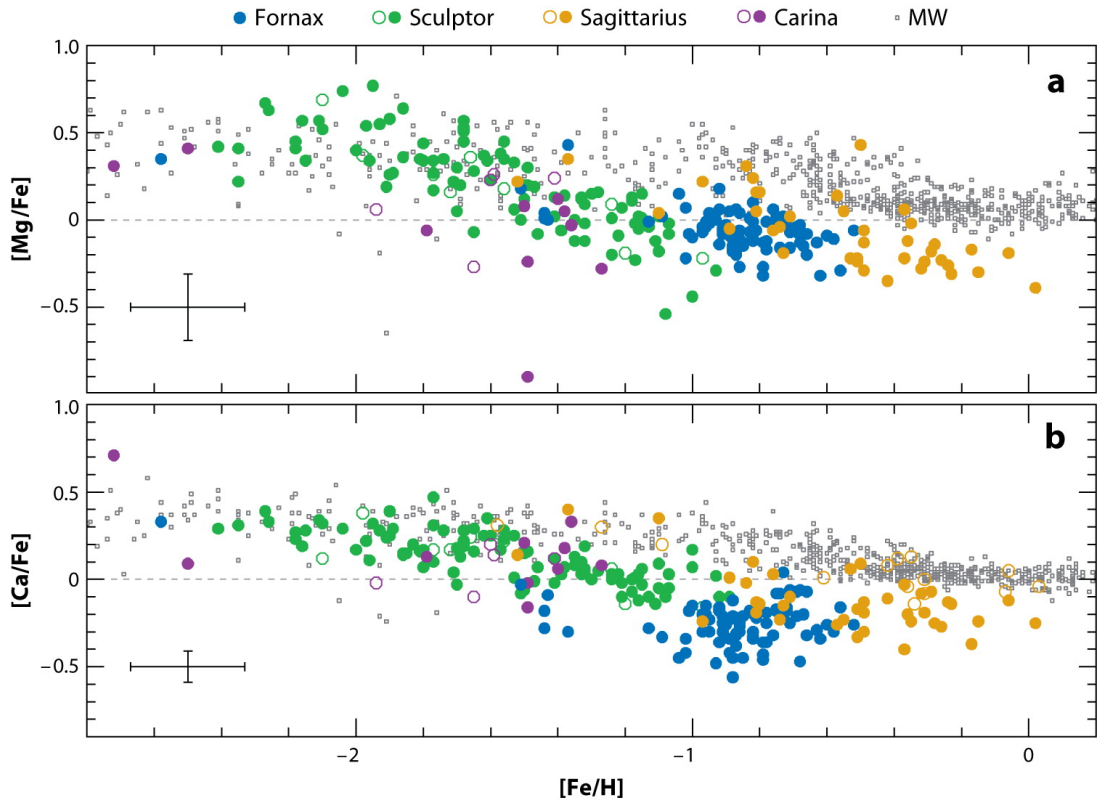


FIGURE 1.7: Stellar mass–metallicity relation for models and the LG dwarf galaxies. Black diamonds, triangles and squares with error bars are the observed value of the MW dSphs, M31 dSphs and the LG dIrrs, respectively (Kirby et al., 2013, K13). The sky-blue dot–dashed line represents the least square fitting of the samples of (Dekel and Woo, 2003, D03): $[\text{Fe}/\text{H}] \propto M_*^{0.40}$. The purple dashed line represents the least-square fitting of K13: $\langle [\text{Fe}/\text{H}] \rangle = (-1.69 \pm 0.04) + (0.30 \pm 0.02) \log (M_*/10^6 M_\odot)$.

The elemental abundance ratios in galaxies give us clues to understand the astrophysical sites of elements and chemodynamical evolution of galaxies. The α -elements (O, Mg, Si, Ca, and Ti) are synthesized by CCSNe. O and Mg are synthesized during the hydrostatic He burning in massive stars. Si, Ca, and Ti are mostly produced during CCSN explosion. On the other hand, Fe is synthesized by both CCSNe and Type Ia SNe (SNe Ia). SNe Ia produce Fe with a typical timescale of ~ 1 Gyr (e.g., Maoz, Mannucci, and Nelemans, 2014). The onset of SNe Ia decreases the $[\alpha/\text{Fe}]$ ratio (e.g.,

Tinsley, 1979; Matteucci and Brocato, 1990). The point where $[\alpha/\text{Fe}]$ ratios start to decrease is called "knee". The $[\alpha/\text{Fe}]$ ratios indicate the speed of chemical evolution in galaxies. Figure 1.8 shows $[\alpha/\text{Fe}]$ as a function of $[\text{Fe}/\text{H}]$ in LG galaxies. At lower metallicity than the knee, $[\alpha/\text{Fe}]$ in dwarf galaxies follows that in the MW halo. This result suggests that the enrichment of α -elements is similar in the MW halo and LG dwarf galaxies at the early epoch of galaxy evolution. On the other hand, the metallicity of the knee is lower than that of the MW halo. Suda et al. (2017) showed that positions of the knee are -2.1 (Fornax), -2.1 (Sculptor), -2.3 (Draco), and -1.0 (MW). This result suggests that the enrichment of Fe is slower than that of the MW halo.




 Tolstoy E, et al. 2009.
Annu. Rev. Astron. Astrophys. 47:371–425

FIGURE 1.8: (a) $[\text{Mg}/\text{Fe}]$ (b) $[\text{Ca}/\text{Fe}]$ as a function of $[\text{Fe}/\text{H}]$ (figure 11 of Tolstoy, Hill, and Tosi, 2009). Blue, green, orange, and purple plots represent α -element abundances in Fornax (Shetrone et al., 2003; Letarte, 2007), Sculptor (Shetrone et al., 2003; Geisler et al., 2005; Hill and DART Collaboration, 2012), Sagittarius (McWilliam and Smecker-Hane, 2005; Monaco et al., 2005; Sbordone et al., 2007), and Carina (Shetrone et al., 2003; Koch et al., 2008). Open and filled symbols respectively denote single-slit spectroscopy measurements and multi-object spectroscopy. The small gray squares show the α -element abundances of the disk and halo of the MW (Venn et al., 2004).

The abundances of the heaviest iron group element, Zn show slightly different

behavior from α -elements. Figure 1.9 shows $[\text{Zn}/\text{Fe}]$ as a function of $[\text{Fe}/\text{H}]$ in LG galaxies. At $[\text{Fe}/\text{H}] \lesssim -2.5$, there is an increasing trend toward lower metallicity (e.g., Cayrel et al., 2004; Nissen et al., 2004; Nissen et al., 2007; Saito et al., 2009; Duffau et al., 2017). At higher metallicity, the increasing trend toward lower metallicity continues in dwarf galaxies while there is a flat $[\text{Zn}/\text{Fe}]$ ratio in the MW halo. Skúladóttir et al. (2017) implied that there are star-to-star scatters of $[\text{Zn}/\text{Fe}]$ ratios at $[\text{Fe}/\text{H}] > -2.5$. However, these behaviors of $[\text{Zn}/\text{Fe}]$ ratios are not well understood due to the poor knowledge of the astrophysical sites of Zn. We will discuss this issue in Chapter 4.

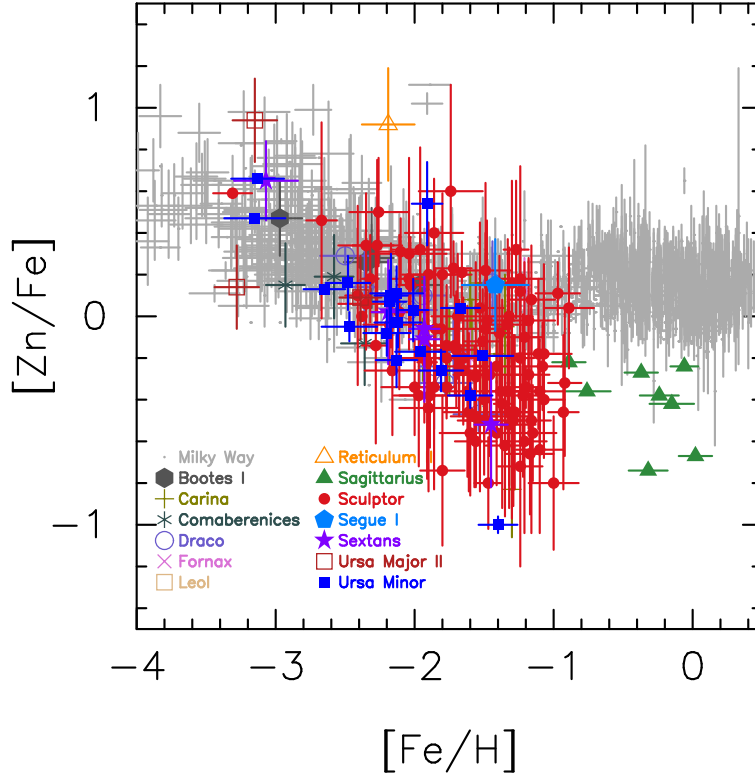


FIGURE 1.9: $[\text{Zn}/\text{Fe}]$ as a function of $[\text{Fe}/\text{H}]$ for the Milky Way (light gray points) and LG dwarf galaxies (colored points). Boötes I: Gilmore et al. (2013), Carina: Shetrone et al. (2003) and Venn et al. (2012), Comaberenices: Frebel et al. (2010), Draco: Shetrone, Côté, and Sargent (2001) and Cohen and Huang (2009), Fornax, Leo I: Shetrone et al. (2003), Reticulum II: Ji et al. (2016a), Sagittarius: Sbordone et al. (2007), Sculptor: Shetrone et al. (2003), Geisler et al. (2005), Simon et al. (2015), Skúladóttir et al. (2015), and Skúladóttir et al. (2017), Segue I: Frebel, Simon, and Kirby (2014), Sextans: Shetrone, Côté, and Sargent (2001) and Honda et al. (2011), Ursa Major II: Frebel et al. (2010), Ursa Minor: Shetrone, Côté, and Sargent (2001), Sadakane et al. (2004), and Cohen and Huang (2010). Error bars indicate the statistical as well as systematic errors given in each reference. All data are compiled using the SAGA database (Suda et al., 2008; Suda et al., 2011; Suda et al., 2017; Yamada et al., 2013).

The abundance ratios of neutron-capture elements are very different from other elements. Figure 1.10 shows $[\text{Ba}/\text{Fe}]$ as a function of $[\text{Fe}/\text{H}]$. Although the s -process

synthesizes 85 % of Ba, we follow Ba as r -process elements. We can eliminate s -process contributions using the [Ba/Eu] ratio because the r -process synthesizes 99% of Eu (Burris et al., 2000). The pure r -process [Ba/Eu] ratio is [Ba/Eu] = -0.89 (Burris et al., 2000). The contribution of the s -process mostly begins from [Fe/H] = -2.75 in the MW halo (Burris et al., 2000). On the other hand, the contribution of the s -process would appear as lower metallicity in dSphs. However, the number of stars in which Eu has been detected is small. We therefore correct the observational value of [Ba/Eu] to be -0.89 for all stars with [Fe/H] > -2.75 .

In the MW halo, [r /Fe] ratios show scatters over 3 dex in EMP stars (e.g., McWilliam et al., 1995; Burris et al., 2000; Fulbright, 2000; Westin et al., 2000; Johnson, 2002; Hill et al., 2002; Honda et al., 2004; Barklem et al., 2005; François et al., 2007; Aoki et al., 2013; Ishigaki, Aoki, and Chiba, 2013; Roederer et al., 2014). This scatter indicates that r -process elements are produced at lower rates than the rate of whole SNe when the spatial distribution of metallicity is not yet homogenized. On the other hand, dSphs do not have stars with [Ba/Fe] > 1 at [Fe/H] $\lesssim -3$. The r -process abundances in UFDs except for Reticulum II are also depleted compared to those of the MW halo. Ji et al. (2016b) found that Reticulum II UFD shows strong enhancement of r -process elements. These observations help us understand the astrophysical sites of r -process elements and evolutionary histories of the LG galaxies (see Chapters 2, 3, 5, and 6).

1.3 Formation and evolution of galaxies

1.3.1 Galaxy formation

Early studies of galaxy formation were based on the observations of kinematics and colors (metallicities) of stars. It has been known that halo stars have fast velocity and low metallicity (Oort, 1922; Oort, 1926; Roman, 1955). Eggen, Lynden-Bell, and Sandage (1962) found that lower metallicity stars have higher eccentricities by the analysis of 221 stars. From their findings, they concluded that the galaxy is formed by the collapse of gas cloud within a few times 10^8 years. This monolithic collapse scenario had long been a standard scenario of galaxy formation.

On the other hand, Searle and Zinn (1978) found that there is no radial dependence on metallicities of globular clusters in the outer halo. They also found that stars on the horizontal branch in these clusters show a wide spread in the color distribution which indicate a broad range of age. These results suggested that the outer halo was formed by the clustering of protogalactic fragments. Yoshii and Saio (1979) found that metallicity and eccentricity were not correlated when they took into account the metal-poor stars with small proper motions. They showed that halo formation timescale is 3×10^9 years. Norris, Bessell, and Pickles (1985) also found that $\sim 20\%$ of their objects are [Fe/H] ≤ -1.0 and the eccentricity less than 0.4. Chiba and Beers (2000) concluded that there is no correlation between [Fe/H] and eccentricity. These results support the model of Searle and Zinn (1978).

Hierarchical structure formation scenario based on Λ CDM cosmology successfully explains the properties of galaxies (e.g., Blumenthal et al., 1984). White and Rees (1978) showed that dark-matter condensed around the time of recombination and clustered gravitationally to form larger systems. Development of tree method

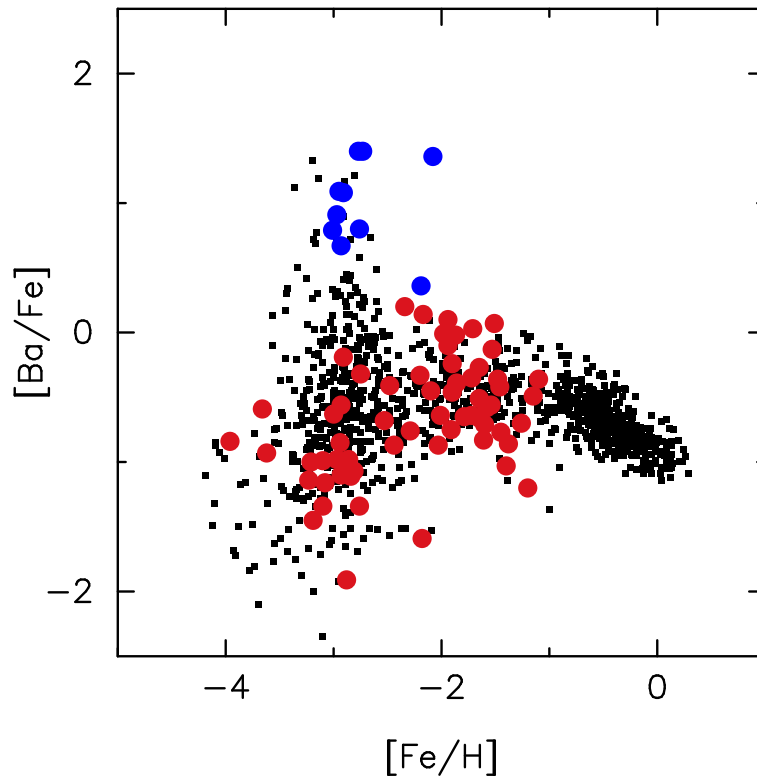


FIGURE 1.10: $[\text{Ba}/\text{Fe}]$ as a function of $[\text{Fe}/\text{H}]$ (SAGA database, Suda et al., 2008; Suda et al., 2011; Suda et al., 2017; Yamada et al., 2013). Ba abundances are corrected to be $[\text{Ba}/\text{Eu}] = -0.89$ to remove the s -process contribution. Black, blue, and red plots respectively represent $[\text{Ba}/\text{Fe}]$ ratios in the MW, Reticulum II, and the other LG dwarf galaxies (Carina, Draco, Leo I, Sculptor, Ursa Minor, Boötes I, Leo IV, Ursa Major II, Comaberenices, and Sextans).

(Barnes and Hut, 1986) for N -body calculation and smoothed particle hydrodynamics (SPH, Gingold and Monaghan, 1977; Lucy, 1977; Monaghan and Lattanzio, 1985) enabled us to compute formation of galaxies in cosmological initial condition. Katz and Gunn (1991) successfully made systems that resemble spiral galaxies by their N -body/hydrodynamic simulations. Steinmetz and Müller (1994) computed the chemodynamical evolution of disk galaxies in a cosmological context. They showed that the disk of the galaxy has a metallicity gradient of $d(\log Z)/dr = -0.05 \text{ kpc}^{-1}$.

Numerical simulations based on the hierarchical structure formation scenario currently become the powerful tool to study galaxy formation. Bekki and Chiba (2000) and Bekki and Chiba (2001) reproduced the observed properties of the MW halo such as the metallicity-eccentricity relation, the radial density profile, and MDFs by their chemodynamical simulations. Bullock and Johnston (2005) found that satellites that contribute to the stellar halo accreted ~ 9 Gyr ago in their hybrid semianalytic plus N -body model. This accretion time is older than that of surviving satellites (~ 5 Gyr). Their result implied that stars in the inner stellar halo should have different chemical compositions from stars in the surviving satellite galaxies.

Recent numerical simulations successfully reproduce several observed properties of galaxies. Figure 1.11 shows an example of such simulation (the EAGLE project Schaye et al., 2015). Some of the simulations can resolve the scale of dwarf galaxies. Governato et al. (2010) showed that the constant density profile in dwarf galaxies can be explained if strong outflows due to SN feedback removes low-momentum gas. Ma et al. (2016) reproduced the mass-metallicity relation of galaxies with $M_* = 10^4 - 10^{11} M_\odot$ in their simulations. Sawala et al. (2016) performed cosmological hydrodynamic simulations of LG galaxies. Their simulated galaxies have the relation of stellar mass and velocity dispersion consistent with LG dSphs.

1.3.2 Galactic chemical evolution

Galactic chemical evolution studies histories of the transformation from gas to stars and enrichment of elements in galaxies. Homogeneous one-zone models have long been used for the studies of galactic chemical evolution (e.g., Tinsley, 1980; Matteucci, 2001). Basic ingredients of galactic chemical evolution models are stellar yields, lifetimes, initial mass function, SF rates (SFRs), and gas flows. One-zone chemical evolution models assume all metals are instantaneously mixed into the ISM. These models derive average abundances of elements in a galaxy. One-zone models are still used as a powerful tool to study the astrophysical sites of elements (e.g., Kobayashi et al., 2006; Matteucci et al., 2014; Ishimaru, Wanajo, and Prantzos, 2015).

In the early phases of galaxy evolution, chemical abundances in the ISM were still inhomogeneous. Chemical abundances in very metal-poor stars reflect such inhomogeneities. Argast et al. (2000) and Argast et al. (2002) introduced the stochastic chemical evolution model that can treat inhomogeneities of chemical abundances in the ISM. In their model, the ISM is divided into a cell of $(50 \text{ pc})^3$. SF takes place in probabilistically selected cells. To treat inhomogeneities, they assume that metals ejected from SNe are mixed into the swept up materials.

Clarifying the enrichment of heavy elements can enhance our understanding of the astrophysical sites of elements and evolutionary history of galaxies. For the r -process,

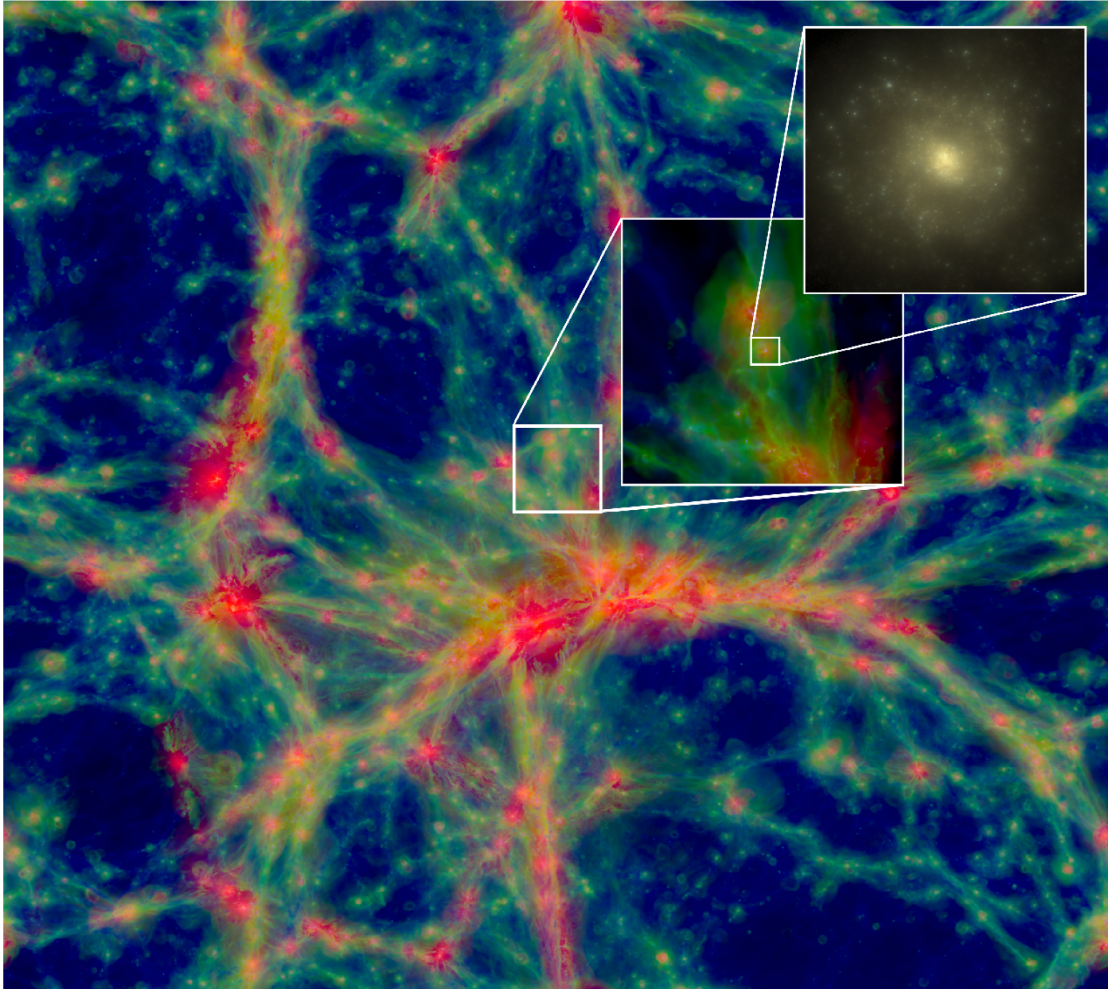


FIGURE 1.11: A galaxy within a halo in the simulation (figure 1 of Schaye et al., [2015](#)). From blue to red, color shows gas temperature. The inset denote zoomed-in image of a galaxy formed in the simulation.

NSMs are thought to be a promising site of r -process from nucleosynthetic studies (see Section 1.1.3.2). On the other hand, Argast et al. (2004) failed to reproduce star-to-star scatters of r -process abundances in EMP stars in the MW halo by NSMs due to their long merger times and low rates (high yields). Binary NSs typically need ~ 100 Myr before they coalesce. Long merger times delay the production of r -process elements in a galaxy. NSMs typically eject $\sim 10^{-2} M_{\odot}$ of r -process elements with $\sim 10^3$ times lower rates of all CCSNe. This low rate causes extremely high abundance of r -process abundances in high metallicity which are not seen in the observations. However, Argast et al. (2004) did not consider the hierarchical structure formation (see Section 1.3.1) and metal mixing processes except for those in SN remnants. Ishimaru, Wanajo, and Prantzos (2015) showed that r -process elements increase at lower metallicity in less massive sub-halos in their one-zone chemical evolution model. NSMs occurred in halos with a size of dSphs have r -process elements in $[\text{Fe}/\text{H}] \lesssim -2.5$ (see Chapter 2). The central density not the total mass of halos affect the early SFRs and r -process abundances (see Chapter 3).

Understanding the enrichment of Zn will connect the chemical evolution from the high redshift to the present universe. Abundances of Zn have been used as a tracer of gas phase metallicity in damped Lyman- α systems at high redshift (e.g., Wolfe, Gawiser, and Prochaska, 2005; Vladilo et al., 2011). Although it is used as a tracer of metallicity, enrichment of Zn is not well understood. Kobayashi et al. (2006) showed that HNe increase the average value of $[\text{Zn}/\text{Fe}]$ ratios. However, they require HN rates ~ 10 times higher than those estimated from long GRBs (Podsiadlowski et al., 2004a; Guetta and Della Valle, 2007). ECSNe may also contribute to the enrichment of Zn (see Chapter 4). For the first step to understand the enrichment of Zn, it is necessary to clarify the role of different kinds of SNe.

The r -process elements and Zn could be used as a tracer of the efficiency of metal mixing in galaxies. Homogeneous chemical abundances in open star clusters are the direct evidence of metal mixing (e.g., De Silva et al., 2007a; De Silva et al., 2007b). Roy and Kunth (1995) studied the sites of metal mixing in gas-rich galaxies. They showed that drivers of metal mixing are divided into three different scales. On the largest scales (1–10 kpc), differential rotation and azimuthal homogenizing homogenize metals with a timescale of ≤ 1 Gyr. On the intermediate scales (100–1000 pc), inter-cloud collisions play an important role in metal mixing. On the small scales (≤ 100 pc), turbulent diffusion mixes metals with a timescale of $\lesssim 1$ Myr. However, which process is dominant in the context of galactic chemical evolution is not known. Comparison between heavy element abundances in simulations and metal-poor stars in LG galaxies can constrain the efficiency of metal mixing (see Chapter 5).

Galactic chemical evolution is related to the galaxy formation. We need to treat the chemical evolution in a context of the dynamical evolution of galaxies to understand evolutionary histories of galaxies fully. Galactic chemodynamical models can treat chemical evolution and galactic dynamics. Kawata and Gibson (2003) developed a chemodynamical evolution code based on N -body/SPH method. They showed that feedback from SNe Ia cannot be ignored in the evolution of elliptical galaxies. Revaz et al. (2009) performed a series of chemodynamical simulations of isolated dwarf galaxy models. Their results suggested that the diversity of SFHs and chemical abundances seen in LG galaxies are due to the intrinsic evolution of dwarf galaxies.

Kobayashi and Nakasato (2011) presented chemodynamical simulations of MW type galaxies. They showed that the enrichment histories of 13 kinds of elements and dynamical properties of stars that can be directly compared to the observations. Abundances of *r*-process elements could constrain the formation and evolution of LG galaxies. The *r*-process rich stars only exist in the MW halo and Reticulum II UFD. High resolution cosmological zoom-in simulations can directly answer this question (see Chapter 6).

1.4 *N-body / smoothed particle hydrodynamics code, ASURA*

Here we describe an *N*-body / SPH code, ASURA (Saitoh et al., 2008; Saitoh et al., 2009) adopted in this dissertation. We adopt three different kinds of particles in our simulations: dark matter, gas, and star particles. We treat dark matter and star particles as collisionless particles. Dark matter particles contribute to the dynamical evolution of our model galaxies. Star particles mainly contribute to feedback of energy and heavy elements produced by SNe and NSMs. We solve the hydrodynamical evolution of gas particles using SPH (e.g., Gingold and Monaghan, 1977; Lucy, 1977; Monaghan and Lattanzio, 1985; Monaghan, 1992). To properly treat a contact discontinuity, we need to modify SPH formalism to the density-independent formalism of SPH (DISPH) (Hopkins, 2013; Saitoh and Makino, 2013; Yamamoto, Saitoh, and Makino, 2015). The difference of the treatment of hydrodynamics significantly affects, for example, the entropy profiles of galaxy clusters (Saitoh and Makino, 2016) and galaxies that experience ram pressure stripping (Nichols, Revaz, and Jablonka, 2014). However, in the case of isolated galaxy simulations, Hopkins (2013) has shown that time-averaged SFRs are not significantly different from the formalisms of SPH. We thus choose widely used standard SPH method in Chapters 2 and 3. We adopt DISPH in Chapters 4–6.

Gravity is calculated by a treecode (Barnes and Hut, 1986) with GRAPE method (Makino, 1991) using the Phantom-GRAPE library (Tanikawa et al., 2012). The code is parallelized following Makino (2004). We set the value of 0.5 for the opening angles for the ordinary three-dimensional spaces and the gravitational softening lengths. The second-order scheme is adopted for time integration (Saitoh and Makino, 2016) using individual-block time step method (McMillan, 1986; Makino, 1991). For integration of self-gravitating fluid system, we adopt the fully asynchronous split time-integrator (FAST) algorithm to reduce calculation cost (Saitoh and Makino, 2010). We use the time-step limiter, which forces the timestep difference among neighbor particles to be less than four times long, in order to follow the evolution of strong shock regions such as SN remnants (Saitoh and Makino, 2009). We use a metallicity dependent cooling/heating function generated by Cloudy (Ferland et al., 1998; Ferland et al., 2013). The cooling/heating function covers the temperature range from 10–10⁹ K. Ultra-violet background heating is implemented following Haardt and Madau (2012). We also implemented the effect of hydrogen self-shielding following the fitting function of Rahmati et al. (2013).

We allow SF when gas particles satisfy three conditions. (1) Gas particles are converging ($\nabla \cdot \mathbf{v} < 0$). (2) The density is higher than threshold density, n_{th} . (3) The

temperature is lower than threshold temperature, T_{th} (e.g., Navarro and White, 1993; Katz, Weinberg, and Hernquist, 1996; Stinson et al., 2006). We adopt $n_{\text{th}} = 100 \text{ cm}^{-3}$ for our fiducial model, which is the mean density of giant molecular clouds (GMCs). We adopt $T_{\text{th}} = 1000 \text{ K}$ for our fiducial model. The value of T_{th} is insensitive to the final structure of galaxies (Saitoh et al., 2008).

When a gas particle satisfies the three conditions above, it becomes eligible to form new collisionless star particles. Star particles are produced by the following probability according to the prescription of Katz (1992) and Katz, Weinberg, and Hernquist (1996):

$$p = \frac{m_{\text{gas}}}{m_{\star}} \left\{ 1 - \exp \left(-c_{\star} \frac{dt}{t_{\text{dyn}}} \right) \right\}, \quad (1.1)$$

where m_{\star} and m_{gas} are the mass of star and gas particles, respectively, and c_{\star} is the dimensionless SFE parameter. We set $m_{\star} = m_{\text{gas}}/3$ following Okamoto et al. (2003) and Okamoto et al. (2005). The mass of a gas particle of our fiducial model is initially assumed as $4.0 \times 10^2 M_{\odot}$, while it is reduced by SF. When the mass of a gas particle becomes lower than one-third of initial mass, the particle is converted into a collisionless particle. The dimensionless SFE parameter of our fiducial model ($c_{\star} = 0.033$) is chosen based on the slow SF model (Zuckerman and Evans, 1974; Krumholz and Tan, 2007). Saitoh et al. (2008) suggest that when $n_{\text{th}} = 100 \text{ cm}^{-3}$ is adopted, the final results are fairly insensitive to the adopted value of c_{\star} in their MW model. In Appendix A, we also confirm this result in our dSph models.

Each star particle is treated as a single stellar population (SSP), i.e., each star particle is assumed to be an assembly of stars with the same age and the same metallicity. The initial mass function (IMF) of star particles is the Salpeter IMF (Salpeter, 1955): $\phi \equiv m^{-x}$, where $x = 1.35$ (Chapter 2 and 3), Kroupa IMF (Kroupa, 2001, Chapters 4 and 6), and Chabrier IMF (Chabrier, 2003, Chapter 5) with mass range of $0.1\text{--}100 M_{\odot}$. We set the progenitor mass of CCSNe to be $8\text{--}40 M_{\odot}$. In this model, stars more massive than $40 M_{\odot}$ end their lives as black holes. Star particles, which explode in a time interval of Δt are selected by the following probability (p_{CCSNe}),

$$p_{\text{CCSNe}} = \frac{\int_{m(t)}^{m(t+\Delta t)} \phi(m') m'^{-1} dm'}{\int_{m(t)}^{8M_{\odot}} \phi(m') m'^{-1} dm'}, \quad (1.2)$$

where $m(t)$ is the turn off mass at age t . Each CCSN explosion distributes thermal energy of 10^{51} erg to the surrounding SPH particles. The mass of one star particle is $\sim 100 M_{\odot}$. When a particle explode as CCSNe, the number of CCSNe inside each star particle corresponds to ~ 1 . Numerical simulations of galaxy formation widely adopt this method (e.g., Okamoto, Nemmen, and Bower, 2008; Saitoh et al., 2008; Dalla Vecchia and Schaye, 2012; Simpson et al., 2013; Vogelsberger et al., 2013; Hopkins et al., 2014). In addition to the SN feedback, we implement heating by H II region formed around young stars. The number of the $\text{Ly}\alpha$ photons is evaluated using PÉGASE (Fioc and Rocca-Volmerange, 1997). The parameters of these baryonic physics are listed in Table 1.1.

TABLE 1.1: Parameters of baryon physics.

Symbol	Fiducial values	Variation
c_{\star}	0.033	0.033, 0.5
n_{th}	100 cm^{-3}	$0.1\text{--}100 \text{ cm}^{-3}$
T_{th}	$1 \times 10^3 \text{ K}$	$1 \times 10^3 - 3 \times 10^4 \text{ K}$
ϵ_{SN}	$1 \times 10^{51} \text{ erg}$	$(0.03 - 1) \times 10^{51} \text{ erg}$

Notes: Fiducial values of c_{\star} , n_{th} , T_{th} , ϵ_{SN} are taken from Saitoh et al. (2008).

1.5 This thesis

This thesis concerns the enrichment of heavy elements (r -process elements and Zn) in dwarf galaxies. It aims at (i) clarifying the contribution of NSMs and different kinds of SNe (CCSNe, HNe, ECSNe, and SNe Ia) to the enrichment of heavy elements (Chapters 2–4), and (ii) constraining the formation and evolution of galaxies using heavy element abundances (Chapters 5 and 6). This work covers enrichment of heavy elements in isolated dwarf galaxies (Chapters 2–5) and a cosmologically formed galaxy (Chapter 6). The key issues that will be discussed in this thesis are as follows.

- Enrichment of r -process elements by NSMs in dSphs (Chapter 2).
- The relation of structures of halos, star formation histories, and enrichment of r -process elements (Chapter 3).
- Enrichment of Zn in dwarf galaxies (Chapter 4).
- Efficiency of metal mixing in dwarf galaxies (Chapter 5).
- Connection between enrichment of r -process elements and galaxy formation (Chapter 6).

Figure 1.12 illustrates the structure of this thesis. The first part of this thesis studies the enrichment of heavy elements in isolated dwarf galaxies. These works clarify the contributions of NSMs and SNe in chemodynamical evolution of dwarf galaxies.

Chapter 2 NSMs are one of the promising astrophysical site of r -process. However, previous chemical evolution models that do not consider the contribution of sub-halos fail to reproduce the observed abundances of r -process elements in metal-poor stars. In this chapter, we perform a series of high-resolution N -body/SPH simulations with simple metal mixing model in the star-forming region of isolated dSphs. This chapter shows that NSMs with a merger time of $\sim 100 \text{ Myr}$ can contribute to the enrichment of r -process elements at $[\text{Fe}/\text{H}] < -2.5$ in a dSph. We find that this is because the metallicity does not increase due to the low SFE up to $\sim 300 \text{ Myr}$ from the beginning of the star formation. This chapter demonstrates that NSMs can be a major astrophysical site of r -process elements in the context of chemodynamical evolution of galaxies.

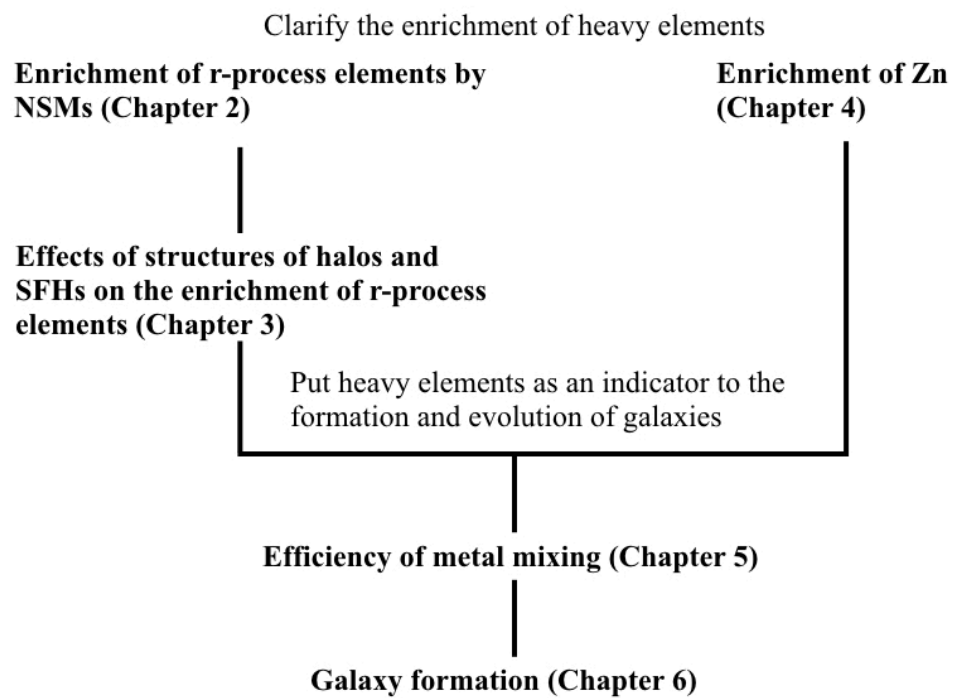


FIGURE 1.12: Structure of this thesis.

Chapter 3 LG dwarf galaxies have various SFHs (Section 1.2.1). This chapter addresses the effects of the SFHs to the enrichment of r -process elements in dwarf galaxies. We change the central density and total mass of halos to produce galaxies with different stellar mass and SFHs in the chemodynamical simulations. We find that galaxies with dynamical times with ~ 100 Myr have SFRs with $\lesssim 10^{-3} M_{\odot} \text{yr}^{-1}$ at 1 Gyr from the beginning of the simulation. These galaxies produce stars with r -process elements in $[\text{Fe}/\text{H}] \lesssim -2.5$. On the other hand, r -process elements appear at higher metallicity in galaxies with dynamical times less than 100 Myr. We also find that early SFRs and enrichment of r -process elements are not affected by the total mass of halos.

Chapter 4 This chapter clarifies the role of SNe (CCSNe, ECSNe, HNe, and SNe Ia) to the enrichment of heavy elements while Chapters 2 and 3 clarify the role of NSMs in the galactic chemical evolution. Zn is a nice tracer to identify the role of SNe in the galactic chemical evolution. Here we newly put the effect of ECSNe into the simulations. We find that the ejecta from ECSNe can contribute to the formation of metal-poor stars with $[\text{Zn}/\text{Fe}] \gtrsim 0.5$. We also find that scatters of $[\text{Zn}/\text{Fe}]$ seen in $[\text{Fe}/\text{H}] \gtrsim -2.5$ due to the contribution of SNe Ia are the same as those of $[\text{Mg}/\text{Fe}]$. This chapter demonstrates that ECSNe or SNe from low mass progenitors can be one of the contributors to the enrichment of Zn in galaxies.

The second part of this thesis studies efficiency of metal mixing and formation of galaxies on the point of enrichment of heavy elements. This part demonstrates abundances of heavy elements in metal-poor stars can be used as a tracer of formation and evolution of galaxies.

Chapter 5 Chemical abundances of metal-poor stars help us understand the efficiency of metal mixing in galaxies. In this chapter, we newly implement the turbulence-induced metal mixing model to our chemodynamical simulations. We use Mg, Ba, and Zn as a tracer of the efficiency of metal mixing in dwarf galaxies. We find that models with scaling factor of metal diffusion less than 0.01 can produce abundances of heavy elements in metal-poor stars consistent with observations. This efficiency of metal mixing corresponds to the timescale of metal mixing less than 40 Myr. This result implies that metals should be mixed with shorter timescales than the dynamical times of dwarf galaxies.

Chapter 6 The ratios of r -process element to Fe in stars with $[\text{Fe}/\text{H}] < -2.5$ in the LG galaxies are (i) star-to-star scatters in the MW halo, (ii) no r -process rich stars in dSphs, (iii) enhanced r -process abundances in Reticulum II UFD (Figure 1.10). These difference may reflect the formation of LG galaxies. This chapter connects the enrichment of r -process elements and galaxy formation. Here we perform a series of high-resolution cosmological zoom-in simulations with metal mixing based on Chapter 5. In the cosmologically formed galaxy, there are star-to-star scatters of r -process abundances in $[\text{Fe}/\text{H}] < -2$. We find that r -process rich stars are formed in the halos with a gas mass of $\sim 10^6 M_{\odot}$. In these small halos, ejecta from a NSM enrich whole gas to high r -process abundances. This result suggests that the r -process enhanced stars seen in the MW halo may come from halos with a size similar to the

present UFDs.

This thesis is concluded in Chapter 7. Chapter 7 summarizes the scenario proposed in this thesis. We also show future prospects of this work.

Chapter 2

Enrichment of r -process elements in dwarf spheroidal galaxies in the chemodynamical evolution models

The r -process is a major process to synthesize elements heavier than iron, but the astrophysical site(s) of r -process is not identified yet. NSMs are suggested to be a major r -process site from nucleosynthesis studies. Previous chemical evolution studies however require unlikely short merger times of NSMs to reproduce the observed large star-to-star scatters in the abundance ratios of r -process elements relative to iron, [Eu/Fe], of extremely metal-poor stars in the MW halo. This problem can be solved by considering chemical evolution in dSphs which would be building blocks of the MW and have lower SFEs than the MW halo. We demonstrate that enrichment of r -process elements in dSphs by NSMs using an N -body/smoothed particle hydrodynamics code. Our high-resolution model reproduces the observed [Eu/Fe] by NSMs with a merger time of 100 Myr when the effect of metal mixing is taken into account. This is because metallicity is not correlated with time up to ~ 300 Myr from the start of the simulation due to low SFE in dSphs. We also confirm that this model is consistent with observed properties of dSphs such as radial profiles and metallicity distribution. The merger times and the Galactic rate of NSMs are suggested to be $\lesssim 300$ Myr and $\sim 10^{-4} \text{ yr}^{-1}$, which are consistent with the values suggested by population synthesis and nucleosynthesis studies. This study supports that NSMs are the major astrophysical site of r -process¹.

2.1 Review: NSMs as a source of r -process elements

Elements heavier than iron are mainly synthesized by the r -process as well as the s - and p -processes. More than 90% of the number of elements such as europium (Eu), gold (Au), and platinum (Pt) in the solar system are synthesized by the r -process (Burris et al., 2000). Sufficiently neutron-rich environment is required in order to synthesize r -process elements with mass number (A) over 110.

The observed r -process elemental abundance ratios, such as [Eu/Fe], in EMP stars ([Fe/H] $\lesssim -3$) show star-to-star scatters of ~ 3 dex in the MW halo (see Figure 1.10). The mechanism of star-to-star scatters in the abundance studies should be clarified simultaneously with the astrophysical site(s) of the r -process.

¹Contents in this chapter have been published in Hirai, Ishimaru, Saitoh, Fujii, Hidaka, and Kajino (2015).

Neutrino-driven winds from proto-neutron stars of CCSNe have long been regarded as one of the possible sites of the r -process (e.g., Meyer et al., 1992; Woosley et al., 1994; Wanajo et al., 2001). Previous chemical evolution studies suggest that the observed [Eu/Fe] scatter is well reproduced by models assuming that CCSNe of low-mass ($8\text{--}10 M_{\odot}$) progenitors produce r -process elements (e.g., Mathews, Bazan, and Cowan, 1992; Ishimaru and Wanajo, 1999; Travaglio et al., 1999; Tsujimoto, Shigeyama, and Yoshii, 2000; Travaglio, Galli, and Burkert, 2001; Travaglio, Galli, and Burkert, 2001; Argast et al., 2004). However, recent hydrodynamical simulations of CCSNe, which include neutrino transport in sophisticated manner, suggest that the proto-neutron star winds of CCSNe do not necessarily produce a neutron-rich condition suitable for the r -process (e.g., Reddy, Prakash, and Lattimer, 1998; Roberts, Reddy, and Shen, 2012; Martínez-Pinedo et al., 2012; Roberts, Reddy, and Shen, 2012; Horowitz et al., 2012). Nucleosynthesis calculations suggest that heavy elements with $A \gtrsim 110$, are difficult to be synthesized in CCSNe due to such too weak neutron-rich environments (e.g., Wanajo, Janka, and Müller, 2011; Wanajo, 2013).

NSMs are also suggested to be a promising site of the r -process (Lattimer and Schramm, 1974; Lattimer and Schramm, 1976; Lattimer et al., 1977; Symbalisty and Schramm, 1982; Eichler et al., 1989; Meyer, 1989). Recent detailed nucleosynthesis calculations show that heavy r -process elements are successfully synthesized in NSMs (Freiburghaus, Rosswog, and Thielemann, 1999; Goriely, Bauswein, and Janka, 2011; Korobkin et al., 2012; Bauswein, Goriely, and Janka, 2013; Rosswog et al., 2014; Wanajo et al., 2014). In addition, near infrared afterglow of the *Swift* short GRB, GRB130603B (Berger, Fong, and Chornock, 2013; Tanvir et al., 2013) is detected. This is suggested to be a piece of evidence that progenitors of short GRBs are compact binary mergers and r -process nucleosynthesis occurs there (Tanaka and Hotokezaka, 2013). Recently, gravitational waves from a NSM and their afterglows are detected (e.g., Abbott et al., 2017b, , see Section 1.1.3.2).

NSMs have long merger times and low rates. The neutron star (NS) binaries lose their energy very slowly due to the gravitational emissions. The merger times are estimated $\gtrsim 100$ Myr from observed binary pulsars (Lorimer, 2008). Recent predictions from population synthesis models also suggest that most of NS binaries merge $\gtrsim 100$ Myr after their formation (Dominik et al., 2012). On the other hand, the NSM rate is estimated to be $10^{-6} - 10^{-3} \text{ yr}^{-1}$ for a MW size galaxy from the observed binary pulsars (Abadie et al., 2010b). However, early studies of galactic chemical evolution pointed out that it is difficult to reproduce the observed trend of [Eu/Fe] of EMP stars by NSMs due to their long merger times and the low rate (Mathews and Cowan, 1990; Argast et al., 2004). Most of other recent studies also conclude that short merger times ($\lesssim 10$ Myr) or a second site of r -process such as jet-like explosions of magnetorotational CCSNe (e.g., Winteler et al., 2012; Nishimura, Takiwaki, and Thielemann, 2015) is required to account for large star-to-star scatters in EMP stars (Matteucci et al., 2014; Komiya et al., 2014; Tsujimoto and Shigeyama, 2014; Cescutti et al., 2015; Wehmeyer, Pignatari, and Thielemann, 2015). On the other hand, detailed population synthesis calculations suggest that production of NSMs with short-merger times (~ 10 Myr) highly depends on the treatment of common envelop phase which is not well understood (e.g., Portegies Zwart and Yungelson, 1998; Dominik et al., 2012; Kinugawa et al., 2014). Dominik et al. (2012) suggest that NSMs with merger times of $\lesssim 10$ Myr cannot be produced

in their most pessimistic model assuming each common envelop with an Hertzsprung gap donor causes a merger (Submodel B in Dominik et al., 2012). In addition, there are no observational clues that exist binary pulsars which merge within ~ 10 Myr so far (Lorimer, 2008).

This discrepancy may be solved, if the Galactic halo is formed via mergers of sub-halos within the framework of hierarchical structure formation scenario (Ishimaru, Wanajo, and Prantzos, 2015). Ishimaru, Wanajo, and Prantzos (2015) calculate the enrichment of r -process elements by NSMs with merger times of 100 Myr (95 % of NSMs) and 1 Myr (5 % of NSMs) in their one-zone chemical evolution model for each sub-halo. They suggest that $[\text{Eu}/\text{Fe}]$ increases at $[\text{Fe}/\text{H}] \leq -3$ if the SFEs are lower in less massive sub-halos. According to their calculations, the observed scatters in $[\text{Eu}/\text{Fe}]$ ratios in metal-poor stars are possibly explained by NSMs with merger times of 100 Myr. Key factors of chemical evolution such as the time variation of the SFR, outflow, and inflow strongly depend on thermodynamical feedback from SNe. Detailed chemodynamical evolution studies in low-mass galaxies like sub-halos are highly desirable to justify their assumptions to describe the enrichment history of r -process elements in a self-consistent manner between dynamical and chemical evolution of galaxies.

Recent hydrodynamical studies performed a series of simulations of galaxy formation assuming that the NSMs are a major site of r -process (van de Voort et al., 2015; Shen et al., 2015). van de Voort et al. (2015) suggest that gas mixing processes such as galactic winds and hydrodynamic flows play the important roles to explain the observed Galactic r -process ratio. Their high-resolution model with $7.1 \times 10^3 M_\odot$ of the mass of one gas particle (m_{gas}) is, however, difficult to reproduce the observed r -process abundance ratios. They imply that additional metal mixing is required to explain the observation. Shen et al. (2015) also suggest that the observed r -process abundance ratios are possibly taken into account in their NSM models if the metal mixing in SF region is implemented. However, the mass resolution ($m_{\text{gas}} = 2.0 \times 10^4 M_\odot$) in their models is as low as the fiducial low-resolution model of van de Voort et al. (2015) ($m_{\text{gas}} = 5.7 \times 10^4 M_\odot$). It is therefore important to demonstrate that if the NSM models account for the observations in independent simulations of much higher resolution.

In this chapter, we calculate enrichment of r -process elements ejected by NSMs in low mass galaxies with high-resolution ($m_{\text{gas}} = 4.0 \times 10^2 M_\odot$) chemodynamical evolution models. We perform N -body/SPH simulations of dSph models using ASURA code (Saitoh et al., 2008; Saitoh et al., 2009). We discuss effects of metal mixing in SF region as well as the dependence on the SFR, the merger times, and the rate of NSMs.

In Section 2.2, we introduce methods and models of dSphs. In Section 2.3, we compare model predictions and observed properties of dSphs generated by our models. In Section 2.4, we discuss enrichment of r -process elements in dSphs. Finally in Section 2.5, we summarize our main results.

2.2 Method and models

2.2.1 Chemical enrichment process

We take into account both SNe and NSMs in our models. We set initial gas metallicity equals to zero. We assume that gas particles around a star particle are enriched with metals when a CCSN or NSM occurs in a star particle. Metals are distributed in 32 nearest neighbor particles using weights of SPH kernel. Mass of element X in the j th neighbor particle ejected by i th star particle, $\Delta M_{X,j}$, is given by

$$\Delta M_{X,j} = \frac{m_j}{\rho_i} M_{X,i} W(r_{ij}, h_{ij}), \quad (2.1)$$

where r_{ij} is the distance between particle i and j , h_{ij} is the smoothing length, and $W(r_{ij}, h_{ij})$ is the SPH kernel given by a cubic spline function (e.g., Kawata, 2001, Chapters 2 and 3) or Wendland kernel C4 (Wendland, 1995; Dehnen and Aly, 2012, Chapters 4–6). The density of the gas particles is given as

$$\rho_i = \sum_{i \neq j} m_j W(r_{ij}, h_{ij}). \quad (2.2)$$

Smoothing length is the scale of containing N_{ngb} nearest neighbor particles. Following Saitoh et al. (2008), we set $N_{\text{ngb}} = 32 \pm 2$ (Chapters 2 and 3) or 128 ± 8 (Chapters 4–6) as a fiducial value.

2.2.2 NSM models

In this thesis, we newly put the effects of NSMs in our simulations. We assume that NSMs synthesize r -process elements. Here we regard Eu and Ba as a representative of r -process elements. Observed r -process elemental abundance ratios such as [Eu/Fe] indicates that the production of r -process elements should have occurred before SNe Ia start to contribute ($\gtrsim 1$ Gyr) to galactic chemical evolution (Maoz and Mannucci, 2012). Minimum merger times of NSMs need to be shorter than the typical delay time of SNe Ia. The most plausible merger times of NSMs is regarded as ~ 100 Myr (e.g., Lorimer, 2008; Dominik et al., 2012). We thus set the merger time of NSMs is 100 Myr as a fiducial value in Chapters 2 and 3. In Chapters 5 and 6, we implement the merger time distribution of NSMs in a similar way as SNe Ia. According to the population synthesis calculations in Dominik et al. (2012), the merger time distribution is close to the power law with its index of -1 . We set the minimum merger time as 10^7 yr, following Dominik et al. (2012).

The NSM rate and the merger times (t_{NSM}) are highly uncertain. We therefore vary them ~ 2 dex in our simulations. We regard a number fraction of NSMs to the total number of neutron stars, f_{NSM} , as a parameter, which determines the NSM rate. In this model, we assume the mass range of NS progenitor mass as $8\text{--}20 M_{\odot}$. We set the upper mass of NSM progenitor stars as $20 M_{\odot}$ from the lower limit of the mass of a black hole formation (Dominik et al., 2012). We set $f_{\text{NSM}} = 0.01$ as a fiducial value. The corresponding NSM rate in a MW size galaxy is $\sim 5 \times 10^{-5} \text{ yr}^{-1}$. It is within the values of the Galactic disk $\sim 10^{-6}\text{--}10^{-3} \text{ yr}^{-1}$, estimated from observed compact binaries (Abadie et al., 2010b).

We distribute the ejecta of r -process elements with the same method we use for SNe following Montes et al. (2016). Ejecta from NSMs might expand to a larger region than SNe (Tsujiimoto and Shigeyama, 2014). For yields of NSMs (Chapters 5 and 6), we assume that each NSM ejects $1.8 \times 10^{-4} M_{\odot}$ of Ba and $2.0 \times 10^{-5} M_{\odot}$ of Eu (Wanajo et al., 2014). In Chapters 2 and 3, yields of NSMs are related to the rate of NSMs following Ishimaru, Wanajo, and Prantzos (2015). $[\text{Eu}/\text{Fe}]$ at $[\text{Fe}/\text{H}] = 0$ is expected to be ~ 0.5 without SNe Ia because solar Fe is estimated to be produced $\sim 60\text{--}65\%$ by SNe Ia, and $\sim 35\text{--}40\%$ by CCSNe (e.g., Goswami and Prantzos, 2000; Prantzos, 2008). We thus simply set the yield of r -process elements to be $[\text{Eu}/\text{Fe}] = 0.5$ at $[\text{Fe}/\text{H}] = 0$.

Binary black hole-NSMs are also expected to eject r -process elements (e.g., Korobkin et al., 2012; Mennekens and Vanbeveren, 2014). However, they affect the rate of production of r -process elements by several factors which are much smaller than the uncertainty of the rate of NSMs. We therefore only implement NSMs for simplicity.

2.2.3 Definition of newly formed stars

The abundance of a star must be identical to the abundance of the gas, which formed the star. The abundance of a newly formed star particle inherits (1) the abundance of the SF gas particle (e.g., Raiteri et al., 1999; van de Voort et al., 2015; Shen et al., 2015); (2) the abundance of the average of gas particles within a SPH kernel (e.g., Steinmetz and Müller, 1994; Kobayashi and Nakasato, 2011; Shen et al., 2015). Method (1) does not have a metal mixing process except for hydrodynamical mixing process such as stellar winds, outflows and inflows due to the SN explosion. $[\text{Eu}/\text{Fe}]$ produced in method (1) is discussed in Section 2.4.1. On the other hand, in method (2), a metal mixing process is taken into account. We use a metallicity averaged over 32 neighbor gas particles in a SPH kernel to a newly born star particle. The region can be regarded as an SF region, which corresponds to $\sim 10^4 M_{\odot}$. This mass corresponds to the typical size of GMCs (e.g., Larson, 1981; Liszt, Delin, and Burton, 1981; Sanders, Scoville, and Solomon, 1985; Solomon et al., 1987; Heyer et al., 2009). We discuss results inferred from method (2) in Section 2.4.2.

Massive stars tend to be born in clusters and associations (Lada and Lada, 2003). Clusters and OB associations form from GMCs. Observations of stars in open clusters suggest that their metallicity is homogeneous (De Silva et al., 2007b; De Silva et al., 2007a; Pancino et al., 2010; Bubar and King, 2010; Ting et al., 2012; Reddy, Giridhar, and Lambert, 2012; Reddy, Giridhar, and Lambert, 2013; De Silva et al., 2013). Feng and Krumholz (2014) theoretically show that turbulent mixing in SF regions causes this homogeneity. The timescale of metal mixing is determined by the local dynamical time of SF regions ($\lesssim 1$ Myr). This timescale is much shorter than the typical timescale of SF ($\gtrsim 10$ Myr) in slow SF model (Zuckerman and Evans, 1974; Krumholz and Tan, 2007). We thus assume that the metals are instantaneously mixed in SF regions. We discuss the effect of different implementation on abundance ratios in galaxies in Section 2.4.1 and 2.4.2. This metal mixing model is adopted in Chapters 2 and 3.

2.2.4 Models of dSphs

We follow initial conditions of dSph models adopted in Revaz et al. (2009) and Revaz and Jablonka (2012). Both dark matter and gas particles follow the pseudo-isothermal profile (Begeman, Broeils, and Sanders, 1991), based on the observed dark matter profiles of nearby dwarf galaxies (Oh et al., 2011; Oh et al., 2015),

$$\rho = \frac{\rho_c}{1 + (r/r_c)^2}, \quad (2.3)$$

where ρ_c is the central density and r_c is the core radius. Gas particles are also distributed along with the profile. We set $r_c = 1.0$ kpc, $r_{\max} = 7.1$ kpc, and $M_{\text{tot}} = 7 \times 10^8 M_{\odot}$, according to Revaz and Jablonka (2012). We adopt 0.15 of mass ratio of gas to dark matter particles (baryon fraction, $f_b \equiv \Omega_b/\Omega_m$). The value of f_b is taken from Planck Collaboration et al. (2014). Adopting particles with different mass may suffer dynamical friction. Massive particles more easily fall into the center of the galaxy by losing angular momentum. In Appendix B, we show the effects of dynamical friction.

Following Revaz et al. (2009), we assume an isotropic velocity dispersion of dark matter particles, $\sigma(r)$, for spherical distribution (Hernquist, 1993; Binney and Tremaine, 2008),

$$\sigma^2(r) = \frac{1}{\rho(r)} \int_r^\infty dr' \rho(r') \frac{\partial \Phi(r')}{\partial r'}, \quad (2.4)$$

where $\Phi(r)$ is the gravitational potential. For gas particles, we set a velocity equal to zero and an initial temperature of 10^4 K. For both dark matter and gas particles, we adopt gravitational softening length (ϵ_g) of 28 pc for runs with the initial total number (N) of 2^{14} , $\epsilon_g = 14$ pc for runs with $N = 2^{16}$, 2^{17} , and 2^{18} , and $\epsilon_g = 7$ pc for runs with $N = 2^{19}$. We run our simulations over 14 Gyr. The parameters of our model galaxies are listed in Table 2.1. Table 2.2 summarizes all runs discussed in this chapter.

TABLE 2.1: Parameters of the initial condition.

Quantity	Values
M_{tot}	$7 \times 10^8 M_{\odot}$
r_c	1 kpc
r_{\max}	7.1 kpc
f_b	0.15

Notes: Values are taken from Revaz et al., 2009; Revaz and Jablonka, 2012.

TABLE 2.2: List of models discussed in this chapter.

Model	N	m_{DM} ($10^3 M_{\odot}$)	m_{gas} ($10^3 M_{\odot}$)	ϵ_{g} (pc)	n_{th} (cm^{-3})	T_{th} (10^3K)	ϵ_{SN} (10^{51}erg)	N_{ngb}	Mixing	t_{NSM} (Myr)	f_{NSM}
s000	2^{19}	2.3	0.4	7	100	1	1	32	no	100	0.01
m000	2^{19}	2.3	0.4	7	100	1	1	32	yes	100	0.01
mN16	2^{19}	2.3	0.4	7	100	1	1	16	yes	100	0.01
mN64	2^{19}	2.3	0.4	7	100	1	1	64	yes	100	0.01
m014	2^{14}	72.6	12.8	28	100	1	1	32	yes	100	0.01
m016	2^{16}	18.2	3.2	14	100	1	1	32	yes	100	0.01
m017	2^{17}	9.1	1.6	14	100	1	1	32	yes	100	0.01
m018	2^{18}	4.5	0.8	14	100	1	1	32	yes	100	0.01
mExt	2^{19}	2.3	0.4	7	0.1	30	0.03	32	yes	100	0.01
mt10	2^{19}	2.3	0.4	7	100	1	1	32	yes	10	0.01
mt500	2^{19}	2.3	0.4	7	100	1	1	32	yes	500	0.01
mr0.001	2^{19}	2.3	0.4	7	100	1	1	32	yes	100	0.001
mr0.1	2^{19}	2.3	0.4	7	100	1	1	32	yes	100	0.1

Notes: Parameters adopted in our models: (1) Model: name of our models. Models named “000” adopt the fiducial parameter set. Model s000 is discussed in Section 2.3 and Section 2.4.1. Models m000 to m018 are discussed in Section 2.4.2. Model mExt is discussed in Section 2.4.3. Models mt10 and mt500 are discussed in Section 2.4.4. Models mr0.001 and mr0.1 are discussed in Section 2.4.5. (2) N : initial total number of particles. (3) m_{DM} : mass of one dark matter particle. (4) m_{gas} : initial mass of one gas particle. (5) ϵ_{g} : gravitational softening length. (6) n_{th} : threshold density for SF. (7) T_{th} : threshold temperature for SF. (8) ϵ_{SN} : SN feedback energy. (9) N_{ngb} : number of nearest neighbor particles. (10) Mixing: with (yes) or without (no) metal mixing in SF region. (11) t_{NSM} : merger times of NSMs. (12) f_{NSM} : fraction of NSMs.

2.3 Chemodynamical evolution of dSphs

2.3.1 Dynamical evolution of dSph models

We discuss chemodynamical evolution of model s000 to confirm that the parameter set of this model is appropriate for the case of dSphs. Parameter dependence is discussed in Appendix A. Figure 2.1 shows the evolution of the spatial distribution of gas and stars of model s000. Upper panels of Figure 2.1 show the gas density maps of model s000 at 0 Gyr, 1 Gyr, 5 Gyr, and 10 Gyr from the beginning of the simulation. The gas monotonically collapses during the first 1 Gyr. Then, gas density reduces by SF and gas outflow by energy feedback of SNe. Red colored area in upper panels of Figure 2.1 corresponds to the SF region where the number density of gas is larger than 100 cm^{-3} . As shown in this figure, SF region is strongly confined at the center of the galaxy. The red area is largest at 1 Gyr. This indicates that SF is most active after ~ 1 Gyr from the beginning of the simulation.

Lower panels of Figure 2.1 show stellar density maps at 0 Gyr, 1 Gyr, 5 Gyr, and 10 Gyr. The distribution of stars at 1 Gyr is associated with the high-density region of gas (red region in Figure 2.1). As shown in these figures, stars continuously form in the inner region of this model galaxy for over 10 Gyr and stellar density distribution expands with time from the center to the outer region. At 10 Gyr, the morphology of the galaxy becomes spherical symmetry.

In order to quantitatively discuss the structural and dynamical properties of models, we investigate the radial profiles. Figure 2.2 shows the radial profiles of model s000. We define the galactic center using potential minimum. The values in each point are calculated in each bin from the center to the outer region. Figure 2.2 (a) shows time variation of the dark matter density profile. At 1 Gyr, the dark matter follows the initial density profile given in Equation (2.3). After the collapse in the first 1 Gyr, the shape of the dark matter profile does not change over 10 Gyr.

Figure 2.2(b) shows time variation of the gas density profile. Inner region ($\lesssim 1$ kpc) of the gas density profile follows the evolution of the dark matter density profile. Outer region of gas is blown away due to the outflow induced by SNe. In addition, the total amount of gas reduces because of SF. However, gas still remains even at 10 Gyr. As in Appendix A, all of our models have gas at 10 Gyr. The observed LG dSphs in contrast have no or little gas (e.g. McConnachie, 2012). This result suggests that physical processes such as ram pressure and tidal stripping are required to remove all gas away from dSphs (Mayer et al., 2006; Nichols, Revaz, and Jablonka, 2014).

In Figure 2.2 (c), we present the stellar density profiles. Stars distribute within ~ 1 kpc, which is consistent with the observed tidal radii ($\sim 0.5 - 3$ kpc) of dSphs in the LG (Irwin and Hatzidimitriou, 1995). The density profile of stars is basically associated with the dark matter density profile.

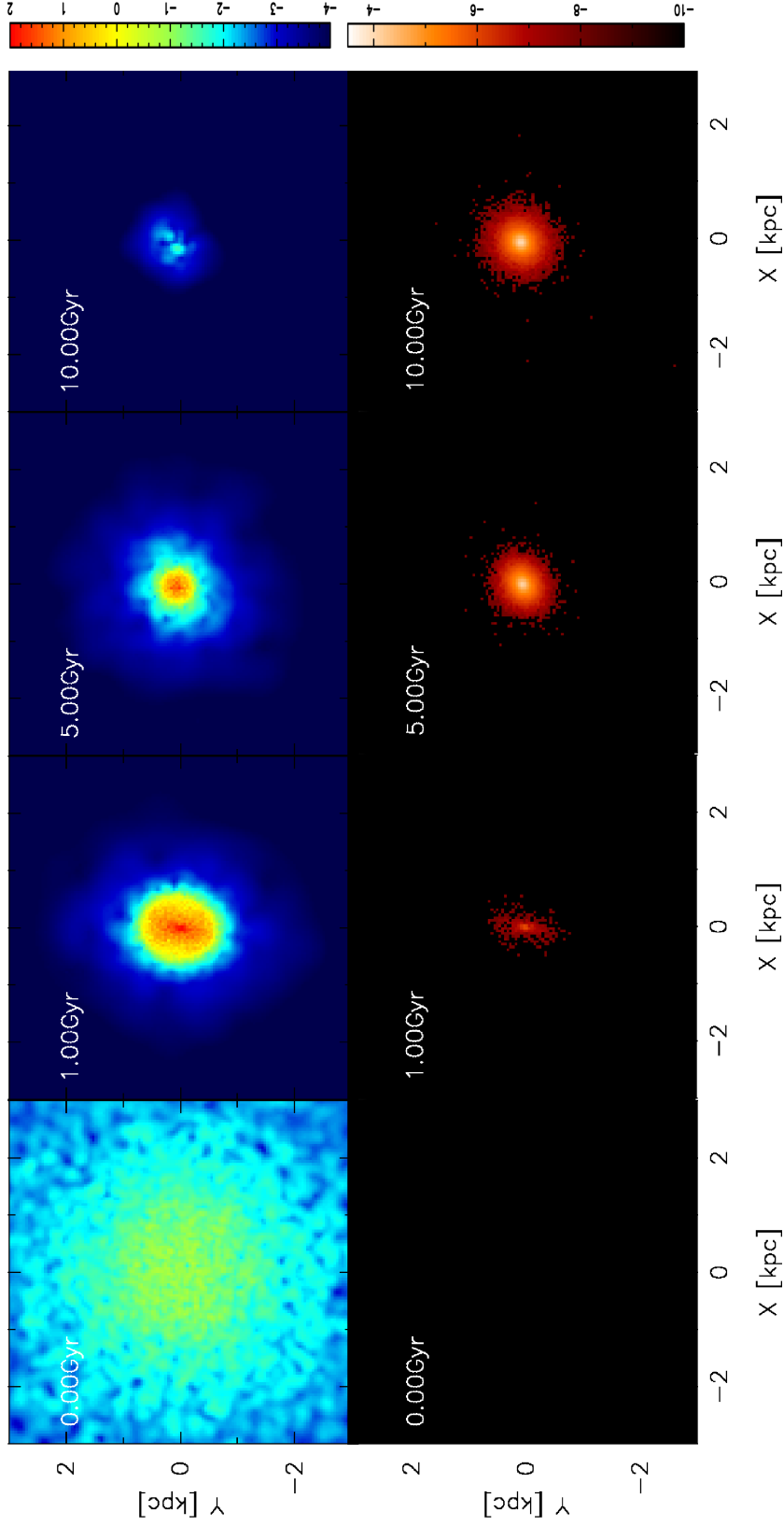


FIGURE 2.1: Evolution of model s000. Upper panels: snapshots of slice gas density in log scale, between 10^{-4} cm^{-3} (blue) and 10^2 cm^{-3} (red). Lower panels: snapshots of stellar surface density with log scale, between $10^{-10} 10^{10} M_{\odot} \text{ kpc}^{-2}$ (black) and $10^{-3.5} 10^{10} M_{\odot} \text{ kpc}^{-2}$ (white).

Figure 2.2 (d) shows the stellar velocity dispersion profile. The observed stellar velocity dispersion of dSphs is almost constant within ~ 1 kpc from the center (Walker et al., 2009). Model s000 has similar properties with the observed radial stellar velocity dispersion profiles inside 1 kpc from the center in the LG dSphs.

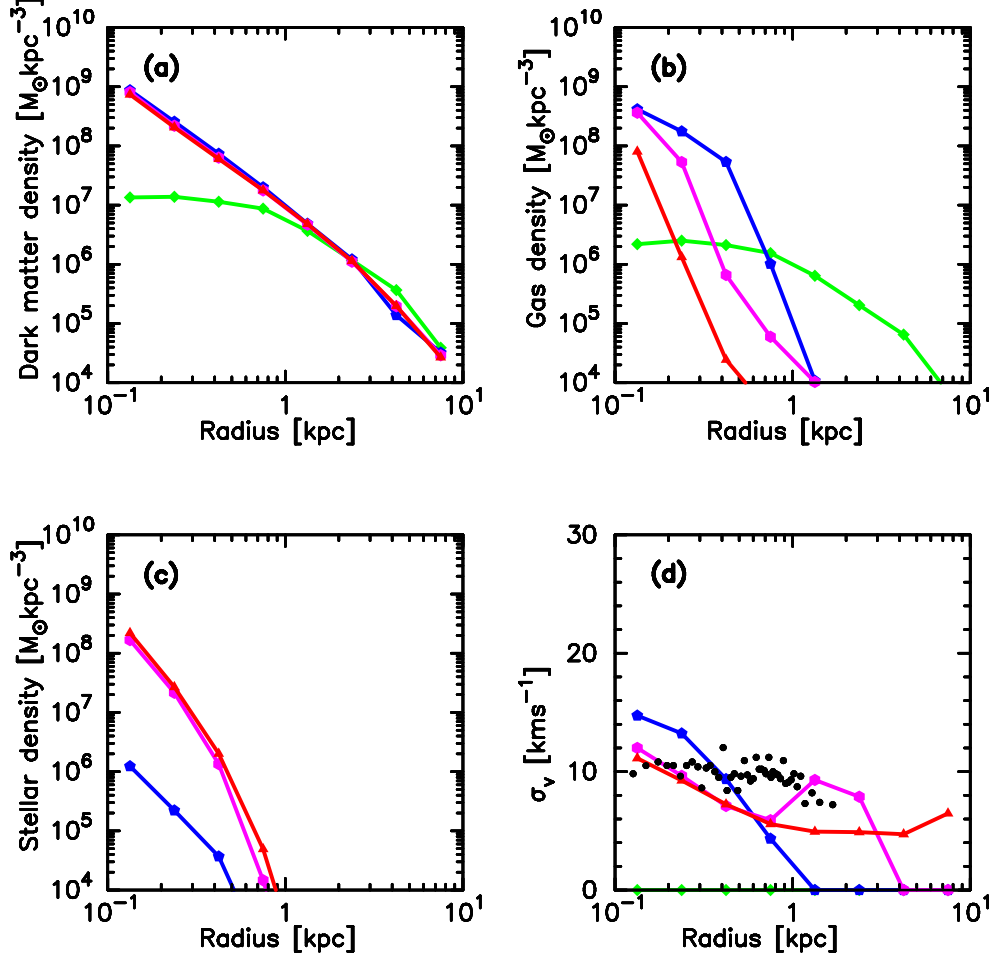


FIGURE 2.2: Radial profiles of model s000 at $t = 0$ Gyr (green), 1 Gyr (blue), 5 Gyr (magenta), and 10 Gyr (red). (a) Radial dark matter density profile. (b) Radial gas density profile. (c) Radial stellar density profile. (d) Radial stellar velocity dispersion profile. Black dots are observed stellar velocity dispersion in the Fornax dSph (Walker et al., 2009).

2.3.2 Time variations of the SFRs

Figure 2.3 shows the time variation of the SFR in model s000 (red curve) and the observed values of the Fornax and the Sculptor dSphs (de Boer et al., 2012b; de Boer et al., 2012a). The SFR of model s000 is peaked at ~ 2 Gyr. Gas density increases with accretion (see Figure 2.2 (b)) and finally reaches the threshold density for SF. On the other hand, SN feedback drives gas away from the inner region to the outer region (Hopkins, Quataert, and Murray, 2011). Because of the shallow gravitational potential and high threshold density for SF ($n_{\text{th}} = 100 \text{ cm}^{-3}$), SN feedback significantly

affects the timescale of gas accretion. It therefore takes long time (~ 1 Gyr) to reach the peak of the SFR. The SFR of model s000 ($\sim 10^{-3} M_{\odot} \text{ yr}^{-1}$) is consistent with the observed value of the Fornax and the Sculptor dSphs inferred from color-magnitude diagram analysis ($\sim 10^{-3} M_{\odot} \text{ yr}^{-1}$, de Boer et al., 2012b; de Boer et al., 2012a). The SFR of model mExt (magenta curve) is discussed in Section 2.4.3.

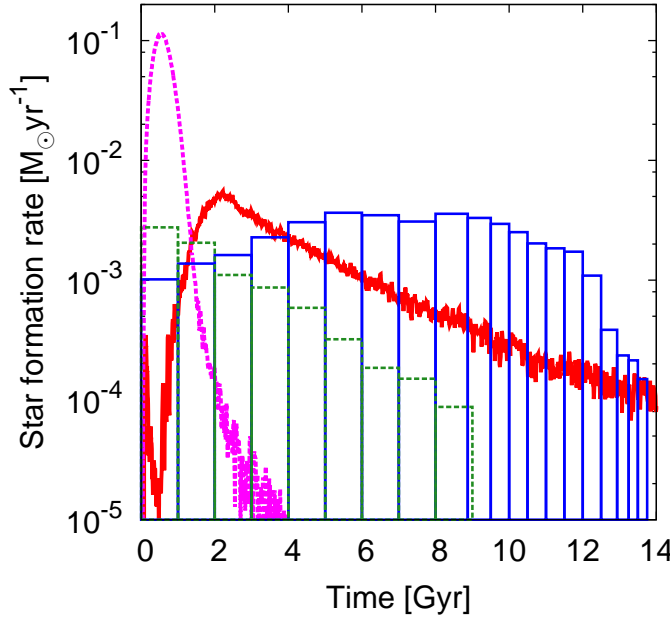


FIGURE 2.3: The SFR as a function of time for our models. Red and magenta-dashed curves represent the SFR of models s000 and mExt, respectively. Blue and green-dashed histograms represent the observed SFR of the Fornax dSph (de Boer et al., 2012a) and the Sculptor dSph (de Boer et al., 2012b), respectively.

2.3.3 Metallicity distribution

Metallicity distribution is one of the best properties to test reliability of chemical evolution models. Figure 2.4 compares metallicity distribution between model s000 and observation. All data of the Fornax (Kirby et al., 2010) and the Sculptor dSphs (Kirby et al., 2009; Kirby et al., 2010; Kirby and Cohen, 2012). Metallicity distribution of model s000 is almost consistent with the observed value of the Sculptor dSph. The metallicity at the peak of the distribution of model s000 is $[\text{Fe}/\text{H}] = -1.57$, which is lower than that of the Fornax dSph, $[\text{Fe}/\text{H}] = -1.06$ (Kirby et al., 2013). This is because we do not implement SNe Ia in this model, while the Fornax dSph must be significantly affected by the metal ejection of SNe Ia (e.g., Kirby et al., 2010). If we take into account of the products of SNe Ia, the peak metallicity is expected to shift by ~ 0.5 dex to the higher metallicity, which is closer value to that of the Fornax dSph.

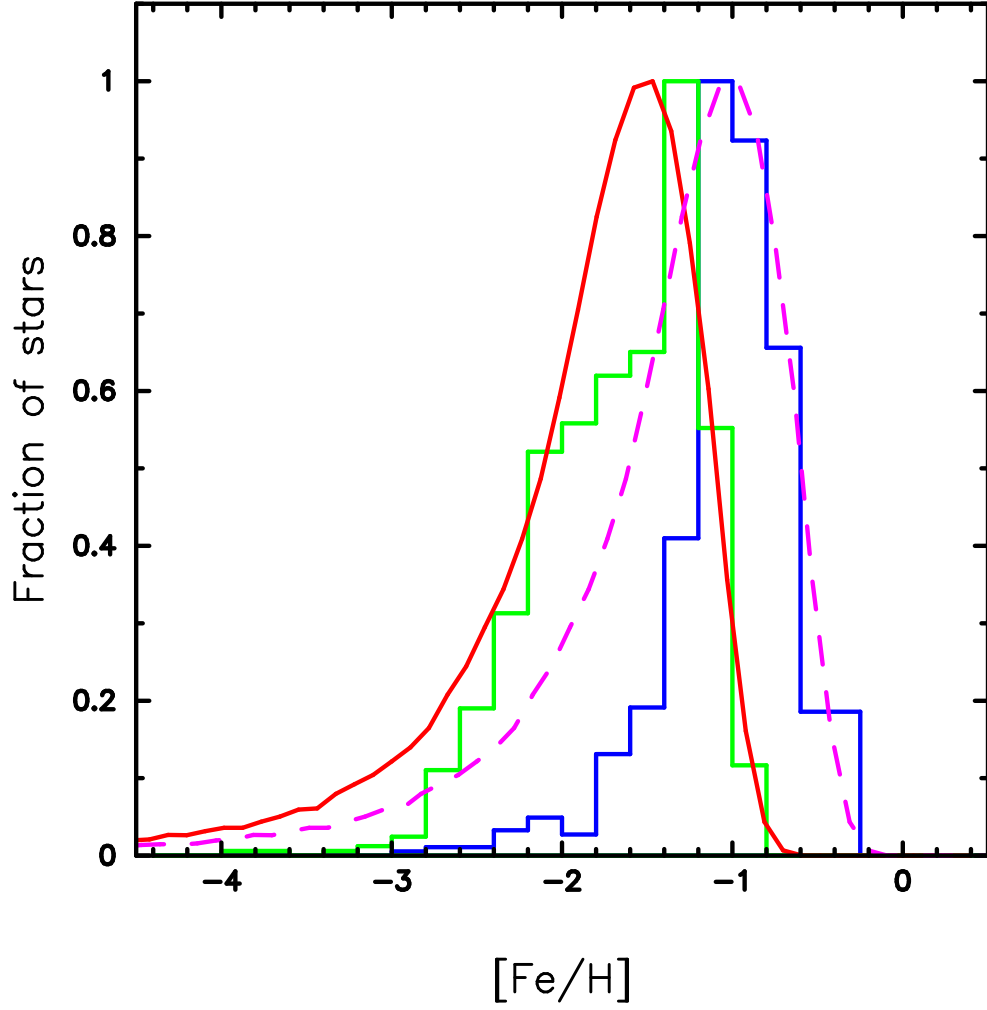


FIGURE 2.4: Metallicity distribution of model s000 (red curve), model s000 but $[\text{Fe}/\text{H}]$ is shifted to 0.5 dex taking into account the effect of SNe Ia (magenta-dashed curve), the observed value of the Fornax dSph (blue histogram) (Kirby et al., 2010), and the Sculptor dSph (green histogram) (Kirby et al., 2009; Kirby et al., 2010; Kirby and Cohen, 2012).

2.4 Enrichment of r -process elements in dwarf spheroidal galaxies

2.4.1 Enrichment of r -process elements without metal mixing in SF region

In this section, we discuss $[\text{Eu}/\text{Fe}]$ as a function of $[\text{Fe}/\text{H}]$ predicted in model s000. In model s000, the metallicity of a star particle inherits that of the gas particle from which the star particle was formed, according to the method (1) in Section 2.2.3. Figure 2.5 shows $[\text{Eu}/\text{Fe}]$ as a function of $[\text{Fe}/\text{H}]$ predicted in model s000. We also put the observed data of the Galactic halo and several dSphs, i.e., Carina, Draco, Leo I, Sculptor, and Ursa Minor dSphs (SAGA database, Suda et al., 2008; Suda et al., 2011; Suda et al., 2017; Yamada et al., 2013), excluding carbon-enhanced stars, which are possibly affected by gas transfer in binaries. We also exclude stars in the Fornax dSph because some of them have extremely high $[\text{Eu}/\text{Fe}]$ (> 0.5 dex) due to significant contamination of the s -process (Letarte et al., 2010). As shown in Figure 2.5, stars of highly r -process enhanced stars; $[\text{Eu}/\text{Fe}] > 1$ (so-called r -II stars), are over-abundant. In addition, r -deficient stars in $-2 < [\text{Fe}/\text{H}] < -1$ are predicted. Such low $[\text{Eu}/\text{Fe}]$ stars are not seen in the observation. These stars are not simply caused by delayed production of Eu by NSMs. In fact, the average value of $[\text{Eu}/\text{Fe}]$ does not increase with metallicity at around $[\text{Fe}/\text{H}] \sim -2$. The significant dispersions of chemical components among gas particles seem to be rather essential. The relations between the galactic age and abundances of Fe and Eu show the reason why such large dispersions are seen in low metallicity region. Figure 2.6 (a) shows $[\text{Fe}/\text{H}]$ as a function of time. Metallicity obviously increases with time, as CCSNe produce iron. The metallicity however has more scatters at the earlier time, especially during the first few Gyrs. Then, later formed stars are enriched by more numerous CCSNe, and as a result, the dispersion of stellar metallicity decreases with time. We denote the stars, which are formed from the gas enriched only by a single CCSN by black circles in Figure 2.6 (a). Their metallicity widely distributes over ~ 3 dex. These stars concentrate only in $\lesssim 2$ Gyr.

Figure 2.6 (b) shows $[\text{Eu}/\text{H}]$ as a function of time. In contrast to Figure 2.6 (a), large star-to-star scatters in $[\text{Eu}/\text{H}]$ remain over the whole evolution of the galaxy. As shown in black circles in Figure 2.6 (b), gas particles affected by one NSM remain over 10 Gyr. One of the reasons must be the low rate of NSMs. The rate of NSMs is one hundred times lower than that of CCSNe in this model. The total number of NSMs may not be enough to converge the $[\text{Eu}/\text{H}]$ in this model.

In addition to the low NSM rate, the efficiency of gas mixing in this model seems to cause unnaturally large scatters in $[\text{Eu}/\text{H}]$. If a star particle contains products from a single NSM, the value of $[\text{Eu}/\text{H}]$ must be determined by the distance from the NSM, which enriched the star forming gas particle. However, as shown in Figure 2.6 (b), dispersion of such stars drags longer than 5 – 10 Gyrs, which is much longer than the merger times of NSMs. It implies that gas particles never change the abundance of Eu, unless other NSMs enrich them again, although in actual, gas clouds are expected to interact with others. Observations of open clusters show that stellar metallicity is quite homogeneous in each cluster (e.g., De Silva et al., 2007b; De Silva et al., 2007a; Pancino et al., 2010; Bubar and King, 2010; Ting et al., 2012; Reddy, Giridhar, and

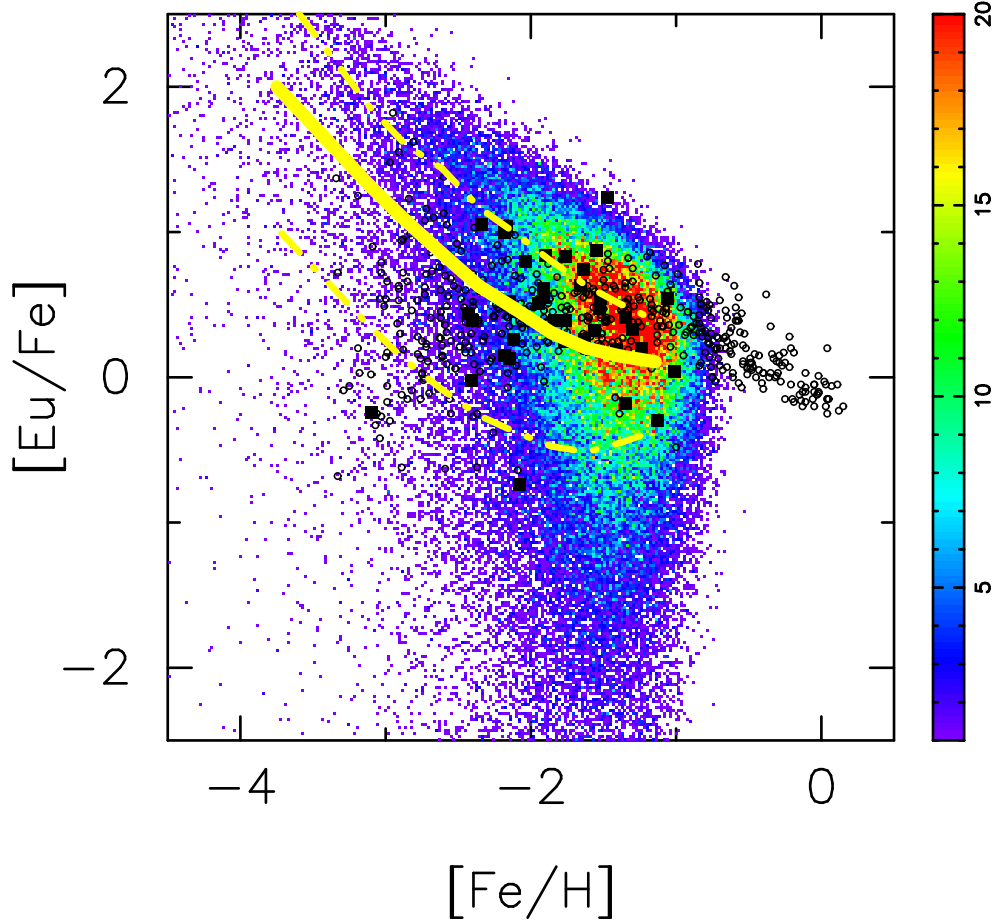


FIGURE 2.5: $[\text{Eu}/\text{Fe}]$ as a function of $[\text{Fe}/\text{H}]$ of model s000. Contour is the number of stars produced in our model, between 0 (purple) and 20 (red). Yellow curve is the median of model prediction. Dash-dotted curves are the first and third quartiles, respectively. Circles are the observed value of the Galactic halo stars (SAGA database, Suda et al., 2008; Suda et al., 2011; Yamada et al., 2013). Squares are the observed value of stars in Carina, Draco, Leo I, Sculptor, and Ursa Minor dSphs (SAGA database, Suda et al., 2017). Stars produced by our model are plotted within 0.5 kpc from the center of our model galaxies.

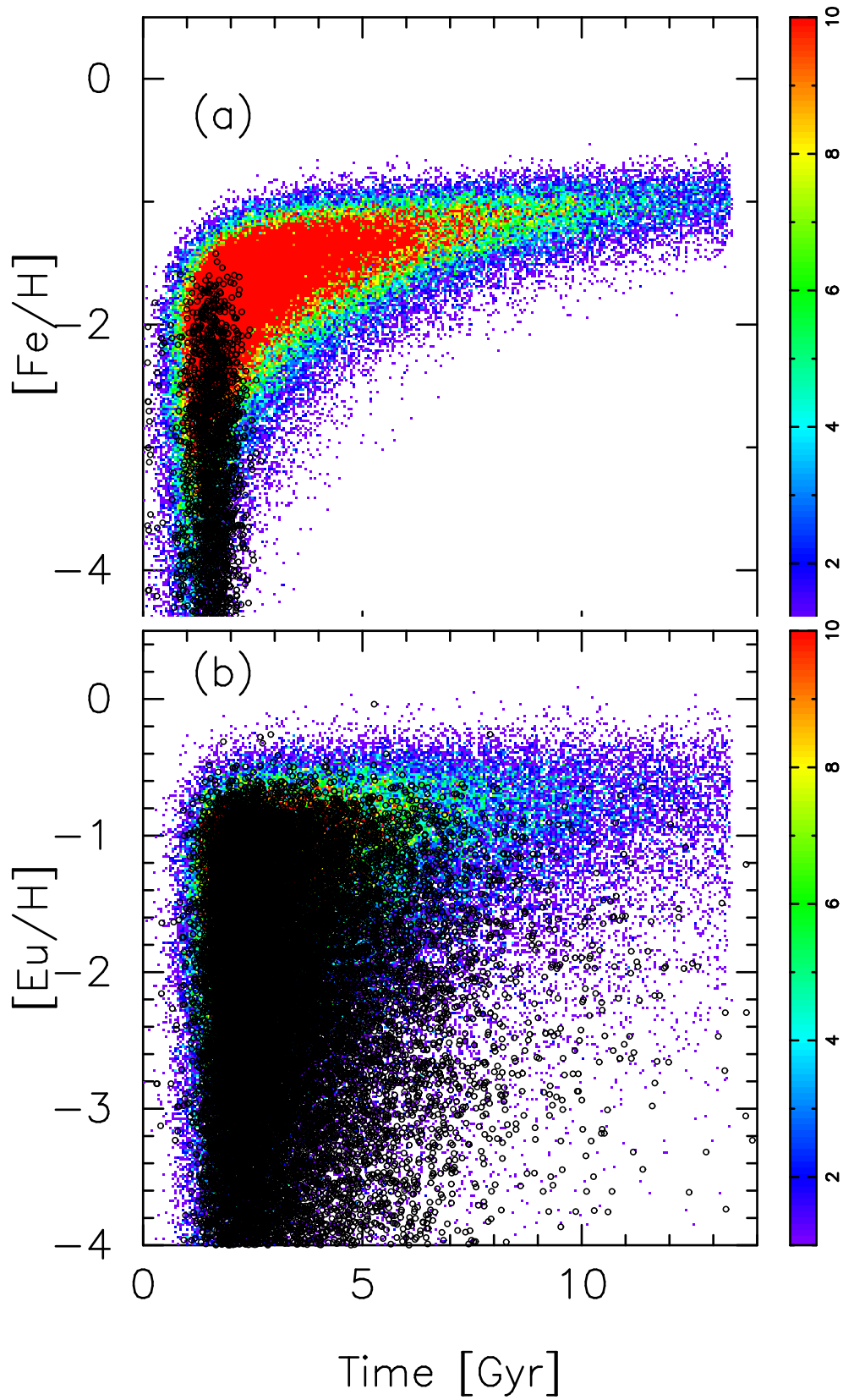


FIGURE 2.6: (a) $[\text{Fe}/\text{H}]$ as a function of time from the start of the simulation of model s000. (b) $[\text{Eu}/\text{H}]$ as a function of time from the start of the simulation of model s000. Black circles are stars formed from gas particles, which are affected by one CCSN. Contour is the same as Figure 2.5.

Lambert, 2012; Reddy, Giridhar, and Lambert, 2013; De Silva et al., 2013). The gas in SF region is possibly homogenized by hydro-dynamical effects, such as turbulent mixing (Feng and Krumholz, 2014). In addition, previous studies suggest that the standard SPH simulations without metal mixing tend to predict a lower amount of gas with low metallicity and higher metallicity of inter galactic medium (Wiersma et al., 2009; Shen, Wadsley, and Stinson, 2010). Shen et al. (2015) suggest that it is difficult to reproduce the observed [Eu/Fe] as a function of [Fe/H] without metal mixing in SF region.

On the other hand, the fiducial model of van de Voort et al. (2015) reproduces the observed [Eu/Fe] of metal-poor stars, although they adopt the same definition of metallicity as our model s000. They suggest that large-scale metal mixing such as galactic winds and hydrodynamical flows is important to reproduce the observed [Eu/Fe] as a function of [Fe/H]. In their model, NSMs eject metals in the region of $3.5 \times 10^6 M_{\odot}$, which is much larger than the swept-up mass of NSMs ($\sim 10^4 M_{\odot}$). The treatment of van de Voort et al. (2015) is identical to implement metal mixing.

2.4.2 Enrichment of *r*-process elements with metal mixing in SF region

As discussed in the previous section, the effect of mixing of enriched gas must be essential to account for the observed values of [Eu/Fe] in metal-poor stars. Therefore, we take into account the effect of metal mixing according to the method (2) in Section 2.2.3, and we adopt the average metallicity of gas particles in the SPH kernel of the progenitor gas particle for the metallicity of newly formed stars. Figure 2.7 shows [Eu/Fe] as a function of [Fe/H] with the metal mixing model, m000. Model m000 has the same parameter set for s000 except for the effect of metal mixing in SF region (see Table 2.2). As shown in this figure, *r*-deficient stars in [Fe/H] of -2 to -1 seen in Figure 2.5 disappear due to metal mixing. The fraction of *r*-II stars is also reduced in this model due to the adoption of averaged metallicity in the SF region. Model m000 apparently reproduces the observational tendency of [Eu/Fe] in metal-poor stars much better than the model s000. Our model does not require the assumption of short merger times ($t_{\text{NSM}} \lesssim 10$ Myr), which is required to reproduce observations in previous studies (e.g., Argast et al., 2004; Matteucci et al., 2014; Komiya et al., 2014; Tsujimoto and Shigeyama, 2014).

Figure 2.8 shows [Eu/Fe] distributions in stars of [Fe/H] < -2.0 predicted in s000 (without mixing model) and m000 (with mixing model). Observational values of the MW (red histogram) and dSphs (blue histogram) are provided by the SAGA database (Suda et al., 2008; Suda et al., 2011; Suda et al., 2017; Yamada et al., 2013). While model s000 overproduces stars with [Eu/Fe] < -1 , model m000 significantly reduces the fraction of *r*-deficient stars. In addition, the fraction of *r*-II stars also reduces in model m000. This result therefore suggests that metal mixing in SF region is fairly important physical process to reproduce the observed [Eu/Fe] as a function of [Fe/H].

The predicted distribution of [Eu/Fe] must be affected by the mass of the mixed gas (M_{mix}), and the initial total number of particles (N). We define $M_{\text{mix}} = N_{\text{ngb}} m_{\text{gas}}$. The mass of one gas particle (m_{gas}) is proportional to N^{-1} . Table 2.3 lists the examined values of parameters and the corresponding mixing mass (M_{mix}). Figure 2.9 (a) shows the median value and the dispersion of [Eu/Fe] of models, which have different N_{ngb} .

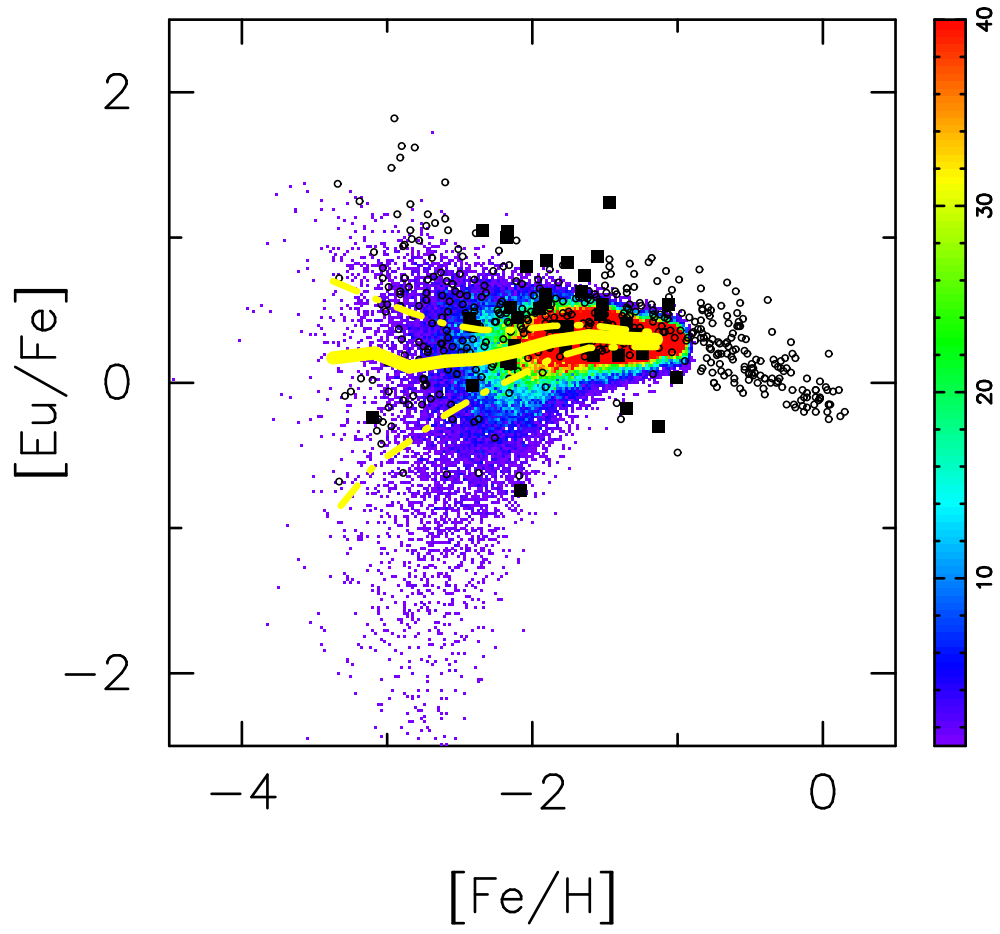


FIGURE 2.7: $[\text{Eu}/\text{Fe}]$ as a function of $[\text{Fe}/\text{H}]$ of the model m000. Symbols are the same as Figure 2.5.

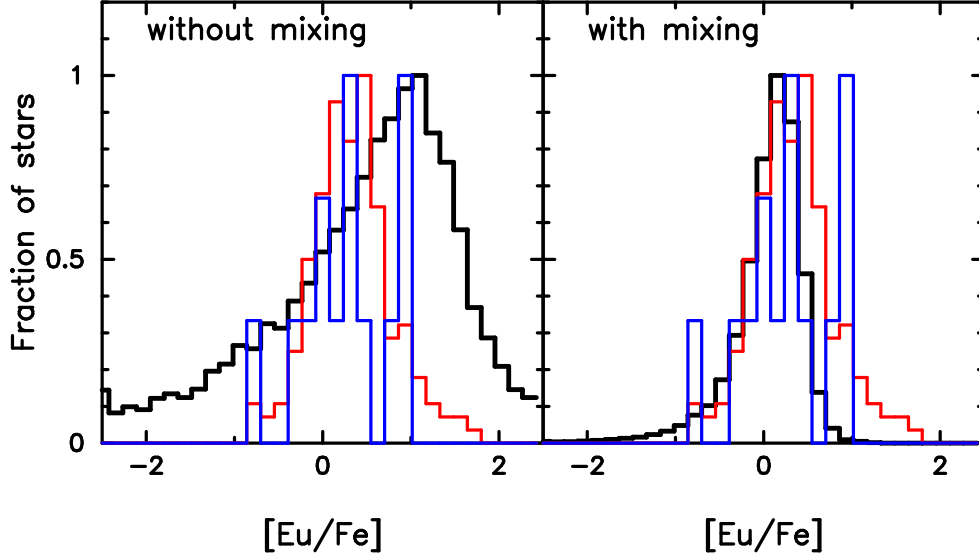


FIGURE 2.8: $[\text{Eu}/\text{Fe}]$ distribution of stars with $[\text{Fe}/\text{H}] < -2.0$ of our models (black histogram) and observation (red histogram: the Galactic halo stars, blue histogram: Carina, Draco, Leo I, Sculptor, and Ursa Minor dSphs). Data are compiled by SAGA database (Suda et al., 2008; Suda et al., 2011; Suda et al., 2017; Yamada et al., 2013). Left panel: plotted model is s000 (without metal mixing in SF region). Right panel: plotted model is m000 (with metal mixing in SF region).

The dispersion of $[\text{Eu}/\text{Fe}]$ becomes smaller with larger N_{ngb} as shown in this figure. When we increase the N_{ngb} , the value of M_{mix} increases and larger mass fraction of gas in the galaxy is mixed. Due to the effects of increasing M_{mix} , the dispersion becomes smaller in the models with larger value of N_{ngb} .

Figure 2.9 (b) shows the median value of $[\text{Eu}/\text{Fe}]$ as a function of $[\text{Fe}/\text{H}]$ of models, which have different N . As shown in Figure 2.9 (b), the dispersion of $[\text{Eu}/\text{Fe}]$ shows the similar tendency irrespective of N , i.e., it decreases with increasing of metallicity. When we adopt the larger value of N , more star particles are produced, i.e., the number of events of metal mixing increases. This means that metals are more mixed in the SF region if M_{mix} is constant. However, M_{mix} is defined to be proportional to N^{-1} . Models with larger value of N have smaller value of M_{mix} . The effect of increasing N offsets the effect made by decreasing M_{mix} . Thus, the dispersion is not affected by N .

2.4.3 The effect of SN feedback to the enrichment of r -process elements

The value and scatters in the abundance ratio of $[\text{Eu}/\text{Fe}]$ must be affected by SFR, especially for metal-poor stars. In order to examine the effect of SFR, we discuss $[\text{Eu}/\text{Fe}]$ as a function of $[\text{Fe}/\text{H}]$ with the model mExt, in which extremely weak SN feedback energy ($\epsilon_{\text{SN}} = 3 \times 10^{49}$ erg) and low threshold density for SF ($n_{\text{th}} = 0.1 \text{ cm}^{-3}$) are assumed (Table 2.2). According to Appendix A, the weaker feedback model produces higher SFR and model with smaller value of n_{th} shifts the peak of SFR to the earlier time. Since mExt has lower values of ϵ_{SN} and n_{th} , stars are more

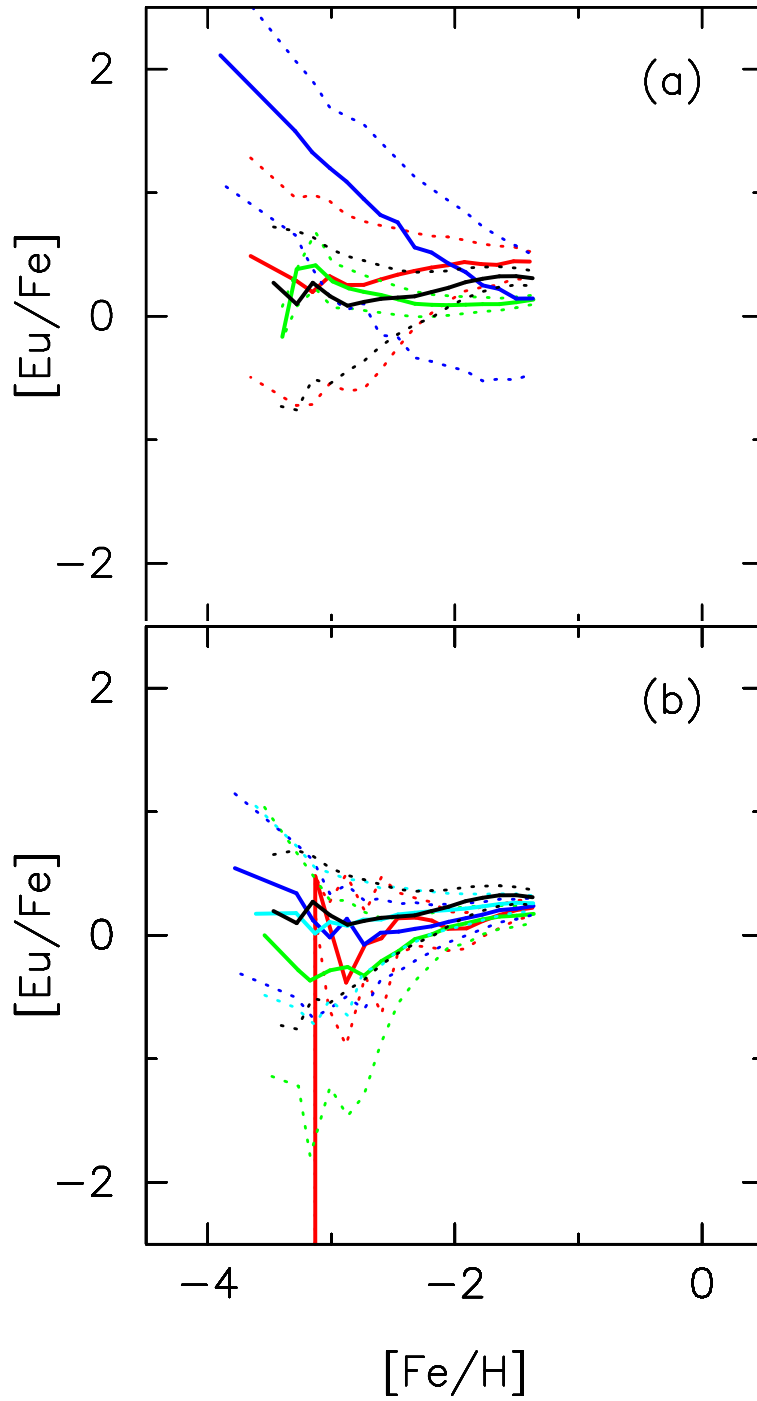


FIGURE 2.9: (a) Median $[\text{Eu}/\text{Fe}]$ as a function of $[\text{Fe}/\text{H}]$ produced by the different number of nearest neighbor particles (N_{ghb}). Solid curves are the median of model prediction and dashed curves are the first and third quartiles. Red curve represents mN16 ($N_{\text{ghb}} = 16$). Black curve represents m000 ($N_{\text{ghb}} = 32$). Green curve represents mN64 ($N_{\text{ghb}} = 64$). Blue curve represents s000 (without metal mixing in SF region). (b) Median $[\text{Eu}/\text{Fe}]$ as a function of $[\text{Fe}/\text{H}]$ produced by different initial number of particles (N). Red curve represents m014 ($N = 2^{14}$). Green curve represents m016 ($N = 2^{16}$). Blue curve represents m017 ($N = 2^{17}$). Sky blue curve represents m018 ($N = 2^{18}$). Black curve represents m000 ($N = 2^{19}$).

TABLE 2.3: Mass of metal mixing region.

Model	N	N_{ngb}	M_{mix} ($10^4 M_{\odot}$)
m000	2^{19}	32	1.3
mN16	2^{19}	16	0.6
mN64	2^{19}	64	2.7
m018	2^{18}	32	2.6
m017	2^{17}	32	5.1
m016	2^{16}	32	10.3
m014	2^{14}	32	41.0

The columns correspond to the name of model, initial total number of particles (N), the number of nearest neighbor particles (N_{ngb}), and mass of the mixing region (M_{mix}).

easily produced comparing to the model m000. The SFR of model mExt during the first 1 Gyr rises rapidly and is larger than $10^{-2} M_{\odot} \text{yr}^{-1}$. The peak of SFR reaches $\sim 10^{-1} M_{\odot} \text{yr}^{-1}$, while that of m000 is $\lesssim 10^{-3} M_{\odot} \text{yr}^{-1}$. The SFR of model mExt at $\lesssim 1$ Gyr is much higher than the observational values (Figure 2.3).

Figure 2.10 shows $[\text{Eu}/\text{Fe}]$ as a function of $[\text{Fe}/\text{H}]$ in model mExt. This model predicts significantly different $[\text{Eu}/\text{Fe}]$ from m000 (Figure 2.7) although both models adopt the same initial distribution of gas particles. Model mExt produces a distribution of r -deficient stars around $[\text{Fe}/\text{H}] \sim -2$. In addition, no stars are produced below $[\text{Fe}/\text{H}] \sim -3$.

This difference is related to the timescale of chemical evolution in the early phase of the galaxy formation. For model m000, the median metallicity of gas particles at 1 Gyr is $[\text{Fe}/\text{H}] = -3.32$. On the other hand, the median metallicity of gas particles in mExt is $[\text{Fe}/\text{H}] = -0.91$ at 1 Gyr. The SFE of model mExt is estimated to be ~ 0.1 – 1 Gyr^{-1} . The value of SFE is comparable to some other inhomogeneous chemical evolution studies (Argast et al., 2004; Cescutti et al., 2015; Wehmeyer, Pignatari, and Thielemann, 2015). Model mExt proceeds chemical evolution much faster than m000 due to the high SFR of mExt ($\sim 10^{-2} M_{\odot} \text{yr}^{-1}$). The $[\text{Eu}/\text{Fe}]$ as a function of $[\text{Fe}/\text{H}]$ in model mExt is inconsistent with the observation due to fast chemical evolution by the high SFR. This result suggests that the SFR and SFE in the early phase of dSphs are $\lesssim 10^{-3} M_{\odot} \text{yr}^{-1}$ and $\lesssim 0.10 \text{ Gyr}^{-1}$, respectively, if the r -process elements are ejected by NSMs with a long merger time ($\sim 100 \text{ Myr}$). As shown in Figure 2.3, the SFR of $\sim 10^{-3} M_{\odot} \text{yr}^{-1}$ is a reasonable agreement with the observed value of the Fornax dSph (de Boer et al., 2012a). This SFR is also consistent with sub-halo models of Ishimaru, Wanajo, and Prantzos (2015) (Case 1 in their model suggests that the appropriate value of SFE for a sub-halo with a stellar mass of $10^7 M_{\odot}$ should be 0.10 Gyr^{-1} , which corresponds to the order of SFR as $\sim 10^{-3} M_{\odot} \text{yr}^{-1}$). They also suggest that the observed $[\text{Eu}/\text{Fe}]$ scatter in metal-poor stars by NSMs with a long merger time.

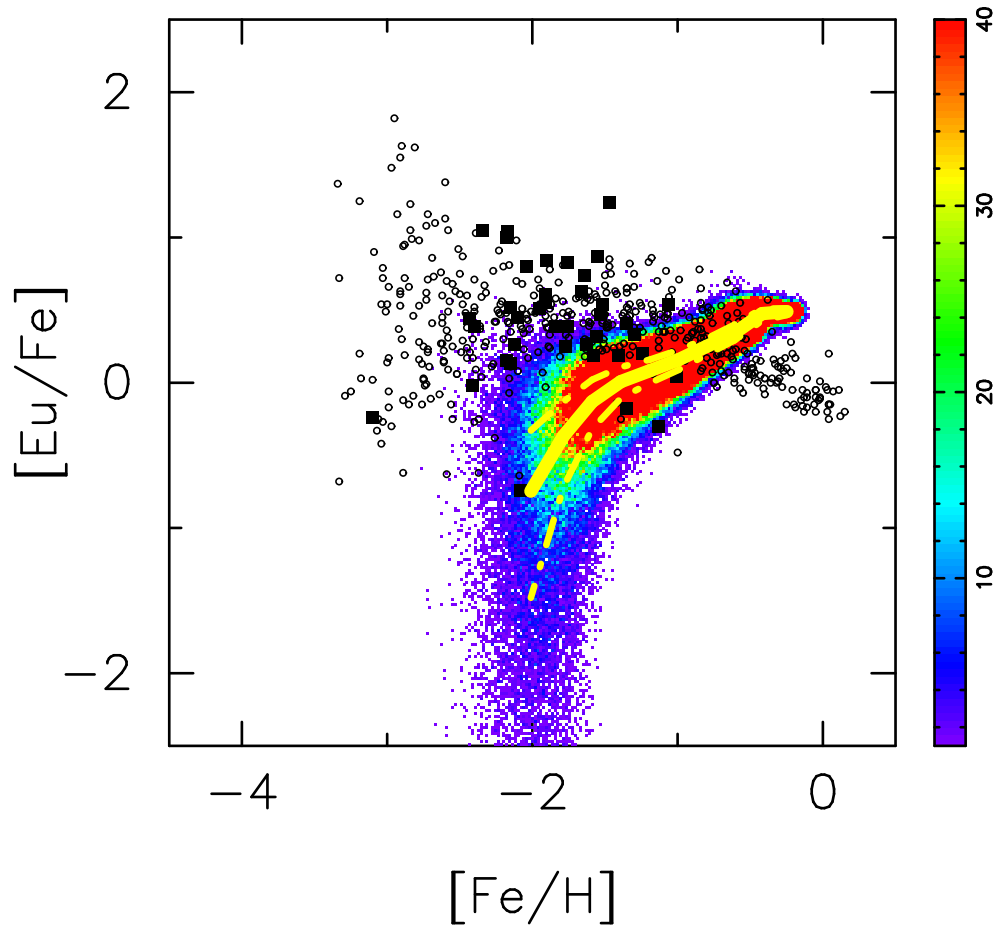


FIGURE 2.10: $[\text{Eu}/\text{Fe}]$ as a function of $[\text{Fe}/\text{H}]$ of model mExt ($M_{\text{tot}} = 7 \times 10^8 M_{\odot}$, $c_{\star} = 0.033$, $n_{\text{th}} = 0.1 \text{ cm}^{-3}$, $\epsilon_{\text{SN}} = 3 \times 10^{49} \text{ erg}$, and $t = 100 \text{ Myr}$). Symbols are the same as Figure 2.5.

2.4.4 Merger times of NSMs

In this section, we discuss the effect of merger times of NSMs. Figure 2.11 shows resultant [Eu/Fe] as a function of [Fe/H] by NSMs with different merger times (t_{NSM}). Eu in Figure 2.11 (a) and (b) are produced by NSMs with $t_{\text{NSM}} = 10$ Myr (mt10) and 500 Myr (mt500), respectively. Although mt10 has a slightly smaller fraction of stars in $-3 < [\text{Fe}/\text{H}] < -2$ than model m000, the global relative abundance ratio is similar to m000 ($t_{\text{NSM}} = 100$ Myr). Contrary to the models m000 and mt10, the model with much longer merger times such as 500 Myr in mt500 shows large scatters in [Eu/Fe] at higher metallicity and cannot account for the observed scatters in $[\text{Fe}/\text{H}] \sim -3$.

Figure 2.12 shows [Fe/H] as a function of the substantial galactic age, i.e., the elapsed time from the rise of the major SF. As shown in Figure 3, we can regard that the major SF arises from 600 Myr from the beginning of the calculation. The average metallicity of stars is almost constant during the first ~ 300 Myr. Due to low SFE of the galaxy, spatial distribution of metallicity is highly inhomogeneous in $\lesssim 300$ Myr. In this epoch, since most of gas particles are enriched only by a single SN, metallicity of stars is mainly determined simply by the distance from each SN to the gas particles which formed the stars. Therefore, NSMs with $t_{\text{NSM}} \sim 100$ Myr can account for the observation of EMP stars, as well as those with $t_{\text{NSM}} \sim 10$ Myr. In contrast, metallicity is well correlated with the galactic age after ~ 300 Myr, irrespective of the distance from each SN to the gas particles. Because SN products have already been well mixed in a galaxy, the stellar metallicity is determined by the number of the SNe, which enriched the stellar ingredients. Therefore, if merger times of NSMs are much longer than ~ 300 Myr, it is too long to reproduce observations.

2.4.5 The rate of NSMs

Although the Galactic rate of NSMs is highly uncertain, the yields of *r*-process elements in our models are related to the NSM rate as already mentioned in Section 2.2.1. The estimated Galactic NSM rate is 10^{-6} to 10^{-3} yr^{-1} based on three observed binary pulsars (Abadie et al., 2010b). Table 2.4 lists yields of models discussed here. Figure 2.13 shows predicted [Eu/Fe] as a function of [Fe/H] assuming different NSM rate. Figure 2.13 (a) and (b) represent models with the NSM fractions $f_{\text{NSM}} = 0.001$ (mr0.001) and $f_{\text{NSM}} = 0.1$ (mr0.1), respectively. The corresponding NSM rate in a MW-like galaxy is $\sim 10^{-5} \text{ yr}^{-1}$ (mr0.001) and $\sim 10^{-3} \text{ yr}^{-1}$ (mr0.1). Model mr0.001 predicts larger scatter and a smaller number of stars at $[\text{Fe}/\text{H}] < -3$ than m000. Model mr0.001 has [Eu/Fe] dispersion by more than 3 dex at $[\text{Fe}/\text{H}] = -2$. In addition, there remains ~ 1 dex dispersion even for stars with $[\text{Fe}/\text{H}] > -2$. In contrast, model mr0.1 predicts smaller scatter than m000, although it does not seem to be inconsistent with observations. Such tendencies are also seen in Argast et al. (2004), Komiya et al. (2014) and van de Voort et al. (2015).

Our fiducial model, m000, reproduces the observed *r*-process ratio as discussed in Section 2.4.2. The NSM rate of m000 for a MW-like galaxy is $\sim 10^{-4} \text{ yr}^{-1}$. The total mass of *r*-process elements produced by each NSM corresponds to $\sim 10^{-2} M_{\odot}$. The value is consistent with recent nucleosynthesis calculations: $10^{-3} M_{\odot}$ to $10^{-2} M_{\odot}$ (e.g., Goriely, Bauswein, and Janka, 2011; Korobkin et al., 2012; Hotokezaka et al., 2013; Bauswein, Goriely, and Janka, 2013; Wanajo et al., 2014).

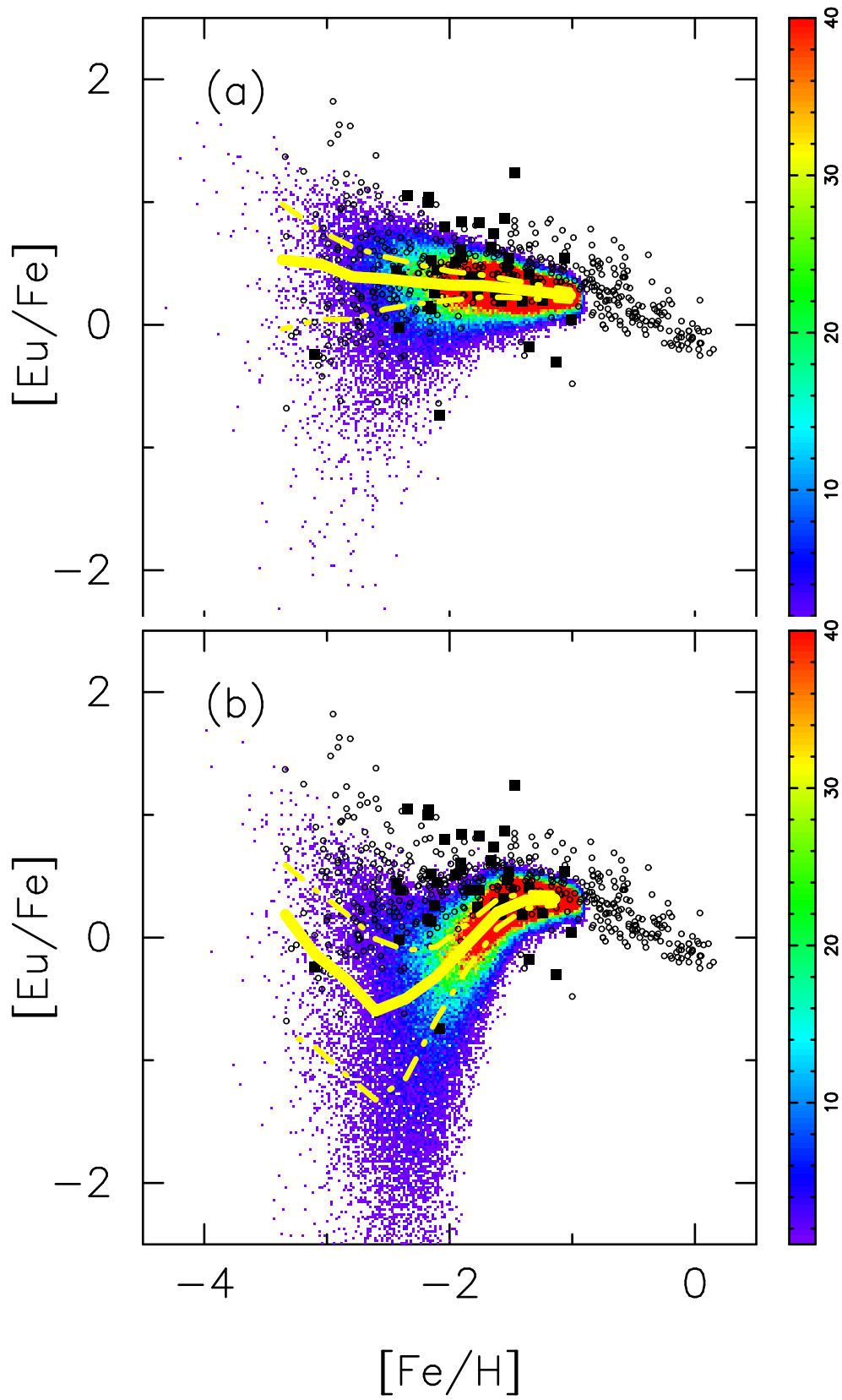


FIGURE 2.11: $[\text{Eu}/\text{Fe}]$ as a function of $[\text{Fe}/\text{H}]$ with different merger times of NSMs. (a): $\text{mt}10$ ($t_{\text{NSM}} = 10$ Myr). (b): $\text{mt}500$ ($t_{\text{NSM}} = 500$ Myr). Symbols are the same as Figure 2.5.

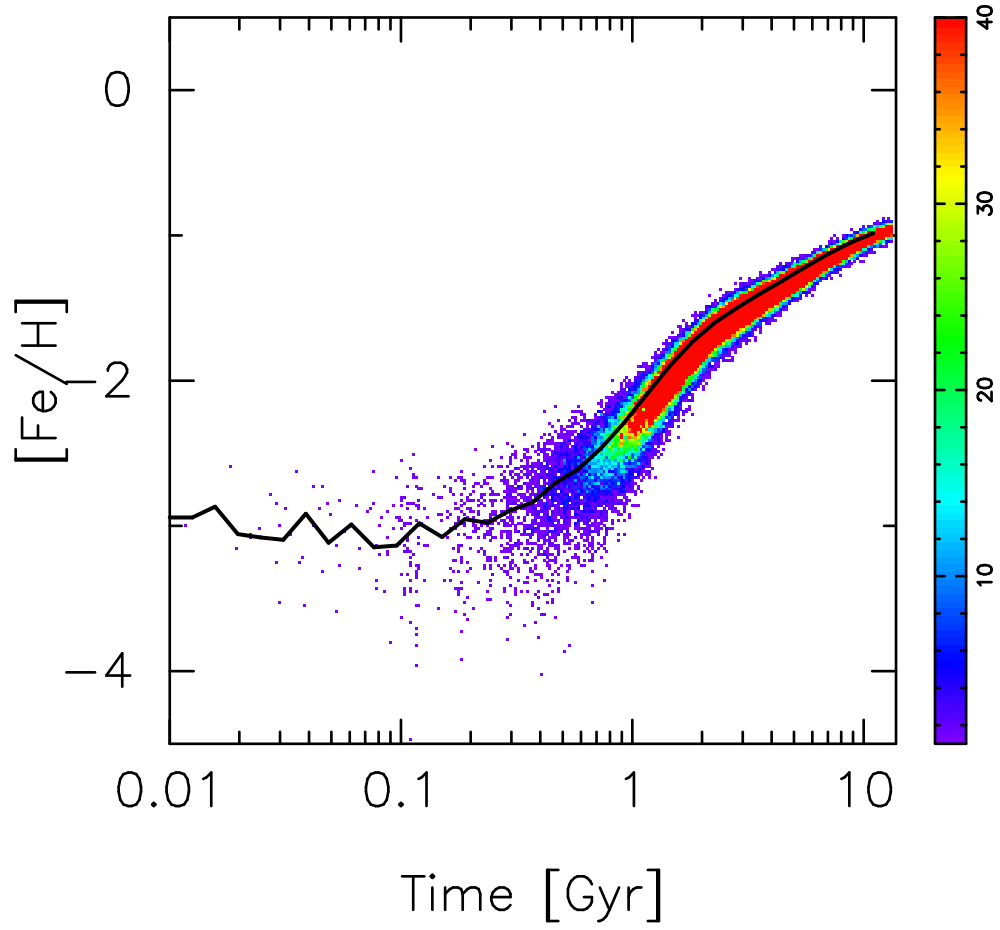


FIGURE 2.12: $[\text{Fe}/\text{H}]$ as a function of time of model m000. The horizontal axis is plotted from 600 Myr from the start of the simulation. Black curve is the average of the metallicity in each age. Contour is the same as Figure 2.5.

TABLE 2.4: List of yields.

Model	f_{NSM}	M_r (M_\odot)
mr0.001	0.001	10^{-1}
m000	0.01	10^{-2}
mr0.1	0.1	10^{-3}

The columns correspond to the name of models, fraction of NSMs (f_{NSM}), and total yields of r -process elements (M_r). Fraction of NSMs is the fraction of stars that cause NSMs in the mass range $8 - 20 M_\odot$.

Argast et al. (2004) construct an inhomogeneous chemical evolution model of the MW halo. Their model is difficult to reproduce [Eu/Fe] by NSMs with the Galactic NSM rate of $2 \times 10^{-4} \text{ yr}^{-1}$ due to high SFE. [Eu/Fe] produced in their model is similar to that of mExt (Figure 2.10).

From the discussion above, NSM rate of $\sim 10^{-4} \text{ yr}^{-1}$ in a MW size galaxy is preferred to reproduce the observed [Eu/Fe]. This rate is consistent with the estimated galactic NSM rate from the observed binary pulsars (Abadie et al., 2010b). Near future gravitational detectors, KAGRA, advanced LIGO, and advanced VIRGO (Abadie et al., 2010a; Kuroda and LCGT Collaboration, 2010; Accadia et al., 2011; Abbott et al., 2016) are expected to detect 10 – 100 events per year of gravitational wave from NSMs.

2.5 Summary

We have carried out numerical simulations of chemodynamical evolution of dSphs using N -body/SPH code, ASURA to investigate the enrichment history of r -process elements. This study suggests that NSMs with merger times of $\sim 100 \text{ Myr}$ and the Galactic event rate of $\sim 10^{-4} \text{ yr}^{-1}$ can explain the dispersion of [Eu/Fe] in reasonable agreement with observations in EMP stars. This study supports that NSMs are the major astrophysical site of the r -process. Our isolated dSph models reproduce basic properties of the observed LG dSphs such as radial profiles, time variations of the SFR as well as metallicity distribution. Here, we summarize the main results.

- (1) The abundance ratio of [Eu/Fe] produced in our models without metal mixing in SF regions has too large dispersion. This is because metals in a gas particle do not diffuse out to mix into the other particles throughout the evolution of galaxies. This issue will be extensively studied in Chapter 5.
- (2) Models with metal mixing in SF region reproduce the observed [Eu/Fe] distribution and its scatter as a function of [Fe/H]. Our model shows good convergence of the resolution. We show that NSMs with $t_{\text{NSM}} = 100 \text{ Myr}$ is favorable for reproducing the observed [Eu/Fe] as a function of metallicity. This result implies that the metal mixing process is critical to reproduce the [Eu/Fe] distribution. In addition, this study suggests that the SFR of dSphs in the early epoch of their evolution ($\sim 1 \text{ Gyr}$) is $\lesssim 10^{-3} M_\odot \text{ yr}^{-1}$.

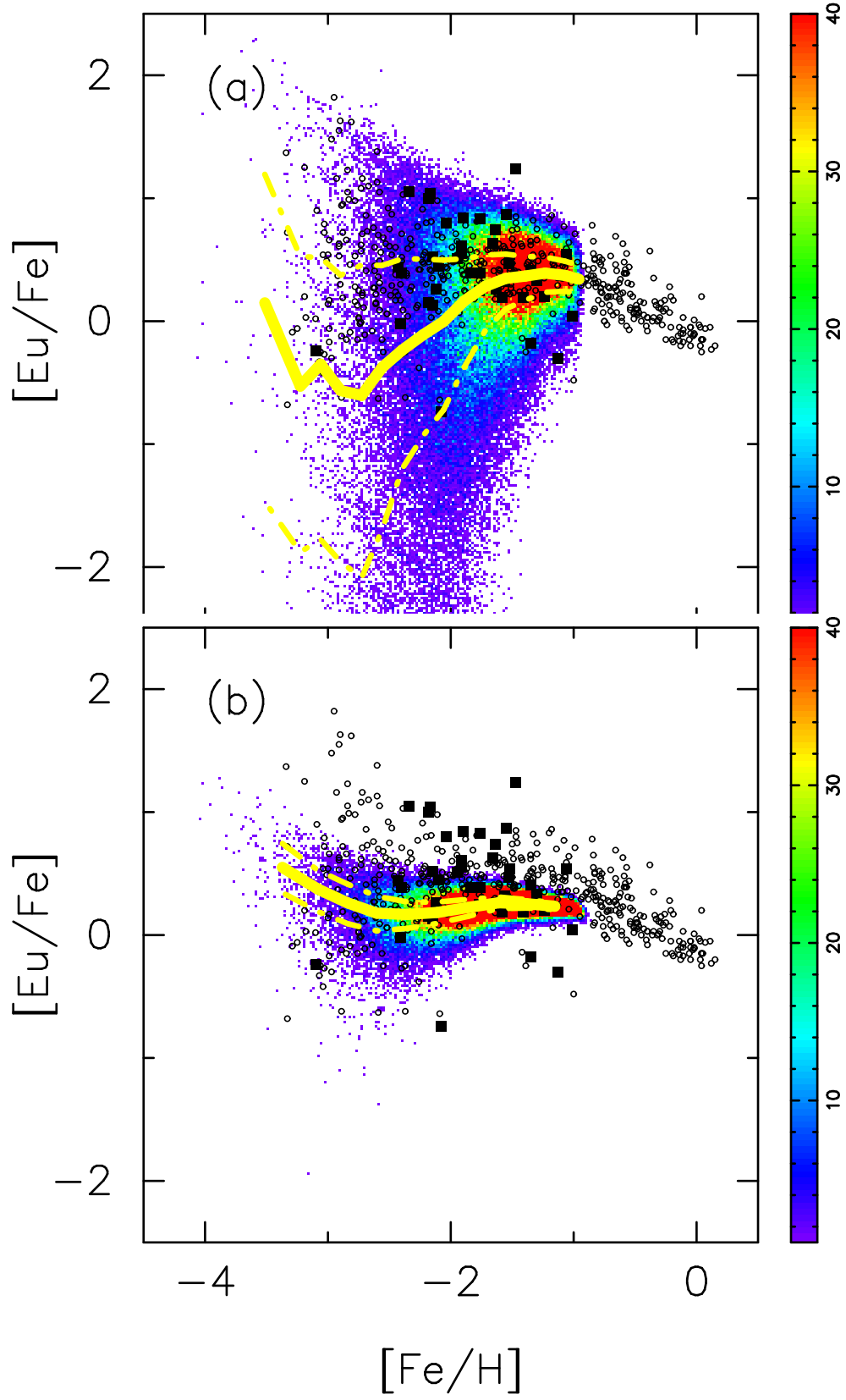


FIGURE 2.13: $[\text{Eu}/\text{Fe}]$ as a function of time with different rate of NSMs. (a): $\text{mr}0.001$ ($f_{\text{NSM}} = 0.001$). (b): $\text{mr}0.1$ ($f_{\text{NSM}} = 0.1$). Symbols are the same as Figure 2.5.

- (3) NSMs with a merger time of $\lesssim 300$ Myr are acceptable to account for the observed abundance of EMP stars. This is because metallicity is not correlated with time up to ~ 300 Myr from the start of the simulation due to low SFE of the model galaxy.
- (4) This study suggests that the Galactic NSM rate to account for the observed r -process abundance scatters is $\sim 10^{-4} \text{ yr}^{-1}$. The total mass of r -process elements ejected by one NSM is $\sim 10^{-2} M_{\odot}$, which is consistent with the value suggested by nucleosynthesis studies (10^{-3} – $10^{-2} M_{\odot}$). Next generation gravitational detectors KAGRA, advanced LIGO and advanced VIRGO are expected to detect gravitational waves from NSMs and their event rates would be over 10 per year. Their detections will give us more reliable galactic NSM rate.

In this study, we have focused on the enrichment history of r -process elements in isolated dSphs with fixed mass. To fully understand the enrichment history of r -process elements in the LG galaxies, it is important to show how the mass and size of galaxies affect the enrichment of r -process elements (Chapter 3).

Recent observations suggest that the low abundance of r -process elements ($[\text{Ba}/\text{Fe}]^2 < -1$) in stars with $[\text{Fe}/\text{H}] < -3.5$. These stars provide clues to understand the astrophysical site(s) of r -process elements and the metal enrichment in the first galaxies. Some studies suggest that the r -process abundance of these stars can be explained by short merger times channel (~ 1 Myr) of NSMs (Ishimaru, Wanajo, and Prantzos, 2015) or accretion of materials from inter stellar medium to the Population III stars (Komiya et al., 2014). Since we have only focused on the star-to-star scatters of $[\text{Eu}/\text{Fe}]$ in stars with $[\text{Fe}/\text{H}] \sim -3$ assuming that NSMs are the major site of r -process in this thesis, we have not discussed the origin of these stars. It is profitable to discuss the origin of these stars by the detailed simulation of galaxies.

To address all of these issues, it is required to understand how the MW halo formed. We need to clarify the relation between the building block galaxies of the MW and the present LG dSphs. Chapter 6 extends our numerical simulations of chemodynamical evolution of dSphs to cosmological zoom-in simulations in order to fully understand the enrichment of r -process elements in the LG galaxies and confirm the validity of the scenario of hierarchical structure formation.

²Barium (Ba) can also be regarded as the r -process element in $[\text{Fe}/\text{H}] \lesssim -3$

Chapter 3

Early chemodynamical evolution of dwarf galaxies deduced from r -process elements

The abundance of r -process elements of EMP stars in the LG galaxies gives us clues to clarify the early evolutionary history of the MW halo. The LG dwarf galaxies would have similarly evolved with building blocks of the MW halo. However, how the chemodynamical evolution of the building blocks affects the abundance of r -process elements is not yet clear. In this chapter, we perform a series of simulations using dwarf galaxy models with various dynamical times and total mass, which determine SFHs. We find that galaxies with dynamical times longer than 100 Myr have SFRs less than $10^{-3} M_{\odot} \text{ yr}^{-1}$ and slowly enrich metals in their early phase. These galaxies can explain the observed large scatters of r -process abundance in EMP stars in the MW halo regardless of their total mass. On the other hand, the first NSM appears at a higher metallicity in galaxies with a dynamical time shorter than typical NSM times. The scatters of r -process elements mainly come from the inhomogeneity of the metals in the interstellar medium whereas the scatters of α -elements are mostly due to the difference in the yield of each SN. Our results demonstrate that the future observations of r -process elements in EMP stars will be able to constrain the early chemodynamical evolution of the LG galaxies¹.

3.1 Review: Enrichment of r -process elements in dwarf galaxies and building blocks of the MW

The chemical abundance of EMP stars ($[\text{Fe}/\text{H}] \lesssim -3$) provides us insight into the early evolutionary history of galaxies. Although observations of the MW halo stars cannot directly show us how the MW progenitor galaxies evolved, the chemical abundances of the LG dwarf galaxies would provide hints to help us understand the evolutionary histories of the building blocks of the MW (e.g., Karlsson, Bromm, and Bland-Hawthorn, 2013; Lee et al., 2013; Lee et al., 2015; Bland-Hawthorn, Sutherland, and Webster, 2015). Each dwarf galaxy seems to have a different distribution of r -process elements whereas observed abundances of elements lighter than Zn in EMP stars of dwarf galaxies are more or less in reasonable agreement with those of the

¹Contents in this chapter have been published in Hirai, Ishimaru, Saitoh, Fujii, Hidaka, and Kajino (2017).

MW halo (Frebel et al., 2010; Frebel, Kirby, and Simon, 2010). The enhancements of *r*-process elements of dSphs are slightly lower than those of the MW halo (e.g., Frebel and Norris, 2015). On the other hand, UFDs have significantly depleted *r*-process abundances in general (e.g., Frebel and Norris, 2015) except for the Reticulum II UFD, which shows substantial enhancement of Eu (Roederer et al., 2016; Ji et al., 2016b; Ji et al., 2016a). Although the distribution of $[r/\text{Fe}]$ seems to differ among dwarf galaxies, the dispersion at the given metallicity in the sum of different dwarf galaxies agrees well with that of the MW halo stars. These observational results imply that the LG dwarf galaxies should have similarly evolved with building blocks of the MW in the early phase.

Ishimaru, Wanajo, and Prantzos (2015) have shown that NSMs with a long merger time of 100 Myr can explain the observed ratio of *r*-process elements to iron such as $[\text{Eu}/\text{Fe}]$ if the MW halo formed via hierarchical mergers of sub-halos with different SFEs. SFEs of progenitor galaxies of the MW are deeply related to the dynamical evolution of galaxies. It is thus required to examine the dependence on the SFEs on dynamical conditions, by using chemodynamical simulations of galaxies beyond simple chemical evolution models. Shen et al. (2015) and van de Voort et al. (2015) performed hydrodynamic MW-formation simulations beginning from cosmological initial conditions. Their simulations can self-consistently follow the evolutionary history of the MW. However, mass resolutions of their models are not enough to discuss sub-structures of the MW halo.

In Chapter 2, we have constructed *N*-body/SPH models of dwarf galaxies with higher resolution. Results in Chapter 2 suggest that the observed $[\text{Eu}/\text{Fe}]$ in EMP stars can be accounted for by NSMs with merger times of $\lesssim 300$ Myr. Low SFE in the early phase of the evolution of dwarf galaxies causes the formation of EMP stars with *r*-process elements that are consistent with observations. They also identified that enrichment of *r*-process elements has a strong connection with the dynamical evolution of galaxies. These simulations were, however, performed for a fixed dark matter halo model producing only one example of the evolutionary history of a dwarf galaxy. On the other hand, observational studies suggest a diversity of SFHs of the LG dwarf galaxies (e.g., Tolstoy, Hill, and Tosi, 2009). We, therefore, perform simulations with the MW progenitor galaxies with different dynamical evolution to examine how the dynamical evolution of galaxies affects the enrichment of *r*-process elements.

In Section 3.2, we describe isolated dwarf galaxy models. In Section 3.3, we compare the properties of our models and the observed dwarf galaxies. In Section 3.4, we show the relation between the dynamical evolution of dwarf galaxies and enrichment of *r*-process elements. Section 3.5 discusses the implication to the MW halo formation. In Section 3.6, we summarize the main results.

3.2 Isolated dwarf galaxy models

In this chapter, we assume isolated dwarf galaxy models described in Section 2.2.4. We set the total number of particles and the gravitational softening length equal to 2^{19} and 7.0 pc, respectively. We take the mass ratio of gas-to-dark matter particle of 0.15 (Planck Collaboration et al., 2014). Both dark matter and gas particles follow the pseudo-isothermal profile (Equation 2.3). The initial values of ρ_c ($0.5 - 10.0 \times 10^7 M_\odot \text{ kpc}^{-3}$) evolve to stellar central density of $\sim 10^{8-10} M_\odot \text{ kpc}^{-3}$ at 13.8 Gyr from the beginning of the simulation. These values are consistent with central densities of the observed nearby dwarf galaxies ($\sim 10^{6-10} M_\odot \text{ kpc}^{-3}$, Oh et al., 2011; Adams et al., 2014; Oh et al., 2015; Burkert, 2015).

The total mass of the galaxy (M_{tot}) satisfies the following equation,

$$M_{\text{tot}} = 4\pi\rho_c r_c^3 \left[\frac{r_{\text{max}}}{r_c} - \arctan\left(\frac{r_{\text{max}}}{r_c}\right) \right], \quad (3.1)$$

where r_{max} is the maximum outer radius. We fix $r_{\text{max}} = 7.1 r_c$ (Chapter 2) except for model D. Model D has $r_{\text{max}} = r_c = 1 \text{ kpc}$ to discuss the chemodynamical evolution of dwarf galaxies having very high density, resulting in a strong inflow at the early evolutionary phase. We summarize parameters of all models in Table 3.1. The central density and total mass are the free parameters of our models. We can estimate the dynamical times of the central region of galaxies from the density of the system ($t_{\text{dyn}} = \sqrt{3/4\pi G\rho_c}$), where G is the gravitational constant. Higher ρ_c therefore gives shorter t_{dyn} . We can calculate other parameters from Equations (2.3) and (3.1) with the total number of particles of 2^{19} .

TABLE 3.1: List of our models discussed in this chapter.

Model	M_{tot} ($10^8 M_{\odot}$)	ρ_c ($10^7 M_{\odot} \text{ kpc}^{-3}$)	m_{DM} ($10^3 M_{\odot}$)	m_{gas} ($10^3 M_{\odot}$)	r_{max} (kpc)	r_c (kpc)	t_{NSM} (Myr)	t_{dyn} (Myr)
A	3.5	0.5	1.1	0.2	7.1	1.0	100	114
A ₁₀	3.5	0.5	1.1	0.2	7.1	1.0	10	114
A ₅₀₀	3.5	0.5	1.1	0.2	7.1	1.0	500	114
B	3.5	1.5	1.1	0.2	4.9	0.7	100	66
B ₁₀	3.5	1.5	1.1	0.2	4.9	0.7	10	66
B ₅₀₀	3.5	1.5	1.1	0.2	4.9	0.7	500	66
C	3.5	10.0	1.1	0.2	2.6	0.4	100	26
C ₁₀	3.5	10.0	1.1	0.2	2.6	0.4	10	26
C ₅₀₀	3.5	10.0	1.1	0.2	2.6	0.4	500	26
D	3.5	10.0	1.1	0.2	1.0	1.0	100	26
D ₁₀	3.5	10.0	1.1	0.2	1.0	1.0	10	26
D ₅₀₀	3.5	10.0	1.1	0.2	1.0	1.0	500	26
E	7.0	0.5	2.3	0.4	8.9	1.3	100	114
F	35.0	0.5	11.3	2.0	15.3	2.2	100	114

From left to right the columns show model name, total mass, initial central density, mass of one dark matter particle, the mass of one gas particle, maximum radius, core radius, merger times of NSMs, and calculated dynamical times of the central density.

We have performed the high-resolution simulation to resolve the scale down to ~ 10 pc properly using ASURA (Saitoh et al., 2008; Saitoh et al., 2009). Section 1.4 describe the details of our code. The mass of a star particle in this simulation is $\sim 100 M_{\odot}$. When the mass of a star particle is $\sim 100 M_{\odot}$, there are ~ 1 SNe in an SSP particle. In this case, the results depend on the way how we sample the IMF (Revaz et al., 2016). We randomly sample the IMF following Okamoto, Nemmen, and Bower (2008). The IMF sampling is significantly important when we discuss the $[\alpha/\text{Fe}]$ ratio in galaxies because SN produces both α -elements and Fe and different mass SNe produce a different ratio of $[\alpha/\text{Fe}]$. On the other hand, when we discuss Eu abundance, the effect of IMF sampling is smaller than the α -element abundance because Eu yield does not depend on the mass of the progenitors of NSMs (Wanajo et al., 2014). We have checked that scatters of $[\text{Eu}/\text{Fe}]$ do not strongly depend on the resolution of the simulation.

The chemodynamical evolution of dwarf galaxies strongly depends on the initial density and total mass (Carraro et al., 2001; Chiosi and Carraro, 2002; Valcke, de Rijcke, and Dejonghe, 2008; Revaz et al., 2009; Revaz and Jablonka, 2012). The initial density affects the SFHs of dwarf galaxies (Carraro et al., 2001). Isolated dwarf galaxy models with different total masses describe various observational properties (Valcke, de Rijcke, and Dejonghe, 2008). These are therefore two critical parameters to understand in the relation between the dynamical evolution and enrichment of r -process elements. They affect the final properties of dwarf galaxies such as metallicity and stellar mass (Revaz and Jablonka, 2012).

Figure 3.1 shows the initial radial density profiles of dark matter particles in our models. The initial central density varies by ~ 1 dex among models A, B, C, and D (Figure 3.1a). On the other hand, models A, E, and F have different values of the total mass, but the central density is the same among them (Figure 3.1b). In Section 3.3, we show that these models reproduce the observed chemical properties of dwarf galaxies.

3.3 Comparison with observed dwarf galaxies

In this section, we compare the predicted and observed properties of dwarf galaxies. Hydrodynamic simulations of galaxies still rely on sub-grid physics such as metal mixing and SN feedback which cannot resolve in simulations of galaxies. It is thus necessary to confirm that our simulations are consistent with fundamental properties of observed galaxies. Here we show that the MDF, mass–metallicity relation and $[\alpha/\text{Fe}]$ as a function of $[\text{Fe}/\text{H}]$ predicted in our models are not significantly different from the observed dwarf galaxies.

3.3.1 Metallicity distribution functions

Figure 3.2 shows the computed MDF after 14 Gyr from the beginning of the simulation. We plot the results at 14 Gyr to compare with observational data of the LG dwarf galaxies. Table 3.2 shows stellar mass, median metallicity, and standard deviations of our models at 14 Gyr. Although we did not try to match the observed dwarf galaxies, standard deviations of MDFs (~ 0.35 – 0.60) lie within that of the observed LG dwarf galaxies (0.32 – 0.66 , Kirby et al., 2013). These MDFs reflect the SFHs of each

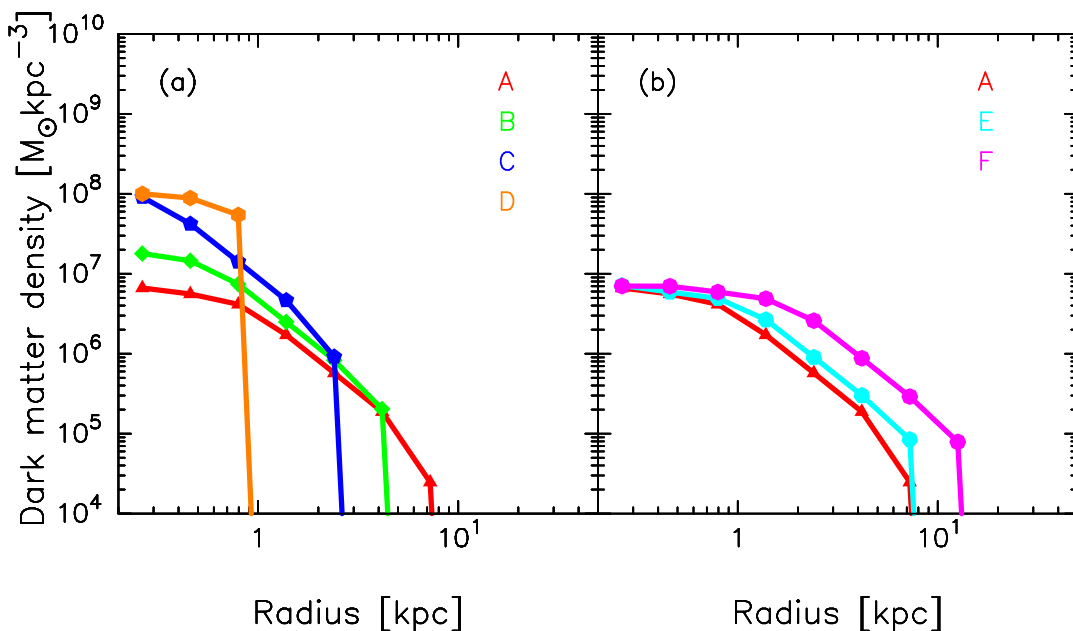


FIGURE 3.1: Initial density profiles of dark matter particles. (a) Radial dark matter profiles of models with different initial densities. Red, green, blue, and orange curves represent models A, B, C, and D, respectively. (b) The same as those in (a) but for different total masses. Red, cyan, and magenta curves represent models A, E, and F, respectively.

galaxy. Higher central density models (A, B, C, and D) have steeper slopes of MDFs in low metallicity (Figure 3.2a). This result implies that metals are enriched faster in higher central density models in their early phase. The MDF of Model D shows a narrow peak with low-metallicity tail due to rapid chemical evolution in its early phase. On the other hand, the MDF of model F has a sharp cut-off in the metal-rich side because the SFR does not decrease too much from its peak value.

Figure 3.3 shows gas MDFs at 0.2 Gyr from the beginning of the SF. This time roughly corresponds to the time when the first NSM occurs. According to this figure, the gas MDFs of models A, B, E, and F are broader than those in models C and D. Inhomogeneity of gas phase metallicity significantly affects the scatters of [Eu/Fe] (see Section 3.4.1).

3.3.2 Mass–metallicity relation

In Figure 3.4, we show the comparison of the predicted mass–metallicity relation to that of the observed dwarf galaxies. The median metallicity in our models increases as the stellar mass increases. This feature is consistent with the observation (Kirby et al., 2013). Both metallicity and stellar mass increase as the density (models A, B, C, and D) or total mass (models A, E, and F) increases. More massive or higher density galaxies have deeper gravitational potential well than less massive or lower-density galaxies. In such galaxies, gas and metals are barely removed from the galaxies (e.g., Dekel and Silk, 1986). In this sense, total mass and density have similar effects on the final stellar mass and metallicity.

TABLE 3.2: Final properties of our models. From left to right the columns show model name, stellar mass, median metallicity, and standard deviation of MDF.

Model	M_* ($10^6 M_\odot$)	$\langle [\text{Fe}/\text{H}] \rangle$	σ
A	0.3	-2.6	0.35
B	1.2	-2.4	0.39
C	3.4	-2.0	0.40
D	6.4	-1.5	0.60
E	8.0	-1.8	0.44
F	170.0	-1.3	0.42

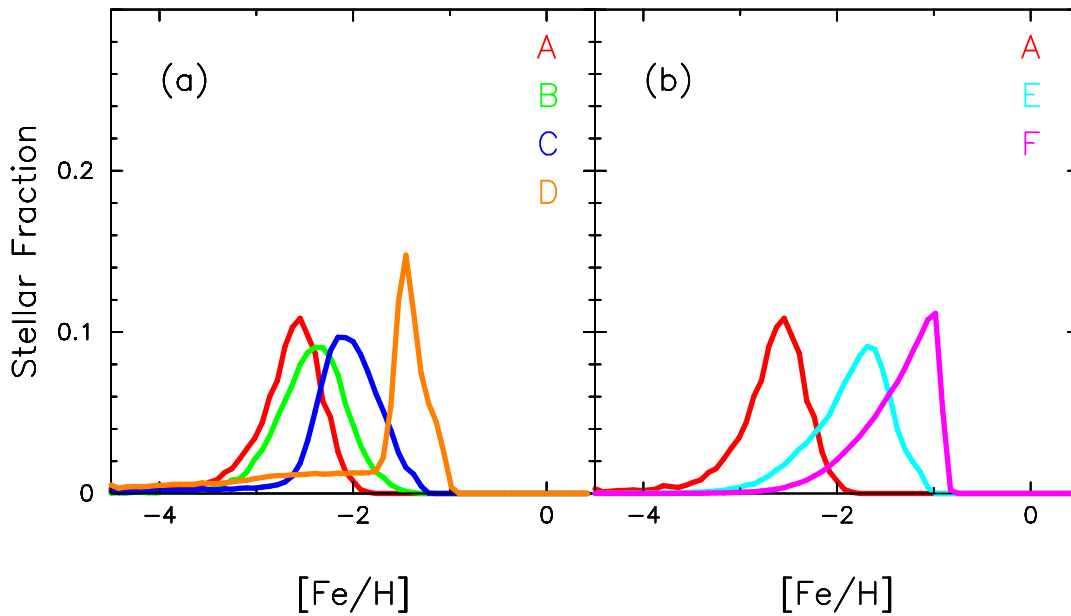


FIGURE 3.2: Stellar metallicity distribution functions at 14 Gyr. (a) MDFs of models with different initial densities. Red, green, blue, and orange curves represent models A, B, C, and D, respectively. (b) The same as those in (a) but for different total masses. Red, cyan, and magenta curves represent models A, E, and F, respectively.

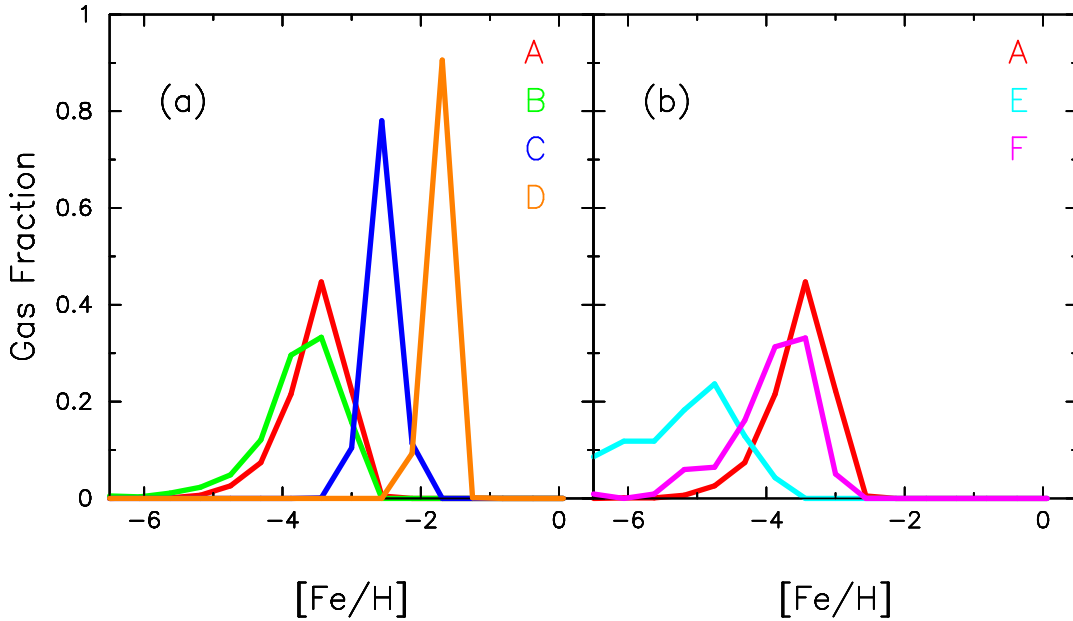


FIGURE 3.3: Gas MDFs at 0.2 Gyr from the onset of SF. This time roughly corresponds to the time when the first NSM occurs. (a) Gas MDFs of models with different initial densities. Red, green, blue, and orange curves represent models A, B, C, and D, respectively. (b) The same as those in (a) but for different total masses. Red, cyan, and magenta curves represent models A, E, and F, respectively.

Slightly lower metallicity by ~ 0.4 dex in our models than that in the observations is due to the lack of SNe Ia. According to the observed $[\alpha/\text{Fe}]$ as a function of $[\text{Fe}/\text{H}]$ in the MW halo stars, SNe II and SNe Ia produce $\sim 35\text{--}40\%$ and $\sim 60\text{--}65\%$ of solar Fe (Goswami and Prantzos, 2000; Prantzos, 2008). Note that the increase of metallicity due to SNe Ia in different galaxies is not a constant value. It is affected by SFHs of each galaxy. However, since the aim of this chapter is to discuss *r*-process elements produced in the early phase of galaxy evolution where the contribution of SNe Ia is negligible, discussion of the effect of SNe Ia is beyond the scope of this chapter. We thus simply shift the metallicity with 0.4 dex in each galaxy to compare with the observation as shown in large symbols in Figure 3.4.

Metallicity in model D is higher than that of the observed mass–metallicity relation. Metals in model D are efficiently retained inside the galaxy because strong inflow caused by a very compact density profile (Figure 3.1) in the early phase prevents metal-outflow. This model is too extreme as an initial condition for the dwarf galaxies and indeed the resulting stellar mass and metallicity deviate from the observed relation. From the viewpoint of the mass–metallicity relation, we can exclude model D from the models that represent the observed LG dwarf galaxies.

The slope of the mass–metallicity relation given by models in Figure 3.4 is slightly steeper than that of the observation. This result might be related to the lack of tidal disruption effect, which we did not implement in this study and insufficient feedback. The stellar mass of small galaxies can be easily reduced by tidal disruptions (e.g., Nichols, Revaz, and Jablonka, 2014). Stellar feedback also affects the slope of the mass–metallicity relation. In our simulations, we only assume thermal feedback from SNe. Okamoto, Shimizu, and Yoshida (2014) point out that the radiation-pressure

feedback from young stars suppresses SF more efficiently in galaxies with higher metallicity and produces a shallower slope of the mass–metallicity relation. Several semi-analytic models, as well as hydrodynamic simulations, report the steeper slope (e.g., Davé et al., 2013; Lu et al., 2014; Torrey et al., 2014; Somerville and Davé, 2015). Isolated dwarf galaxy models adopted in this study might, however, oversimplify the evolutionary history of dwarf galaxies. We will study the evolutionary history of the LG galaxies in the context of standard Λ CDM cosmology in Chapter 6.

3.3.3 α -element abundance

Figure 3.5 shows $[\text{Mg}/\text{Fe}]$ as a function of $[\text{Fe}/\text{H}]$ for stars before the onset of SNe Ia (after 1 Gyr from the onset of the SF). The scatters in the observed $[\text{Mg}/\text{Fe}]$ in EMP stars are less than 0.2 dex. According to Figure 3.5, all models reproduce the low scatters of $[\text{Mg}/\text{Fe}]$. Besides, the metallicity of all models except for model D is $[\text{Fe}/\text{H}] \lesssim -2$ at 1 Gyr. These results suggest that SNe Ia start to contribute at around $[\text{Fe}/\text{H}] \sim -2$ in these models, i.e., $[\text{Mg}/\text{Fe}]$ begins to decrease at around this metallicity that is consistent with the observed MW dSphs. On the other hand, the metallicity of model D is already too high to explain $[\text{Mg}/\text{Fe}]$ in the MW dSphs. Decreasing trend of $[\text{Mg}/\text{Fe}]$ in models C and D reflects the adopted yield that more massive stars produce higher $[\text{Mg}/\text{Fe}]$ ratio (Nomoto et al., 2006).

Figure 3.6 shows the standard deviation of $[\text{Mg}/\text{Fe}]$ as a function of $[\text{Fe}/\text{H}]$. We can confirm that scatters of all models have lower than 0.2 dex. Standard deviations of all models decrease as the metallicity increases. This result reflects that the spatial distribution of metallicity becomes homogeneous in higher metallicity. Figure 3.7 shows $[\text{Mg}/\text{Fe}]$ as a function of $[\text{Fe}/\text{H}]$ for gases at 1 Gyr. According to this figure, the scatters of $[\text{Mg}/\text{Fe}]$ are also small in the ISM of our models. According to these results, we confirm that all models have low $[\text{Mg}/\text{Fe}]$ scatters in EMP stars. This result ensures that the metal mixing scheme adopted here is not too unnatural.

The small scatter of $[\text{Mg}/\text{Fe}]$ mainly come from the difference in the yields of each SN rather than the spatial inhomogeneity of the abundance of Mg and Fe. Since SNe synthesize both Mg and Fe, the spatial variations of the abundance of Mg and Fe are related. When the abundance of Fe is high in a region, Mg is also high in many cases. Therefore, they offset each other due to the above relation making the resultant scatters of $[\text{Mg}/\text{Fe}]$ very small.

3.4 Enrichment of r -process elements

3.4.1 Effects of initial density of halos

The difference in dynamical evolution directly affects the time variations of SFRs that strongly influence the enrichment of r -process elements. Here we show the effects of initial density of halos (models A, B, C, and D). Figure 3.8 shows the SFHs in models A, B, C, and D. The gases collapse during the initial dynamical time, t_{dyn} and then the first SF occurs. Dynamical times in models A and B are much longer than the

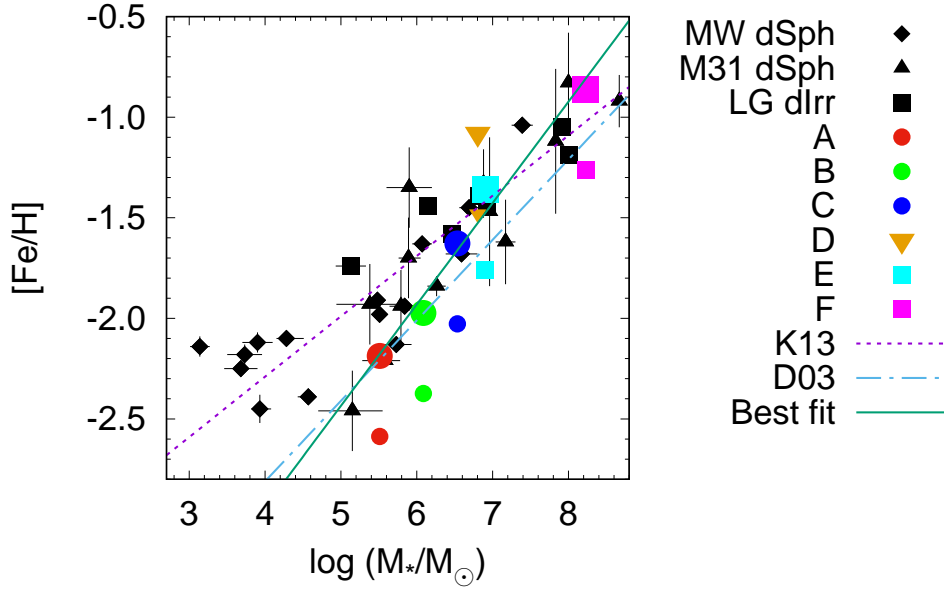


FIGURE 3.4: Stellar mass–metallicity relation for models and the LG dwarf galaxies. Large, colored dots stand for 0.4 dex shifted metallicity to account for lack of SNe Ia in models A (red filled circle), B (green filled circle), C (blue filled circle), D (orange inverted triangle), E (cyan filled square), and F (magenta filled square). Small colored dots stand for the same models, but their metallicity is not corrected. Black diamonds, triangles, and squares with error bars are the observed value of the MW dSphs, M31 dSphs, and the LG dIrrs, respectively (Kirby et al., 2013, K13). The sky-blue dot–dashed line represents the least square fitting of the samples of (Dekel and Woo, 2003, D03): $[\text{Fe}/\text{H}] \propto M_*^{0.40}$. The purple dashed line represents the least-square fitting of K13: $\langle [\text{Fe}/\text{H}] \rangle = (-1.69 \pm 0.04) + (0.30 \pm 0.02) \log(M_*/10^6 M_\odot)$. The green line represents the least-square fitting of models except for model D: $\langle [\text{Fe}/\text{H}] \rangle = (-1.93 \pm 0.05) + (0.50 \pm 0.04) \log(M_*/10^6 M_\odot)$.

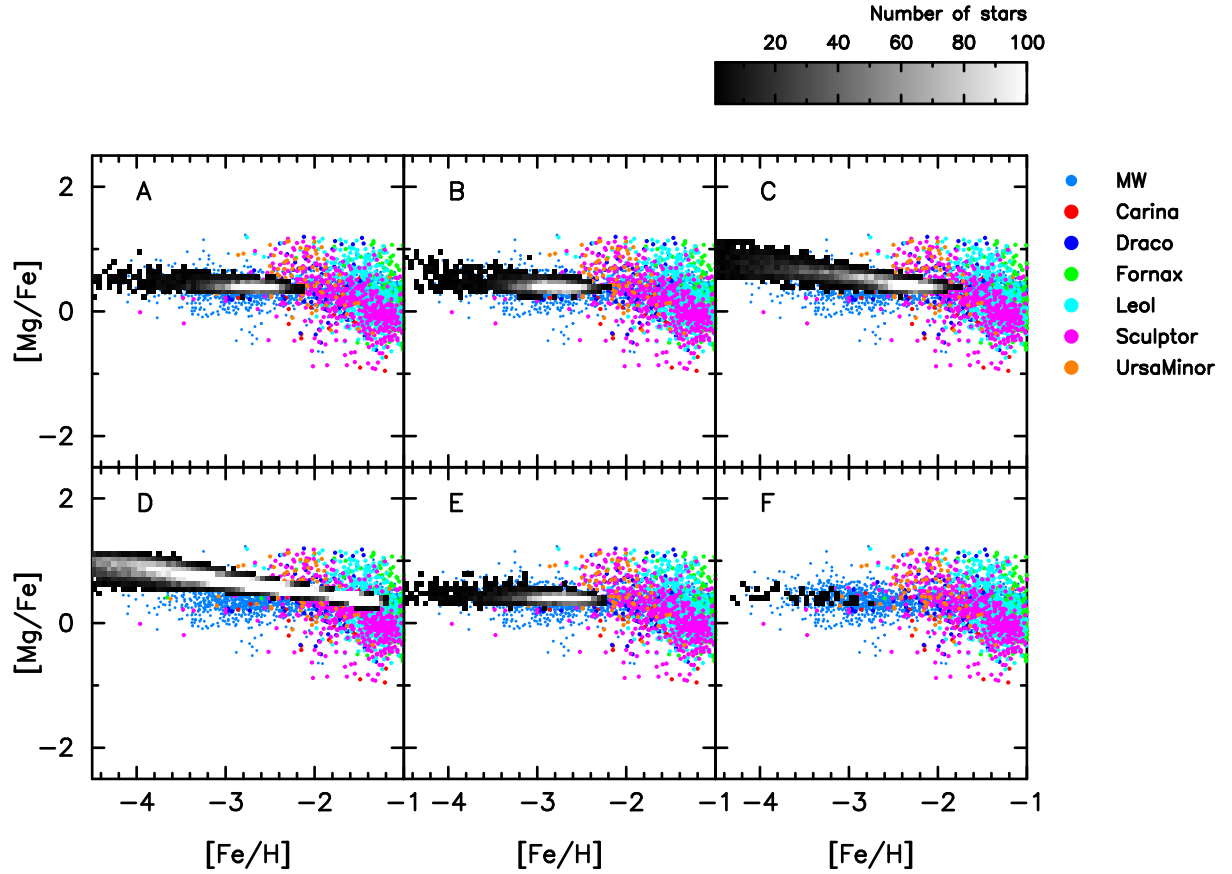


FIGURE 3.5: $[Mg/Fe]$ as a function of $[Fe/H]$ for stars predicted by models after 1 Gyr evolution, i.e., before the onset of SNe Ia. The time of the onset of SF from the start of the simulation in models A, B, C, D, E, and F is 0.21, 0.06, 0.02, 0.02, 0.27, and 0.10 Gyr, respectively. We plot models A, B, C, and D, E, F from left to right in top and bottom panels, respectively. Gray scales are the number of stars predicted in our models, between 1 (black) and 100 (white). The small dots are the observed value of the MW halo stars. Red, blue, green, cyan, magenta, and orange dots are the observed value of Carina, Draco, Fornax, Leo I, Sculptor, and Ursa Minor dwarf galaxies, respectively. We compile all data in SAGA database (Suda et al., 2008; Suda et al., 2011; Suda et al., 2014; Yamada et al., 2013).

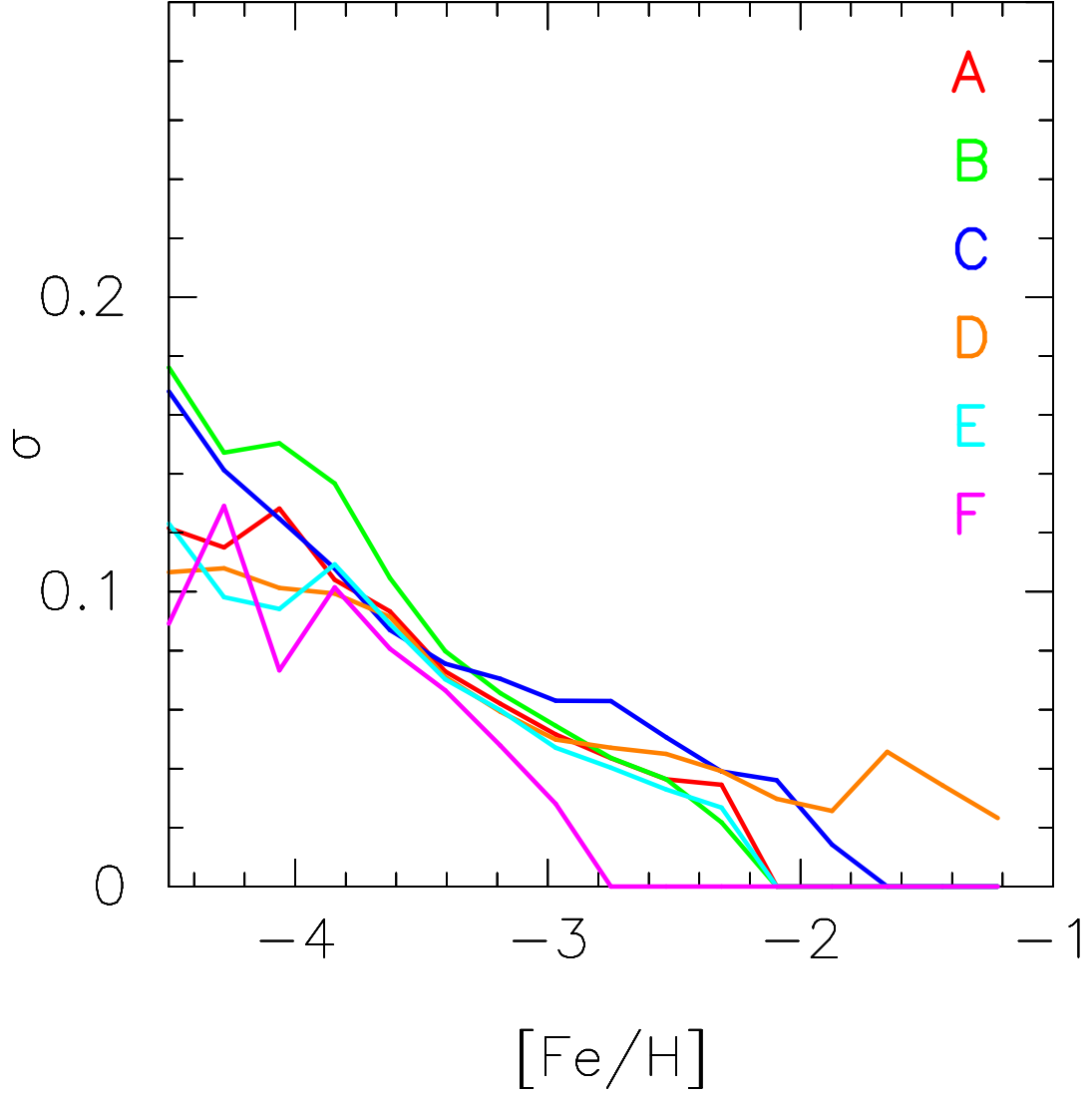


FIGURE 3.6: Standard deviation of stellar $[\text{Mg}/\text{Fe}]$ (σ) as a function of $[\text{Fe}/\text{H}]$ after 1 Gyr from the onset of SF. Red, green, blue, orange, cyan, and magenta curves represent models A, B, C, D, E, and F, respectively.

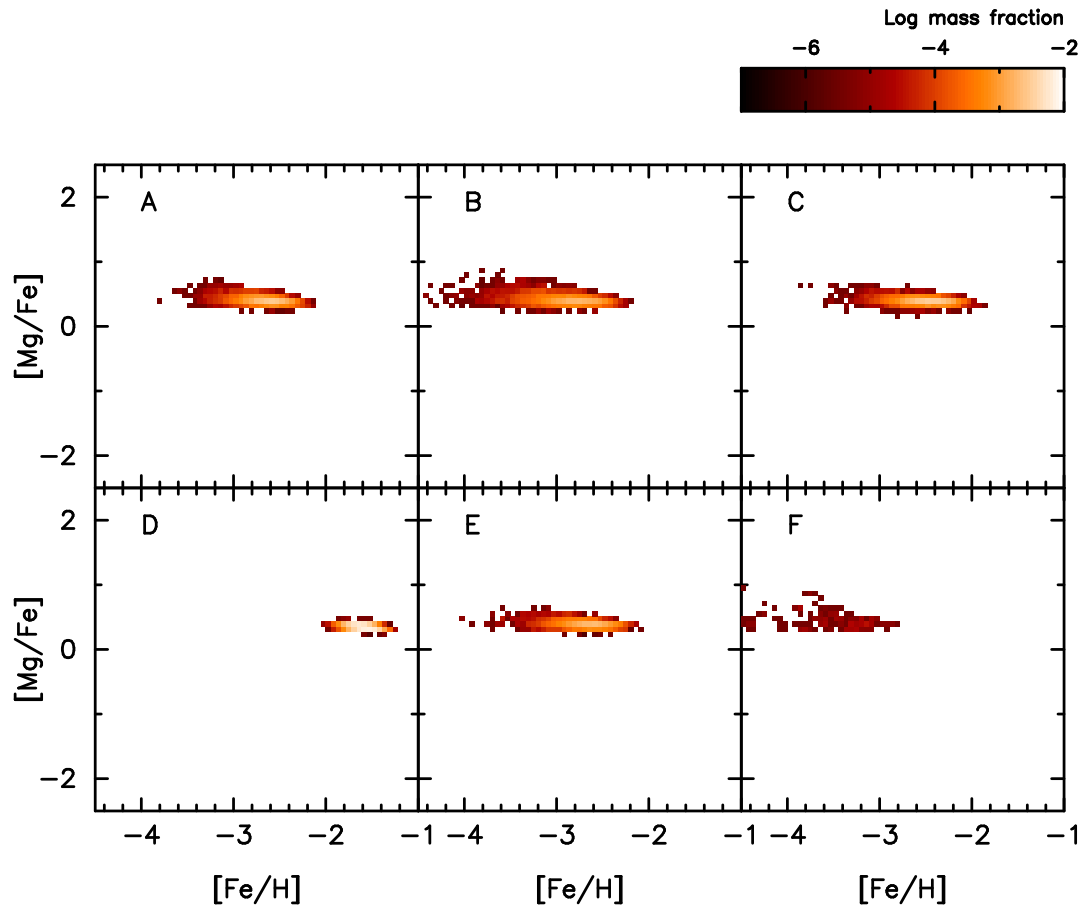


FIGURE 3.7: $[Mg/Fe]$ as a function of $[Fe/H]$ for gas computed by models at 1 Gyr from the onset of SF. We plot models A, B, C, and D, E, F from left to right in top and bottom panels, respectively. Contours are the mass fraction of gas.

lifetimes of SN progenitors (~ 10 Myr). This fact means that SN feedback from the first generation stars heats the ISM to prevent the subsequent collapse of gases and the formation of the next generation stars. The SFR in the early epoch is therefore as low as $\lesssim 10^{-3} M_{\odot} \text{yr}^{-1}$ in models A and B (Figure 3.8), which is consistent with the average observed SFR of the LG dwarf galaxies estimated from color–magnitude diagrams (e.g., de Boer et al., 2012b; de Boer et al., 2012a; Weisz et al., 2014).

On the other hand, dynamical times in models C and D are comparable to the time-scale of the first SN feedback. In these models, SFRs are not suppressed by the SN feedback due to short dynamical times. The SFR in the early epoch thus significantly rises as shown in Figure 3.8. When the contribution of SN feedback increases as the time passes, the SFR is suppressed in these models.

In Figure 3.9, we show the mean stellar $[\text{Fe}/\text{H}]$ in each model as a function of time. The cross symbol indicates the mean value of $[\text{Fe}/\text{H}]$ at 100 Myr after the first SF takes place in each model. This metallicity corresponds to the metallicity at which the first NSM occurred. Hereafter, we denote this value of metallicity as $[\text{Fe}/\text{H}]_0$. As shown in Figure 3.9, the value of $[\text{Fe}/\text{H}]_0$ increases from lower to higher density models, i.e., $[\text{Fe}/\text{H}]_0 = -3.2, -3.0, -2.2$, and -1.4 for models A, B, C, and D, respectively. These metallicities roughly correspond to those at which the large dispersion in $[\text{Eu}/\text{Fe}]$ appears. The value of $[\text{Fe}/\text{H}]_0$ depends on the rate of increase in metallicity before the first NSM occurs. Higher SFRs of models C and D increase metallicity before the first NSM occurs resulting in a higher value of $[\text{Fe}/\text{H}]_0$ as shown in Figure 3.9. Metallicities in models C and D become almost constant after the time for $[\text{Fe}/\text{H}]_0$ due to suppressed SFRs.

Figure 3.10 shows $[\text{Eu}/\text{Fe}]$ of stars formed in our simulations as functions of $[\text{Fe}/\text{H}]$ at 1 Gyr from the beginning of the SF, i.e., before the onset of SNe Ia. From models A to C, as the central density increases, the average $[\text{Fe}/\text{H}]$ at which the first NSM occurs shifts from lower to higher metallicity and the dispersion of $[\text{Eu}/\text{Fe}]$ decreases. Stars enriched by r -process elements appear at around $[\text{Fe}/\text{H}] \sim -3$ in models A and B. Few EMP stars are however formed in model C. This means that star-to-star scatters of the r -process elements at $[\text{Fe}/\text{H}] \sim -3$ seen in the MW halo do not come from dwarf galaxies like those in model C. These galaxies contribute to the stars in higher metallicity in the MW halo. Model D shows the scatters of $[\text{Eu}/\text{Fe}]$ in $[\text{Fe}/\text{H}] > -2$, which contradict the observations. This result indicates that the assumption of an extremely flat initial dark matter profile (Figure 3.1) is unrealistic. We can, therefore, exclude model D from the MW progenitor galaxies at least in terms of Eu abundance.

The star-to-star scatters of $[\text{Eu}/\text{Fe}]$ can come from inhomogeneous spatial distribution of metals in ISM of dwarf galaxies (Chapter 2). Figure 3.11 shows the standard deviation of $[\text{Eu}/\text{Fe}]$ (σ) as a function of $[\text{Fe}/\text{H}]$. Models A and B in Figure 3.11 lead to larger dispersion ($\sigma > 1$) than model C ($\sigma < 0.4$) in $[\text{Fe}/\text{H}] \lesssim -2.5$. As shown in Figure 3.3, models A and B have broader gas MDFs than those of models C and D. These results suggest that the spatial distribution of metals is still inhomogeneous in models A and B when NSMs have first occurred whereas the ISM must have been already homogenized in model C.

To quantify the inhomogeneity of metallicity in galaxies, Argast et al. (2000) introduced a metal pollution factor (f_{poll}). We define it with $M_{\text{poll}}/M_{\text{gas}}$, where M_{poll} is the gas mass polluted by SNe and M_{gas} is the total gas mass in the galaxy. According

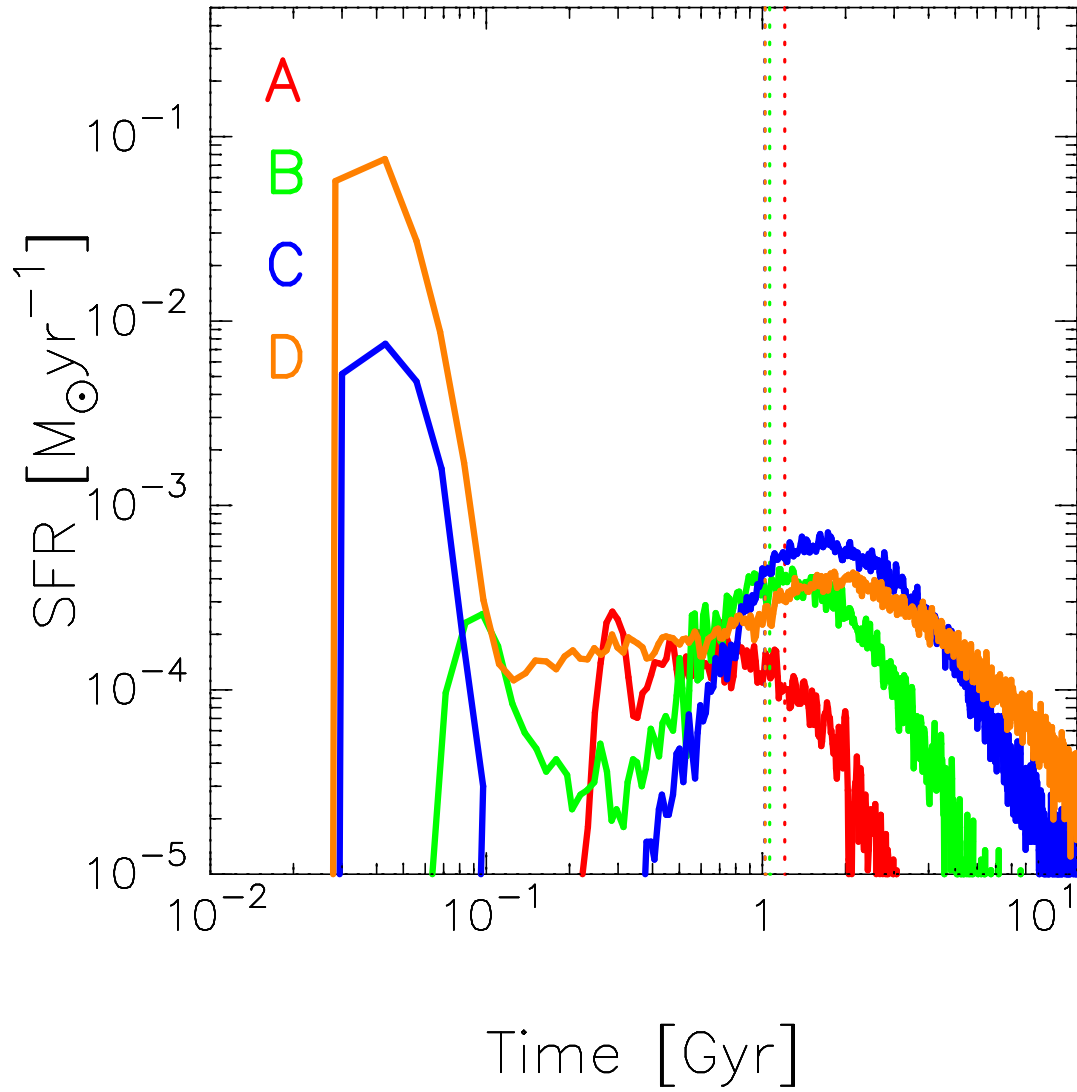


FIGURE 3.8: SFRs as a function of time. Red, green, blue and orange curves show models A, B, C, and D, respectively. Vertical dotted lines show the time 1 Gyr after the formation of first stars in each model. These lines correspond to the time when Figure 3.10 is plotted. Vertical dotted lines of model C (blue), and D (orange) are overlapped.

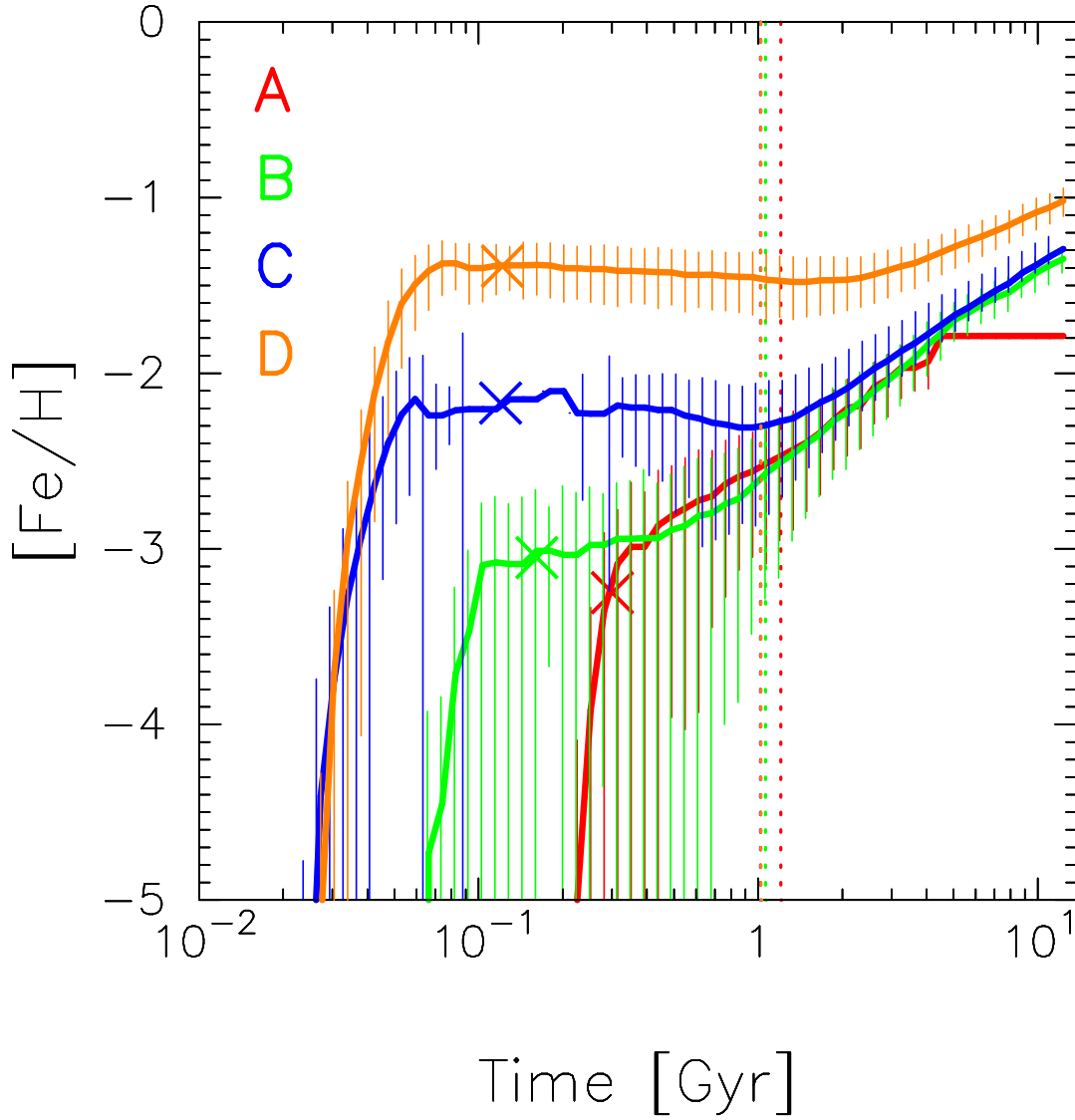


FIGURE 3.9: The mean stellar $[\text{Fe}/\text{H}]$ as a function of time (solid curves). Red, green, blue and orange curves show models A, B, C, and D, respectively. Vertical lines are the dispersion of 2σ . We plot these lines when the number of stars is more than two. Around 0.1 Gyr, there is only one star in model C in each bin. Crosses indicate the value of $[\text{Fe}/\text{H}]_0$. Vertical dotted lines show the time 1 Gyr after the formation of first stars in each model. These lines correspond to the time when Figure 3.10 is plotted. Vertical dotted lines of model C (blue), and D (orange) are overlapped.

to Argast et al. (2000), M_{poll} is equal to $N_{\text{SN}}M_{\text{sw}}$, where N_{SN} is the number of SNe and M_{sw} is the gas mass swept up by an SN. In our case, we need to add the term of metal mixing in an SF region to f_{poll} defined in Argast et al. (2000). The pollution factor in this study is equal to $N_{\text{SN}}M_{\text{sw}} + N_{\star}M_{\text{mix}}$, where M_{sw} is the gas mass within SPH kernel when we distribute metals, N_{\star} is the number of stars and M_{mix} is the gas mass used for metal mixing in an SF region. If $f_{\text{poll}} \gtrsim 1$, the whole galaxy is polluted by SNe, i.e., the spatial distribution of metallicity in galaxies is homogeneous. On the other hand, if $f_{\text{poll}} \lesssim 1$, the spatial distribution of metallicity is still inhomogeneous, i.e., scatters appear in $[\text{Eu}/\text{Fe}]$ as a function of $[\text{Fe}/\text{H}]$. When we calculate f_{poll} in our models, the values of f_{poll} at 0.2 Gyr from the beginning of the SF are 0.71 (model A), 0.26 (model B), 2.5 (model C), and 41.1 (model D). These results mean that model C and D that have SFRs of $\gtrsim 10^{-2} M_{\odot}\text{yr}^{-1}$ in the early phase is already homogeneous in metallicity when the first NSMs occurred.

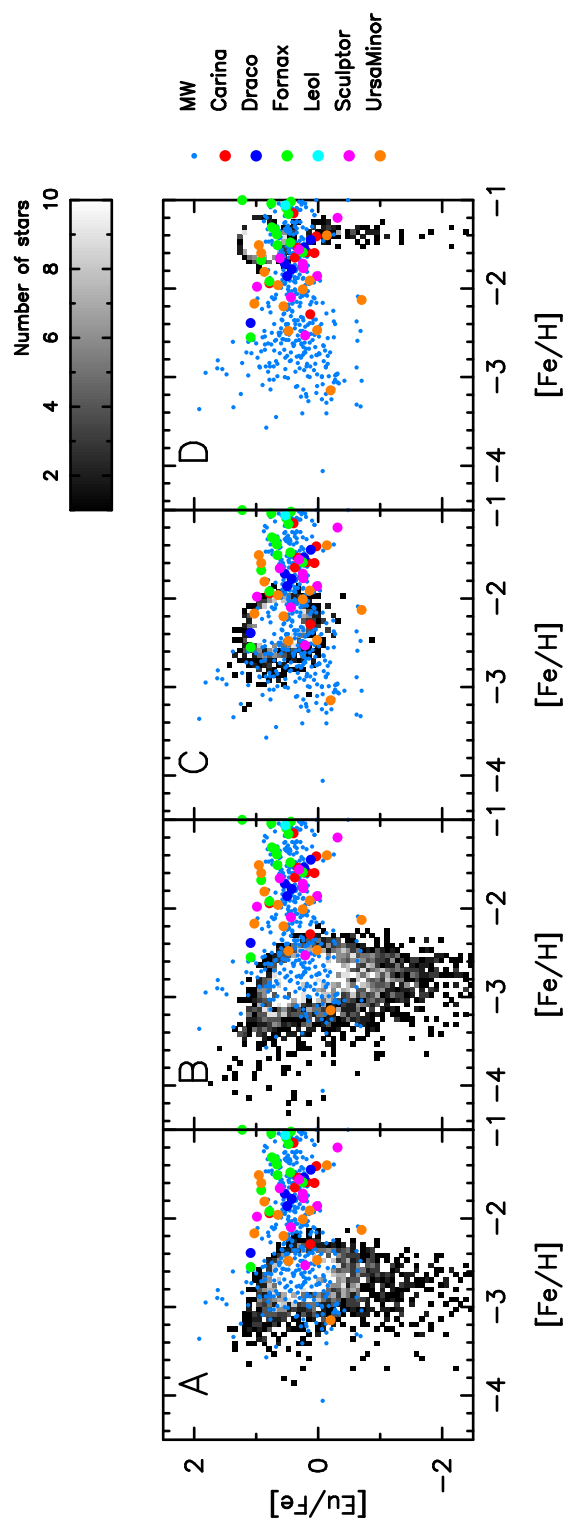


FIGURE 3.10: $[\text{Eu}/\text{Fe}]$ as a function of $[\text{Fe}/\text{H}]$ for stars predicted by models with different central density after 1 Gyr from the onset of SF. We plot models A to D from left to right. Gray scales are the number of stars predicted in our models, between 1 (black) and 10 (white). The small dots are the observed value of the MW halo stars (e.g., Roederer et al., 2014). Red, blue, green, cyan, magenta, and orange dots are the observed value of Carina (Shetrone et al., 2003; Lemasle et al., 2012; Venn et al., 2012), Draco (Shetrone, Côté, and Sargent, 2001; Cohen and Huang, 2009), Fornax (Lemasle et al., 2012), Leo I (Shetrone et al., 2003), Sculptor (Shetrone et al., 2003; Geisler et al., 2005) and Ursa Minor (Shetrone, Côté, and Sargent, 2001; Sadakane et al., 2004; Cohen and Huang, 2010) dwarf galaxies, respectively. All data are compiled in SAGA data base (Suda et al., 2011; Suda et al., 2014; Yamada et al., 2013).

The observed dwarf galaxies such as Carina, Draco, Fornax, and Sculptor contain r -process elements in EMP stars, although the number of observed EMP stars is insufficient to allow us to discuss the star-to-star scatters of r -process elements (e.g., Frebel and Norris, 2015). The early SFRs of these galaxies inferred from the color-magnitude diagrams are $\sim 10^{-3} M_{\odot}\text{yr}^{-1}$ (de Boer et al., 2012b; de Boer et al., 2012a). These values are consistent with models A and B. This result implies that the initial dynamical time of these dSphs might have been of ~ 100 Myr.

As discussed in Section 3.4.1, if the SFR is high such as model C, only high-metallicity stars are enriched by the r -process. The Sagittarius dwarf galaxy is a candidate for galaxies like model C because it has r -process elements only in $[\text{Fe}/\text{H}] > -1$ if we can sample enough number of stars that have been a member of the Sagittarius dwarf galaxy since it was formed. Most stars in the Sagittarius dwarf galaxy are older than 5 Gyr (de Boer, Belokurov, and Koposov, 2015). The Sagittarius dwarf galaxy might have formed with a high initial density and formed stars with a high SFR. However, the number of observed stars is not sufficient to permit us to conclude. We need statistics of the stars at $[\text{Fe}/\text{H}] < -1$ to confirm that r -process elements are absent in this galaxy.

According to the above discussion, we find that the initial density of halos of galaxies significantly affects the early SF and the enrichment of r -process elements. Although we should confirm this in cosmological simulations of the formation of dwarf galaxies, we expect that their evolutions are similar to our model results once they become a self-gravitating system.

3.4.2 Effects of total mass of halos

According to the hierarchical merging paradigm, the MW halo is formed via accretions of sub-halos with different masses. The total mass of each galaxy, as well as the density, is also an important parameter that affects the final metallicity and stellar mass of galaxies (Revaz and Jablonka, 2012). Thus, it is necessary to examine the enrichment of r -process elements in dwarf galaxies with different masses.

Figure 3.12 shows time variation of SFRs in models A, E, and F. SN feedback suppresses SFRs in all these models in the early phase. Their dynamical times are of the order ~ 100 Myr, which is longer than the lifetime of massive stars. In these models, SN feedback can heat the gas around the SF region and prevents subsequent new SF.

Figure 3.13 shows the mean stellar $[\text{Fe}/\text{H}]$ as a function of time. The average metallicities at 100 Myr, $[\text{Fe}/\text{H}]_0$, in models A, E, and F are $[\text{Fe}/\text{H}]_0 < -3.1$ due to suppressed SFR in these models. The value of f_{poll} is equal to 0.33 (model A), 0.0023 (model E), and 0.011 (model F) at 100 Myr. This result means that the spatial distribution of metallicity has not yet homogenized in all models at this phase. As shown in Figure 3.13, all models show large scatters of metallicity over one dex in this phase as indicated by vertical solid lines. Figure 3.13 suggests that the rate of increase in $[\text{Fe}/\text{H}]$ is an almost identical trend irrespective of the total mass.

Figure 3.14 shows the distributions of stars in the $[\text{Eu}/\text{Fe}]$ versus $[\text{Fe}/\text{H}]$ diagrams predicted in models A, E, and F. Large dispersion in $[\text{Eu}/\text{Fe}]$ appears at $[\text{Fe}/\text{H}] \sim -3$ in models A and E. Figure 3.15 shows the standard deviation of $[\text{Eu}/\text{Fe}]$ as a function of $[\text{Fe}/\text{H}]$. According to Figure 3.15, models A, E, and F have $\sigma > 1$ in $[\text{Fe}/\text{H}]$

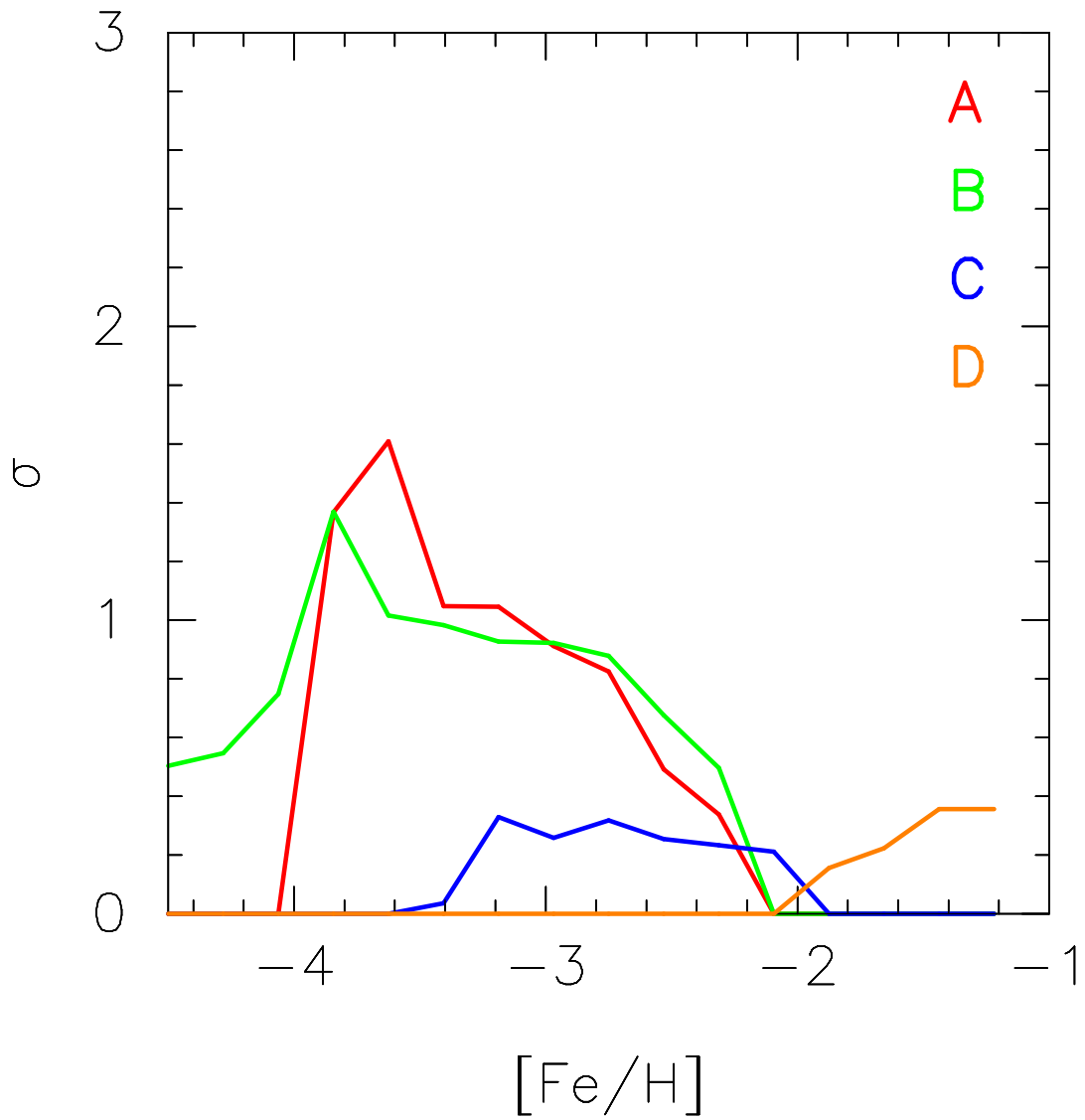


FIGURE 3.11: Standard deviation of $[\text{Eu}/\text{Fe}]$ (σ) as a function of $[\text{Fe}/\text{H}]$ after 1 Gyr from the onset of SF. Red, green, blue, and orange curves represent models A, B, C, and D, respectively.

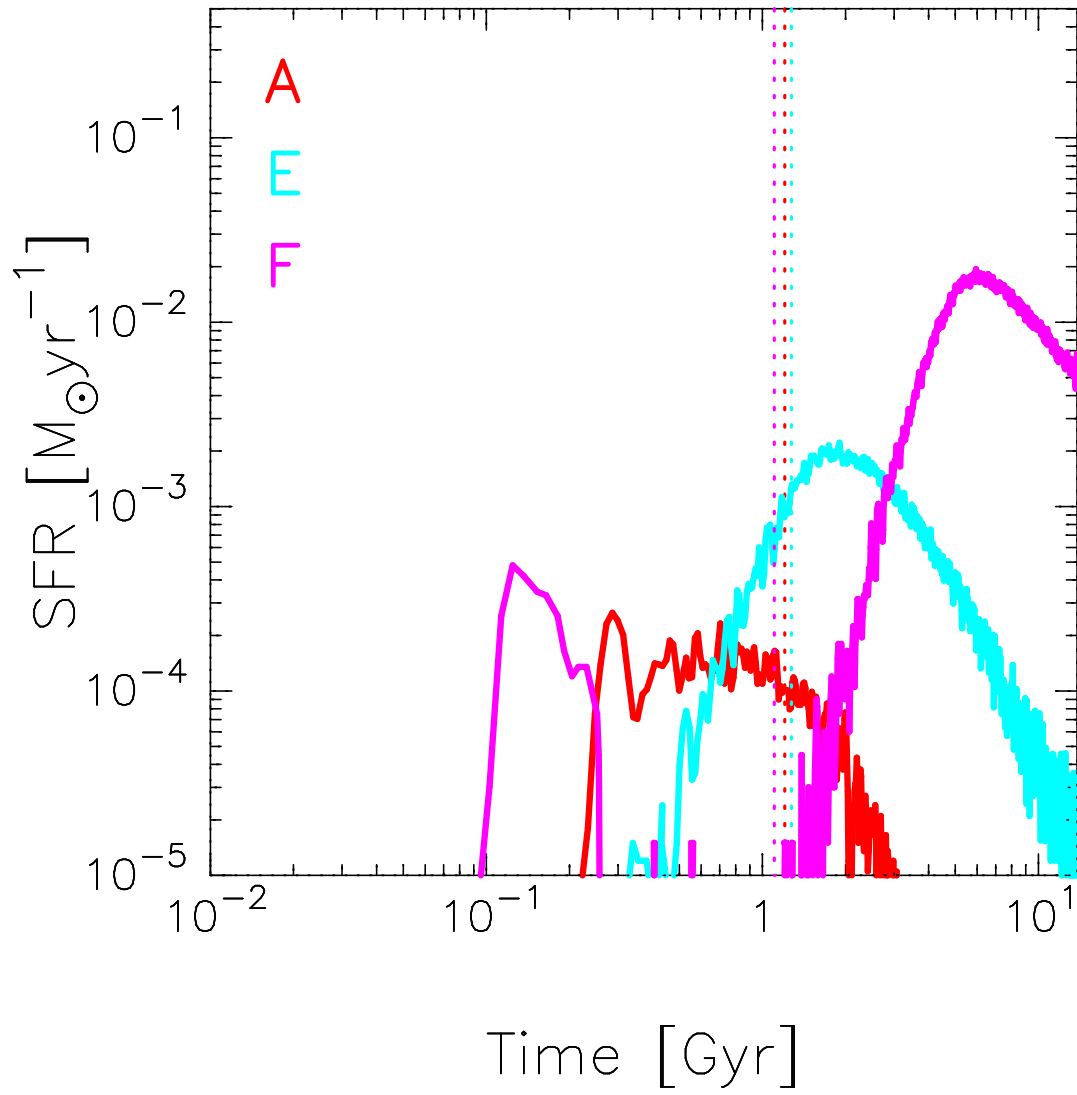


FIGURE 3.12: SFRs as a function of time. Red, cyan, and magenta curves show models A, E, and F, respectively. Vertical dotted lines show the time 1 Gyr after the formation of first stars in each model.

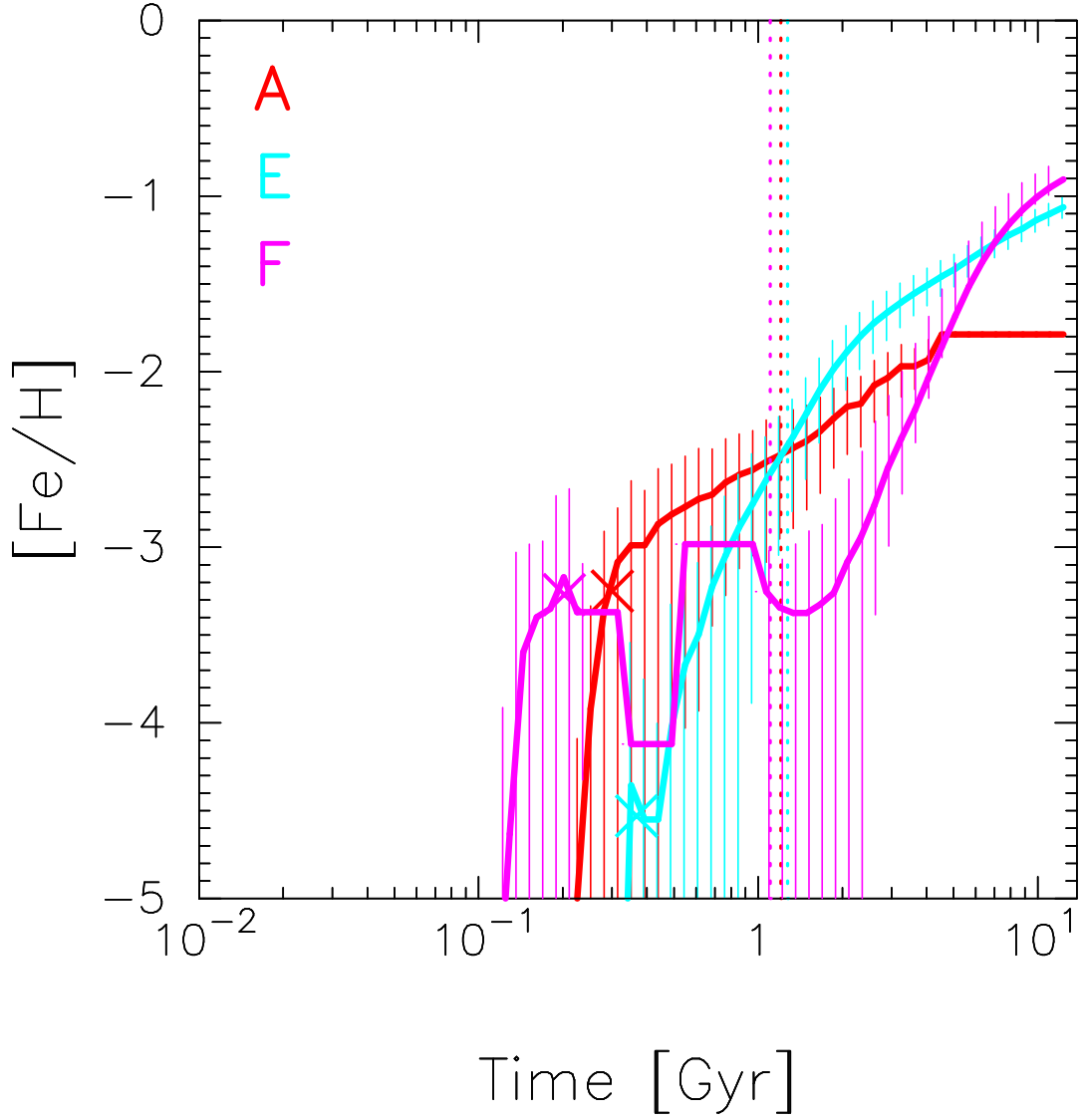


FIGURE 3.13: The mean stellar $[\text{Fe}/\text{H}]$ as a function of time (solid curves). Red, cyan, and magenta curves show models A, E, and F, respectively. Symbols and lines are the same as in Figure 3.9.

$\lesssim -3$. This result reflects the slow chemical evolution in the early evolutionary phase. Model F predicts almost no EMP stars with 1 Gyr due to the suppressed SF. A sufficient number of stars which contain Eu are formed after ~ 3 Gyr in model F. The distribution looks similar to those in models A and E. The major SF in model F starts after ~ 2 Gyr has passed since the beginning of the simulation. The dispersion in $[\text{Eu}/\text{Fe}]$ at 3 Gyr in model F is thus comparable to those of models A and B at 1 Gyr. These results suggest that $[\text{Eu}/\text{Fe}]$ versus $[\text{Fe}/\text{H}]$ does not depend on the total mass of the system.

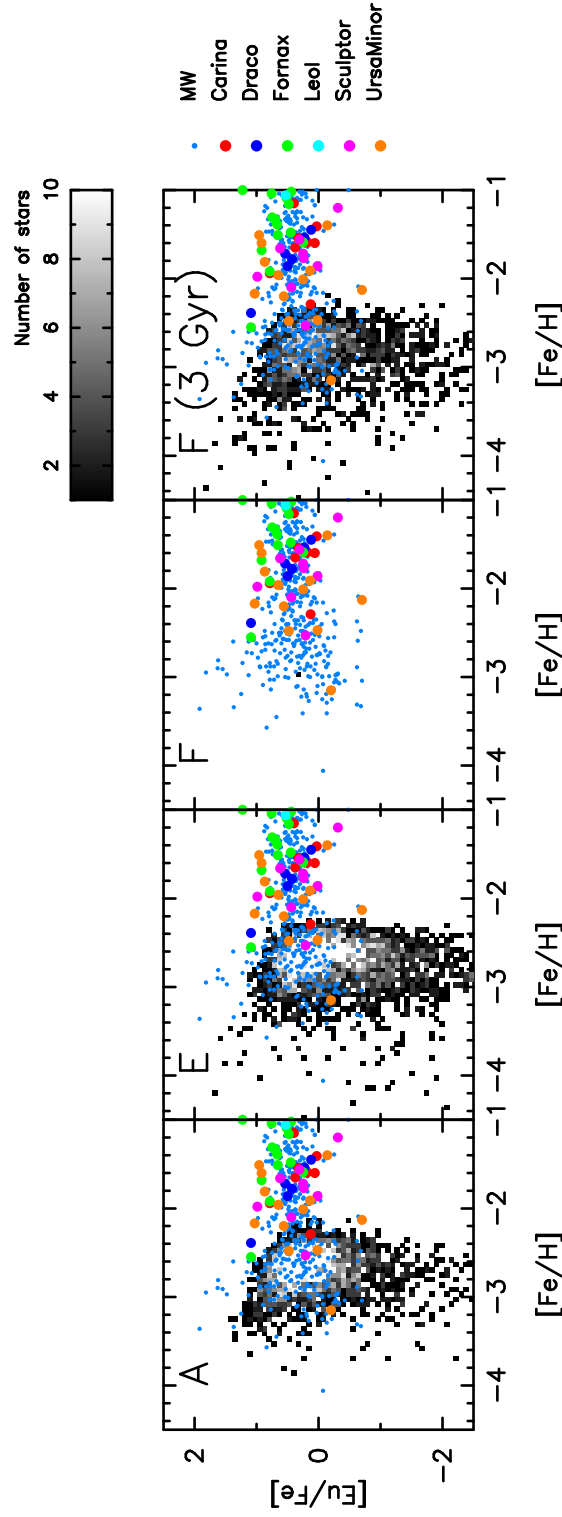


FIGURE 3.14: $[\text{Eu}/\text{Fe}]$ as a function of $[\text{Fe}/\text{H}]$ for stars. From left to right, we plot models A, E, and F. We plot models in three left-hand panels at 1 Gyr after the onset of SF. We plot model F in the rightmost panel at 3 Gyr from the start of the simulation. Symbols are the same as in Figure 3.10.

3.4.3 Merger times of NSMs

Here, we discuss the effect of merger times of NSMs. In the previous section, we find that the SFR in the early phase determines the metallicity at the time when the first NSM occurs. The star-to-star scatters of $[\text{Eu}/\text{Fe}]$ decrease as the central density increases depending on the models adopted here (Figure 3.10). As the central density increases, the dynamical time becomes shorter and the star-to-star scatter of $[\text{Eu}/\text{Fe}]$ decreases. To quantitatively examine the relation among three quantities of the distribution in $[\text{Eu}/\text{Fe}]$ versus $[\text{Fe}/\text{H}]$ diagram, dynamical times, and NSM times, we carried out simulations assuming NSM times of 10 and 500 Myr. These merger times are respectively shorter and longer than our fiducial value (100 Myr). Dominik et al. (2012) suggest that the distribution of merger times has a power law with an index of -1 and the minimum time is ~ 10 Myr in their binary stellar evolution models. Eu in EMP stars should come from NSMs whose merger times are shorter than the typical lifetime of SNe Ia progenitors, i.e., ~ 1 Gyr. We thus adopt NSM times of 10 and 500 Myr for models A, B, C, and D.

Figure 3.16 shows $[\text{Eu}/\text{Fe}]$ as a function of $[\text{Fe}/\text{H}]$ for models A_{10} , B_{10} , C_{10} , and D_{10} with NSM times of 10 Myr. The star-to-star scatters of $[\text{Eu}/\text{Fe}]$ in models A_{10} and B_{10} are not significantly different from each other as those in Figure 3.10. As shown in Figure 3.16, a large scatter of $[\text{Eu}/\text{Fe}]$ is seen at $[\text{Fe}/\text{H}] \lesssim -2$ in model C_{10} when an NSM time is assumed to be 10 Myr. However, it is difficult to explain Eu in low metallicity region ($[\text{Fe}/\text{H}] \lesssim -3$). In the case of model D_{10} , it does not explain Eu at all in $[\text{Fe}/\text{H}] < -2$. According to Figure 3.9, the average metallicities for models C_{10} , and D_{10} reach $[\text{Fe}/\text{H}] > -2.5$ in the first 10 Myr from the beginning of the simulation. It suggests that Fe increases too fast in these models to explain the dispersion in $[\text{Eu}/\text{Fe}]$ of EMP stars.

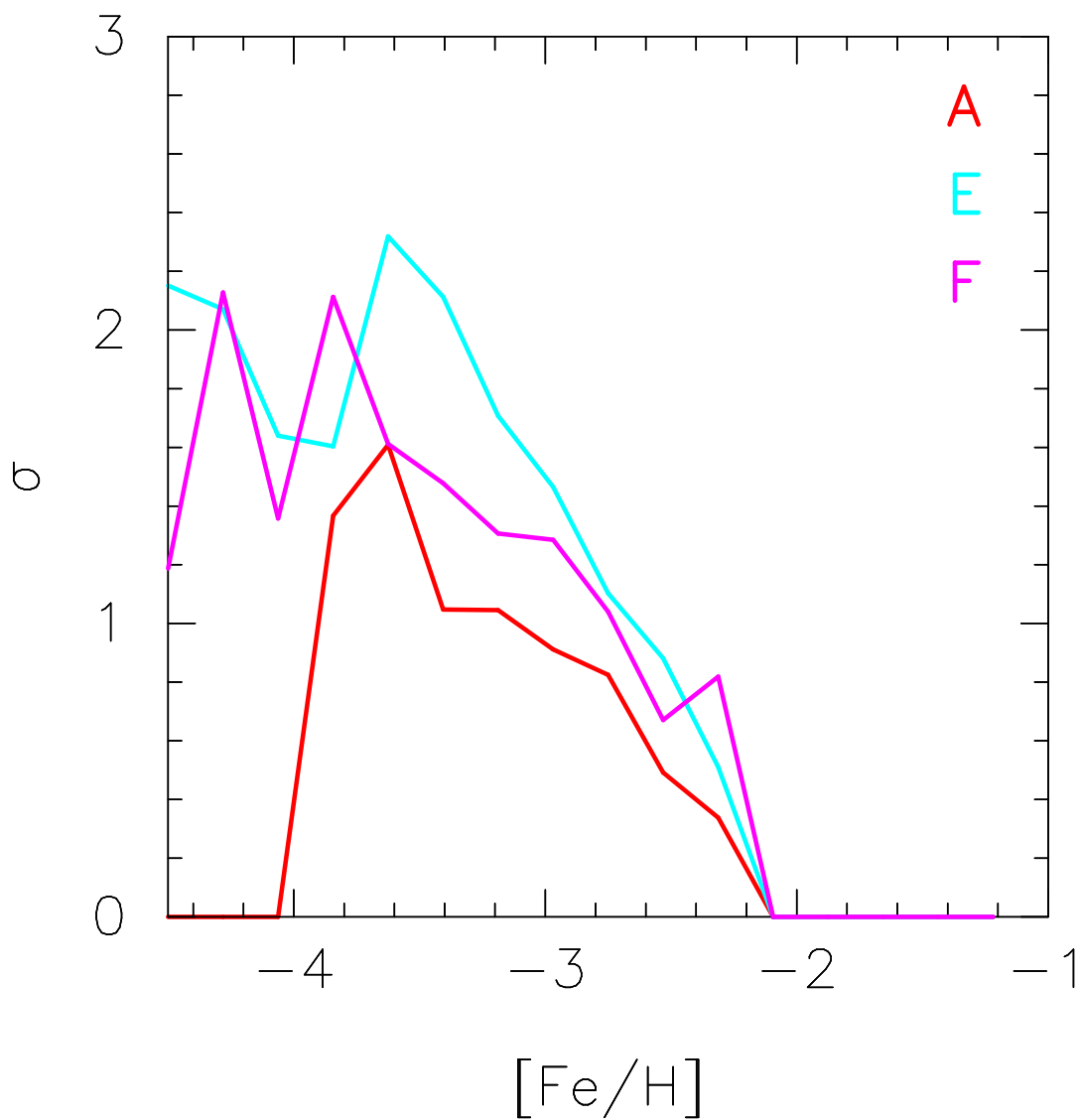


FIGURE 3.15: Standard deviation of $[\text{Eu}/\text{Fe}]$ (σ) as a function of $[\text{Fe}/\text{H}]$ after 1 Gyr for models A, E, and 3 Gyr for model F from the onset of SF. Red, cyan and magenta curves represent models A, E, and F, respectively.

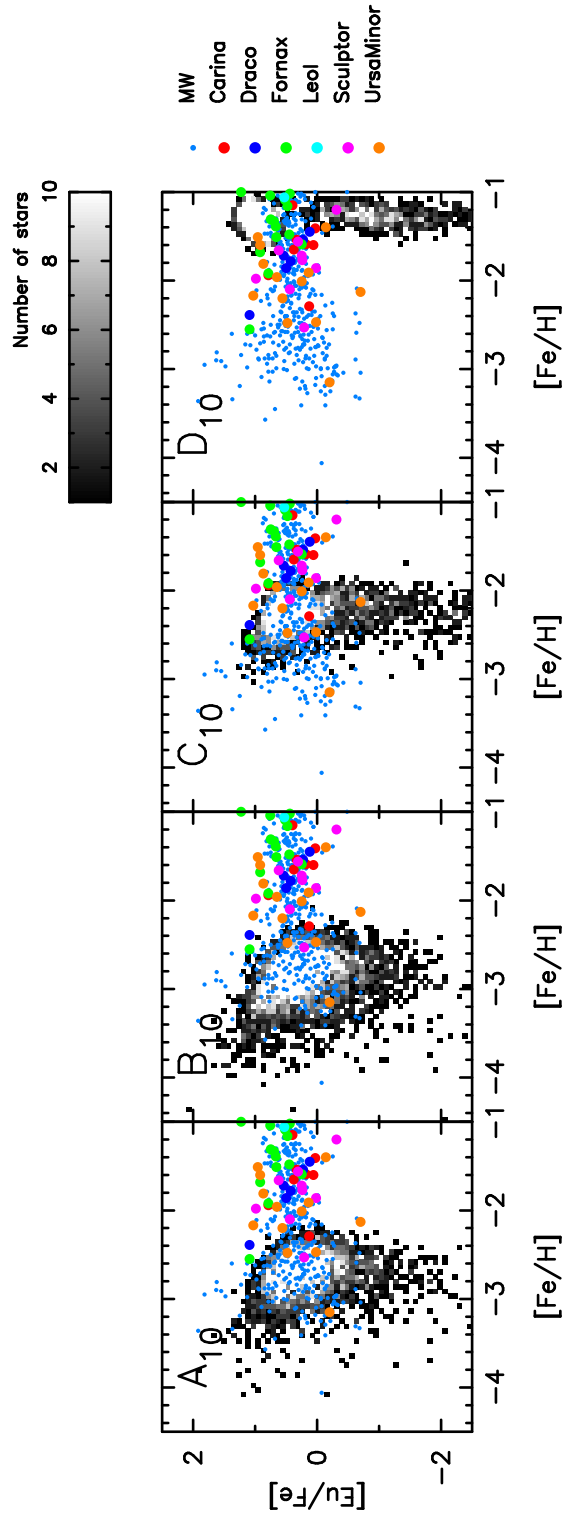


FIGURE 3.16: $[\text{Eu}/\text{Fe}]$ as a function of $[\text{Fe}/\text{H}]$ for stars produced by NSMs with a merger time of 10 Myr after 1 Gyr from the onset of SF. From left to right, we plot models A₁₀, B₁₀, C₁₀, and D₁₀. Symbols are the same as Figure 3.10.

Figure 3.17 shows $[\text{Eu}/\text{Fe}]$ as a function of $[\text{Fe}/\text{H}]$ for NSM times of 500 Myr for models A_{500} , B_{500} , C_{500} , and D_{500} . The dispersions of $[\text{Fe}/\text{H}]$ in models A_{500} and B_{500} are still over one dex at 500 Myr from the beginning of SF (Figure 3.8). The large scatter of $[\text{Eu}/\text{Fe}]$ therefore appear even if we assume an NSM time as 500 Myr. Models C_{500} , and D_{500} in Figure 3.17 likewise show that $[\text{Eu}/\text{Fe}]$ distribution is not strongly altered if we assume a merger time of 500 Myr.

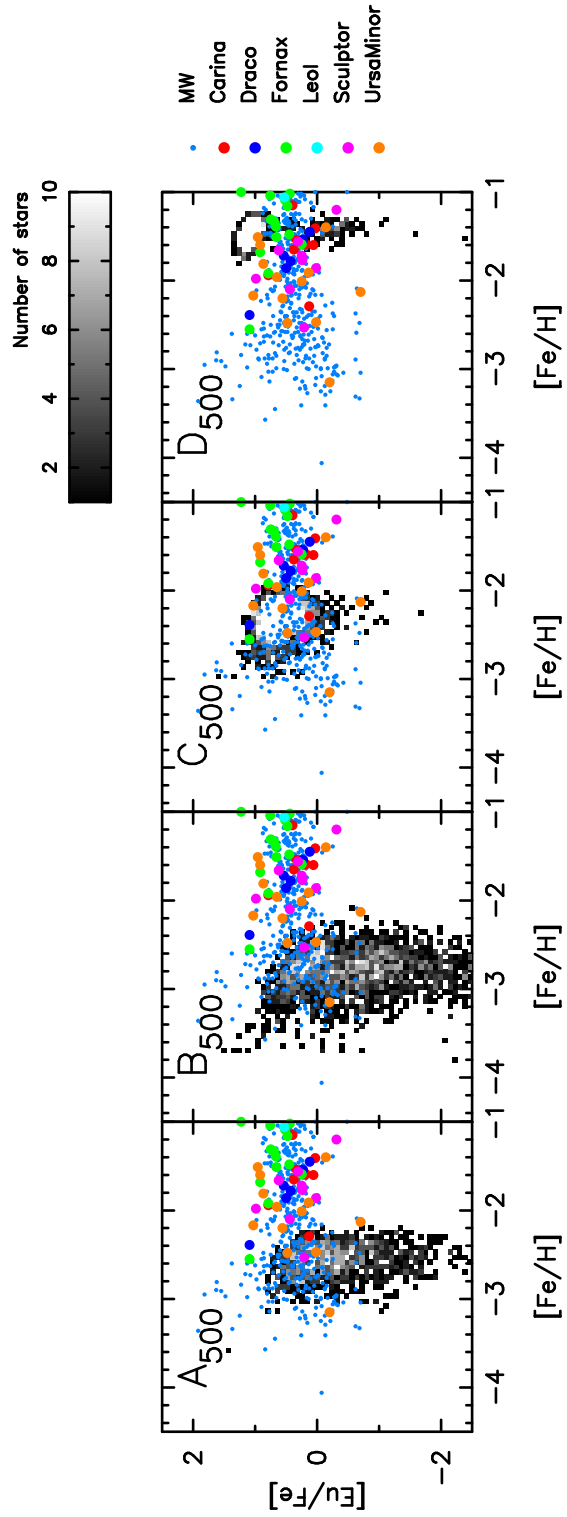


FIGURE 3.17: $[\text{Eu}/\text{Fe}]$ as a function of $[\text{Fe}/\text{H}]$ for stars produced by NSMs with a merger time of 500 Myr after 1 Gyr from the onset of SF. From left to right, we plot models A₅₀₀, B₅₀₀, C₅₀₀, and D₅₀₀. Symbols are the same as Figure 3.10.

From these results, we find that star-to-star scatters of r -process elements are not strongly affected by the merger time in the range 10 – 500 Myr. This result suggests that even if NSMs have a distribution of merger times, the distribution of [Eu/Fe] in EMP stars does not significantly change as shown in the previous studies (Hirai et al., 2015; Shen et al., 2015).

3.5 Implications to the formation of the MW halo

As discussed in Section 3.4, models with low SFR ($\lesssim 10^{-3} M_{\odot} \text{ yr}^{-1}$) at the beginning can reproduce the large scatters in [Eu/Fe] of EMP stars. Therefore, if the EMP stars in the MW halo formed in accreting sub-halos, the SFR in the sub-halos would be suppressed such as in models A, B, E, and F. On the other hand, the average metallicity of the MW halo is [Fe/H] = -1.6 (Ryan and Norris, 1991). Also, the constant α -element to iron ratio in the MW halo stars ([α /Fe] ≈ 0.5) indicates no contribution of SNe Ia. This observation means that the metallicity of the MW halo reaches [Fe/H] = -1.6 before beginning of the contribution of SNe Ia (~ 1 Gyr). According to Figures 3.9 and 3.13, the average metallicity in models A, B, E, and F is [Fe/H] $\lesssim -2.5$ at 1 Gyr. This result means that the contribution of SNe Ia starts to occur at [Fe/H] ~ -2 in models A, B, E, and F. This contradicts the observed [α /Fe] abundance in the MW halo. Assembly of galaxies as in models A, B, E, and F is not possible to explain the whole metallicity range of the MW halo. It is thus required to consider other reasons to explain the stars with [Fe/H] > -2 in the MW halo.

In this study, we adopt isolated dwarf galaxy models. This assumption would underestimate the rate of increase in metallicity. The main halo of the MW should have encountered mergers of sub-halos in the context of hierarchical structure formation. This event may induce high SFRs and increase the metallicity later forming EMP stars. The star-to-star scatters of r -process elements would be formed in halos like models A, B, E, and F. Stars with [Fe/H] > -2 observed in the MW halo would be formed in halos like model C. It is possible to prove whether these events really occur or not by analyzing MW formation simulations with higher resolution.

3.6 Summary

We performed a series of N -body/SPH simulations of the chemodynamical evolution of dwarf galaxies by varying the initial central density and the total mass of the models by one order of magnitude. We find that the distribution of r -process elements in EMP stars significantly depends on the dynamical evolution of galaxies reflecting different dynamical structures of galaxies (Figure 3.10). The initial density, which determines the dynamical time (t_{dyn}) of galaxies, is the most important fundamental parameter to determine the distribution of stars in [Eu/Fe] versus [Fe/H]. The dynamical times of dwarf galaxies significantly affect the time variations of SFRs (Figure 3.8). Models with longer dynamical times tend to form stars more slowly. We find that the early SFR is suppressed to be less than $10^{-3} M_{\odot} \text{ yr}^{-1}$ in galaxies with dynamical times of ~ 100 Myr. If the value of t_{dyn} is similar, such models show a similar distribution of [Eu/Fe] versus [Fe/H] regardless of the total mass, which is consistent with the observation of EMP stars. With a higher initial density of galaxies, in contrast, [Eu/Fe] distribution

shifts to a higher metallicity and the star-to-star scatters diminish. We confirm that the scatters of [Eu/Fe] mainly come from the inhomogeneity of the metals in the ISM whereas the scatters of α -elements are predominantly due to the difference in the yield of each SN.

These results suggest that the observed star-to-star scatters of [Eu/Fe] in EMP stars in the MW halo can be explained by NSMs if the MW halo formed via accretion of dwarf galaxies with the initial central density of $< 10^8 M_{\odot} \text{kpc}^{-3}$. Our results also imply that [Eu/Fe] distribution in individual galaxies reflects the early SFR and dynamical times of galaxies.

We also find that NSM times between 10 and 500 Myr do not strongly affect the final results. Low-density models such as models A and B can predict star-to-star scatters in [Eu/Fe] even if we assume an NSM time of 500 Myr (Figure 3.17). To explain the final abundance, we do not need to adopt unlikely short merger times if the SFR is suppressed to be less than $10^{-3} M_{\odot} \text{yr}^{-1}$.

We expect that future precise observations of EMP stars in dwarf galaxies will prove the early evolutionary history of the LG galaxies. If the star-to-star scatters of [Eu/Fe] would appear in galaxies at similar metallicities with different stellar mass, the SFR of galaxies should be lower than $10^{-3} M_{\odot} \text{yr}^{-1}$ regardless of their total mass. On the other hand, if the smaller scatters would appear at higher metallicities in galaxies with higher stellar mass, this could be a signal that the early SFRs for heavier galaxies is higher due to higher initial central density. This study suggests that the future high-dispersion spectroscopic observations of the abundance of r -process elements will be able to constrain the early evolutionary histories of LG galaxies.

Chapter 4

Enrichment of zinc in dwarf galaxies

Chapters 2 and 3 clarified the role of NSMs to the enrichment of heavy elements. This chapter clarifies the role of SNe (CCSNe, ECSNe, HNe, and SNe Ia) to the galactic chemical evolution. We focus on the enrichment of Zn in this chapter. The heaviest iron-peak element, Zn has been used as an important tracer of cosmic chemical evolution. Spectroscopic observations of the metal-poor stars in LG galaxies show that an increasing trend of $[\text{Zn}/\text{Fe}]$ ratios toward lower metallicity. However, enrichment of Zn in galaxies is not well understood due to the poor knowledge of astrophysical sites of Zn as well as metal mixing in galaxies. Here we show possible explanations for the observed trend by taking into account ECSNe as one of the sources of Zn in our chemodynamical simulations of dwarf galaxies. We find that the ejecta from ECSNe contribute to stars with $[\text{Zn}/\text{Fe}] \gtrsim 0.5$. We also find that scatters of $[\text{Zn}/\text{Fe}]$ in higher metallicity originate from the ejecta of type Ia supernovae. On the other hand, it appears difficult to explain the observed trends if we do not consider ECSNe or low mass Fe CCSNe as a source of Zn. These results suggest that ECSNe or low mass Fe CCSNe can be one of the contributors to the enrichment of Zn in galaxies¹.

4.1 Review: Astrophysical sites of Zn

Astrophysical sites of Zn are highly complicated. Since massive stars have relatively shorter lifetimes than those of lower-mass stars, Zn ejected by SNe can be a dominant source of the enrichment of Zn at low metallicity ($[\text{Fe}/\text{H}] \lesssim -2$). Stars more massive than $\sim 10 M_{\odot}$ explode as CCSNe. They synthesize ^{64}Zn during complete Si-burning and $^{66-70}\text{Zn}$ by neutron-capture process (Woosley and Weaver, 1995; Kobayashi et al., 2006). Several chemical evolution studies have been conducted to understand the Galactic enrichment history of Zn (Matteucci et al., 1993; Timmes, Woosley, and Weaver, 1995; Goswami and Prantzos, 2000; François et al., 2004; Ishimaru, Wanajo, and Prantzos, 2006; Kobayashi et al., 2006). Timmes, Woosley, and Weaver (1995) suggest that the amount of Zn in the observation can be explained if they reduce the Fe yields by a factor of two. Kobayashi et al. (2006) show that the CCSN yields of Nomoto et al. (1997) cannot give enough Zn to explain the observation.

HNe have been suggested as a possible astrophysical site of Zn (Umeda and Nomoto, 2002; Umeda and Nomoto, 2005; Kobayashi et al., 2006; Tominaga, Umeda, and Nomoto, 2007). HNe produce ~ 1 dex larger kinetic energies than those of normal

¹Contents in this chapter have been published in Hirai, Saitoh, Ishimaru, and Wanajo (2018).

CCSNe (e.g., Tanaka et al., 2009) and are thought to be observed as long gamma-ray bursts (GRBs, Podsiadlowski et al., 2004b; Guetta and Della Valle, 2007). The outward Si-burning regions in HNe synthesize larger amounts of Zn. Kobayashi et al. (2006) show that if half of the stars heavier than $20 M_{\odot}$ explode as HNe, the $[\text{Zn}/\text{Fe}]$ ratio increases ~ 1 dex compared to the prediction of Nomoto et al. (1997). Tominaga, Umeda, and Nomoto (2007) suggest that the increasing trend can be reproduced if EMP stars reflect each yield of HN with a different progenitor mass.

ECSNe can also be the astrophysical sites of Zn. The lowest-mass ($\lesssim 10 M_{\odot}$) progenitors of CCSNe that develop oxygen-neon-magnesium cores cause this type of SNe (e.g., Miyaji et al., 1980; Nomoto et al., 1982; Hillebrandt, Nomoto, and Wolff, 1984; Nomoto, 1984; Nomoto, 1987; Miyaji and Nomoto, 1987). The explosion occurs in stars with core mass of $1.367 M_{\odot}$ (Takahashi, Yoshida, and Umeda, 2013) when the electrons captured by ^{24}Mg and ^{20}Ne remove the pressure support. Hydrodynamic simulations show that the explosion energy of ECSN is $\sim 10^{50}$ erg (e.g., Kitaura, Janka, and Hillebrandt, 2006; Janka et al., 2008; Janka et al., 2012; Wanajo, Janka, and Müller, 2011). Doherty et al. (2015) predicted that the mass range of progenitors of ECSNe is $9.8\text{--}9.9 M_{\odot}$ at solar metallicity by their stellar evolution calculation. This range depends on the treatment of mass-loss rate, the efficiency of third dredge-up, and convection (e.g., Siess, 2007; Poelarends et al., 2008; Jones et al., 2013; Jones, Hirschi, and Nomoto, 2014; Woosley and Heger, 2015; Doherty et al., 2017). Wanajo et al. (2009) and Wanajo, Janka, and Müller (2011) estimated that the upper limit of the fraction of ECSNe in all CCSNe was about 30 % based on their nucleosynthesis calculations. ECSNe can be observed as optically bright SNe characterized by the short plateau with a faint tail luminosity curve (e.g., Tominaga, Blinnikov, and Nomoto, 2013; Smith, 2013; Moriya et al., 2014). The crab nebula (SN 1054) is one of the most promising candidates of an ECSN remnant (e.g., Davidson et al., 1982; Nomoto et al., 1982).

Nucleosynthesis studies based on two-dimensional hydrodynamic simulations of an $8.8 M_{\odot}$ ECSN show that ECSNe produce all the stable isotopes of Zn in neutron-rich ejecta with the electron fraction (proton-to-nucleon ratio) of $\sim 0.4\text{--}0.5$ (Wanajo, Janka, and Müller, 2011; Wanajo et al., 2018). ECSNe also synthesize a small amount of Fe. These features of nucleosynthesis lead to higher values of $[\text{Zn}/\text{Fe}]$ than those of normal CCSNe. In addition to Zn, ECSNe may contribute to the enrichment of light trans-iron elements (e.g., Wanajo, Janka, and Müller, 2011; Hansen, Andersen, and Christlieb, 2014; Aoki et al., 2017), ^{48}Ca (Wanajo, Janka, and Müller, 2013a), and ^{60}Fe (Wanajo, Janka, and Müller, 2013b). There are several studies on the enrichment of r -process elements by ECSNe (e.g., Ishimaru and Wanajo, 1999; Ishimaru et al., 2004). However, their role in the enrichment of Zn in galaxies has not yet been studied.

The main purpose of this chapter is to clarify the enrichment of Zn in dwarf galaxies using a series of high-resolution galactic chemodynamical simulations. We aim to constrain the astrophysical sites of Zn in galaxies by comparing our simulations with observations of metal-poor stars. Section 4.2 describes models adopted in this chapter. In Section 4.3, we show the SFHs, the metallicity distributions, and the α -element abundances computed by our fiducial model. In Section 4.4, we show the enrichment of Zn computed in our dwarf galaxy models. We discuss the astrophysical sites of Zn in galaxies implied from the enrichment histories of Zn. In Section 4.5,

we summarize the results of this chapter.

4.2 Models

We adopt Chemical Evolution Library (CELIB) to compute stellar feedback and chemical evolution (Saitoh, 2016; Saitoh, 2017) in ASURA (Section 1.4). We adopt the IMF of Kroupa (2001) from 0.1 to $100 M_{\odot}$. We assume that stars more massive than $8 M_{\odot}$ explode as CCSNe and distribute the thermal energy of $\sim 10^{51}$ erg to surrounding gas particles. We also assume that a certain fraction (f_{HN}) of stars more massive than $20 M_{\odot}$ explode as HNe. They distribute the thermal energy of $\sim 10^{52}$ erg to surrounding gas particles. We adopt $f_{\text{HN}} = 0, 0.05$, and 0.5 in this study. The value of $f_{\text{HN}} = 0.05$ is taken from the observed rate of long GRBs (Podsiadlowski et al., 2004b; Guetta and Della Valle, 2007). The value of $f_{\text{HN}} = 0.5$ is taken from the chemical evolution model of Kobayashi et al. (2006). We adopt the nucleosynthesis yields of Nomoto, Kobayashi, and Tominaga (2013, hereafter, N13) in our fiducial models. We also test the nucleosynthesis yields of Chieffi and Limongi (2004, hereafter, CL04) at $Z \geq 10^{-5} Z_{\odot}$ and Limongi and Chieffi (2012) at $Z < 10^{-5} Z_{\odot}$ for comparison (Appendix C). SNe Ia are assumed to occur in stars with $3\text{--}6 M_{\odot}$ in this simulation. We adopt the empirical delay time distribution of SNe Ia presented in Maoz and Mannucci (2012). The number of SNe Ia (N_{SNIa}) per unit time can be written as

$$\frac{dN_{\text{SNIa}}}{dt} = \epsilon_{\text{SNIa}} \left(\frac{t}{10^9 \text{yr}} \right)^{\alpha_{\text{SNIa}}}, \quad (4.1)$$

where $\epsilon_{\text{SNIa}} = 4 \times 10^{-13}$ and $\alpha_{\text{SNIa}} = -1$ following Maoz and Mannucci (2012) to be consistent with the observed rate and delay time of SNe Ia. We set the minimum delay time of SNe Ia to be 10^8 yr (Totani et al., 2008). The energy from SNe Ia is distributed in the same way as CCSNe. We adopt the model N100 of Seitenzahl et al. (2013) for the nucleosynthesis yields of SNe Ia. We assume that each SN Ia produces $0.74 M_{\odot}$ of Fe and does not produce Zn.

4.2.1 ECSN models

We newly consider the role of ECSNe in our simulation. We adopt the nucleosynthesis yields of model e8.8 in Wanajo et al. (2018); the same as those in Wanajo, Janka, and Müller (2011), Wanajo, Janka, and Müller (2013a), and Wanajo, Janka, and Müller (2013b). When an ECSN occurs, the thermal energy of 9×10^{49} erg is distributed to the surrounding gas particles according to Wanajo et al. (2018). The mass range of ECSN progenitors is taken from the stellar evolution calculations of Doherty et al. (2015). At $Z = 0.0001$, the lower and upper progenitor masses of ECSNe are $8.2 M_{\odot}$ and $8.4 M_{\odot}$, respectively. At $Z = 0.02$, the mass range becomes $9.8\text{--}9.9 M_{\odot}$. We also adopt the mass range computed by Poelarends (2007). Their models show more pronounced metallicity dependences on the mass ranges than those of Doherty et al. (2015). Also, we consider the case of a constant mass range of $8.5\text{--}9.0 M_{\odot}$. Table 4.1 summarizes the mass ranges of ECSN progenitors adopted in this study. We discuss the effects of adopted mass ranges in Section 4.4.3.

TABLE 4.1: The mass ranges of ECSN progenitors.

Z	Doherty et al. (2015)		Poelarends (2007)		Constant mass range	
	M_l (M_\odot)	M_u (M_\odot)	M_l (M_\odot)	M_u (M_\odot)	M_l (M_\odot)	M_u (M_\odot)
0.02	9.8	9.9	9.0	9.3	8.5	9.0
0.008	9.5	9.6	8.7	9.3	8.5	9.0
0.004	8.8	9.0	8.4	9.1	8.5	9.0
0.001	8.3	8.4	7.6	8.4	8.5	9.0
0.0001	8.2	8.4	6.9	8.2	8.5	9.0
0.00001	8.2	8.4	6.4	8.2	8.5	9.0

From left to right, columns show metallicity (Z), the lower (M_l) and upper (M_u) mass of ECSN progenitors.

4.2.2 Nucleosynthesis yields of zinc

We adopt the nucleosynthesis yields of Zn for ECSNe (Wanajo et al., 2018), normal CCSNe (N13 or CL04), and HNe (N13). The former (ECSNe) and latter (CCSNe and HNe) are based on the solar-metallicity and metallicity-dependent models, respectively. Table 4.2 lists the yields of ECSNe, CCSNe, and HNe for selected metallicities adopted in this study. The solar-metallicity model of an ECSN is used for all the other metallicities because of its insensitivity to the initial compositions (Wanajo, Janka, and Müller, 2011; Wanajo et al., 2018). Wanajo et al. (2018) show that all stable Zn isotopes are predominantly synthesized in neutron-rich ejecta with the electron fraction from 0.4 to 0.5. ECSNe produce sufficient amounts of such neutron-rich ejecta. This leads to the production of Zn in ECSNe. On the other hand, higher entropy ejecta from HNe than those from normal CCSNe result in a strong α -rich freeze out from nuclear statistical equilibrium. This leads to greater production of ^{64}Zn in HNe than that in normal CCSNe (e.g., N13).

TABLE 4.2: Yields of Fe and Zn of each type of SN.

Elements	ECSNe		CCSNe		HNe							
	e8.8 (M_{\odot})		15 (M_{\odot})	20 (M_{\odot})	25 (M_{\odot})	30 (M_{\odot})	40 (M_{\odot})	20 (M_{\odot})	25 (M_{\odot})	30 (M_{\odot})	40 (M_{\odot})	
$Z = 0$												
Fe	3.07×10^{-3}		7.24×10^{-2}	7.23×10^{-2}	7.38×10^{-2}	7.46×10^{-2}	8.00×10^{-2}	8.49×10^{-2}	9.94×10^{-2}	1.64×10^{-1}	2.63×10^{-1}	
Zn	1.13×10^{-3}		1.23×10^{-4}	8.34×10^{-5}	2.56×10^{-5}	3.08×10^{-6}	4.44×10^{-10}	3.85×10^{-11}	2.66×10^{-4}	5.90×10^{-4}	6.96×10^{-4}	
$Z = 0.001$												
Fe	3.07×10^{-3}		7.20×10^{-2}	7.23×10^{-2}	7.18×10^{-2}	7.26×10^{-2}	7.93×10^{-2}	8.19×10^{-2}	1.52×10^{-1}	2.04×10^{-1}	2.64×10^{-1}	
Zn	1.13×10^{-3}		6.84×10^{-5}	3.32×10^{-5}	4.86×10^{-5}	8.21×10^{-5}	1.08×10^{-4}	3.59×10^{-4}	5.66×10^{-4}	8.54×10^{-4}	7.28×10^{-4}	
$Z = 0.004$												
Fe	3.07×10^{-3}		7.05×10^{-2}	7.08×10^{-2}	6.88×10^{-2}	7.31×10^{-2}	7.38×10^{-2}	2.63×10^{-2}	7.81×10^{-2}	1.50×10^{-1}	2.74×10^{-1}	
Zn	1.13×10^{-3}		1.18×10^{-4}	8.47×10^{-5}	2.18×10^{-5}	2.64×10^{-4}	5.71×10^{-4}	6.03×10^{-5}	4.03×10^{-4}	5.44×10^{-4}	1.00×10^{-3}	
$Z = 0.02$												
Fe	3.07×10^{-3}		6.55×10^{-2}	6.15×10^{-2}	5.85×10^{-2}	6.09×10^{-2}	5.22×10^{-2}	9.29×10^{-3}	9.35×10^{-2}	7.31×10^{-2}	2.57×10^{-1}	
Zn	1.13×10^{-3}		7.13×10^{-5}	2.25×10^{-4}	9.16×10^{-4}	7.08×10^{-4}	3.02×10^{-6}	1.60×10^{-4}	1.12×10^{-3}	1.32×10^{-4}	3.33×10^{-3}	

The first column shows metallicity or names of elements. From the second left to right, columns show yields of Fe and Zn. Yields of ECSN are taken from Wanajo et al. (2018). We take the solar-metallicity model of ECSNe because they are insensitive to the initial composition. For yields of CCSNe and HNe, we take those from N13.

Figure 4.1 shows the IMF-integrated yields of $[\text{Zn}/\text{Fe}]$ as a function of metallicity. ECSNe produce higher $[\text{Zn}/\text{Fe}]$ ratios than those of CCSNe and HNe. This is because ECSNe synthesize sufficiently small amounts of Fe compared to the other types of SNe. HNe synthesize sufficient Fe as well as Zn. This feature of nucleosynthesis results in the lower values of $[\text{Zn}/\text{Fe}]$ than those of ECSNe. The yield of Zn from a CCSN is sensitive to the location of the mass cut that divides the ejected material and the remnant core. We discuss the effects of different yields of SNe in Appendix C.1.

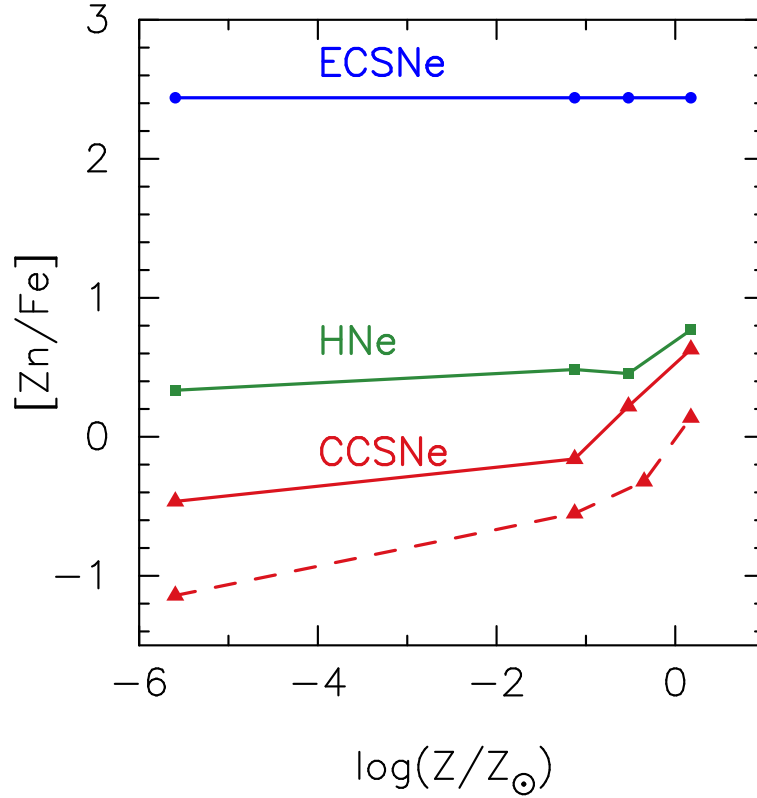


FIGURE 4.1: The IMF integrated yields of $[\text{Zn}/\text{Fe}]$ as a function of metallicity. Blue circles, green squares, and red triangles connected with solid lines represent the IMF weighted yields of ECSNe, HNe, and CCSNe, respectively. The ECSN yields are taken from Wanajo et al. (2018). The HN and CCSN yields are taken from N13. The red dashed line shows the CCSN yields of CL04. Yields for $Z = 0$ are plotted at $\log_{10}(Z/Z_{\odot}) = -5.6$. We adopt $Z_{\odot} = 0.0134$ (Asplund et al., 2009).

Figure 4.2 shows the mass fractions of Zn isotopes relative to the solar values (production factors). The black dotted line indicates the production factor of 10 that is taken as the lower bound for each astrophysical site to be a main contributor of a given isotope (e.g., Woosley and Heger, 2007). At $Z = 0$, the production factors of $^{66,67,68,70}\text{Zn}$ from HNe and CCSNe are significantly lower than this lower bound. The production factors of these isotopes increase with metallicity. This is because the weak s -process, which synthesizes $^{66,67,68,70}\text{Zn}$ in CCSNe, is more efficient at higher metallicity (Kobayashi et al., 2006). Kobayashi, Karakas, and Umeda (2011) show that the ratio of $^{64}\text{Zn}/^{66,67,68,70}\text{Zn}$ continuously decreases toward higher metallicity. However, they find that the ratio is too low to explain the solar isotopic ratios at

$Z = Z_{\odot}$. On the other hand, ECSNe synthesize all isotopes of Zn (independent of metallicities) in a nuclear statistical equilibrium (Wanajo, Janka, and Müller, 2011; Wanajo et al., 2018). As shown in Figure 4.2, the production factors of the Zn isotopes in ECSNe are between 1.5×10 and 1.2×10^2 . This suggests that a contribution of ECSNe with a rate of several percent of all CCSNe can explain most of the solar isotopic abundances of Zn.

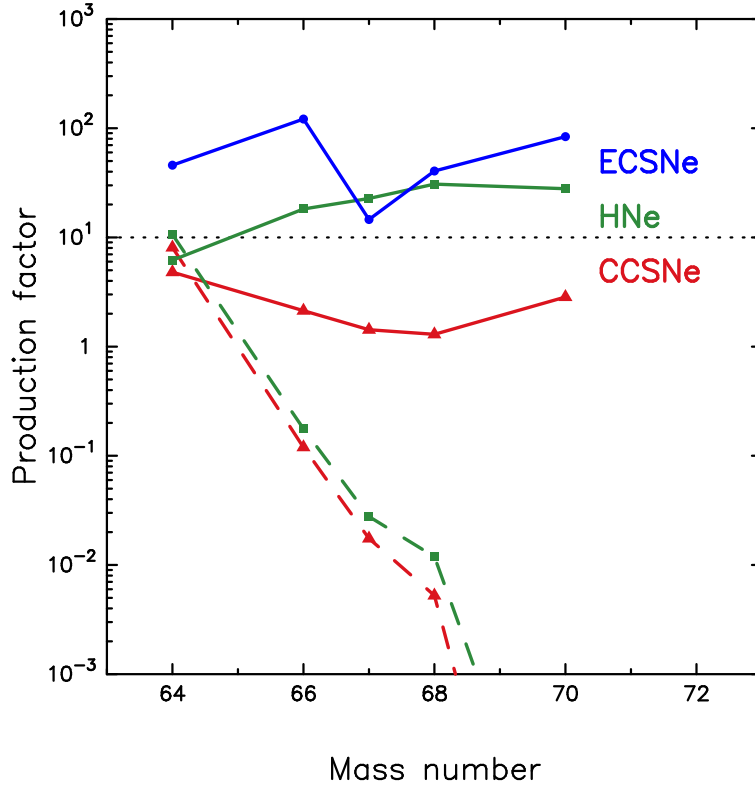


FIGURE 4.2: Production factors of Zn isotopes. Blue circles, green squares, and red triangles connected with solid lines represent the production factors of ECSNe ($8.8 M_{\odot}$), HNe ($25 M_{\odot}$), and CCSNe ($15 M_{\odot}$) at the solar metallicity, respectively. Green and red dashed lines denote the production factors of HNe ($25 M_{\odot}$) and CCSNe ($15 M_{\odot}$) at $Z = 0$, respectively. Yields of isotopes are taken from (Wanajo et al., 2018) for ECSNe and N13 for HNe and CCSNe. The black dotted line indicates the production factor of 10 that is taken as the lower bound for each astrophysical site to be a main contributor of a given isotope (e.g., Woosley and Heger, 2007).

4.2.3 Metal mixing models

In SPH simulations without a metal-mixing scheme, the metals inherited from SNe are locked in a gas particle throughout the galaxy evolution. In this study, we take a shear-based metal-mixing model (Shen, Wadsley, and Stinson, 2010; Saitoh, 2017).

The time derivative of i th metal (Z_i) follows diffusion equation,

$$\begin{aligned}\frac{dZ_i}{dt} &= \nabla(D\nabla Z_i), \\ D &= C_d |S_{ij}| h^2,\end{aligned}\tag{4.2}$$

where D is the diffusion coefficient, C_d is the scaling factor for diffusion coefficient, S_{ij} is the trace-free shear tensor, and h is the smoothing length of SPH particle. Chapter 5 shows that the value of $C_d \gtrsim 0.01$ is appropriate to explain the observational trends of r -process elements in dSphs. We discuss the efficiency of metal mixing in Chapter 5.

4.3 Chemodynamical evolution of dwarf galaxies

We adopt the isolated dwarf galaxy model presented in Section 2.2.4. We confirm that this model can reproduce the observed properties, such as MDFs, mass–metallicity relation, and velocity dispersion profiles, of the LG dwarf galaxies (Chapters 2 and 3). The total number of particles is 2^{18} . The halo mass and central density are $7 \times 10^8 M_\odot$ and $5.0 \times 10^7 M_\odot \text{ kpc}^{-3}$, respectively. The masses of one dark matter and gas particles are $4.5 \times 10^3 M_\odot$ and $8.0 \times 10^2 M_\odot$, respectively. We have confirmed that effects of IMF sampling (Revaz et al., 2016) do not strongly affect our results. We show that our main results do not strongly depend on the resolution of simulations (Appendix C.2). We set the gravitational softening length as 7.8 pc and scaling factor for metal diffusion. $C_d = 0.01$. The final stellar mass of this galaxy is $5 \times 10^6 M_\odot$. Table 4.3 lists all the models adopted in this study.

TABLE 4.3: List of models discussed in this chapter.

Model	ECSN mass range	f_{HN}
G	Doherty et al. (2015)	0.05
H	Poelarends (2007)	0.05
I	$8.5 - 9.0 M_\odot$	0.05
J		0.5
K		0.05
L	Doherty et al. (2015)	
M	$8.5 - 9.0 M_\odot$	

From left to right, columns show the names of models, the mass ranges of ECSN progenitors, and the HN fractions.

Here we show the SFHs, the metallicity-distribution functions, and the α -element abundances computed in our models. Although we do not intend to construct models that are relevant to specific LG dwarf galaxies, we confirm that our models have properties similar to those of the observed dwarf galaxies, as follows:

Figure 4.3 shows the time variations of SFRs in model G. Star formation begins after a sufficient gas fall onto the central region of the galaxy. The oscillating behavior of SFRs is due to discontinuous SN feedbacks. As shown in this figure, a typical

SFR in this model is $\sim 10^{-3} M_{\odot} \text{yr}^{-1}$. This value is roughly consistent with the SFHs of LG dSphs such as Sculptor and Fornax estimated from color-magnitude diagrams (de Boer et al., 2012a; de Boer et al., 2012b).

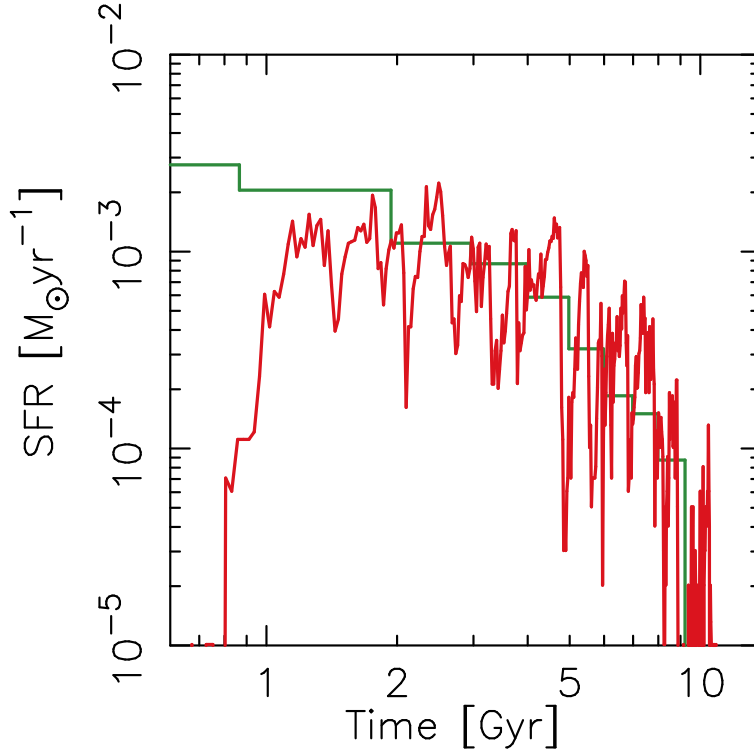


FIGURE 4.3: Time variations of SFRs in model G (red curve). The green line shows the SFH of the Sculptor dSph estimated from the color-magnitude diagram (de Boer et al., 2012b).

Figure 4.4 shows the metallicity distribution function of model G at 13.8 Gyr from the beginning of the simulation. The median metallicity and the final stellar mass are $[\text{Fe}/\text{H}] = -1.34$ and $M_* = 3.72 \times 10^6 M_{\odot}$, respectively. These values are consistent with those of LG dwarf galaxies such as the Sculptor dSph ($[\text{Fe}/\text{H}] = -1.68$ and $M_* = 3.9 \times 10^6 M_{\odot}$) and the Leo I dSph ($[\text{Fe}/\text{H}] = -1.45$ and $M_* = 4.9 \times 10^6 M_{\odot}$) within the observational errors (Kirby et al., 2013).

Figure 4.5 shows the α -element abundance ratios ($[\text{Mg}/\text{Fe}]$) as a function of $[\text{Fe}/\text{H}]$ in model G. Stars with $[\text{Fe}/\text{H}] \lesssim -2.8$ in this model show star-to-star scatters of $[\text{Mg}/\text{Fe}]$ less than 0.1 dex. Such small scatters of $[\text{Mg}/\text{Fe}]$ also are reported for the EMP stars in some LG galaxies (e.g., Frebel and Norris, 2015). The observed values of $[\text{Mg}/\text{Fe}]$ decrease as the metallicity increases for stars with $[\text{Fe}/\text{H}] \gtrsim -2.5$. This trend can be interpreted as a consequence of the contribution of SNe Ia that do not produce α -elements. In our model, the values of $[\text{Mg}/\text{Fe}]$ start to decrease at $[\text{Fe}/\text{H}] \approx -2.5$, which is consistent with the case of the Sculptor dSph reported in Suda et al. (2017).

The slope of computed $[\text{Mg}/\text{Fe}]$ as a function of $[\text{Fe}/\text{H}]$ is shallower than the observed one. This may be due to the different SFH between our model and Sculptor or modeling of SNe Ia. de Boer et al. (2012b) show that Sculptor has steadily decreasing SFH from 14 to 7 Gyr ago. On the other hand, our models have a constant SFH over 9 Gyr (Figure 4.3). When the SFH is peaked at the very early stages,

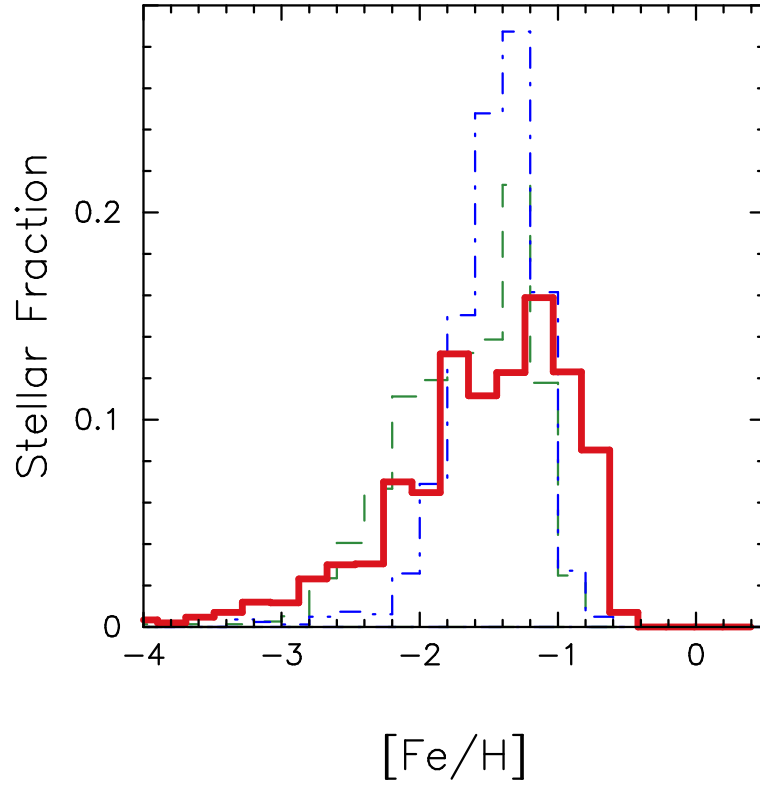


FIGURE 4.4: Predicted and observed metallicity distribution functions. The red histogram represents the metallicity distribution function of model G at 13.8 Gyr from the beginning of the simulation. The green dashed, and blue dash-dotted histograms show the observed metallicity distribution functions of the Sculptor and Leo I dSphs (Kirby et al., 2009; Kirby et al., 2010; Kirby and Cohen, 2012). All observed data are compiled using the SAGA database (Suda et al., 2017).

the computed slope of $[\text{Mg}/\text{Fe}]$ tends to be steeper than the slopes of models with SFHs peaked at later phases (Homma et al., 2015). Another possibility to cause the different slope can be attributed to our modeling of SNe Ia. We model the delay time distribution of SNe Ia with power-law distribution with the minimum delay time of 0.1 Gyr. Kobayashi and Nomoto (2009) show that SN Ia rates should be very low in $[\text{Fe}/\text{H}] \lesssim -1$ to reproduce observed α -element abundances. Homma et al. (2015) suggest that the minimum delay time of SNe Ia is estimated to be 0.5 Gyr from the α -element abundances in dSphs. Since discussing these effects is beyond the scope of this chapter, we do not discuss these possibilities further here.

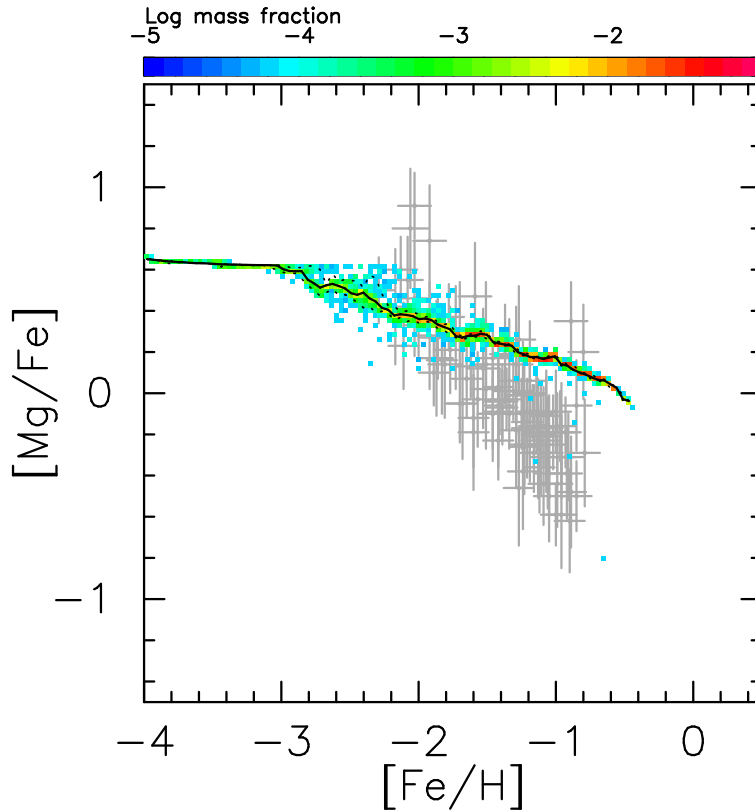


FIGURE 4.5: $[\text{Mg}/\text{Fe}]$ as a function of $[\text{Fe}/\text{H}]$ in model G. The color-coded stellar mass fractions are displayed in the logarithmic scale. The solid black curves show that the median values of computed data at each $[\text{Fe}/\text{H}]$ bin. The dotted curves show the 5 % and 95 % significance levels. Gray dots represent the observed values for Sculptor dSph (Kirby et al., 2010). We plot observed values with internal errors of $\Delta[\text{Fe}/\text{H}] < 0.15$, $\Delta[\text{Mg}/\text{Fe}] < 0.30$ to be consistent with high resolution data (Hill et al. in prep) following Hill and DART Collaboration (2012).

4.4 Enrichment of Zn

4.4.1 Enrichment of Zn at $[\text{Fe}/\text{H}] \lesssim -2.5$

The observation of $[\text{Zn}/\text{Fe}]$ is characterized by an increasing trend toward lower metallicity. In Figure 4.6, we plot observed data of Sculptor and the MW halo. We plot the binned MW halo data at $[\text{Fe}/\text{H}] < -2.5$ because observed data of dSphs are not enough to compare with our models. Skúladóttir et al. (2017) show that the abundance ratios of $[\text{Zn}/\text{Fe}]$ in Sculptor are consistent with those of the MW halo at $[\text{Fe}/\text{H}] \lesssim -2$. Here we mainly focus on figuring out conditions to form stars with $[\text{Zn}/\text{Fe}] \gtrsim 0.5$, which are seen in the observations. We also compare the slopes of $[\text{Zn}/\text{Fe}]$ as a function of $[\text{Fe}/\text{H}]$ in our models and observations.

Figure 4.6 shows $[\text{Zn}/\text{Fe}]$ as a function of $[\text{Fe}/\text{H}]$ computed in model G. Stars with $[\text{Zn}/\text{Fe}] \gtrsim 0.5$ at $[\text{Fe}/\text{H}] \lesssim -2$ reflect the high $[\text{Zn}/\text{Fe}]$ ratios in the ejecta of ECSNe (Figure 4.1). On the other hand, the ejecta from HNe and CCSNe contribute to increasing the average values of $[\text{Zn}/\text{Fe}]$. The average values of $[\text{Zn}/\text{Fe}]$ are determined by the IMF weighted values of Zn yield of all astrophysical sites of Zn. In model G, the average values of Zn are lower than those of observations at $[\text{Fe}/\text{H}] \lesssim -3$. In Section 4.4.3, we show that these values are related to the rates of ECSNe and HNe.

The stellar $[\text{Zn}/\text{Fe}]$ ratios of model G slightly increase toward lower metallicity. We performed the chi-squared linear fitting to our data at $-4.0 < [\text{Fe}/\text{H}] < -2.5$. We choose this metallicity range because the effects of SNe Ia are negligible at $[\text{Fe}/\text{H}] < -2.5$ and there are not enough observed data at $[\text{Fe}/\text{H}] < -4.0$. The linear fitting of our result shows that the slope of $[\text{Zn}/\text{Fe}]$ as a function of $[\text{Fe}/\text{H}]$ is -0.12 ± 0.01 . On the other hand, the linear fitting of the observed data of the MW halo (SAGA database, Suda et al., 2008; Suda et al., 2011; Yamada et al., 2013) shows the slope of -0.26 ± 0.04 . We take the observed data of the MW halo because the number of observed data of dwarf galaxies is not enough to analyze in this metallicity range. The flatter slope than that of the observations is due to the adopted mass ranges of the ECSN progenitors in low metallicity. We adopt the stellar evolution model of Doherty et al. (2015) in model G. They show that the mass range of ECSN varies only $0.1 M_{\odot}$ from $Z = 10^{-5}$ to $10^{-3} Z_{\odot}$. This almost constant mass range in low metallicity makes it difficult to reproduce the increasing trend toward lower metallicity. At $[\text{Fe}/\text{H}] \gtrsim -2.9$, SNe Ia start contributing to decrease the $[\text{Zn}/\text{Fe}]$ ratio toward higher metallicity.

The stars of model G with the highest $[\text{Zn}/\text{Fe}]$ ratios for given metallicity bins have an increasing trend toward lower metallicity. Figure 4.6 shows that the highest $[\text{Zn}/\text{Fe}]$ ratio at $[\text{Fe}/\text{H}] = -2.5$ is $[\text{Zn}/\text{Fe}] = 0.4$. The highest value increases to $[\text{Zn}/\text{Fe}] = 1.0$ at $[\text{Fe}/\text{H}] = -3.5$. This trend comes from the inhomogeneity of the spatial metallicity distribution in the early epoch of galaxy evolution. Figure 4.7 shows the time evolutions of $[\text{Fe}/\text{H}]$ and $[\text{Zn}/\text{Fe}]$. As shown in Figure 4.7a, stars with $[\text{Fe}/\text{H}] < -2$ are formed until 2 Gyr from the beginning of the simulation. ECSNe synthesize an appreciable amount of Zn with a small amount of Fe (Figure 4.1). When the first ECSN occurs in the galaxy, stars subsequently formed around the ejecta of ECSNe have high values of $[\text{Zn}/\text{Fe}]$ (~ 1). These stars can only be formed in the early epoch of galaxy evolution ($t < 2$ Gyr in this model, Figure 4.7b). The fraction of ECSNe out of all SNe is 3.1 % at $Z = 0.0001$ in this model. Due to the low event rate of ECSNe, the Zn abundances in the ISM are highly inhomogeneous during the

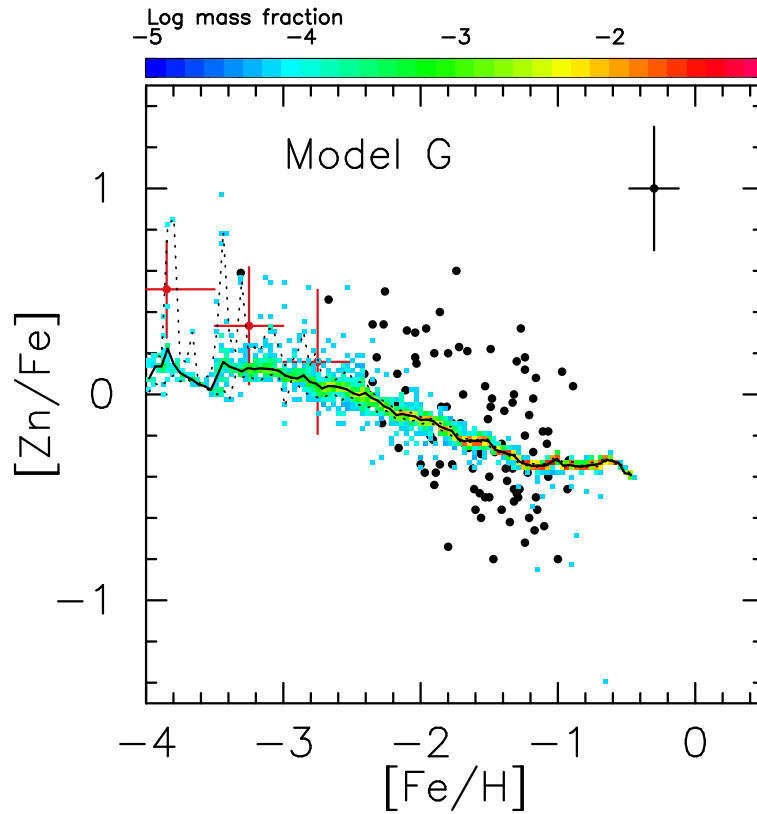


FIGURE 4.6: Same as Figure 4.5, but for $[Zn/Fe]$ as a function of $[Fe/H]$ in model G. Black dots denote observed values of Sculptor dSph (Shetrone et al., 2003; Geisler et al., 2005; Simon et al., 2015; Skúladóttir et al., 2015; Skúladóttir et al., 2017). Typical error bars of the observation (Skúladóttir et al., 2017) are shown in the top right corner of the figure. The red points show the average values of $[Zn/Fe]$ in the MW halo stars (Saito et al., 2009). The vertical error bars on red points indicate the difference between the maximum and minimum values of $[Zn/Fe]$ in each metallicity bin. The horizontal bars on red points represent the range of $[Fe/H]$ in each bin.

early epoch of galaxy evolution. As time passes, an increase of Fe by SNe as well as metal mixing reduces the fraction of gases with high $[\text{Zn}/\text{Fe}]$ values.

Figure 4.8 shows $[\text{Zn}/\text{Fe}]$ versus $[\text{Fe}/\text{H}]$ for the models H and I (Table 4.3) assuming different mass ranges of ECSN progenitors as well as HNe with $f_{\text{HN}} = 0.05$. As shown in this figure, both models tend to have stars with higher $[\text{Zn}/\text{Fe}]$ ratios at lower metallicities than those in model G (Figure 4.6) as a consequence of adopting wider range of progenitors of ECSNe than the stellar evolution models in Doherty et al. (2015). The fractions of ECSNe out of all CCSNe are 38.2 % and 6.9 % in models H and I, respectively (3.1 % in model G). Although the slope of $[\text{Zn}/\text{Fe}]$ is still shallower than that of the observation, the average values of $[\text{Zn}/\text{Fe}]$ are consistent with the observation in model I. These results suggest that the increasing trends of $[\text{Zn}/\text{Fe}]$ toward lower metallicity can be reproduced if the rates of ECSNe are higher in lower metallicity. The rates of ECSNe in low metallicity are determined by the mass range and lifetimes of progenitors of ECSNe. However, we cannot constrain the mass range of ECSNe in this model because there are large uncertainties in models of galaxies as well as of stellar evolution. Stripped-envelope stars in close binaries can be the progenitors of ECSNe (Tauris et al., 2013; Tauris, Langer, and Podsiadlowski, 2015; Moriya and Eldridge, 2016). The mass range for ECSNe in binary systems is predicted to be wider than that for single stars (Podsiadlowski et al., 2004a; Poelarends et al., 2017). Yoshida et al. (2017) suggest that ultra-stripped SNe synthesize large amounts of iron-peak elements. Wanajo et al. (2018) show that the SNe from the low-mass end of the progenitors with iron-cores can also synthesize Zn as large as that of ECSNe. In the case of chemodynamical simulations of galaxies, we currently treat star particles as SSPs, i.e., the yields produced by star particles are IMF weighted values of CCSNe, HNe, or ECSNe. Future chemodynamical simulations of galaxies that can resolve each star will make it possible to discuss the effects of different yields of individual SNe.

4.4.2 Enrichment of Zn at $[\text{Fe}/\text{H}] \gtrsim -2.5$

At higher metallicity, the MW halo, and dSphs have different trends of $[\text{Zn}/\text{Fe}]$ as a function of $[\text{Fe}/\text{H}]$ (Figure 1.9). Sculptor has increasing trends toward lower metallicity while the MW halo stars have constant $[\text{Zn}/\text{Fe}]$ ratios. Skúladóttir et al. (2017) imply that there are star-to-star scatters of $[\text{Zn}/\text{Fe}]$ in Sculptor at $[\text{Fe}/\text{H}] \gtrsim -1.8$. They show that several stars with the same metallicity have apparently different $[\text{Zn}/\text{Fe}]$ ratios. However, they cannot confirm these scatters of $[\text{Zn}/\text{Fe}]$ ratios because of their low signal-to-noise data. The scatters are mostly consistent with their error-bars.

For $-2.5 \lesssim [\text{Fe}/\text{H}] \lesssim -1.0$, the increasing contribution of SNe Ia makes the slope of $[\text{Zn}/\text{Fe}]$ steeper than that in lower metallicity. Since SNe Ia do not produce Zn, stars formed from the gas polluted by the ejecta of SNe Ia have low $[\text{Zn}/\text{Fe}]$ values. Scatters of $[\text{Zn}/\text{Fe}]$ values for $[\text{Fe}/\text{H}] \gtrsim -2$ reflect the inhomogeneity of $[\text{Zn}/\text{Fe}]$ abundances affected by SNe Ia. Stars with $[\text{Zn}/\text{Fe}] < -0.5$ are formed under substantial influence from the ejecta of SNe Ia. As shown in Figure 4.7b, all stars with $[\text{Zn}/\text{Fe}] < -0.5$ are formed within 4 Gyr from the beginning of the simulation.

Scatters of $[\text{Zn}/\text{Fe}]$ at $[\text{Fe}/\text{H}] \gtrsim -2.5$ are not different from those of α -elements in our models. Figure 4.9 shows standard deviations of $[\text{Mg}/\text{Fe}]$ and $[\text{Zn}/\text{Fe}]$ as a

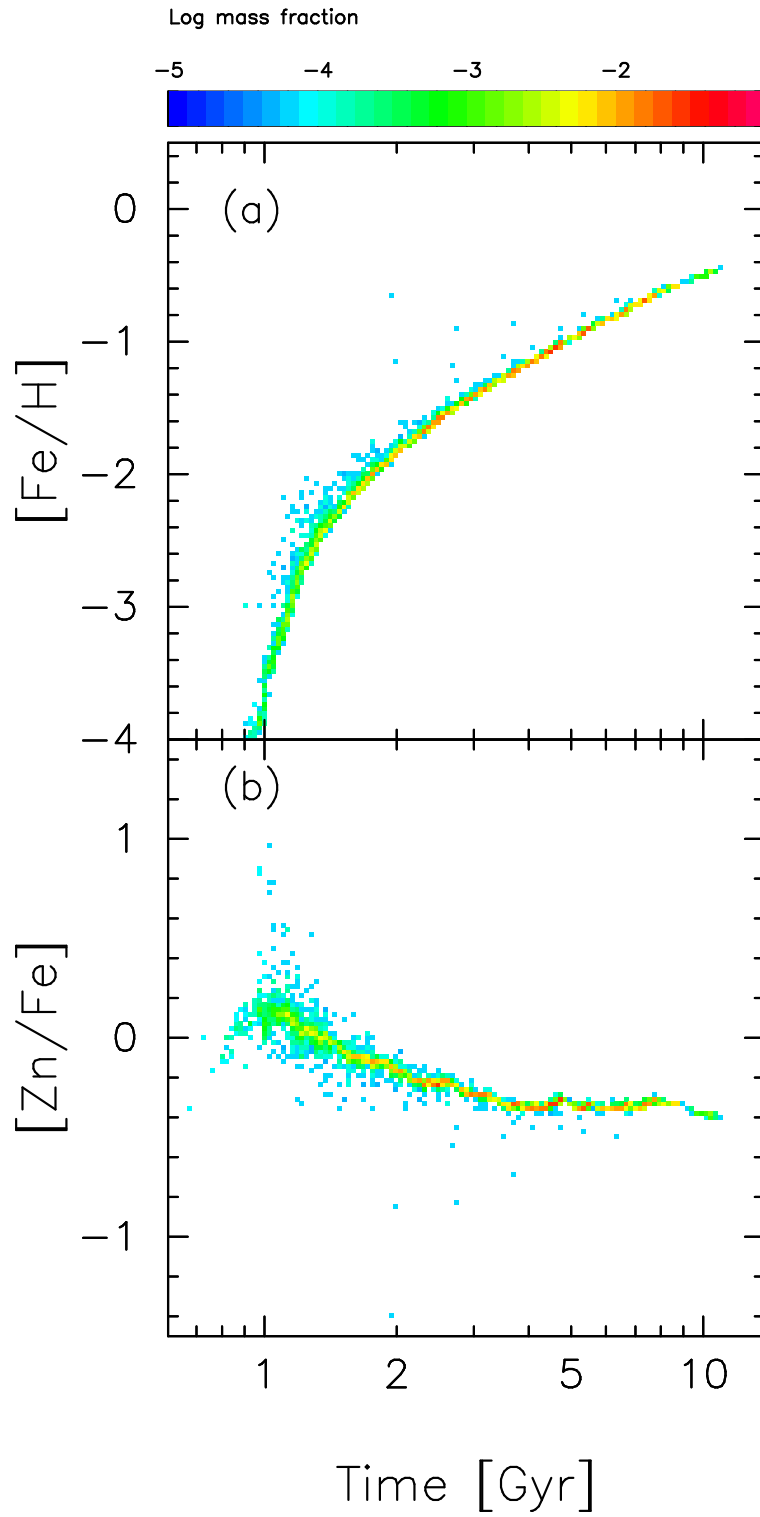


FIGURE 4.7: (a) $[\text{Fe}/\text{H}]$ and (b) $[\text{Zn}/\text{Fe}]$ as a function of time in model G. The color-coded stellar mass fractions are displayed in the logarithmic scale.

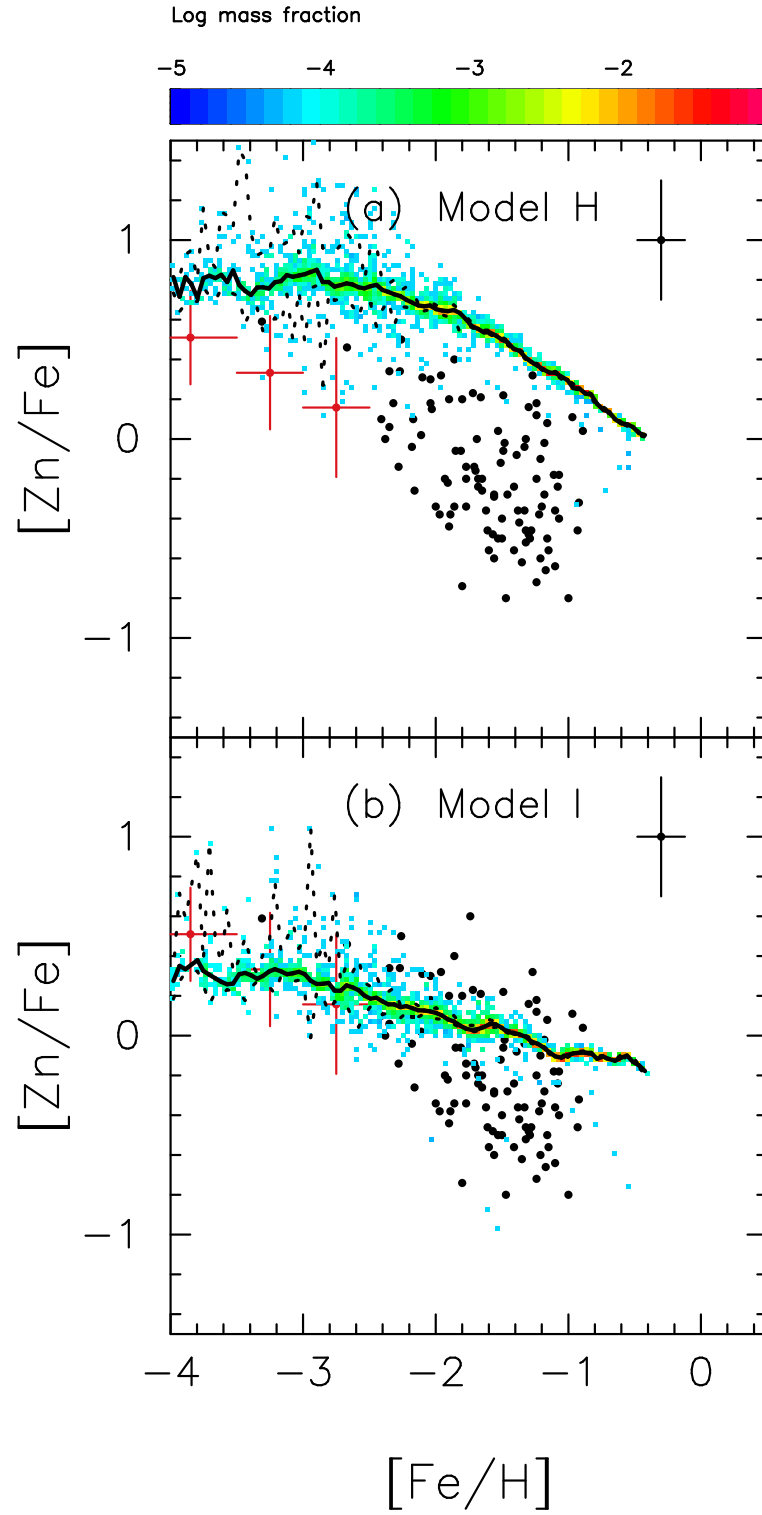


FIGURE 4.8: Same as Figure 4.6 but for (a) model H and (b) model I. Model H adopts the metallicity dependent mass range of ECSN progenitors computed by the stellar evolution model in Poelarends (2007). Model I assumes that stars from 8.5 to $9.0 M_{\odot}$ become ECSNe in all the metallicity range.

function of $[\text{Fe}/\text{H}]$. At $[\text{Fe}/\text{H}] > -2.5$, scatters of $[\text{Zn}/\text{Fe}]$ and $[\text{Mg}/\text{Fe}]$ almost overlap with each other. Larger scatters of $[\text{Zn}/\text{Fe}]$ than those of $[\text{Mg}/\text{Fe}]$ at $[\text{Fe}/\text{H}] \lesssim -2.5$ are caused by the ejection of Zn from ECSNe to the ISM that is still inhomogeneous in metallicity. This result suggests that scatters seen in Skúladóttir et al. (2017) are mostly caused by observational errors.

At $[\text{Fe}/\text{H}] \gtrsim -1$, most stars have $[\text{Zn}/\text{Fe}] \sim -0.4$ (Figure 4.6). This feature reflects the increase of the yield of Zn in CCSNe at higher metallicities (Figure 4.1). This increase of Zn yield is caused by the neutron-capture process during He and C burning at higher metallicity (Kobayashi et al., 2006).

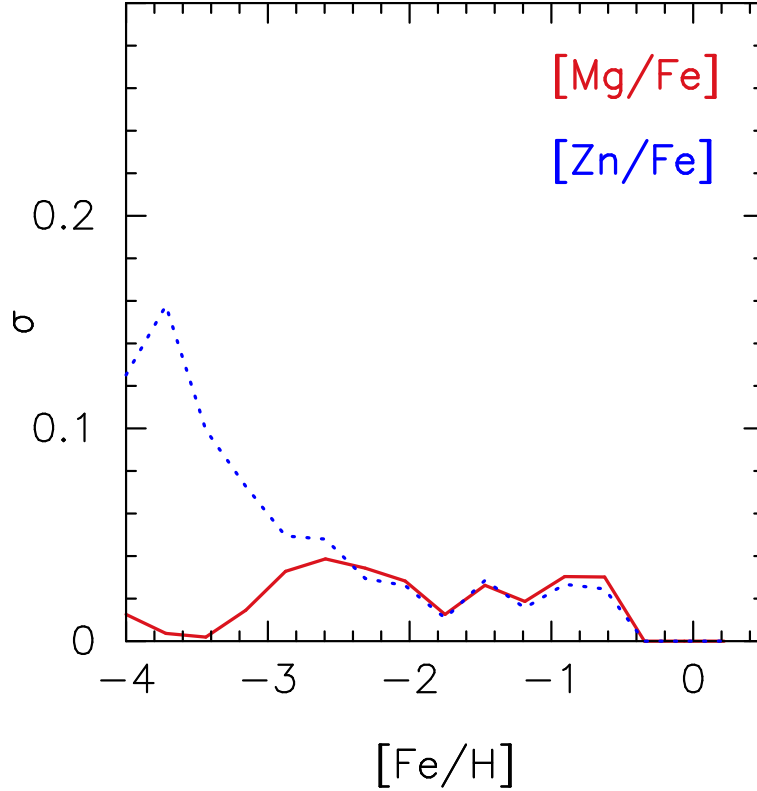


FIGURE 4.9: Standard deviations (σ) of $[\text{Mg}/\text{Fe}]$ (the red solid curve) and $[\text{Zn}/\text{Fe}]$ (the blue dotted curve) as a function of $[\text{Fe}/\text{H}]$ in model G.

4.4.3 Effects of ECSNe and HNe on the enrichment of Zn

In this chapter, we consider ECSNe, HNe, and normal CCSNe as the astrophysical sites of Zn. As shown in Figure 4.1, ECSNe and HNe have higher ratios of $[\text{Zn}/\text{Fe}]$ than those of normal CCSNe. This result means that ECSNe and HNe would have a significant impact on the enrichment of Zn. However, we do not know how these sites affect the enrichment of Zn in a galaxy. Rates of ECSNe and HNe are not well determined. This uncertainty would affect the enrichment history of Zn. Here we discuss how each expected source of Zn affects the enrichment of Zn in the galaxy.

Figure 4.10 shows $[\text{Zn}/\text{Fe}]$ as a function of $[\text{Fe}/\text{H}]$ for the models assuming that ECSNe do not contribute to the enrichment of Zn. Figure 4.10a represents the result of model J. The HN fraction for model J ($f_{\text{HN}} = 0.5$) is taken from Kobayashi et al.

(2006). According to Figure 4.10a, the $[\text{Zn}/\text{Fe}]$ ratios are flat at low metallicities. The observed stars with $[\text{Zn}/\text{Fe}] \gtrsim 0.5$ at $[\text{Fe}/\text{H}] \lesssim -2$ cannot be explained, which is consistent with the result in Kobayashi et al. (2006). Previous studies show that the increasing trend of the $[\text{Zn}/\text{Fe}]$ ratios toward low metallicity can be explained if the yields of individual SNe are reflected in the abundances of EMP stars (Umeda and Nomoto, 2002; Umeda and Nomoto, 2005; Tominaga, Umeda, and Nomoto, 2007). However, our results suggest that the metal mixing erases these signatures even at $[\text{Fe}/\text{H}] \sim -3$.

Figure 4.10b shows the $[\text{Zn}/\text{Fe}]$ ratios computed in model K. The HN fraction of model K ($f_{\text{HN}} = 0.05$) is taken to be consistent with the observed rate of long GRBs (Podsiadlowski et al., 2004b; Guetta and Della Valle, 2007). The $[\text{Zn}/\text{Fe}]$ ratios of all stars at $[\text{Fe}/\text{H}] \lesssim -3$ in this model are lower than those of the observation. This result suggests that if the rate of HNe is consistent with the observed rate of long GRBs, it is not possible to explain even the mean value of $[\text{Zn}/\text{Fe}]$ in EMP stars without another source of Zn such as ECSNe.

We also consider another possibility that HNe do not contribute to the enrichment of Zn. This is because nucleosynthesis of Zn in HNe highly depends on the model parameters such as a position of mass cut. Moreover, HNe alone cannot explain the solar isotopic abundances of Zn because they cannot synthesize enough Zn isotopes except for ^{64}Zn at low metallicity (e.g., Kobayashi et al., 2006; Kobayashi, Karakas, and Umeda, 2011) as discussed in Section 4.2.2.

Figure 4.11 represents the $[\text{Zn}/\text{Fe}]$ ratios computed by the models without HNe but with ECSNe. The values of $[\text{Zn}/\text{Fe}]$ for $[\text{Fe}/\text{H}] < -2.5$ in model L are lower than the observations. On the other hand, the values of $[\text{Zn}/\text{Fe}]$ for $[\text{Fe}/\text{H}] < -2.5$ in model M are high enough to be consistent with those in the observations. This difference is caused by the different rates of ECSNe in these models. The mass range of the progenitors of ECSNe in model L is $8.2 - 8.4 M_{\odot}$ at $Z = 0.0001$. The fraction of ECSNe from this mass range corresponds to 6.9 % of all CCSNe. Although the result is sensitive to the mass range of ECSNe in low metallicity, these results suggest that it is possible to explain the observed abundances of metal-poor stars without the contribution of HNe.

Astrophysical sites of Zn may be more tightly constrained by examining the enrichment of Sr and other trans-iron elements with Zn. Wanajo et al. (2018) show that not only Zn but also other light trans-iron elements from Zn to Zr are enhanced in the ejecta of ECSNe. We find that the model G predicts the stars with $[\text{Fe}/\text{H}] < -3$ having $[\text{Sr}/\text{Fe}] > -0.3$. On the other hand, the observations of LG galaxies show that 65 % of stars with $[\text{Zn}/\text{Fe}] > 0.5$ have $[\text{Sr}/\text{Fe}] > -0.3$ (SAGA database, Suda et al., 2008; Suda et al., 2011; Suda et al., 2017; Yamada et al., 2013). Aoki et al. (2017) report that there is a diversity of the abundances of light neutron-capture elements from Sr to Pd. They show that the nucleosynthesis models with different electron fractions (Wanajo, Janka, and Müller, 2011) or proto-neutron star masses (Wanajo, 2013) may explain such diversity. The *s*-process in fast-rotating massive stars may also cause a variation of $[\text{Sr}/\text{Fe}]$ ratios (e.g., Chiappini et al., 2011; Cescutti et al., 2013; Cescutti and Chiappini, 2014). We do not consider these possibilities in our simulations.

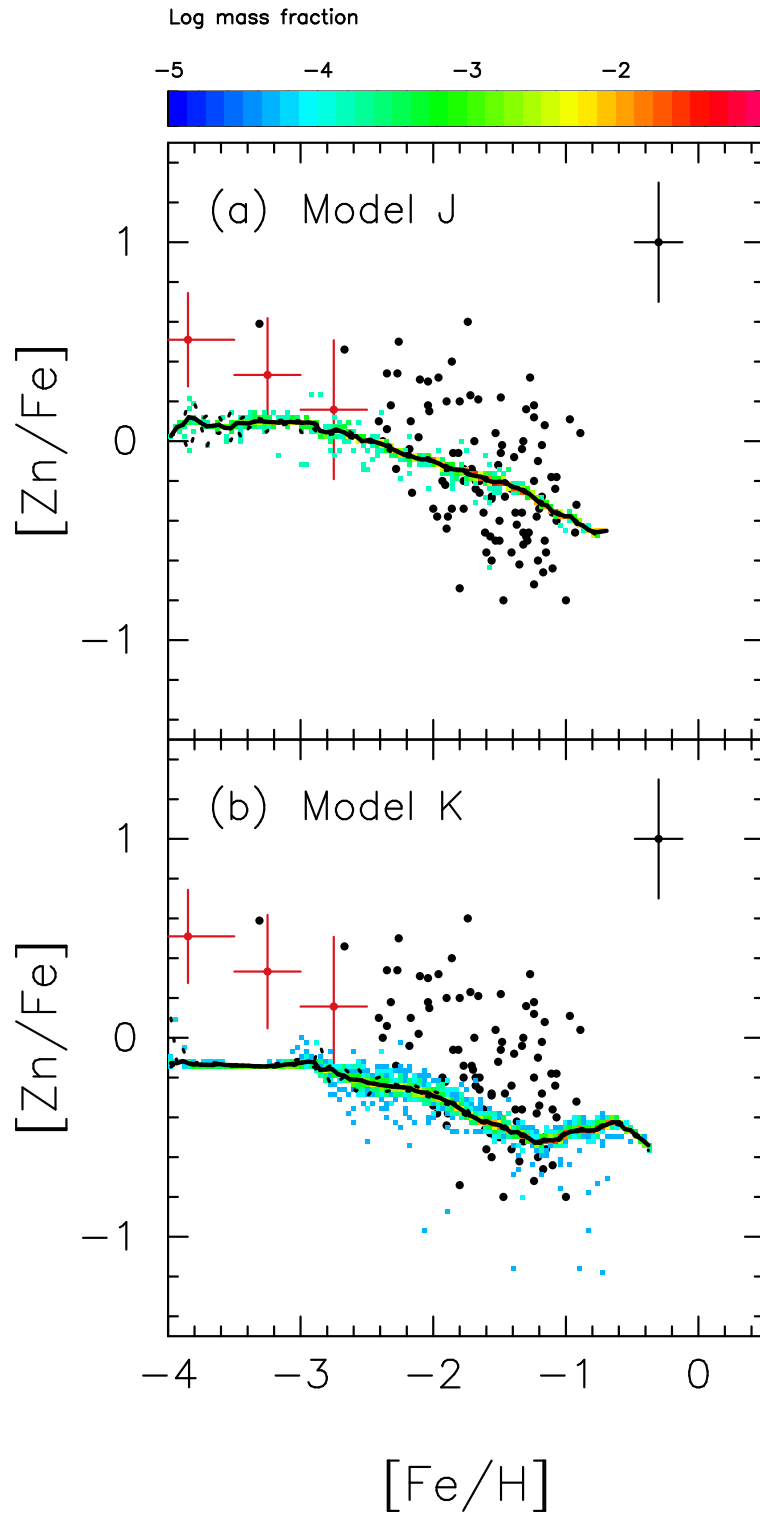


FIGURE 4.10: Same as Figure 4.6 but for the models without ECSNe. Panels (a) and (b) represent the models with $f_{HN} = 0.5$ and 0.05 (models J and K, respectively).

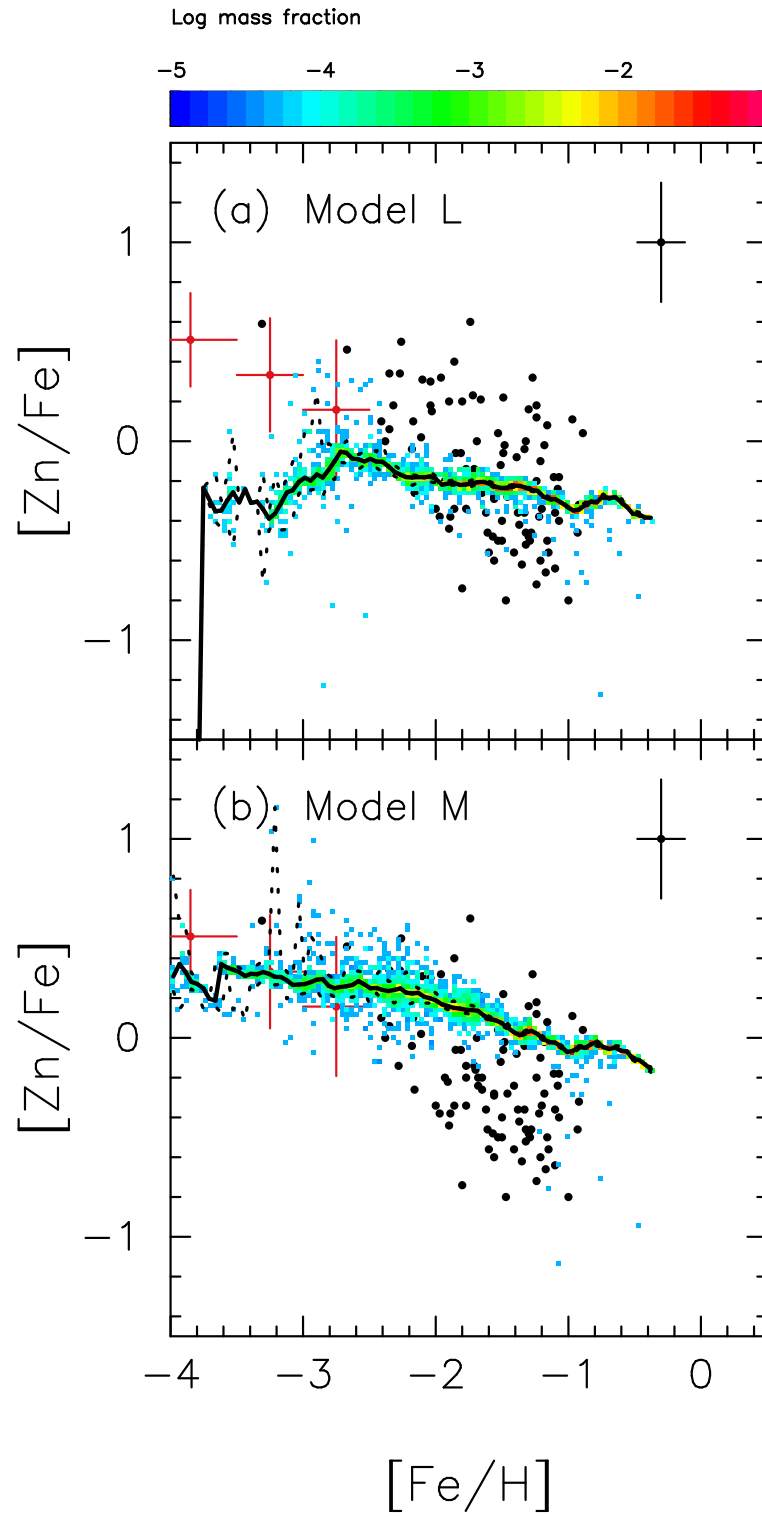


FIGURE 4.11: Same as Figure 4.6 but for the models without HNe. Panels (a) and (b) represent models L and M, respectively.

4.5 Summary

We studied the enrichment histories of Zn in dwarf galaxies using a series of high-resolution chemodynamical simulations. We newly considered ECSNe as sources of Zn. The final stellar mass of our model was $5 \times 10^6 M_{\odot}$. This model is comparable to the observed natures (stellar masses, metallicity distributions, and α -element evolutions) of LG dSphs such as the Sculptor and Leo I dSphs.

We found that stars with $[\text{Zn}/\text{Fe}] \gtrsim 0.5$ in our models reflected the nucleosynthetic abundances of ECSNe (Figure 4.6). In the early phase of galaxy evolution, gases with high $[\text{Zn}/\text{Fe}]$ ratios owing to ECSNe remained due to the inhomogeneity of spatial distribution of metallicity.

Our results suggest that scatters of $[\text{Zn}/\text{Fe}]$ in higher metallicities come from the contribution of SNe Ia. These stars were formed at $\lesssim 4$ Gyr from the beginning of the simulation (Figure 4.7). We found that the scatters of $[\text{Zn}/\text{Fe}]$ are consistent with the scatters of $[\text{Mg}/\text{Fe}]$ at $[\text{Fe}/\text{H}] \gtrsim -2.5$.

In this chapter, we examined the contribution from several astrophysical sources of Zn. If we do not take into account the contribution of ECSNe, we cannot reproduce stars with $[\text{Zn}/\text{Fe}] > 0.5$ (Figure 4.10). On the other hand, the observed trend of $[\text{Zn}/\text{Fe}]$ could be reproduced without assuming the production of Zn from HNe (Figure 4.11). These results suggest that ECSNe or low mass Fe CCSNe can be one of the contributors to the enrichment of Zn in galaxies.

Chapter 5

Efficiency of metal mixing in dwarf galaxies

This chapter uses heavy elements as an indicator of metal mixing in galaxies. Metal mixing plays critical roles in the enrichment of metals in galaxies. The abundance of elements such as Mg, Fe, Zn, and Ba in metal-poor stars help us understand the metal mixing in galaxies. However, the efficiency of metal mixing in galaxies is not yet understood. Here we report a series of N -body/SPH simulations of dwarf galaxies with different efficiencies of metal mixing using a turbulence-induced mixing model. We show that metal mixing apparently occurs in dwarf galaxies from Mg, Ba, and Zn abundance. We find that the scaling factor for metal diffusion larger than 0.01 is necessary to reproduce the observation of Ba abundance in dwarf galaxies. This value is consistent with the value expected from turbulence theory and experiments. We also find that timescale of metal mixing is less than 40 Myr. This timescale is shorter than that of typical dynamical times of dwarf galaxies. We demonstrate that the determination of a degree of scatters of Ba abundance by the observation will help us constrain the efficiency of metal mixing more precisely¹.

5.1 Review: Heavy elements as an indicator of metal mixing

Understanding metal mixing in galaxies could help us clarify various fields in astrophysics, such as galactic chemical evolution, turbulent diffusion in the ISM, and the mechanism for transition from Population III stars to Population II stars (e.g., Karlsson, Bromm, and Bland-Hawthorn, 2013). Metal mixing occurs on a wide range of scales, from SF regions (~ 10 pc) to large galactic scales (~ 10 kpc).

Interstellar turbulence is the main cause of metal mixing. Power sources of interstellar turbulence include SNe, HII regions, fluid instabilities, galactic rotation, and galactic interactions (e.g., Elmegreen and Scalo, 2004). Observations of power spectra of CO emission, H I emission, and absorption can be used to determine power-law slopes of the spectra that characterize the interstellar turbulence.

Elemental abundance ratios in metal-poor stars give us signatures to constrain metal mixing processes. Astronomical spectroscopic observations of EMP stars in

¹Contents in this chapter have been in part published in Hirai and Saitoh (2017) and Hirai, Saitoh, Ishimaru, and Wanajo (2018).

the LG galaxies have shown that star-to-star scatters of α -elements are less than 0.2 dex, which is comparable to the observational errors (e.g., Frebel and Norris, 2015).

On the other hand, r -process elements show scatters of over 3 dex in EMP stars in the MW halo (Figure 1.10). The scatters of r -process elements decrease as the metallicity increases. The LG dSphs show lower abundances of r -process elements than those of the MW halo. There are no very metal-poor stars with $[\text{Ba}/\text{Fe}] \gtrsim 1$ in dSphs (Frebel and Norris, 2015). Only the Reticulum II UFD has enhanced r -process abundance (Ji et al., 2016b; Roederer et al., 2016). These observational facts could provide evidence to constrain metal mixing in galaxies.

The different behaviors of the abundances of α - and r -process elements reflect the astrophysical sites of these elements. In the case of CCSNe, they synthesize both α -elements and iron (e.g., Nomoto, Kobayashi, and Tominaga, 2013). This means that inhomogeneity in the abundance of Fe and Mg is related in many cases, i.e., if Fe is high in a region, Mg is also high. The scatters of $[\alpha/\text{Fe}]$ in EMP stars are thus mainly determined by the yields of CCSNe. The scatters in the ratios of α -elements and iron are therefore only ~ 0.2 dex. On the other hand, although the astrophysical site of r -process elements is not yet well understood, NSMs are one of the most likely sites of r -process elements (e.g., Wanajo et al., 2014). In this case, r -process elements and iron are produced in a different site. This means that the ratio of r -process elements and iron easily reflects the inhomogeneity of these elements (Chapter 3). Lower abundances of r -process elements in dSphs suggest that the metal mixing was efficient in these galaxies.

Previous hydrodynamic simulations have shown that metal mixing significantly affects the metal content in galaxies. Shen, Wadsley, and Stinson (2010) introduced a metal diffusion model in their SPH simulations, following Smagorinsky (1963). Their results suggest that metal diffusion increases the metal content of gas in galaxies and decreases it in the intergalactic medium. Revaz et al. (2016) systematically studied the scatters of α -elements with different parameters. They showed that metal mixing is required to reduce the scatters of α -elements in particle-based simulations. Williamson, Martel, and Kawata (2016) studied the effects of different metal diffusion strengths. They found that a stronger diffusion produces a tighter $[\text{O}/\text{Fe}]$ versus $[\text{Fe}/\text{H}]$. They also found that the efficiency of metal mixing does not strongly affect stellar metallicity distribution.

However, the efficiency of metal mixing is not yet understood. Revaz et al. (2016) pointed out that the scaling factor for their metal diffusion of 10^{-3} reproduces the low scatters of α -elements in dSphs, but more efficient mixing is required to reproduce that of a MW-like galaxy. Low scatters of α -elements (~ 0.2 dex) make it difficult to constrain the efficiency of metal mixing. This value is comparable to the observational errors. We need additional signatures to constrain the efficiency of metal mixing.

The aim of this chapter is to constrain the metal mixing through a series of hydrodynamic simulations of galaxies and abundances of r - and α -elements. We study metal mixing in dSphs. They are the ideal site to study metal mixing because of their simple structures (e.g., Lee et al., 2013; Bland-Hawthorn, Sutherland, and Webster, 2015). In this chapter, we examine how the metal mixing affects the chemical abundance in dSphs.

5.2 Metal diffusion models

Here we adopt metal diffusion models for gas particles instead of adopting simple metal mixing models described in Section 2.2.3. For metal diffusion, we have implemented a turbulent metal mixing model in DISPH (Saitoh, 2017), based on Smagorinsky (1963) and Shen, Wadsley, and Stinson (2010). The k th element in i th gas particle $Z_{k,i}$, diffuses to surrounding gas particles with

$$\frac{dZ_{k,i}}{dt} = - \sum_j \frac{m_i}{(\rho_i + \rho_j)/2} \frac{4D_i D_j}{(D_i + D_j)} \frac{(Z_{k,i} - Z_{k,j})}{|r_{ij}|^2} \mathbf{r}_{ij} \cdot \nabla W_{ij}, \quad (5.1)$$

$$\hat{S}_{ab,i} = \frac{1}{q_i} \sum_j U_j (v_{b,i} - v_{a,j}) \nabla_a W_{ij}, \quad (5.2)$$

$$S_{ab,i} = \frac{1}{2} (\hat{S}_{ab,i} + \hat{S}_{ba,i}) - \delta_{ab} \frac{1}{3} \text{Trace } \hat{S}_{ab,i}, \quad (5.3)$$

$$D_i = C_d |S_{ab,i}| h_i^2, \quad (5.4)$$

where a and b are the direction of x , y , and z axes, δ_{ab} is the Kronecker's delta, U_i is the internal energy, and q_i is the energy density defined by

$$q_i = \sum_j U_j W_{ij}. \quad (5.5)$$

Here we changed C_d to compute models with different efficiency of metal mixing.

5.3 Results

We adopt an isolated dwarf galaxy model such as those in Chapters 2–4. We take the same structural parameters in Chapter 4. The initial total number of particles and the gravitational softening length are 2^{18} and 7.8 pc, respectively. The total mass of halo is $7 \times 10^8 M_\odot$. The final stellar mass of our model is $5 \times 10^6 M_\odot$, which is similar to those of the Sculptor and Leo I dSphs (McConnachie, 2012). We have confirmed that changing the resolution of the simulation does not strongly affect the results. Table 5.1 lists adopted values of C_d .

TABLE 5.1: Adopted value of the scaling factor for metal diffusion.

Model	C_d
d1000	0.1
d0100	0.01
d0010	0.001
d0001	0.0001
d0000	

The first column shows the name of models. The second column shows the value of the scaling factor for metal diffusion.

Figure 5.1 shows $[\text{Mg}/\text{Fe}]$ as a function of $[\text{Fe}/\text{H}]$. Computed scatters of $[\text{Mg}/\text{Fe}]$ lie within the observed scatters at $[\text{Fe}/\text{H}] < -2$ when we implement the metal mixing (Figure 5.1a–d). On the other hand, model d0000 has several stars with $[\text{Mg}/\text{Fe}] > 1$ or $[\text{Mg}/\text{Fe}] < -1$ at $[\text{Fe}/\text{H}] \lesssim -2.5$ (red hatched area in Figure 5.1f). These stars have not been reported in the observation. In the SPH scheme, the abundance of metals in each SPH particle cannot diffuse to the surrounding gas particles if we do not implement metal mixing. Model d0000 forms these stars with an artificial effect. These results indicate that we need to implement the metal mixing model in SPH simulations when we discuss the scatters of elemental abundance ratios.

However, it is difficult to constrain the efficiency of metal mixing when only using the $[\text{Mg}/\text{Fe}]$ ratio. All models with metal mixing show a smaller dispersion of $[\text{Mg}/\text{Fe}]$ than that of the observation at $[\text{Fe}/\text{H}] < -2$. Models d0010 and d0001 seem to reproduce the sub-solar $[\text{Mg}/\text{Fe}]$ ratio seen in $[\text{Fe}/\text{H}] > -2$, but the statistical and observational errors of these stars typically have over 0.5 dex. We cannot conclude that models d0010 and d0001 are superior to models d1000 and d0100.

In the case of $[\text{Ba}/\text{Fe}]$, the metal mixing is expected to be more important than $[\text{Mg}/\text{Fe}]$ because $[\text{Ba}/\text{Fe}]$ shows large scatters in $[\text{Fe}/\text{H}] \lesssim -3$. Figure 5.2 shows $[\text{Ba}/\text{Fe}]$ as a function of $[\text{Fe}/\text{H}]$. As shown in Figure 5.2, the difference of the efficiency of metal mixing alters the scatters of $[\text{Ba}/\text{Fe}]$ significantly. Models with $C_d \leq 0.001$ produce stars with $[\text{Ba}/\text{Fe}] > 1$ (Figure 5.2 c–e). These stars are located in the red hatched area in Figure 5.2f, i.e., they are not reported in the observation. On the other hand, models d1000 and d0100 do not have stars with $[\text{Ba}/\text{Fe}] > 1$ due to efficient metal mixing. This result is consistent with the observation that shows no stars with $[\text{Ba}/\text{Fe}] > 1$ at $[\text{Fe}/\text{H}] < -2.5$.

The value of C_d controls the fraction of stars that highly deviate from the average value of metallicity. Models with the higher value of C_d form a larger fraction of stars around average values of metallicity in each epoch. This effect can be seen in Figure 5.2. Ba abundance first appears at $[\text{Fe}/\text{H}] \sim -3$ in models with high values of C_d (Figure 5.2a, b, and c). This metallicity reflects the average value of $[\text{Fe}/\text{H}]$ at the time the first NSM occurs. Note that the different ranges of $[\text{Fe}/\text{H}]$ between Figures 5.1 and 5.2 reflect the delayed production of Ba due to the long merger times of NSMs.

Abundances of Zn in metal-poor stars will be another indicator to constrain the efficiency of metal mixing. Here we discuss the effect of metal mixing on the enrichment of Zn. Figure 5.3 shows $[\text{Zn}/\text{Fe}]$ versus $[\text{Fe}/\text{H}]$ computed for the models with different efficiencies of metal mixing. Figure 5.3a represents the result of model d0010. This model adopts a ten times lower value of diffusion coefficient of metal mixing (C_d) than that of model d0100. Due to the lower efficiency of metal mixing, model d0010 tends to have a larger fraction of stars with $[\text{Zn}/\text{Fe}] > 0.5$ in EMP stars than other models do. Also, scatters of $[\text{Zn}/\text{Fe}]$ for $[\text{Fe}/\text{H}] > -2$ are more clearly seen in model d0010. Figure 5.3b denotes the result of model d1000. This model has smaller scatters of $[\text{Zn}/\text{Fe}]$ in $[\text{Fe}/\text{H}] \lesssim -3$ than those of models d0100 and d0010. According to these results, models with the value of $C_d \sim 0.001$ to 0.1 do not significantly deviate from the observed abundances of Zn.

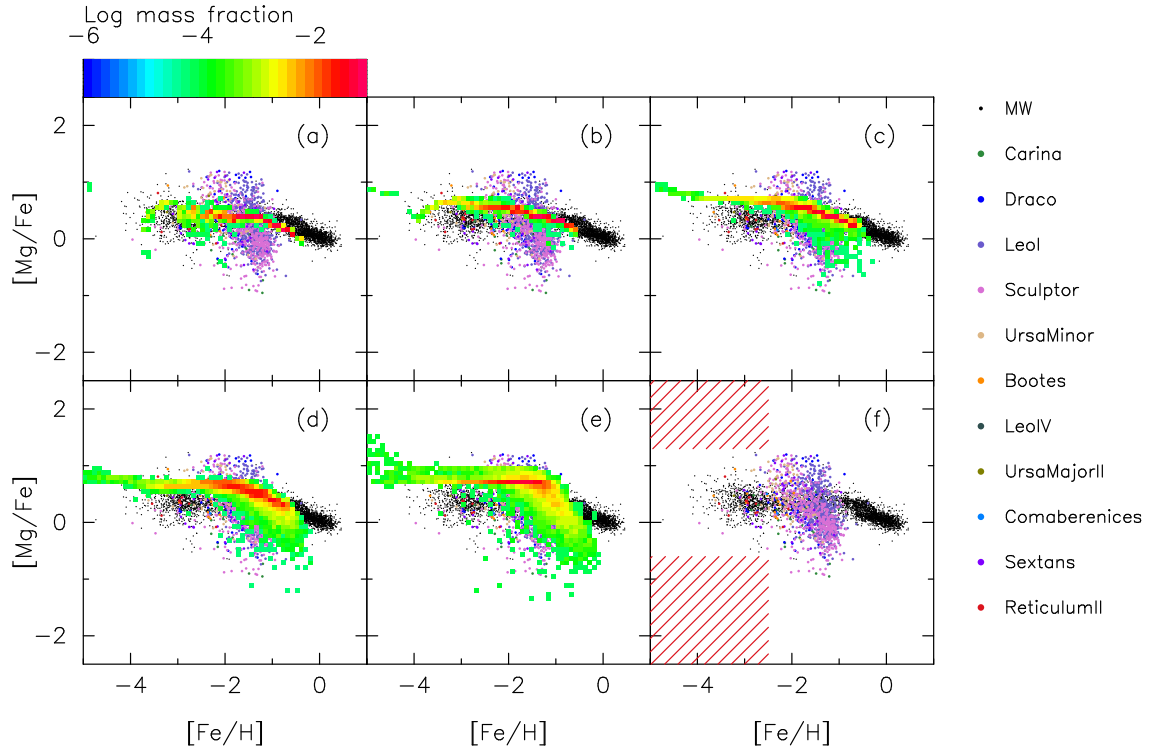


FIGURE 5.1: Stellar $[Mg/Fe]$ as a function of $[Fe/H]$. Panels (a), (b), (c), (d), and (e) represent the results of models d1000, d0100, d0010, d0001, and d0000, respectively. Panel (f) represents observational data. The red hatched area shows the region that there are no stars with Mg. Color contours show computed stellar abundances in the logarithm of a mass fraction in each grid. The black dots represent the observed abundances of the MW. The colored dots represent the observed abundances of the LG dwarf galaxies (green: Carina, blue: Draco, purple: LeoI, magenta: Sculptor, ocher: Ursa Minor, orange: Boötes I, dark green: Leo IV, grass green: Ursa Major II, sky-blue: Coma Berenices, red-purple: Sextans, and red: Reticulum II). We compile all observed data using the SAGA database (Suda et al., 2008; Suda et al., 2011; Suda et al., 2014; Yamada et al., 2013).

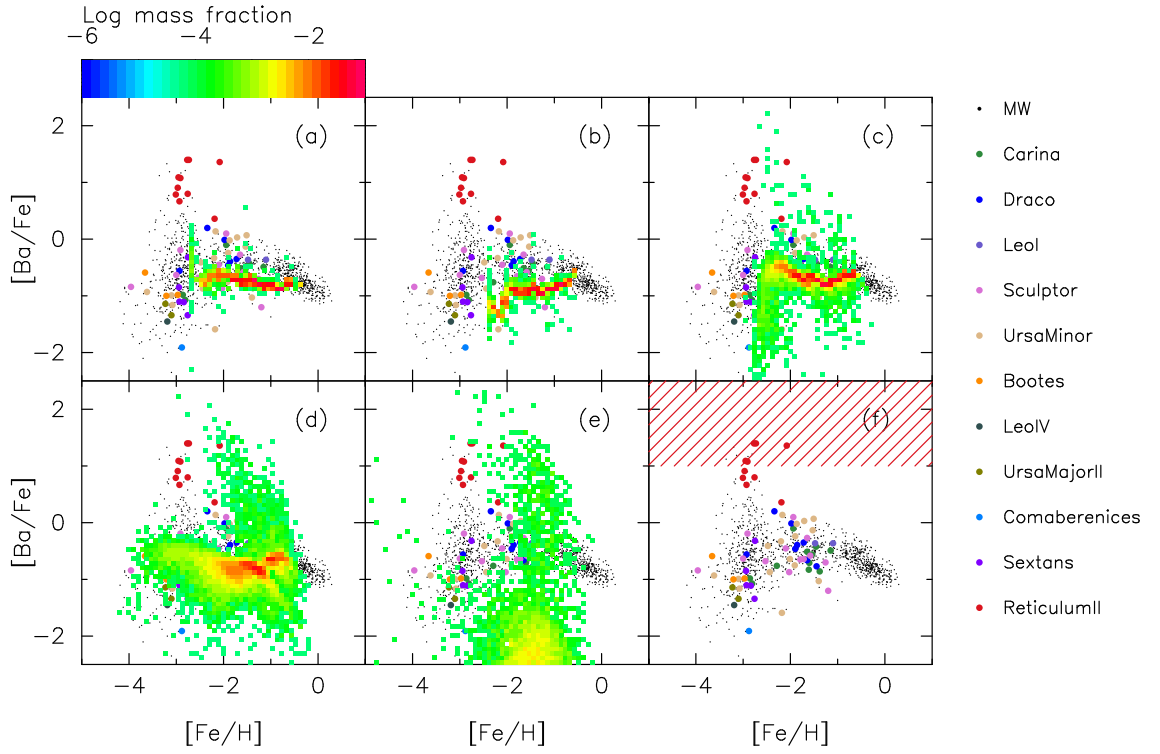


FIGURE 5.2: Stellar $[\text{Ba}/\text{Fe}]$ as a function of $[\text{Fe}/\text{H}]$. Panels (a), (b), (c), (d), and (e) represent the results of models d1000, d0100, d0010, d0001, and d0000, respectively. Panel (f) represents observational data. The red hatched area shows the region in which there are no stars with Ba in dSphs except for the Reticulum II UFD. The symbols are the same as in Figure 5.1. We correct the observational value of $[\text{Ba}/\text{Eu}]$ to be -0.89 for all stars with $[\text{Fe}/\text{H}] > -2.75$. We compile all observed data using the SAGA database (Suda et al., 2008; Suda et al., 2011; Suda et al., 2014; Yamada et al., 2013).

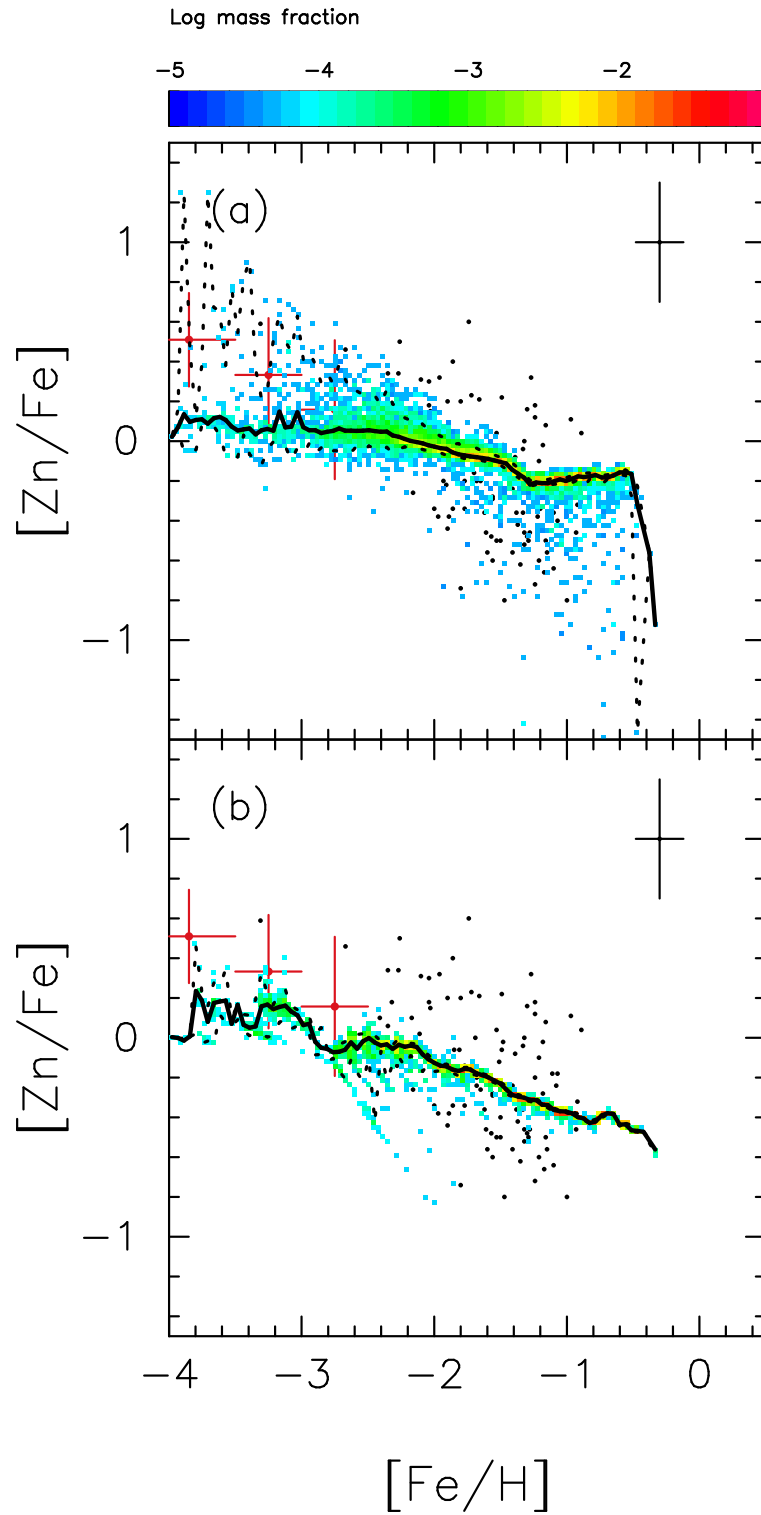


FIGURE 5.3: Same as Figure 4.6 but for the different efficiencies of metal mixing. Panels (a) and (b) show models d0010 ($C_d = 0.001$) and d1000 ($C_d = 0.1$), respectively.

5.4 Discussion

In the last section, we show that the value of $C_d \gtrsim 0.01$ is necessary to prevent the formation of stars with $[\text{Ba}/\text{Fe}] \gtrsim 1$ in dSphs. This result suggests that the formation of these stars, which does not occur in the LG dSphs, is strongly related to the efficiency of metal mixing. When NSMs occur in a galaxy, some surrounding gas will have the value of $[\text{Ba}/\text{Fe}] \gtrsim 1$. This gas mixes into gas with a lower r -process abundance. Stars with high r -process abundance are only formed when gas with a high r -process abundance remains in a galaxy. This means that the timescale of metal mixing plays a critical role in forming these stars.

Here we compute the average time that the gas with $[\text{Ba}/\text{Fe}] > 1$ becomes less than $[\text{Ba}/\text{Fe}] < 0$ (hereafter we define this time as t_{mix}). We find that models d1000 and d0100 have $t_{\text{mix}} \lesssim 10$ and ≈ 40 Myr, respectively². These values are smaller than the dynamical time of the system (~ 100 Myr), which determines the early star formation rate in a galaxy (Chapter 3). On the other hand, models d0010 and d0001 have $t_{\text{mix}} \approx 360$ Myr and 1.6 Gyr, respectively. These results suggest that the r -process elements are mixed with a shorter timescale than the timescale of SF in galaxies.

Stars with high r -process abundance are only formed in UFDs with an initial gas mass with $\sim 10^6 M_\odot$ (Ji et al., 2016b). In these galaxies, even if all metals are mixed in a whole galaxy, the gas mass is not enough to prevent the formation of r -process enhanced stars. These results imply that r -process enhanced stars in the MW halo originate from UFDs accreted to the MW halo.

In this chapter, we adopt the isolated dwarf galaxy model. According to the cosmological hydrodynamic simulations of Jeon, Besla, and Bromm (2017), the lowest metallicity stars are formed in external enriched halos that are accreted later in the main halo. If we consider a fully cosmological structure formation, lower-metallicity stars formed by external enrichment would be seen such as in Figure 5.2a, b, and c. We expect that these external enriched stars have a low $[\text{Ba}/\text{Fe}]$ value, as well as a low $[\text{Fe}/\text{H}]$ value, because both Fe and Ba will be well diluted in the ISM when they reach the subhalo around the main halo. These stars may account for observed stars with $[\text{Fe}/\text{H}] < -3.5$ and $[\text{Ba}/\text{Fe}] < 0.0$ plotted in Figure 5.2.

The diffusion coefficient inferred from the Ba abundance is consistent with the theoretical and experimental values. If we assume a Kolmogorov constant as 1.41, the value of C_d is 0.0324 (e.g., Meneveau and Katz, 2000). In the case of a turbulent mixing layer and a turbulent channel flow, optimal values of C_d are 0.0225 and 0.01, respectively (Horiuti, 1987). Although the Smagorinsky model has the problem that the coefficient may depend on the flow field, our results can be an independent check on the Smagorinsky model regarding metal mixing in galaxies.

The metal mixing efficiency of models with $C_d \gtrsim 0.01$ are also consistent with the models of Ji, Frebel, and Bromm (2015). They find that signatures from Population III stars are efficiently wiped out by Population II supernovae. Their adopted diffusion coefficients are $2.4 \times 10^{-5} \text{ kpc}^2 \text{ Myr}^{-1}$ and $8.1 \times 10^{-4} \text{ kpc}^2 \text{ Myr}^{-1}$ for their mini-halo and atomic cooling halo models, respectively. The average diffusion coefficients calculated following Equation (5.4) at 1 Gyr from the beginning of our simulation are $2 \times 10^{-4} \text{ kpc}^2 \text{ Myr}^{-1}$ and $2 \times 10^{-5} \text{ kpc}^2 \text{ Myr}^{-1}$ for models d1000 and d0100,

²We cannot compute times less than 10 Myr because the time interval of the snapshots in this simulation is 10 Myr.

respectively. This result means that we can draw conclusions similar to those of Ji, Frebel, and Bromm (2015) if we adopt the metal mixing parameter of $C_d \gtrsim 0.01$.

In this study, we adopt the metal diffusion model of Shen, Wadsley, and Stinson (2010). Greif et al. (2009) also constructed a metal diffusion model. They used velocity dispersion to determine the diffusion coefficient. Williamson, Martel, and Kawata (2016) compared the difference between the diffusion model of Greif et al. (2009) and Shen, Wadsley, and Stinson (2010). They found that the diffusion coefficient computed in Greif et al. (2009) is about twice as large as that of Shen, Wadsley, and Stinson (2010). They also found that the gas properties do not depend on the method for calculating the diffusion coefficient. We confirm that adopting the diffusion model of Greif et al. (2009) yields almost the same results as the results presented in this chapter.

In this chapter, we treat ejecta of SNe and NSMs the same way. On the other hand, the ejecta from NSMs would expand to a larger region than those of SNe because compared to SNe, NSMs eject materials at higher speeds ($\sim 0.1c$) (Tsujimoto and Shigeyama, 2014). Tsujimoto, Yokoyama, and Bekki (2017) estimated that the mass of interstellar materials mixed by ejecta from NSMs is $\sim 3.5 \times 10^6 M_\odot$, which is 100 times larger than that of SNe. In this case, fewer stars with an extremely high abundance of r -process elements would be formed.

To more precisely constrain the efficiency of metal mixing, we need to observe a greater number of metal-poor stars in dSphs. It is important to determine the degree of scatter in the abundance of r -process elements to constrain the efficiency of metal mixing. Additionally, we find that the fraction of EMP stars is smaller in models with more efficient metal mixing. Although several EMP stars were recently reported in UFDs, Helmi et al. (2006) reported that a lack of EMP stars in dSphs. This result could be related to the efficiency of metal mixing. We expect that the fraction of EMP stars in each dSph could also be an indicator of the efficiency of metal mixing.

5.5 Summary

In this chapter, we performed a series of N -body/SPH simulations of dwarf galaxies with a turbulence motivated metal diffusion model. We find that the scaling factor for metal diffusion larger than 0.01 is necessary to reproduce the observation of abundances of r -process elements and Zn in dwarf galaxies. This value is consistent with the value expected from turbulence theory and experiment. We also find that the timescale of metal mixing is less than 40 Myr. This timescale is shorter than that of typical dynamical times of dwarf galaxies. These results mean that the value of $C_d \sim 0.01$ appears to be suitable for SPH simulations of galaxies if we adopt the shear-based metal-diffusion model (Shen, Wadsley, and Stinson, [2010](#); Saitoh, [2017](#)).

Chapter 6

Enrichment of r -process elements in a cosmological context

This chapter connects the enrichment of r -process elements to the formation of LG galaxies. Enrichment of r -process elements is associated with galaxy formation. In the hierarchical structure formation scenario, galaxies are thought to be formed by clustering of smaller systems. Star-to-star scatters of the ratios of r -process elements in the MW halo should be reflected such process. However, the enrichment of r -process elements in a cosmological context is not yet understood. Here we performed a series of high-resolution cosmological zoom-in simulations of galaxies with halo mass of $10^{10} M_{\odot}$ at redshift 2. We find that most of the EMP stars are formed before 1 Gyr from the beginning of the simulation. In the simulations, there are three r -process rich EMP stars. All of these stars are formed in the halo with a gas mass of $10^6 M_{\odot}$ at the early stages of galaxy formation. This result suggests that r -process rich stars seen in the MW halo come from small size halos with the mass comparable to the LG UFDs.

6.1 Review: Enrichment of r -process elements and galaxy formation

Abundances of r -process elements in metal-poor stars help us understand the early stages of the MW halo formation. Astronomical high-dispersion spectroscopic observations have shown that there are star-to-star scatters of over 3 dex in the MW halo at $[\text{Fe}/\text{H}] \leq -2.5$ (e.g., Frebel and Norris, 2015). Beers and Christlieb (2005) classified r -process rich stars. According to their classification, stars with $0.3 \leq [\text{Eu}/\text{Fe}] \leq 1.0$ and $[\text{Ba}/\text{Eu}] < 0$ are called r-I stars. On the other hand, stars with $[\text{Eu}/\text{Fe}] > 1.0$ and $[\text{Ba}/\text{Eu}] < 0$ are r-II stars. As shown in Figure 1.10, r-II stars have not found in the LG dSphs. Ji et al. (2016b) discovered seven r-II stars in Reticulum II UFD. Roederer et al. (2016) also found two r-II stars in their sample of Reticulum II. Another UFDs have depleted abundances of r -process elements (e.g., Frebel and Norris, 2015).

The most promising astrophysical sites of r -process elements are NSMs. Nucleosynthetic studies have shown that NSMs can synthesize r -process elements heavier than $A = 110$ (e.g., Freiburghaus, Rosswog, and Thielemann, 1999; Goriely, Bauswein, and Janka, 2011; Korobkin et al., 2012; Bauswein, Goriely, and Janka, 2013; Rosswog et al., 2014; Wanajo et al., 2014). The existence of NSMs is confirmed by the detection of gravitational waves and multi-messenger observations of

an NSM, GW170817 (e.g., Abbott et al., 2017b; Abbott et al., 2017c). The optical and infrared afterglow of GW170817 suggested that they produced $\approx 0.03 M_{\odot}$ of r -process elements (e.g., Utsumi et al., 2017; Tanaka et al., 2017).

Chemical evolution studies taking into account the hierarchical structure formation scenario successfully explained the observed r -process abundances in the MW by NSMs. Ishimaru, Wanajo, and Prantzos (2015) found that the [Eu/Fe] ratio increases at lower metallicity in halos with smaller SFEs in their one-zone chemical evolution model. In Chapter 2 and 3, we have shown that r -process abundances in these halos are consistent with observation because their SFRs are suppressed by SN feedback, resulting in slow chemical evolution. Komiya and Shigeyama (2016) showed that the ejecta from NSMs can enrich intergalactic medium by their semi-analytic models.

Previous cosmological hydrodynamic simulations also showed that there are good agreements between simulated results and observations of r -process abundances in the MW halo. Shen et al. (2015) reported that their results are insensitive to the merger rate and delay time distributions. van de Voort et al. (2015) showed that metal-poor stars with r -process elements are formed in high redshift and large galactocentric radius. However, their resolution is not enough to resolve the scale of satellite dwarf galaxies. Ojima et al. (2017) showed that r-II stars would come from accreted halos with the mass similar to observed UFDs based on the model of Ishimaru, Wanajo, and Prantzos (2015). It thus needs to perform simulations that can resolve the scale of satellite dwarf galaxies.

In this chapter, we aim to discuss the enrichment of r -process elements in a cosmological context with high-resolution cosmological zoom-in simulations. In Section 6.2, we describe our code and cosmological zoom-in simulations. In Section 6.3, we show the results of our simulations. In Section 6.4, we discuss the formation site of r-II stars.

6.2 Cosmological zoom-in simulations

We have performed a series of cosmological “zoom-in” simulations. A preflight low-resolution cosmological N -body simulation is performed with GADGET-2 (Springel, 2005). We adopt the Λ CDM cosmology with a total matter density $\Omega_m = 0.308$, a dark energy density $\Omega_{\Lambda} = 0.692$, a baryon density $\Omega_b = 0.0484$, a Hubble constant $H_0 = 67.8 \text{ km s}^{-1}$, an amplitude of the matter power spectrum $\sigma_8 = 0.815 \text{ km s}^{-1}$, and a tilted scalar spectral index $n_s = 0.968$ (Planck Collaboration et al., 2016). The initial condition is generated by MUSIC using second-order Lagrangian perturbation theory (Hahn and Abel, 2011). The box size is $(4.0 h^{-1} \text{ Mpc})^3$ with 256^3 particles. Mass of one dark matter particle is $3.3 \times 10^5 M_{\odot}$. The gravitational softening length is $625 h^{-1} \text{ pc}$. The initial redshift of this simulation is $z_i = 100$.

We then select the halo-of-interest from the snapshot at $z = 0$ of the preflight simulation. For halo find, we use the AMIGA Halo Finder (AHF; Gill, Knebe, and Gibson, 2004; Knollmann and Knebe, 2009). We have selected a halo with total mass of $2.72 \times 10^{10} M_{\odot}$ at $z = 0$. This halo mass is smaller than that of the MW and larger than those of dSphs. Ideally, we should compute the MW-mass halos. However, it is difficult to compute such halos with sufficient resolution to resolve satellite dwarf galaxies. We thus chose the halo with $10^{10} M_{\odot}$ with small box size. The zoomed-in initial condition is generated by MUSIC. The cuboid Lagrangian

volume for re-simulation is carefully selected to avoid contamination of low-resolution particles.

After selecting the halos, we performed a series of cosmological zoom-in simulations using ASURA (Saitoh et al., 2008; Saitoh et al., 2009) described in Section 1.4. A symmetrized form of the softened gravitational potential is adopted to deal with systems which have particles with different gravitational softening lengths (Saitoh and Makino, 2012). The effective resolutions of zoomed regions are 512^3 particles. The total number of particles in the zoomed-in region is 2.51×10^6 . We set gravitational softening lengths for gas and dark matter particles 20 and 50 pc, respectively. Masses of one gas and dark matter particles are $6.4 \times 10^3 M_\odot$ and $3.4 \times 10^4 M_\odot$, respectively.

6.3 Results

In this section, we show the result at $z = 2.0$ because this halo experience a major merger at $z = 1.0$, which is not thought to occur in the MW halo. We confirm that most of the EMP stars are formed at $z > 2.0$ in this simulation. The central halo mass at $z = 2.0$ is $M_{\text{tot}} = 1.4 \times 10^{10} M_\odot$. Throughout this chapter, we define M_{tot} as the virial mass of halos.

Figure 6.1 shows stellar and gas surface density at $z = 2.0$. As shown in this figure, a spiral galaxy is formed in this simulation. The stellar mass and gas mass are $1.4 \times 10^9 M_\odot$ and $3.3 \times 10^8 M_\odot$, respectively. The stellar mass to halo mass ratio is $M_*/M_{\text{tot}} = 0.1$. This value is larger than that estimated from the abundance matching ($M_*/M_{\text{tot}} = 0.002$; Behroozi, Wechsler, and Conroy, 2013). This is because we only assume a thermal form of SN feedback. This result suggests that another form of feedbacks such as radiation pressure from massive stars (Hopkins, Quataert, and Murray, 2011) and kinetic form of SN feedback (Okamoto et al., 2005) to reproduce the stellar to halo mass ratio.

Figure 6.2 shows SFRs of the central galaxy within 30 kpc from the galactic center. The SFR at $t < 0.6$ Gyr is dominated by metal-poor stars with $[\text{Fe}/\text{H}] \leq -1$. According to this figure, most EMP stars ($[\text{Fe}/\text{H}] \leq -3$, orange curve) are formed at $t < 1.0$ Gyr from the beginning of the simulation. A peak of the SFR at 1.67 Gyr is due to a merger of a galaxy. Figure 6.3 shows metallicity distribution of the halo of the simulated galaxy. The median $[\text{Fe}/\text{H}]$ is $[\text{Fe}/\text{H}] = -1.70$. This value is close to the peak value ($[\text{Fe}/\text{H}] \approx -1.7$) of metallicity distribution of the MW halo. Figure 6.4 shows $[\text{Mg}/\text{Fe}]$ as a function of $[\text{Fe}/\text{H}]$. The decrease of $[\text{Mg}/\text{Fe}]$ is due to the contribution of SNe Ia. Scatters of $[\text{Mg}/\text{Fe}]$ are ~ 1 dex at $[\text{Fe}/\text{H}] = -3.0$. Low $[\text{Mg}/\text{Fe}]$ stars around $[\text{Fe}/\text{H}] = -2$ are due to accreted dwarf galaxies.

Figure 6.5 shows $[\text{Eu}/\text{Fe}]$ as a function of $[\text{Fe}/\text{H}]$ within 30 kpc from the center of the galaxy. At $[\text{Fe}/\text{H}] > -1.5$, most stars located around $[\text{Eu}/\text{Fe}] \sim 0.0$. These stars are in the bulge and disk of the galaxy. The small scatter (~ 1 dex) at $[\text{Fe}/\text{H}] > -1.5$ suggests that spatial distribution of metallicity is homogeneous at the site of the formation of the bulge and disk. On the other hand, at $[\text{Fe}/\text{H}] < -1.5$, there are star-to-star scatters of over 3 dex in $[\text{Eu}/\text{Fe}]$ ratios. Most of these stars are in the halo.

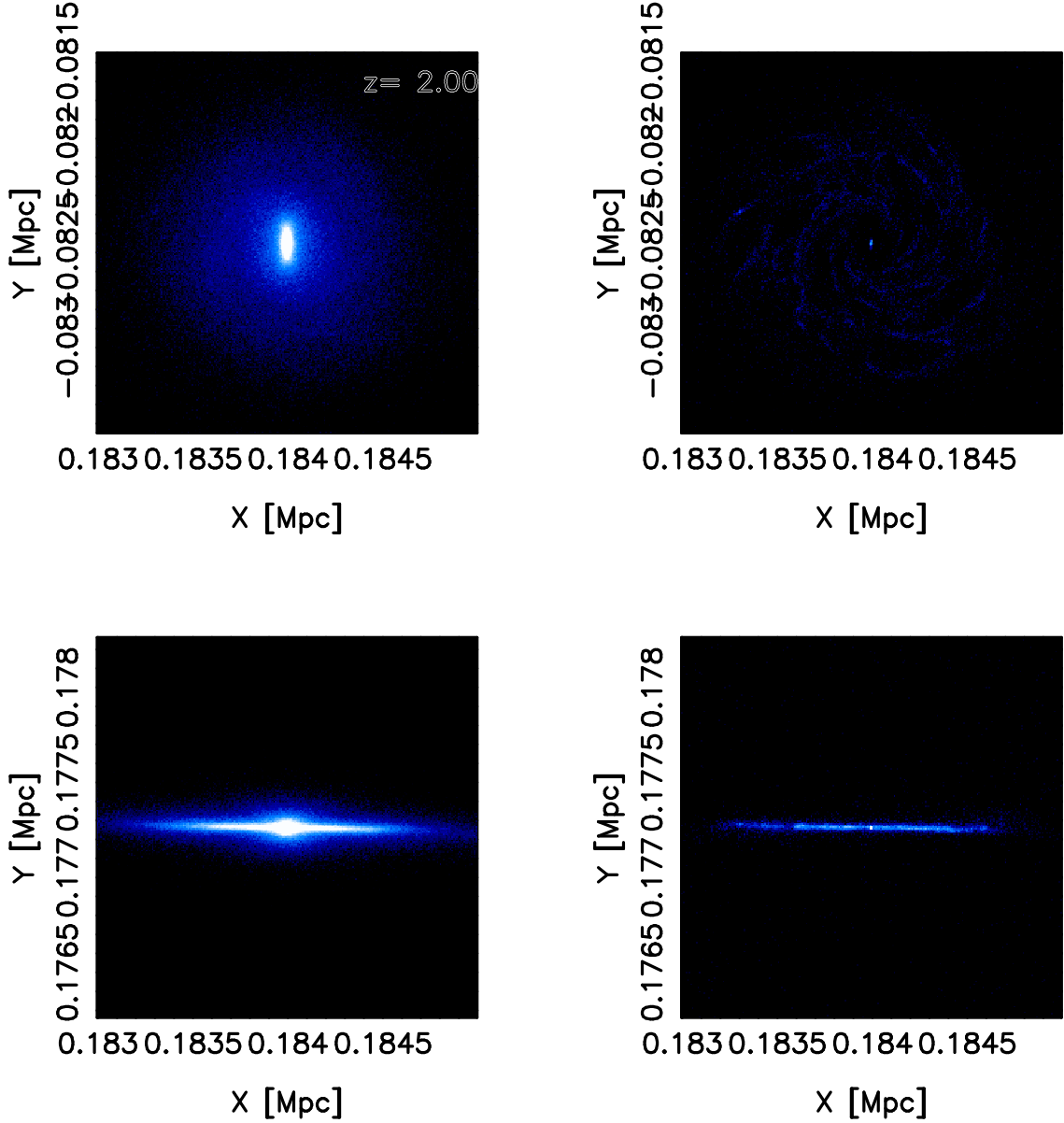


FIGURE 6.1: Stellar and gas surface density at $z = 2.0$. Top left panel shows face-on view of stellar surface density. Top right panel shows face-on view of gas surface density. Bottom left panel shows edge-on view of stellar surface density. Bottom right panel shows edge-on view of gas surface density. From black to white, the color scale denotes surface density from $10^{1.0}$ to $10^{3.8} M_{\odot} \text{pc}^{-2}$.

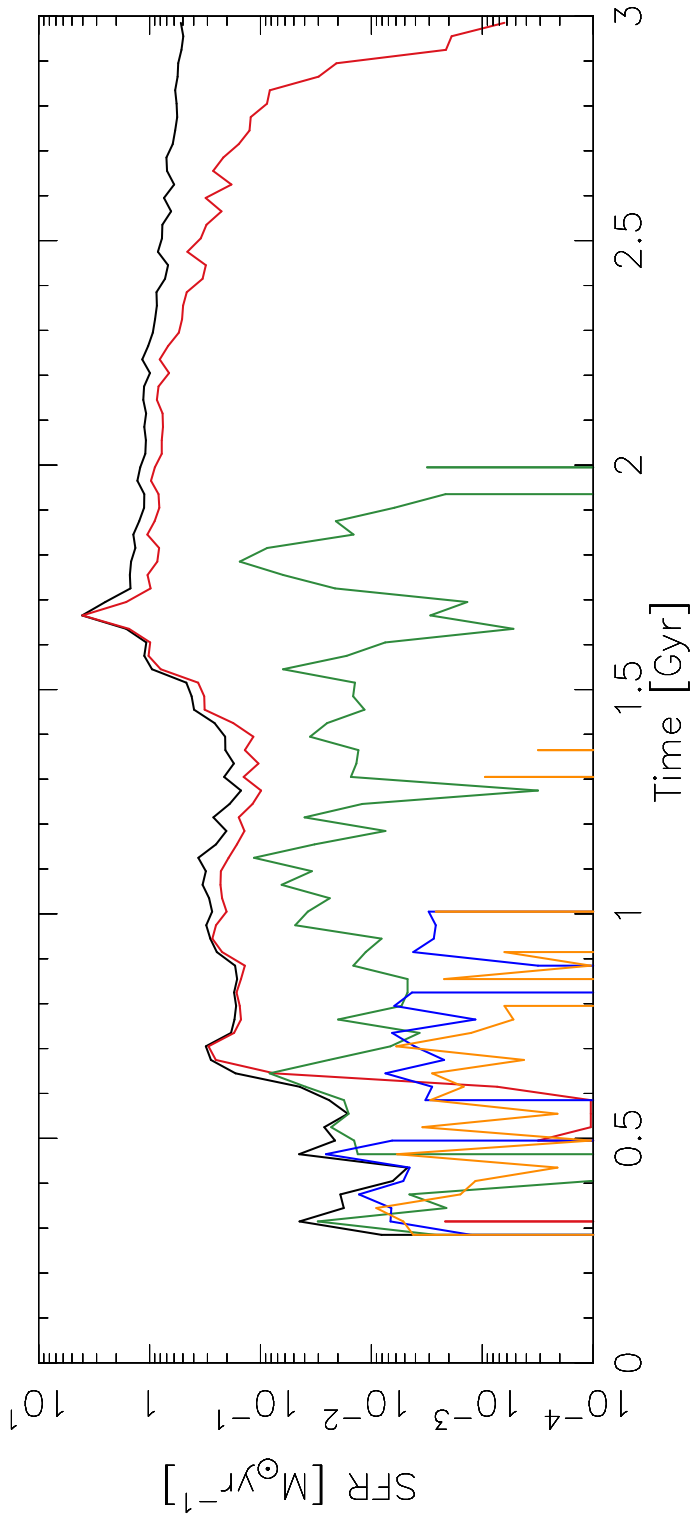


FIGURE 6.2: Time variations of SFRs. The SFRs are plotted within 30 kpc from the center of the galaxy. The black curve denotes the total SFR. Colored curves represent formation rates of stars with different metallicities. Red, green, blue, and orange curves denote formation rates of stars with $-1 < [\text{Fe}/\text{H}] \leq 0$, $-2 < [\text{Fe}/\text{H}] \leq -1$, $-3 < [\text{Fe}/\text{H}] \leq -2$, and $[\text{Fe}/\text{H}] \leq -3$, respectively.

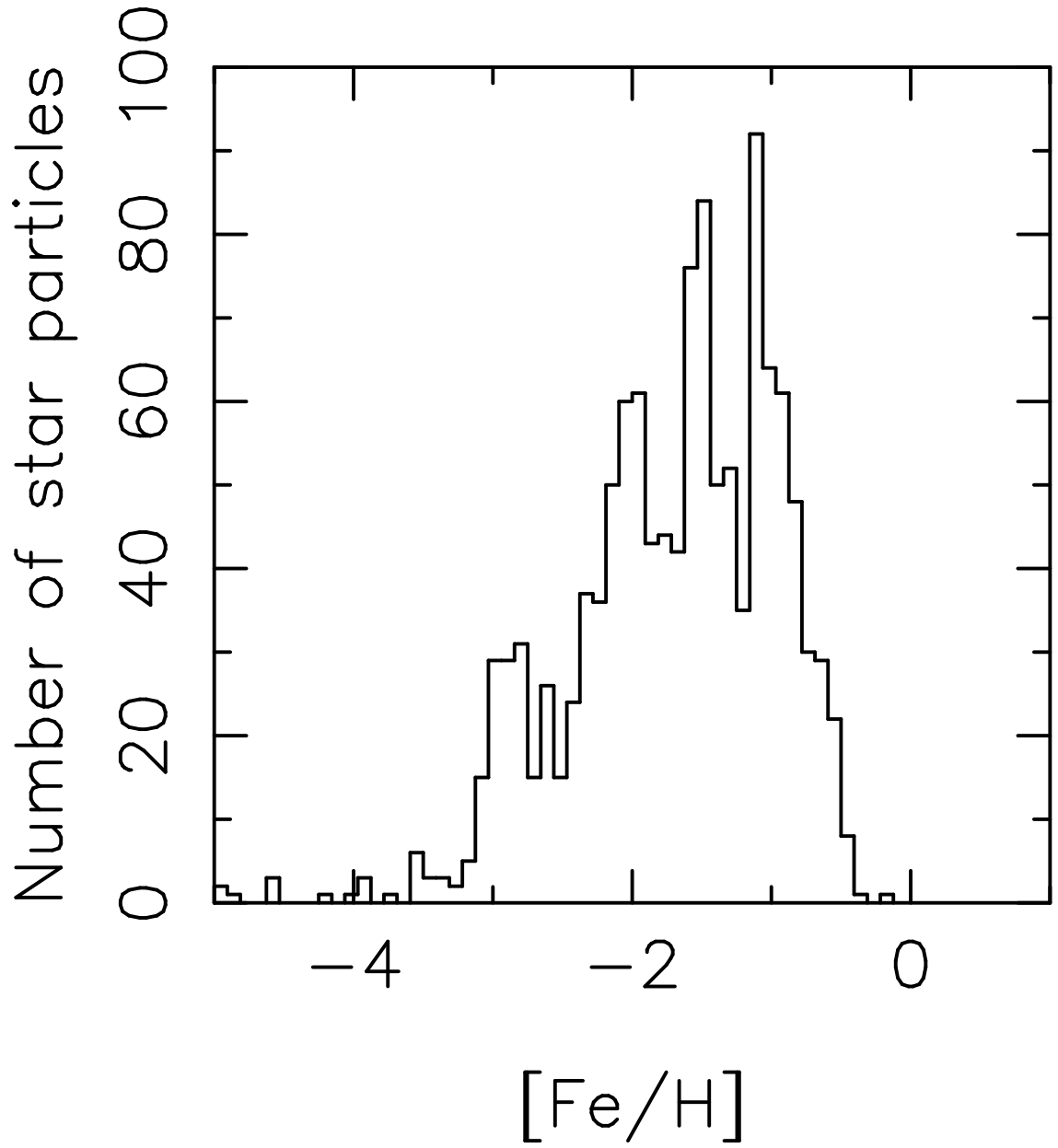


FIGURE 6.3: Metallicity distribution of the halo. We plot the metallicity distribution within 30 kpc from the galactic center and 1 kpc above the galactic disk.

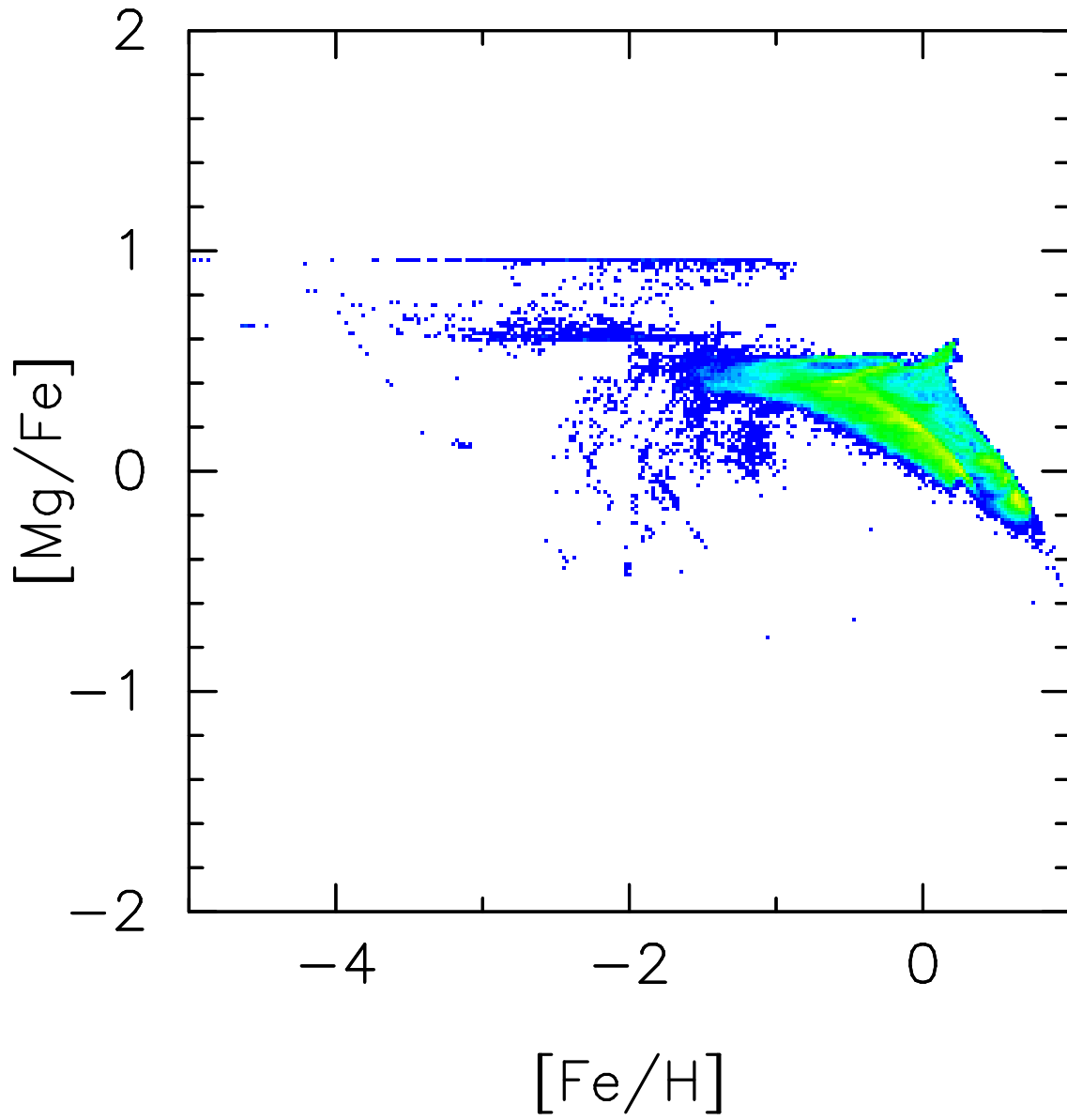


FIGURE 6.4: $[\text{Mg}/\text{Fe}]$ as a function of $[\text{Fe}/\text{H}]$ within 30 kpc from the center of the galaxy. The color scale is the same as in Figure 4.6.

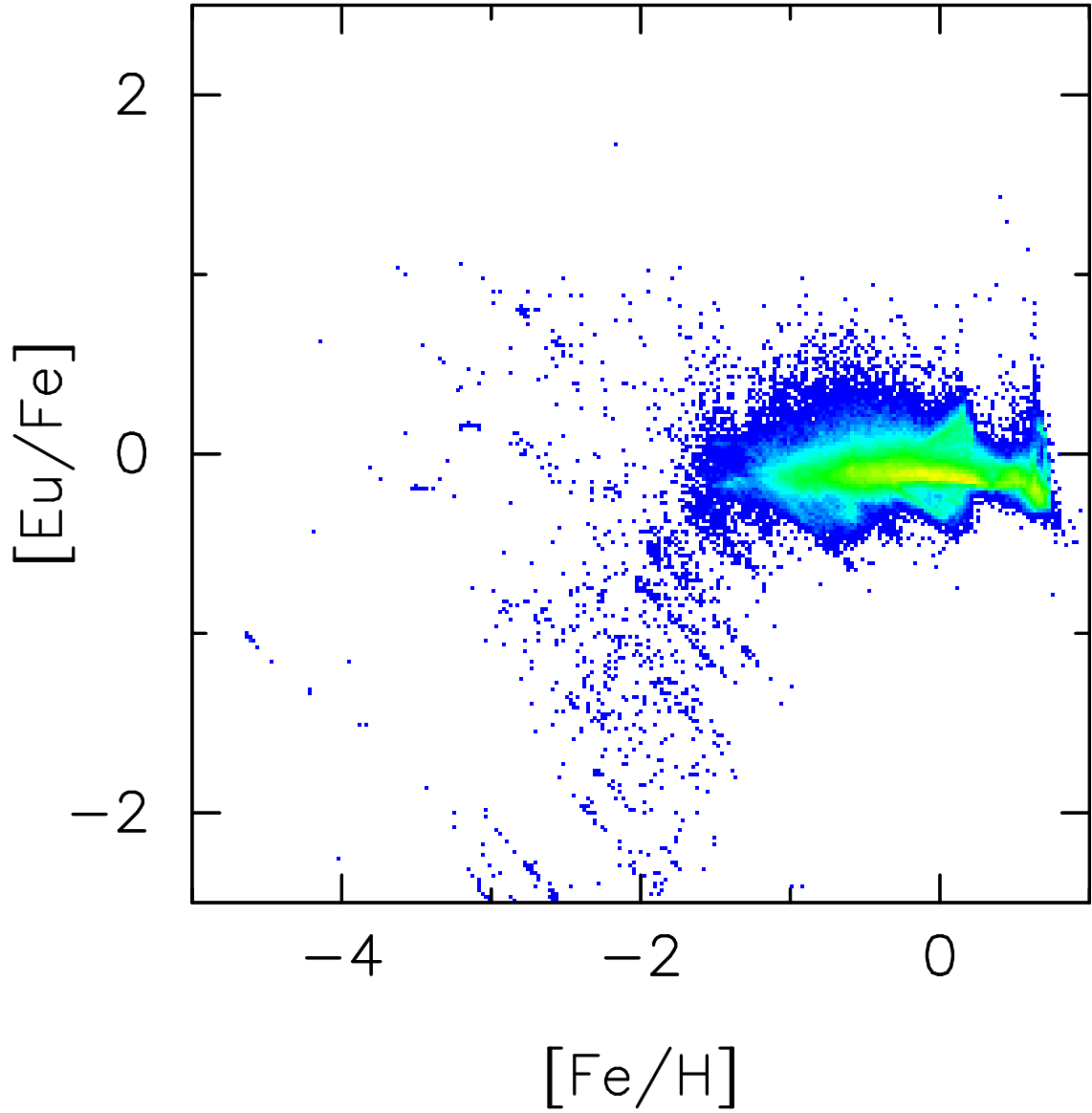


FIGURE 6.5: $[\text{Eu}/\text{Fe}]$ as a function of $[\text{Fe}/\text{H}]$ within 30 kpc from the center of the galaxy. The color scale is the same as in Figure 4.6.

6.4 Discussion

Here we discuss the formation sites of r-II stars. In Chapter 5, we show that metals should be mixed within ~ 40 Myr to explain the observed low abundances of r -process elements in the LG dSphs. On the other hand, Ji et al. (2016b) and Roederer et al. (2016) reported that there are enhanced r -process abundances in Reticulum II UFD. The MW halo also has several r-II stars (e.g., Honda et al., 2004; Frebel and Norris, 2015).

Figure 6.5 shows there are r-II stars in $[\text{Fe}/\text{H}] < -2$ even if we adopt the same scaling factor for metal diffusion with Chapter 5. We find three r -process enhanced stars at $[\text{Fe}/\text{H}] < -3$ in our simulations. Two stars are formed at 0.37 Gyr from the beginning of the simulation. These stars are formed in a halo with $M_{\text{tot}} = 1.32 \times 10^8 M_{\odot}$ and $M_{\text{gas}} = 8.59 \times 10^6 M_{\odot}$. The other star is formed at 0.45 Gyr in a halo with $M_{\text{tot}} = 1.32 \times 10^8 M_{\odot}$ and $M_{\text{gas}} = 7.08 \times 10^6 M_{\odot}$. Although these stars are formed in different halos, the gas mass of halos that formed r-II stars is similar.

The enhancement of r -process abundances can be understood regarding mass of halos that formed stars with r -process elements. Here we assume that one NSM distributes $10^{-2} M_{\odot}$ of r -process elements and these elements are mixed into a whole halo at $[\text{Fe}/\text{H}] = -3$. If an NSM occurs in a halo with a gas mass of $\sim 10^6 M_{\odot}$, the $[\text{Eu}/\text{Fe}]$ ratios are expected to be $[\text{Eu}/\text{Fe}] = 1.56$. In the case of a halo with a gas mass of $\sim 10^8 M_{\odot}$, the $[\text{Eu}/\text{Fe}]$ ratio should be -0.34 . Results of our simulation support this argument. Our results suggest that r-II stars in the MW halo are formed in halos with a gas mass of $\sim 10^6 M_{\odot}$. These halos can be found at the early stages of MW halo formation or later accreted sub-halos.

6.5 Summary

In this chapter, we performed a series of cosmological zoom-in simulations of a galaxy to obtain the self-consistent picture for the formation of the Milky Way halo and satellite dwarf galaxies through the enrichment of heavy elements. We computed the galaxy with a halo mass of $10^{10} M_{\odot}$ at redshift 2 to resolve the scale of satellite dwarf galaxies. Most extremely metal-poor stars are formed before 1 Gyr from the beginning of the simulation. In the galaxy, there are star-to-star scatters of r -process elements in low metallicity. We find that r -process rich metal-poor stars are formed in halos with a total mass of $\sim 10^8 M_{\odot}$ and gas mass of $7\text{--}9 \times 10^6 M_{\odot}$.

Chapter 7

Conclusions and future prospects

7.1 Conclusions

In this thesis, we performed a series of N -body/smoothed particle hydrodynamics simulations of dwarf galaxies to clarify the enrichment of heavy elements. This thesis aimed to understand (1) the contribution of NSMs and SNe (CCSNe, HNe, ECSNe, and SNe Ia) to the enrichment of heavy elements and (2) the relation between the chemodynamical evolution of galaxies and the abundances of heavy elements. Here we show the new findings in this thesis.

In Chapter 2, we performed a series of chemodynamical simulations of an isolated dwarf galaxy model assuming that NSMs are the major astrophysical site of the r -process. We found that models with metal mixing in a star-forming region can produce stars with [Eu/Fe] in EMP stars. NSMs with a merger timescale of 100 Myr contribute to the enrichment of r -process elements in dSphs. Due to the suppressed SFR ($\sim 10^{-3} M_{\odot} \text{ yr}^{-1}$) in the early phases, [Fe/H] does not increase at $\lesssim 300$ Myr in our model. This result suggests that NSMs with timescales of $\lesssim 300$ Myr can contribute to the enrichment of r -process elements in dwarf galaxies. We also found that NSMs with a rate of $\sim 1000 \text{ Gpc}^{-3} \text{ yr}^{-1}$ are enough to explain the observed [Eu/Fe] ratio if they produce $\sim 10^{-2} M_{\odot}$ of r -process elements in one event. These rate and yield are consistent with the estimation from the observation of the gravitational waves from an NSM (Abbott et al., 2017b; Tanaka et al., 2017).

Chapter 3 discussed the relation among structure of halos, SFHs, and enrichment of r -process elements. To produce galaxies with different SFHs and stellar mass, we changed the central density and total mass of halos of our isolated dwarf galaxy model. We found that the distribution of r -process elements in EMP stars depends on the SFRs in the early phases of galaxy evolution. Models with SFRs less than $10^{-3} M_{\odot} \text{ yr}^{-1}$ produce stars with r -process elements in [Fe/H] $\lesssim -3$. The SFRs in the early phase depends on the central density not on the total mass of halos. We found the early SFR is suppressed to be less than $10^{-3} M_{\odot} \text{ yr}^{-1}$ in galaxies with dynamical times of ~ 100 Myr. NSMs with merger timescales from 10 to 500 Myr do not affect the result significantly. We do not need NSMs with unlikely short merger timescale to explain the observation of r -process elements if the SFR is suppressed to be less than $10^{-3} M_{\odot} \text{ yr}^{-1}$.

In Chapter 4, we newly put the effect of ECSNe into a series of chemodynamical simulations. We found that stars with [Zn/Fe] $\gtrsim 0.5$ reflect the nucleosynthetic abundances of ECSNe. In the early phases of galaxy evolution, gases with high [Zn/Fe] ratios from the ejecta of ECSNe remain due to the inhomogeneity of spatial

distribution of metallicity. Scatters of $[\text{Zn}/\text{Fe}]$ at $[\text{Fe}/\text{H}] > -2.5$ come from the contribution of SNe Ia. These stars are formed at $\lesssim 4$ Gyr from the beginning of the simulation. The scatters of $[\text{Zn}/\text{Fe}]$ are consistent with $[\text{Mg}/\text{Fe}]$. We also found that it is difficult to explain the observed relation of $[\text{Zn}/\text{Fe}]$ in low metallicity without the contribution from ECSNe. On the other hand, the observed $[\text{Zn}/\text{Fe}]$ can be explained without the contribution of HNe.

Chapter 5 showed that abundances of heavy elements can be used as a tracer of efficiency of metal mixing in galaxies. We use Mg, Ba, and Zn as a tracer of metal mixing. We found that the scaling factor for metal diffusion should be less than 0.01 to explain the observed Ba abundances in dwarf galaxies. This value is consistent with the estimation of the turbulence theory and experiment. The timescale of metal mixing is estimated to be ~ 40 Myr from the gas phase Ba abundances. This timescale is shorter than the dynamical timescales (~ 100 Myr) of dwarf galaxies. The scaling factor for metal diffusion from ~ 0.01 can also explain the $[\text{Zn}/\text{Fe}]$ ratio in metal-poor stars. This value is consistent with the estimation from Ba abundances.

In Chapter 6, we performed a series of high-resolution cosmological zoom-in simulations to connect enrichment of r -process elements to the galaxy formation. We found that most EMP stars are formed before 1 Gyr from the beginning of the simulation. This result implies that EMP stars observed in the LG galaxies contain enrichment history of elements within 1 Gyr from the formation of first stars. In $[\text{Fe}/\text{H}] < -2$, there are star-to-star scatters of $[\text{Eu}/\text{Fe}]$ ratios. This feature is seen in stars in the MW halo. Scatters of $[\text{Eu}/\text{Fe}]$ ratios caused by the contribution of accreted dwarf galaxies in the early phases of galaxy formation. We found that the r -process rich metal-poor stars are formed in halos with a gas mass of $7\text{--}9 \times 10^6 M_{\odot}$. This result suggests that r -process rich stars seen in the MW halo may come from the accreted galaxies similar to Reticulum II UFD.

Figure 7.1 illustrates the scenario proposed in this thesis. We found that NSMs can be the major contributor to the enrichment of r -process elements in galaxies. We also found that ECSNe contribute to the enrichment of Zn in low metallicity. By using the heavy element abundances, we showed that the timescale of metal mixing is ~ 40 Myr in galaxies. We can extend these results to the enrichment of heavy elements in a cosmological context. From the cosmological zoom-in simulations with enrichment of r -process elements, we propose the scenario that r -process rich stars in the MW halo are formed in small halos with the size comparable to those of the present UFDs. This result demonstrates that abundances of heavy elements in LG galaxies can be a nice tracer of the early phases of evolutionary histories of LG galaxies.

7.2 Future prospects

In this thesis, we performed high-resolution chemodynamical simulations of dwarf galaxies newly including the effects of NSMs and ECSNe. For NSMs, we assume the rates within the range of estimation from observed binary pulsars (Chapters 2, 3, 5, and 6). This rate is still very uncertain even if there is an observation of gravitational waves from an NSM (Abbott et al., 2017b). In Chapter 4, we studied the enrichment of Zn, but we cannot reproduce fully the increasing trend of $[\text{Zn}/\text{Fe}]$ ratios toward lower metallicity. Also, even if we performed one of the highest resolution simulations, we

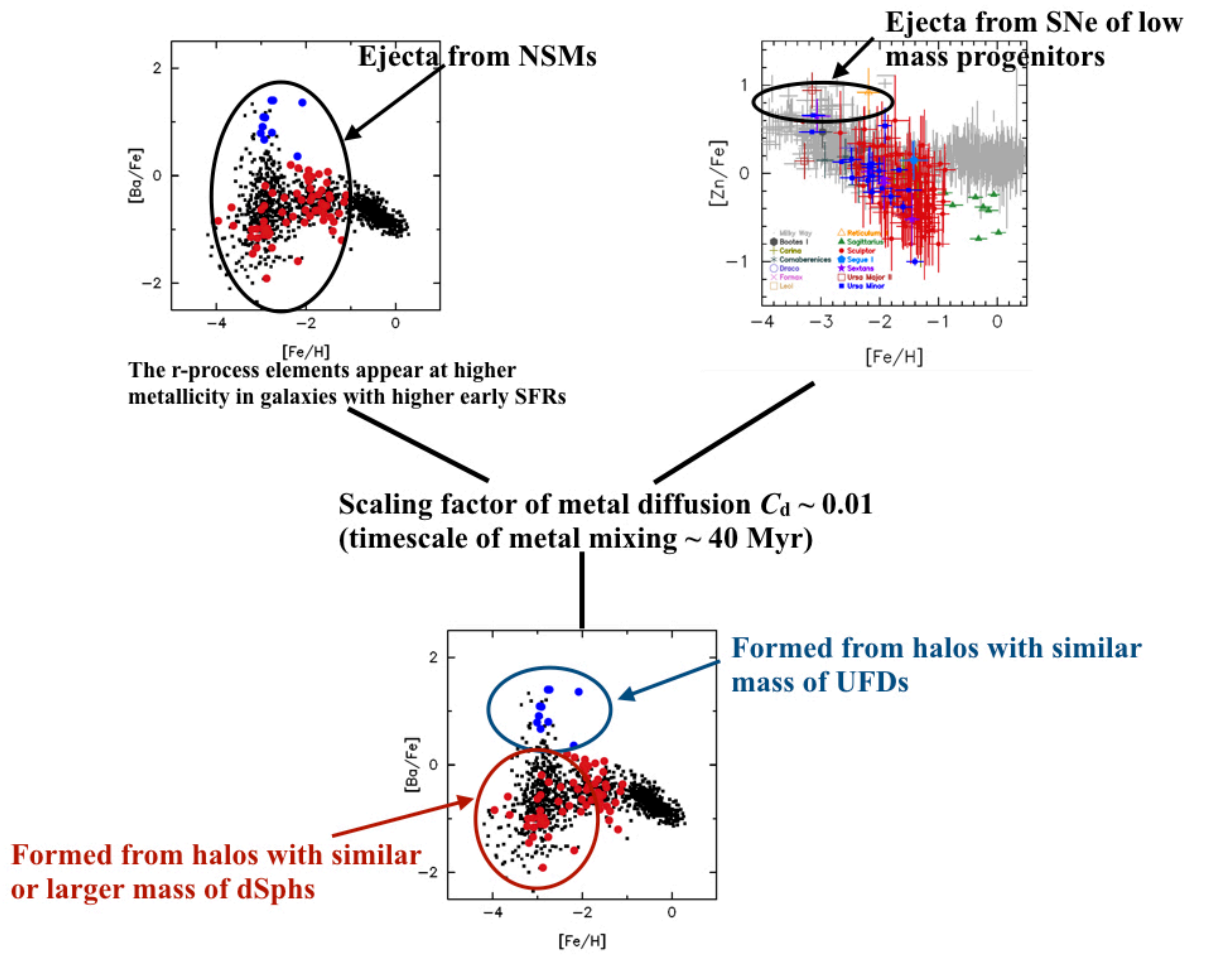


FIGURE 7.1: The scenario proposed in this thesis.

are still unable to resolve each star in the simulation. These problems will be resolved in the near future.

7.2.1 Multi-messenger astronomy

Enrichment of r -process elements from NSMs will be able to study using the multi-wavelength observations and detailed simulations. The third observation run (O3) will be operated around 2019 in the gravitational wave detector, LIGO, and Virgo. The other detector, KAGRA will start operation at 2020. Full operation of three detectors will be started around 2022. In the full operation, we expect to detect NSMs ~ 10 events per year. These observations will improve the estimation of the rate of NSMs. These observations will also be able to constrain the yields, delay time distributions, and NS kick distributions.

Estimation of rates and kick distributions is critical to understand fully the enrichment of r -process elements. NSs receive kick when the SN explosion. Binary NSs with kick velocities larger than the escape velocity of the host galaxy will merge outside of the galaxy. Safarzadeh and Côté (2017) showed that $\sim 40\%$ of all formed binary NSs do not contribute to the enrichment of r -process elements. These escaped binary NSs do not contribute to the enrichment of r -process elements inside the galaxy but distribute elements to the intergalactic medium.

In the MW halo, stars with $[\text{Fe}/\text{H}] \lesssim -3.5$ have low-level Ba abundances ($[\text{Ba}/\text{Fe}] \sim -1.5$). UFDs except for Reticulum II also have depleted abundances of r -process elements (Frebel and Norris, 2015). Origin of these stars is not yet understood. Materials ejected to the intergalactic medium would account for forming such stars. We expect that future chemodynamical simulations including the effects of NS kick resolve these issues.

7.2.2 Star-by-star simulations

It is our quest to understand the evolutionary histories of galaxies from the formation of first stars to the present. Understanding small systems such as UFDs and globular clusters is the key to clarify the evolutionary histories of the MW halo. These objects contain information about the early Universe. To understand the formation and evolution of these systems, we need to perform a series of very high-resolution simulations that can resolve each star (star-by-star simulations). These simulations will be able to perform using the future upgraded supercomputing systems and improved computational codes.

Recent surveys discovered many UFDs in the LG (e.g., Simon and Geha, 2007). Weisz et al. (2014) showed that star formation stops earlier in lower mass galaxies. SN feedback is effective in these galaxies (Okamoto et al., 2010). By analyzing SFHs of UFDs, it is possible to constrain the efficiency of SN feedback, which is not well understood.

Formation of globular clusters is one of the open questions in astronomy. Globular clusters are one of the main components in the LG. They consist of old stars with ages over 10 Gyr. There are star-to-star scatters of r -process elements, but no scatters of Fe in the globular cluster, M15 (Snedden et al., 1997; Otsuki et al., 2006). This observation points to the astrophysical sites of r -process elements and evolutionary

histories of globular clusters. We expect that future simulations that can resolve each star will be able to clarify the formation and evolution of globular clusters.

7.2.3 Connection between near and far fields

Our simulations can apply to distant and larger objects. Understanding the enrichment of Zn in galaxies will clarify the chemical evolution in the Universe. Zn has been used for the indicator of metallicity in damped Ly α systems. The increasing trend of [Zn/Fe] ratios toward lower metallicity would be resolved in star-by-star simulations that can reflect the yields of each SN. Chemical evolution in the high redshift universe will be clarified by the simulations of damped Ly α systems including enrichment of Zn from SNe.

The cosmological zoom-in simulations discussed in Chapter 6 can apply for clusters of galaxies. X-ray observations of Perseus clusters showed that the ratio of iron-peak elements and Fe is consistent with those of solar system (Hitomi Collaboration et al., 2017). The metallicity distributions in the intergalactic medium are uniform in the outskirts of Perseus and Virgo clusters (Werner et al., 2013; Simionescu et al., 2015). These observations give us insight into the metal mixing in the intergalactic medium. Future simulations of a cluster of galaxies will probe the metal mixing in a larger scale.

Future observations will give us the data that can directly compare with the high-resolution simulations. The Gaia mission will provide astrometry and photometry data over one billion stars down to the magnitude of ~ 20 (Gaia Collaboration et al., 2016b; Gaia Collaboration et al., 2016a). The Subaru prime focus spectrograph will give us chemodynamical data of the LG galaxies (Takada et al., 2014). The next generation large telescopes such as the Thirty Meter Telescope (TMT), the Giant Magellan Telescope (GMT), and the European Extremely Large Telescope (E-ELT) will observe the Universe down to the era of the formation of first galaxies. The comparison between future simulations and observations will lead us to understand the formation and evolution of galaxies.

Appendix A

Parameter dependence

In this thesis, we performed a series of N -body/SPH simulations of galaxies. Here we show the effects of parameters adopted in the simulations. We adopt the models shown in Chapter 2.

A.1 Radial profile

We compare models with different threshold densities for SF (n_{th}), dimensionless SFE parameters (c_{\star}), and SN feedback energies (ϵ_{SN}). Table A.1 lists all models discussed here. Figure A.1 shows the radial profiles of our models. Horizontal axis of Figure A.1 is the distance from the galactic center. Figure A.1 (a) shows the dark matter density profile. We find that all models have similar dark matter profiles. The dark matter profile is not affected by physical parameters such as threshold density for SF, dimensionless SFE parameters, and SN feedback energy.

Gas density, stellar density, and stellar velocity dispersion profiles have variations among these models. The gas density of sn10 and se01 is lower than that of s000 (Figure A.1 (b)). In these models, most of gas is consumed in the early phase of their evolution. The gas density of se01 is truncated at 0.3 kpc while the gas profiles of the other models continue over 10 kpc. This is because the feedback energy in se01 is too weak to blow the gas away to the outer region of the galaxy.

Stellar density profiles for all models (Figure A.1 (c)) are truncated within a few kpc, which is consistent with the observed truncation radius ($\sim 0.5 - 3$ kpc) of dSphs in the LG (Irwin and Hatzidimitriou, 1995). In sn10, stars distribute to a larger radius than the other models. When a low value of n_{th} is used, stars can form in the outer region of the galaxy. If the SN feedback is weak (model se01), stellar distribution concentrates on the central region of the galaxy.

Figure A.1 (d) shows the velocity dispersion profile. All models except for se01 are consistent with the observed radial velocity dispersion profiles inside 1 kpc from the center in the LG dSphs (Walker et al., 2007; Walker et al., 2009). Model se01 has higher velocity dispersion at the center of our model galaxy due to the high central concentration of stars.

In contrast to n_{th} and ϵ_{SN} , the dimensionless SFE parameter (c_{\star}) does not greatly affect the radial profiles. Figure A.1 shows all profiles of s000 (red curve) and sc50 (blue curve) are similar although they have different value of the dimensionless SFE parameter. These features suggest that radial properties of galaxies are insensitive to the value of c_{\star} when we adopt a reasonable value of n_{th} ($= 100 \text{ cm}^{-3}$) (Saitoh et al., 2008).

TABLE A.1: List of models.

Model	n_{th} cm^{-3}	c_{\star}	ϵ_{SN} 10^{51} erg
s000	100	0.033	1
sn10	10	0.033	1
sc50	100	0.5	1
se01	100	0.033	0.1

Parameters adopted in our models: (1) Model: Name of our models. (2) n_{th} : Threshold density for SF. (3) c_{\star} : Dimensionless SFE parameter. (4) ϵ_{SN} : SN feedback energy.

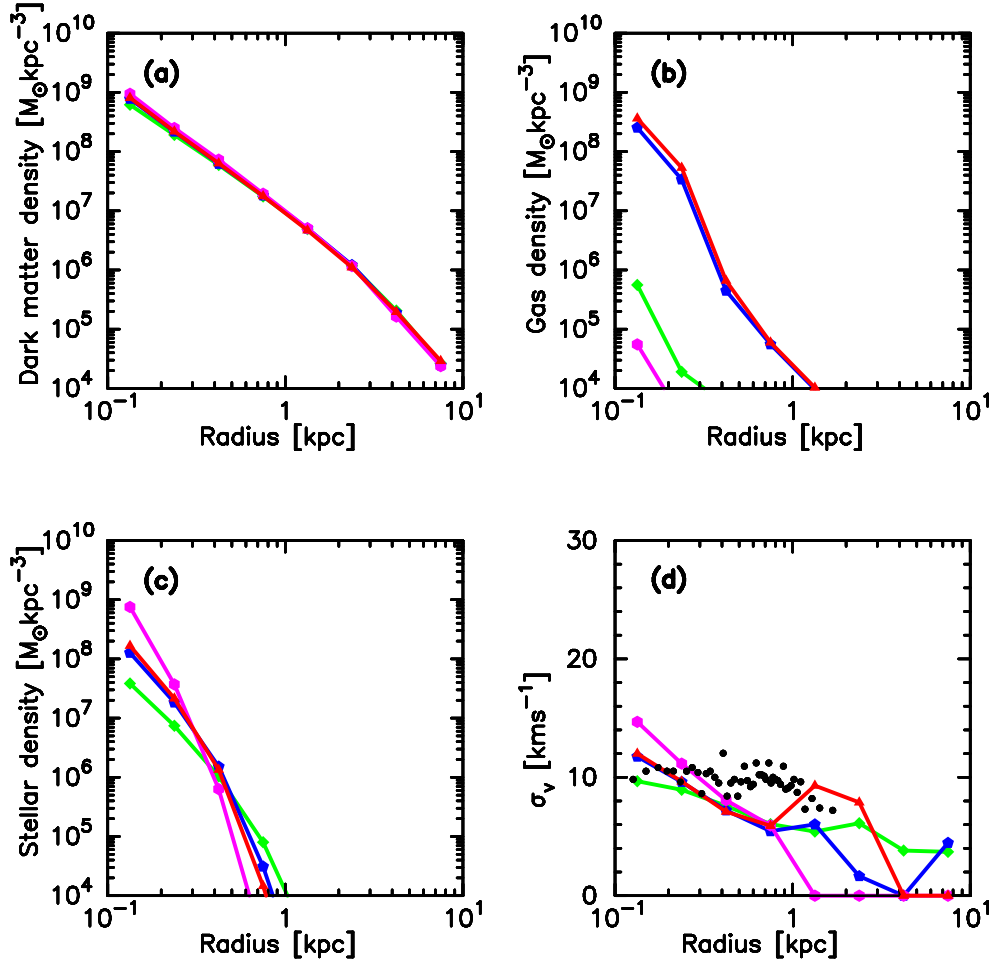


FIGURE A.1: Radial profiles of models of different parameters at $t = 5.0$ Gyr. Red triangles, green diamonds, blue pentagons, and magenta hexagons represent model s000, sn10 ($n_{\text{th}} = 10 \text{ cm}^{-3}$), c050s ($c_{\star} = 0.5$), and se01 ($\epsilon_{\text{SN}} = 10^{50} \text{ erg}$), respectively. (a): Radial dark matter density profile. (b): Radial gas density profile. (c): Radial stellar density profile. (d): Radial velocity dispersion profile.

A.2 Time variations of the SFR and metallicity distribution

Figures A.2 and A.3 show SFRs as a function of time and metallicity distribution, respectively. SFRs as a function of time and metallicity distribution are characterized by the threshold density for SF and SN feedback energy. Model sn10 has lower n_{th} ($= 10 \text{ cm}^{-3}$) than that of s000 ($n_{\text{th}} = 100 \text{ cm}^{-3}$). The second peak of the SFR of sn10 is earlier than s000. This reflects time required to reach n_{th} is shorter than s000 because of using low n_{th} value in sn10. In addition, the first peak of SFR of sn10 is higher than s000. Gas is consumed by SF and removed by outflow at $< 0.1 \text{ Gyr}$ in sn10. Its SFR is therefore ~ 2 dex lower than s000. The early bursty SF of sn10 produces more metal-poor stars than s000 (see green dashed and red curves in Figure A.3). Higher SFR of sn10 at $\sim 0.1 \text{ Gyr}$ produces more CCSNe in this phase. CCSNe produce outflow. Model sn10 thus loses larger amount of gas around $\sim 0.1 \text{ Gyr}$. Chemical evolution of sn10, therefore, quenches at $> 0.1 \text{ Gyr}$ and produces few metal-rich stars.

SN feedback energy also significantly affects the time variation of SFR and metallicity distribution. The SN feedback energy of se01 ($\epsilon_{\text{SN}} = 10^{50} \text{ erg}$) is ten times smaller than that of s000 ($\epsilon_{\text{SN}} = 10^{51} \text{ erg}$). The peak of the SFR of se01 is over 1 dex higher than that of s000. SN feedback energy gives thermal energy to gas particles. It prevents collapse of gas particles. As a result, SF is suppressed due to SN feedback energy. SN feedback energy of se01 is too weak to suppress SF. The peak of SFR of se01 is thus ~ 1 dex higher than s000. Gas is consumed for SF due to high SFR around 2 Gyr of se01, and the SFR at $> 4 \text{ Gyr}$ is eventually suppressed. Due to the low SN feedback energy in model se01, the peak of metallicity distribution of se01 is ~ 0.5 dex higher metallicity than s000.

On the other hand, the value of the dimensionless SFE parameter does not significantly affect the results. Models s000 and sc50 have different value of $c_{\star} = 0.033$ and 0.5, respectively. The time variation of the SFR and metallicity distribution of sc50 is however similar to that of s000. This result suggests that the time variation of the SFR and metallicity distribution are insensitive to the value of c_{\star} if we use a reasonable value of n_{th} ($= 100 \text{ cm}^{-3}$). Slightly lower metallicity of sc50 than s000 is due to slightly lower SFRs of sc50 than s000. This result suggests that the value of c_{\star} does not affect the metallicity distribution as well as radial profiles and the SFR. When we adopt $n_{\text{th}} = 100 \text{ cm}^{-3}$, it takes much longer local dynamical time to flow from the reservoir ($n_{\text{H}} \sim 1 \text{ cm}^{-3}$) to the SF regions ($n_{\text{H}} \gtrsim 100 \text{ cm}^{-3}$). This timescale does not depend on c_{\star} (Saitoh et al., 2008). Our results are, thus, independent of c_{\star} .

These results suggest that the time variation of the SFR and metallicity distribution is significantly affected by the threshold density for SF and SN feedback energy. Low n_{th} model (sn10) produces too many EMP stars. In contrast, low ϵ_{SN} model (se01) has too many metal-rich stars. These differences in metallicity distribution are due to the difference of the time variation of the SFR among models. On the other hand, model s000 reproduces observation of metallicity distribution as well as dynamical properties. Parameters of s000 are taken from the observed values. Threshold density of s000 ($n_{\text{th}} = 100 \text{ cm}^{-3}$) is taken from mean density of GMCs. SN feedback energy of s000 ($\epsilon_{\text{SN}} = 10^{51} \text{ erg}$) is taken from the canonical explosion energy of CCSNe (e.g., Nomoto et al., 2006). We thus treat s000 as a model that has fiducial parameter sets.

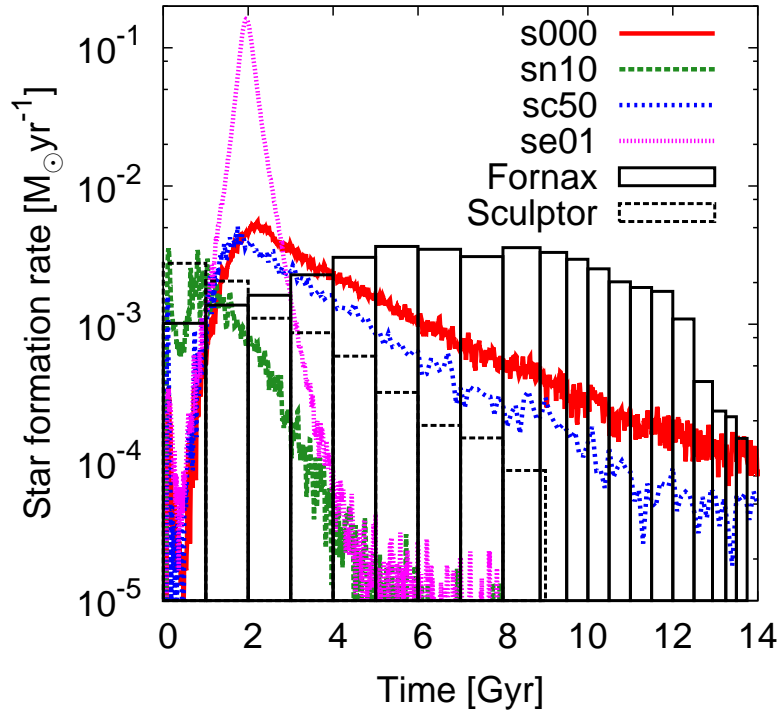


FIGURE A.2: The SFR as a function of time for our models. Red curve, green dashed curve, blue short-dashed curve, and magenta dotted curve represent models s000, sn10 ($n_{\text{th}} = 10 \text{ cm}^{-3}$), sc50 ($c_{\star} = 0.5$), and se01 ($\epsilon_{\text{SN}} = 10^{50} \text{ erg}$), respectively. The black histogram and black-dotted histogram represent the observed SFR of the Fornax dSph (de Boer et al., 2012a) and the Sculptor dSph (de Boer et al., 2012b), respectively.

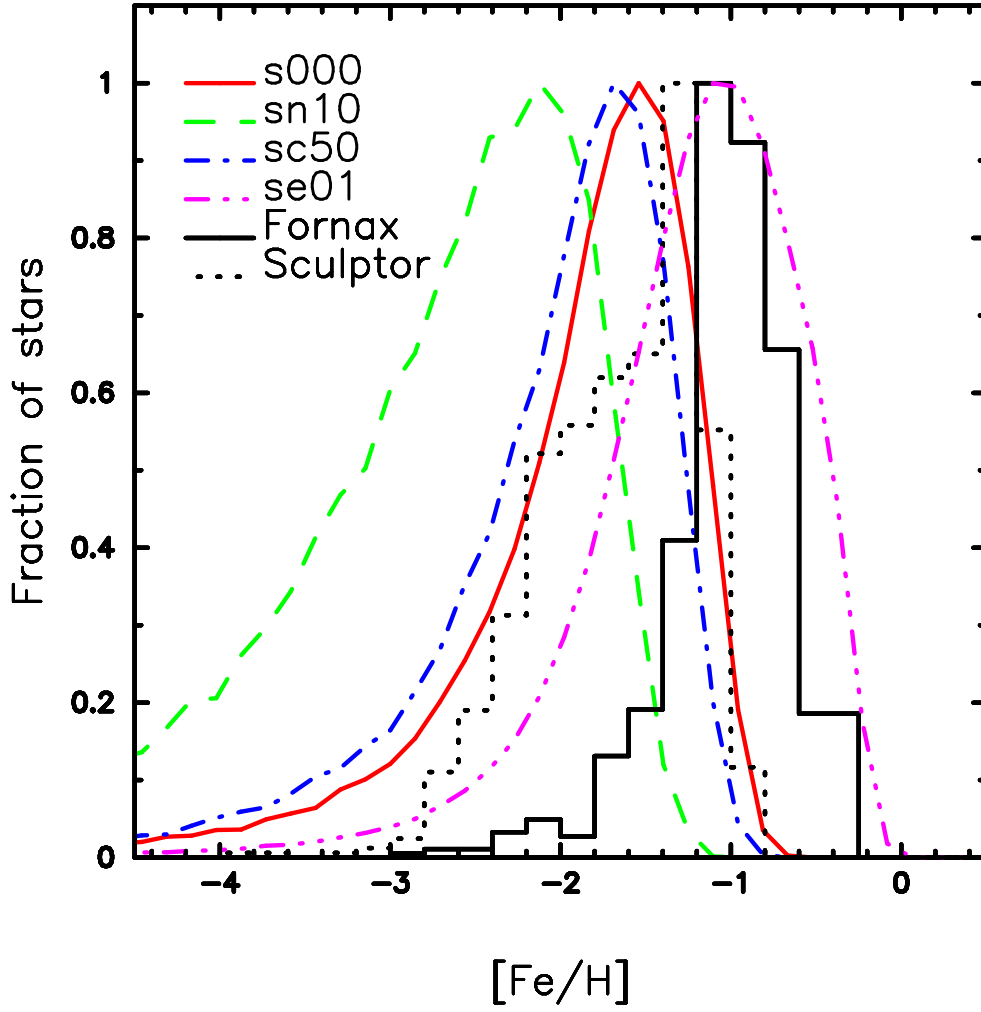


FIGURE A.3: Metallicity distribution of our models. The black histogram and black-dotted histogram are observed metallicity distribution of the Fornax dSph (Kirby et al., 2010) and the Sculptor dSph (Kirby et al., 2009; Kirby et al., 2010; Kirby and Cohen, 2012), respectively. Red curve, green dashed curve, blue dashed-dotted curve, and magenta dashed-dotted-dotted curve represent s000, sn10 ($n_{\text{th}} = 10 \text{ cm}^{-3}$), sc50 ($c_{\star} = 0.5$), and se01 ($\epsilon_{\text{SN}} = 10^{50} \text{ erg}$), respectively.

Appendix B

Dynamical friction

Here we show the effects of dynamical friction. In this thesis, we assume the same number of gas and dark matter particles. To be consistent with the baryon fraction, $f_b = 0.15$ (Planck Collaboration et al., 2014), we set $m_{\text{DM}} = 5.7 m_{\text{gas}}$. Massive (dark matter) particles fall into the center by the dynamical friction. Provided that the density distribution is a singular isothermal sphere,

$$\rho(r) = \frac{v_c^2}{4\pi G r^2}, \quad (\text{B.1})$$

where v_c^2 is the constant circular speed, r is the radius, massive particles (dark matter particles) lose angular momentum (L) at a rate,

$$\frac{dL}{dt} = -0.428 \ln \Lambda \frac{G m_{\text{DM}}^2}{r}, \quad (\text{B.2})$$

where

$$\Lambda = \frac{b_{\text{max}}}{b_{90}} \approx \frac{b_{\text{max}} v_t^2}{G m_{\text{DM}}}, \quad (\text{B.3})$$

and b_{max} , b_{90} , v_t are the maximum value of impact parameter, 90° deflection radius, and typical relative velocity (Binney and Tremaine, 2008). The angular momentum at the radius r in the singular isothermal sphere is $L = m_{\text{DM}} r v_c$. Substituting this to the Equation (B.2),

$$r \frac{dr}{dt} = -0.302 \ln \Lambda \frac{G m_{\text{DM}}^2}{\sigma}. \quad (\text{B.4})$$

Here we use $v_c = \sqrt{2}\sigma$. From the Equation (B.4), we obtain the timescale that massive particles reach the center of the halo,

$$t_{\text{fric}} = \frac{19 \text{ Gyr}}{\ln \Lambda} \left(\frac{r}{5 \text{ kpc}} \right)^2 \frac{\sigma}{200 \text{ kms}^{-1}} \frac{10^8 M_\odot}{m_{\text{DM}}}. \quad (\text{B.5})$$

In the isolated dwarf galaxy model adopted in this thesis, typical values are $b_{\text{max}} = 1 \text{ kpc}$, $m_{\text{DM}} = 10^4 M_\odot$, and $v_t \approx \sigma = 10 \text{ kms}^{-1}$. In this case, $\ln \Lambda = 7.75$. From Equation (B.5), the timescale of dynamical friction is $t_{\text{fric}} = 49.0 \text{ Gyr}$. This timescale is sufficiently longer than the cosmic time. On the other hand, in the case of simulations massive galaxies ($b_{\text{max}} = 5 \text{ kpc}$, $v_t \approx \sigma = 200 \text{ kms}^{-1}$) with $m_{\text{DM}} = 10^8 M_\odot$ (e.g., Katz and Gunn, 1991; Kobayashi, 2004), $t_{\text{fric}} = 3.1 \text{ Gyr}$. In this case, dynamical friction affects the evolution of simulated galaxies.

To confirm that the dynamical friction does not affect the results of this work, we performed a series of simulations adopting $m_{\text{DM}} = m_{\text{gas}}$. Table B.1 lists models compared in this appendix. Other parameters are the same as those in model G in Chapter 4. Figure B.1 shows radial density profiles of dark matter, gas, and stars. According to this figure, radial profiles of both models G and Q are overlapped. Figure B.2 denotes the time variations of SFRs in these models. Both models show SFRs of $\sim 10^{-3} M_{\odot} \text{yr}^{-1}$. We cannot see any significant difference between models G and Q. These results indicate that dynamical friction due to adopting particles with different mass does not affect the results of this work.

TABLE B.1: List of models discussed in Appendix B.

Model	N_{DM}	N_{gas}	m_{DM} $10^3 M_{\odot}$	m_{gas} $10^3 M_{\odot}$
G*	131072	131072	4.5	0.8
Q	873813	131072	0.8	0.8

*Models G is the same model as listed in Table 4.3.

From left to right, columns show names of models, initial total number of dark matter and gas particles, the mass of one dark matter and gas particle.

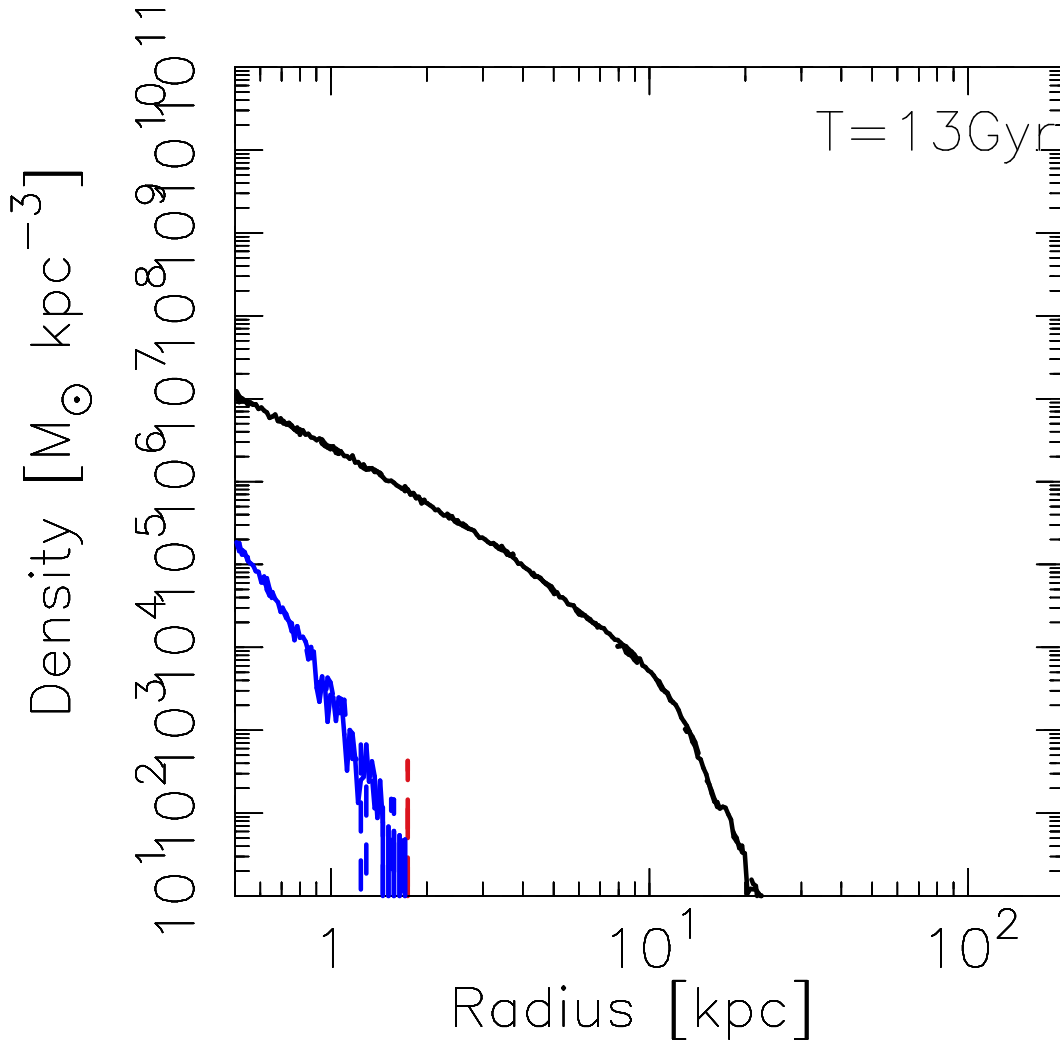


FIGURE B.1: Radial density profiles of dark matter (black), gas (red) and stars (blue) at 13.8 Gyr from the beginning of the simulation. Solid and dashed curves denote the model G and Q. Both curves are mostly overlapped.

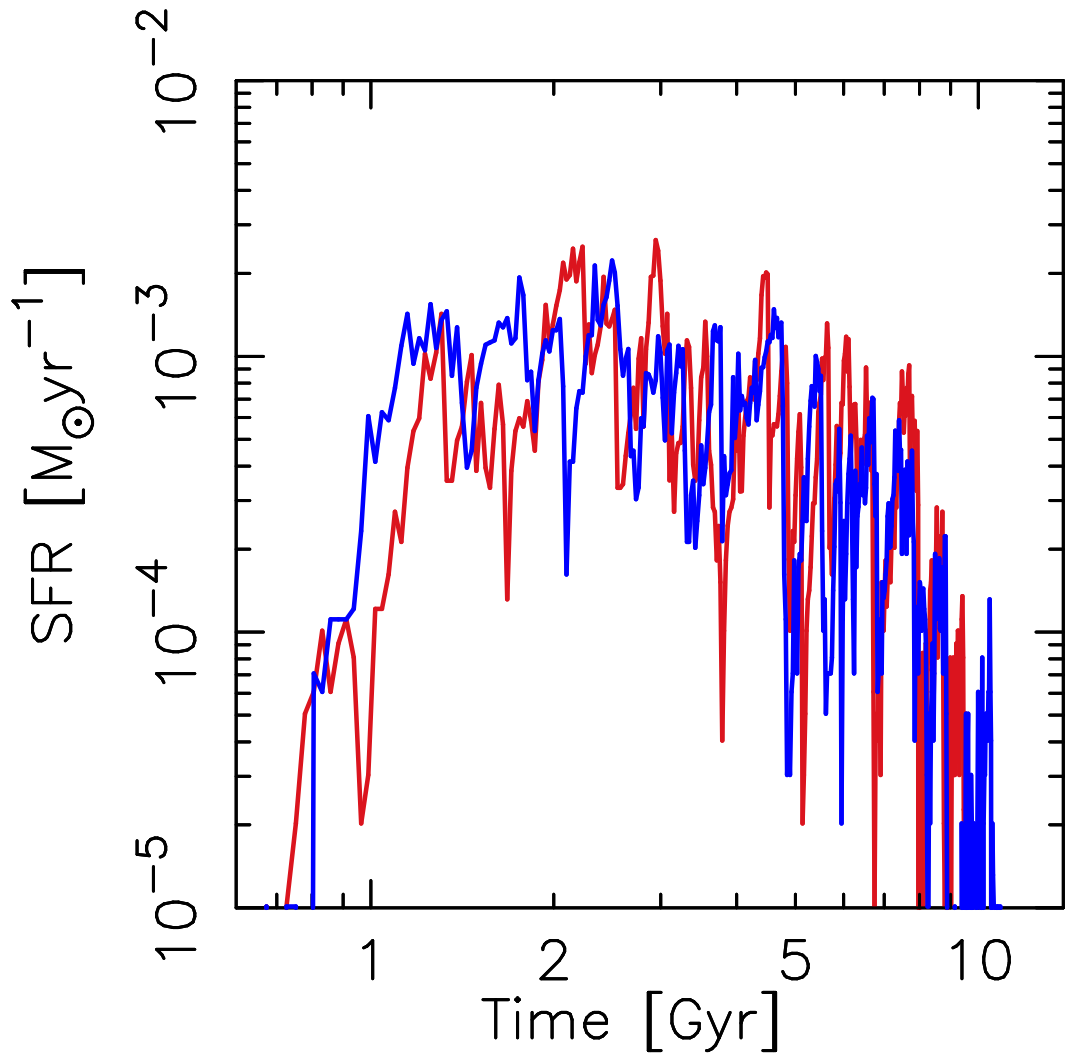


FIGURE B.2: Time variations of SFRs in model G (blue) and Q (red).

Appendix C

Effects of supernova yields of zinc and dependence on the resolution

Here we show the effects of different SN yields of Zn and dependence on the spatial resolution of simulation. Table C.1 lists models discussed in this Appendix.

TABLE C.1: List of models discussed in Appendix C.

Model	N	ϵ_g pc	SN Yields
G*	2^{18}	7.8	N13
N	2^{18}	7.8	CL04
O	2^{17}	9.9	N13
P	2^{16}	14.1	N13

*Model G is the same model as listed in Table 4.3.

From left to right, columns show names of models, initial total number of particles, gravitational softening length, and adopted SN yields.

C.1 Effects of supernova yields of zinc

As we have shown in Figure 4.1, SN yields of Zn and Fe depend on stellar evolution models (e.g., Sukhbold et al., 2016). This can affect the results of this study. Figure C.1 compares the computed evolution of $[\text{Zn}/\text{Fe}]$ versus $[\text{Fe}/\text{H}]$ in models G and N. Models G and N adopt SN yields of N13 and CL04, respectively. As shown in Figure C.1, both models have the increasing trend toward lower metallicities. Model N has a ~ 0.3 dex lower median value of $[\text{Zn}/\text{Fe}]$ than that of model G. In addition, model N has larger scatters in $[\text{Zn}/\text{Fe}]$ at $[\text{Fe}/\text{H}] > -0.5$ than those in model G. These differences reflect the lower production of Zn in CL04 than that in N13. However, both results are within the range of scatters in observed $[\text{Zn}/\text{Fe}]$. This result implies that the effects of the difference of SN yields do not substantially affect the enrichment history of Zn.

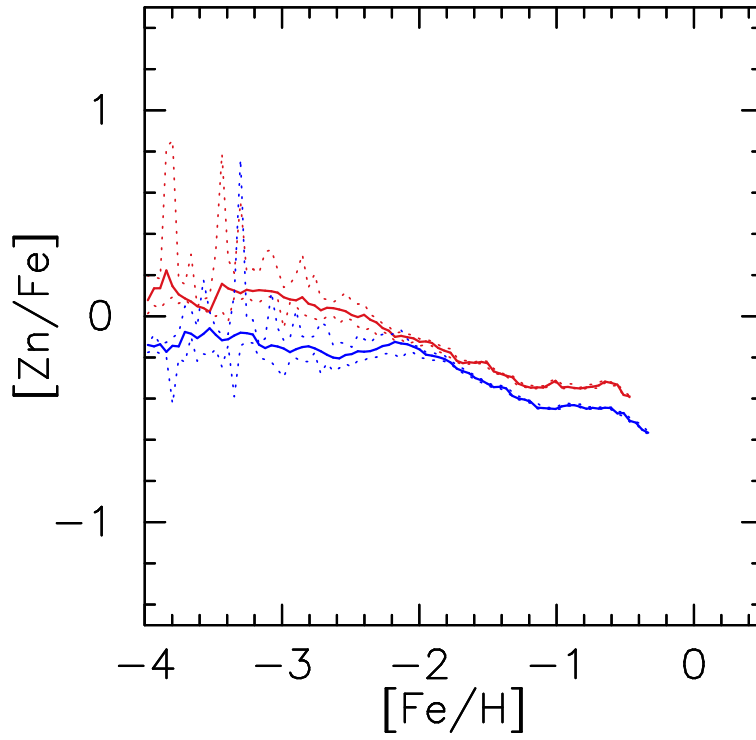


FIGURE C.1: Comparison of the $[\text{Zn}/\text{Fe}]$ evolution for the models assuming different SN yields. Model G (red curves) adopts the nucleosynthesis yield of N13. Model N (blue curves) adopts the yield of CL04. Solid curves show the median values. Dotted curves indicate the 5 % and 95 % significance levels at each $[\text{Fe}/\text{H}]$ bin.

C.2 Dependence on the resolution

Figure C.2 compares the $[\text{Zn}/\text{Fe}]$ evolutions for different resolution models. The levels of scatters in $[\text{Zn}/\text{Fe}]$ do not substantially differ among these models. The number fraction of stars with $[\text{Fe}/\text{H}] \gtrsim -0.6$ seen in model O is less than 0.04, i.e., the number of these stars is negligible. We therefore conclude that the spatial resolution of simulations does not change our main results.

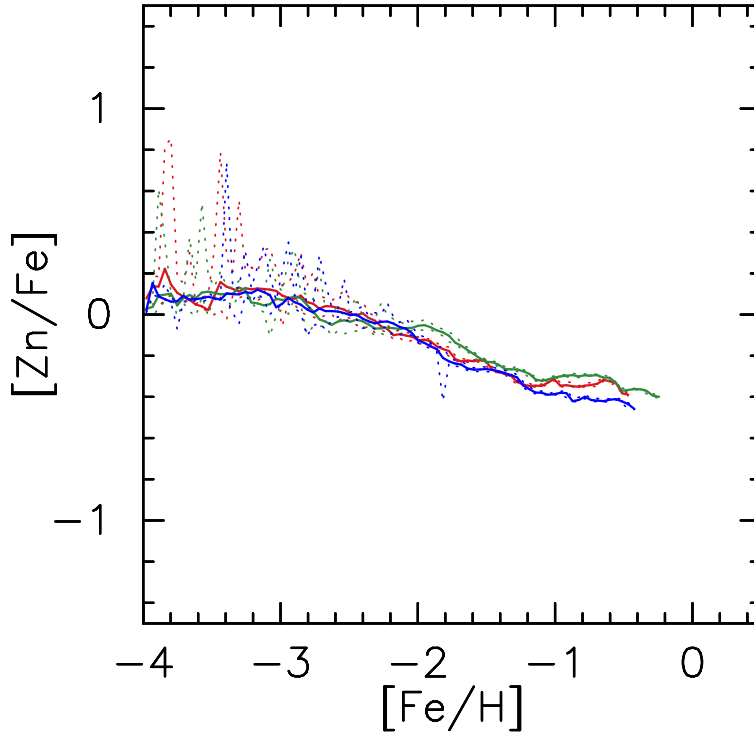


FIGURE C.2: Same as Figure C.1 but for models with different resolution. Red, green, and blue curves represent models G ($N = 2^{18}$), O ($N = 2^{17}$), and P ($N = 2^{16}$), respectively.

Bibliography

- Abadie, J., B. P. Abbott, R. Abbott, M. Abernathy, C. Adams, R. Adhikari, P. Ajith, B. Allen, G. Allen, E. Amador Ceron, and et al. (2010a). “Calibration of the LIGO gravitational wave detectors in the fifth science run”. *Nuclear Instruments and Methods in Physics Research A* 624, pp. 223–240.
- Abadie, J., B. P. Abbott, R. Abbott, M. Abernathy, T. Accadia, F. Acernese, C. Adams, R. Adhikari, P. Ajith, B. Allen, and et al. (2010b). “TOPICAL REVIEW: Predictions for the rates of compact binary coalescences observable by ground-based gravitational-wave detectors”. *Classical and Quantum Gravity* 27.17, 173001.
- Abbott, B. P., R. Abbott, T. D. Abbott, M. R. Abernathy, F. Acernese, K. Ackley, C. Adams, T. Adams, P. Addesso, R. X. Adhikari, and et al. (2016). “Prospects for Observing and Localizing Gravitational-Wave Transients with Advanced LIGO and Advanced Virgo”. *Living Reviews in Relativity* 19.
- Abbott, B. P., R. Abbott, T. D. Abbott, F. Acernese, K. Ackley, C. Adams, T. Adams, P. Addesso, R. X. Adhikari, V. B. Adya, and et al. (2017a). “Gravitational Waves and Gamma-Rays from a Binary Neutron Star Merger: GW170817 and GRB 170817A”. *The Astrophysical Journal Letters* 848, L13.
- (2017b). “GW170817: Observation of Gravitational Waves from a Binary Neutron Star Inspiral”. *Physical Review Letters* 119.16, 161101.
- (2017c). “Multi-messenger Observations of a Binary Neutron Star Merger”. *The Astrophysical Journal Letters* 848, L12.
- Accadia, T. et al. (2011). “Status of the Virgo project”. *Classical and Quantum Gravity* 28.11, 114002.
- Adams, J. J., J. D. Simon, M. H. Fabricius, R. C. E. van den Bosch, J. C. Barentine, R. Bender, K. Gebhardt, G. J. Hill, J. D. Murphy, R. A. Swaters, J. Thomas, and G. van de Ven (2014). “Dwarf Galaxy Dark Matter Density Profiles Inferred from Stellar and Gas Kinematics”. *The Astrophysical Journal* 789, 63.
- Alexander, K. D., E. Berger, W. Fong, P. K. G. Williams, C. Guidorzi, R. Margutti, B. D. Metzger, J. Annis, P. K. Blanchard, D. Brout, D. A. Brown, H.-Y. Chen, R. Chornock, P. S. Cowperthwaite, M. Drout, T. Eftekhari, J. Frieman, D. E. Holz, M. Nicholl, A. Rest, M. Sako, M. Soares-Santos, and V. A. Villar (2017). “The Electromagnetic Counterpart of the Binary Neutron Star Merger LIGO/Virgo GW170817. VI. Radio Constraints on a Relativistic Jet and Predictions for Late-time Emission from the Kilonova Ejecta”. *The Astrophysical Journal* 848, L21.
- Aoki, M., Y. Ishimaru, W. Aoki, and S. Wanajo (2017). “Diversity of Abundance Patterns of Light Neutron-Capture Elements in Very-metal-poor Stars”. *The Astrophysical Journal* 837, 8.
- Aoki, W., T. Suda, R. N. Boyd, T. Kajino, and M. A. Famiano (2013). “Explaining the Sr and Ba Scatter in Extremely Metal-poor Stars”. *The Astrophysical Journal Letters* 766, L13.

- Arcavi, I., G. Hosseinzadeh, D. A. Howell, C. McCully, D. Poznanski, D. Kasen, J. Barnes, M. Zaltzman, S. Vasylyev, D. Maoz, and S. Valenti (2017a). “Optical emission from a kilonova following a gravitational-wave-detected neutron-star merger”. *Nature* 551, pp. 64–66.
- Arcavi, I., C. McCully, G. Hosseinzadeh, D. A. Howell, S. Vasylyev, D. Poznanski, M. Zaltzman, D. Maoz, L. Singer, S. Valenti, D. Kasen, J. Barnes, T. Piran, and W.-f. Fong (2017b). “Optical Follow-up of Gravitational-wave Events with Las Cumbres Observatory”. *The Astrophysical Journal Letters* 848, L33.
- Argast, D., M. Samland, O. E. Gerhard, and F.-K. Thielemann (2000). “Metal-poor halo stars as tracers of ISM mixing processes during halo formation”. *Astronomy and Astrophysics* 356, pp. 873–887.
- Argast, D., M. Samland, F.-K. Thielemann, and O. E. Gerhard (2002). “Implications of O and Mg abundances in metal-poor halo stars for stellar iron yields”. *Astronomy and Astrophysics* 388, pp. 842–860.
- Argast, D., M. Samland, F.-K. Thielemann, and Y.-Z. Qian (2004). “Neutron star mergers versus core-collapse supernovae as dominant r-process sites in the early Galaxy”. *Astronomy and Astrophysics* 416, pp. 997–1011.
- Arlandini, C., F. Käppeler, K. Wisshak, R. Gallino, M. Lugaro, M. Busso, and O. Straniero (1999). “Neutron Capture in Low-Mass Asymptotic Giant Branch Stars: Cross Sections and Abundance Signatures”. *The Astrophysical Journal* 525, pp. 886–900.
- Asplund, M., N. Grevesse, A. J. Sauval, and P. Scott (2009). “The Chemical Composition of the Sun”. *Annual Review of Astronomy and Astrophysics* 47, pp. 481–522.
- Barklem, P. S., N. Christlieb, T. C. Beers, V. Hill, M. S. Bessell, J. Holmberg, B. Marsteller, S. Rossi, F.-J. Zickgraf, and D. Reimers (2005). “The Hamburg/ESO R-process enhanced star survey (HERES). II. Spectroscopic analysis of the survey sample”. *Astronomy and Astrophysics* 439, pp. 129–151.
- Barnes, J. and P. Hut (1986). “A hierarchical $O(N \log N)$ force-calculation algorithm”. *Nature* 324, pp. 446–449.
- Bauswein, A., S. Goriely, and H.-T. Janka (2013). “Systematics of Dynamical Mass Ejection, Nucleosynthesis, and Radioactively Powered Electromagnetic Signals from Neutron-star Mergers”. *The Astrophysical Journal* 773, 78.
- Beers, T. C. and N. Christlieb (2005). “The Discovery and Analysis of Very Metal-Poor Stars in the Galaxy”. *Annual Review of Astronomy and Astrophysics* 43, pp. 531–580.
- Begeman, K. G., A. H. Broeils, and R. H. Sanders (1991). “Extended rotation curves of spiral galaxies - Dark haloes and modified dynamics”. *Monthly Notices of the Royal Astronomical Society* 249, pp. 523–537.
- Behroozi, P. S., R. H. Wechsler, and C. Conroy (2013). “The Average Star Formation Histories of Galaxies in Dark Matter Halos from $z = 0$ –8”. *The Astrophysical Journal* 770, 57.
- Bekki, K. and M. Chiba (2000). “Formation of the Galactic Stellar Halo: Origin of the Metallicity-Eccentricity Relation”. *The Astrophysical Journal Letters* 534, pp. L89–L92.
- (2001). “Formation of the Galactic Stellar Halo. I. Structure and Kinematics”. *The Astrophysical Journal* 558, pp. 666–686.

- Berger, E., W. Fong, and R. Chornock (2013). “An r-process Kilonova Associated with the Short-hard GRB 130603B”. *The Astrophysical Journal Letters* 774, L23.
- Binney, J. and S. Tremaine (2008). *Galactic Dynamics: Second Edition*. Princeton University Press.
- Bland-Hawthorn, J., R. Sutherland, and D. Webster (2015). “Ultrafaint Dwarf Galaxies the Lowest-mass Relics from Before Reionization”. *The Astrophysical Journal* 807, 154.
- Blumenthal, G. R., S. M. Faber, J. R. Primack, and M. J. Rees (1984). “Formation of galaxies and large-scale structure with cold dark matter”. *Nature* 311, pp. 517–525.
- Bubar, E. J. and J. R. King (2010). “Spectroscopic Abundances and Membership in the Wolf 630 Moving Group”. *The Astronomical Journal* 140, pp. 293–318.
- Buckley, D. A. H., I. Andreoni, S. Barway, J. Cooke, S. M. Crawford, E. Gorbovskoy, M. Gromadski, V. Lipunov, J. Mao, S. B. Potter, M. L. Pretorius, T. A. Pritchard, E. Romero-Colmenero, M. M. Shara, P. Vaisanen, and T. B. Williams (2018). “A comparison between SALT/SAAO observations and kilonova models for AT 2017gfo: the first electromagnetic counterpart of a gravitational wave transient - GW170817”. *Monthly Notices of the Royal Astronomical Society: Letters* 474, pp. L71–L75.
- Bullock, J. S. and K. V. Johnston (2005). “Tracing Galaxy Formation with Stellar Halos. I. Methods”. *The Astrophysical Journal* 635, pp. 931–949.
- Burbidge, E. M., G. R. Burbidge, W. A. Fowler, and F. Hoyle (1957). “Synthesis of the Elements in Stars”. *Reviews of Modern Physics* 29, pp. 547–650.
- Burkert, A. (2015). “The Structure and Dark Halo Core Properties of Dwarf Spheroidal Galaxies”. *The Astrophysical Journal* 808, 158.
- Burris, D. L., C. A. Pilachowski, T. E. Armandroff, C. Sneden, J. J. Cowan, and H. Roe (2000). “Neutron-Capture Elements in the Early Galaxy: Insights from a Large Sample of Metal-poor Giants”. *The Astrophysical Journal* 544, pp. 302–319.
- Cameron, A. G. W. (1957). “Stellar Evolution, Nuclear Astrophysics, and Nucleogenesis”. *Chalk River report*, CLR–41.
- Carraro, G., C. Chiosi, L. Girardi, and C. Lia (2001). “Dwarf elliptical galaxies: structure, star formation and colour-magnitude diagrams”. *Monthly Notices of the Royal Astronomical Society* 327, pp. 69–79.
- Cayrel, R., E. Depagne, M. Spite, V. Hill, F. Spite, P. François, B. Plez, T. Beers, F. Primas, J. Andersen, B. Barbuy, P. Bonifacio, P. Molaro, and B. Nordström (2004). “First stars V - Abundance patterns from C to Zn and supernova yields in the early Galaxy”. *Astronomy and Astrophysics* 416, pp. 1117–1138.
- Cescutti, G. and C. Chiappini (2014). “Explaining the Ba, Y, Sr, and Eu abundance scatter in metal-poor halo stars: constraints to the r-process”. *Astronomy and Astrophysics* 565, A51.
- Cescutti, G., C. Chiappini, R. Hirschi, G. Meynet, and U. Frischknecht (2013). “The s-process in the Galactic halo: the fifth signature of spinstars in the early Universe?” *Astronomy and Astrophysics* 553, A51.
- Cescutti, G., D. Romano, F. Matteucci, C. Chiappini, and R. Hirschi (2015). “The role of neutron star mergers in the chemical evolution of the Galactic halo”. *Astronomy and Astrophysics* 577, A139.

- Chabrier, G. (2003). “Galactic Stellar and Substellar Initial Mass Function”. *Publications of the Astronomical Society of the Pacific* 115, pp. 763–795.
- Chiappini, C., U. Frischknecht, G. Meynet, R. Hirschi, B. Barbuy, M. Pignatari, T. Decressin, and A. Maeder (2011). “Imprints of fast-rotating massive stars in the Galactic Bulge”. *Nature* 472, pp. 454–457.
- Chiba, M. and T. C. Beers (2000). “Kinematics of Metal-poor Stars in the Galaxy. III. Formation of the Stellar Halo and Thick Disk as Revealed from a Large Sample of Nonkinematically Selected Stars”. *The Astronomical Journal* 119, pp. 2843–2865.
- Chieffi, A. and M. Limongi (2004). “Explosive Yields of Massive Stars from $Z = 0$ to $Z = Z_{\text{solar}}$ ”. *The Astrophysical Journal* 608, 405–410 (CL04).
- Chiosi, C. and G. Carraro (2002). “Formation and evolution of elliptical galaxies”. *Monthly Notices of the Royal Astronomical Society* 335, pp. 335–357.
- Chornock, R. et al. (2017). “The Electromagnetic Counterpart of the Binary Neutron Star Merger LIGO/Virgo GW170817. IV. Detection of Near-infrared Signatures of r-process Nucleosynthesis with Gemini-South”. *The Astrophysical Journal Letters* 848, L19.
- Cohen, J. G. and W. Huang (2009). “The Chemical Evolution of the Draco Dwarf Spheroidal Galaxy”. *The Astrophysical Journal* 701, pp. 1053–1075.
- (2010). “The Chemical Evolution of the Ursa Minor Dwarf Spheroidal Galaxy”. *The Astrophysical Journal* 719, pp. 931–949.
- Cowperthwaite, P. S. et al. (2017). “The Electromagnetic Counterpart of the Binary Neutron Star Merger LIGO/Virgo GW170817. II. UV, Optical, and Near-infrared Light Curves and Comparison to Kilonova Models”. *The Astrophysical Journal Letters* 848, L17.
- Dalla Vecchia, C. and J. Schaye (2012). “Simulating galactic outflows with thermal supernova feedback”. *Monthly Notices of the Royal Astronomical Society* 426, pp. 140–158.
- Davé, R., N. Katz, B. D. Oppenheimer, J. A. Kollmeier, and D. H. Weinberg (2013). “The neutral hydrogen content of galaxies in cosmological hydrodynamic simulations”. *Monthly Notices of the Royal Astronomical Society* 434, pp. 2645–2663.
- Davidson, K., T. R. Gull, S. P. Maran, T. P. Stecher, R. A. Fesen, R. A. Parise, C. A. Harvel, M. Kafatos, and V. L. Trimble (1982). “The ultraviolet spectrum of the Crab Nebula”. *The Astrophysical Journal* 253, pp. 696–706.
- de Boer, T. J. L., E. Tolstoy, V. Hill, A. Saha, E. W. Olszewski, M. Mateo, E. Starkenburg, G. Battaglia, and M. G. Walker (2012a). “The star formation and chemical evolution history of the Fornax dwarf spheroidal galaxy”. *Astronomy and Astrophysics* 544, A73.
- de Boer, T. J. L., E. Tolstoy, V. Hill, A. Saha, K. Olsen, E. Starkenburg, B. Lemasle, M. J. Irwin, and G. Battaglia (2012b). “The star formation and chemical evolution history of the sculptor dwarf spheroidal galaxy”. *Astronomy and Astrophysics* 539, A103.
- de Boer, T. J. L., E. Tolstoy, B. Lemasle, A. Saha, E. W. Olszewski, M. Mateo, M. J. Irwin, and G. Battaglia (2014). “The episodic star formation history of the Carina dwarf spheroidal galaxy”. *Astronomy and Astrophysics* 572, A10.

- De Silva, G. M., K. C. Freeman, M. Asplund, J. Bland-Hawthorn, M. S. Bessell, and R. Collet (2007a). “Chemical Homogeneity in Collinder 261 and Implications for Chemical Tagging”. *The Astronomical Journal* 133, pp. 1161–1175.
- De Silva, G. M., K. C. Freeman, J. Bland-Hawthorn, M. Asplund, and M. S. Bessell (2007b). “Chemically Tagging the HR 1614 Moving Group”. *The Astronomical Journal* 133, pp. 694–704.
- De Silva, G. M., V. D’Orazi, C. Melo, C. A. O. Torres, M. Gieles, G. R. Quast, and M. Sterzik (2013). “Search for associations containing young stars: chemical tagging IC 2391 and the Argus association”. *Monthly Notices of the Royal Astronomical Society* 431, pp. 1005–1018.
- de Boer, T. J. L., V. Belokurov, and S. Koposov (2015). “The star formation history of the Sagittarius stream”. *Monthly Notices of the Royal Astronomical Society* 451, pp. 3489–3503.
- Dehnen, W. and H. Aly (2012). “Improving convergence in smoothed particle hydrodynamics simulations without pairing instability”. *Monthly Notices of the Royal Astronomical Society* 425, pp. 1068–1082.
- Dekel, A. and J. Silk (1986). “The origin of dwarf galaxies, cold dark matter, and biased galaxy formation”. *The Astrophysical Journal* 303, pp. 39–55.
- Dekel, A. and J. Woo (2003). “Feedback and the fundamental line of low-luminosity low-surface-brightness/dwarf galaxies”. *Monthly Notices of the Royal Astronomical Society* 344, pp. 1131–1144.
- Díaz, M. C. et al. (2017). “Observations of the First Electromagnetic Counterpart to a Gravitational-wave Source by the TOROS Collaboration”. *The Astrophysical Journal Letters* 848, L29.
- Doherty, C. L., P. Gil-Pons, L. Siess, J. C. Lattanzio, and H. H. B. Lau (2015). “Super- and massive AGB stars - IV. Final fates - initial-to-final mass relation”. *Monthly Notices of the Royal Astronomical Society* 446, pp. 2599–2612.
- Doherty, C. L., P. Gil-Pons, L. Siess, and J. C. Lattanzio (2017). “Super-AGB Stars and their Role as Electron Capture Supernova Progenitors”. *Publications of the Astronomical Society of Australia* 34, e056.
- Dominik, M., K. Belczynski, C. Fryer, D. E. Holz, E. Berti, T. Bulik, I. Mandel, and R. O’Shaughnessy (2012). “Double Compact Objects. I. The Significance of the Common Envelope on Merger Rates”. *The Astrophysical Journal* 759, 52.
- Duffau, S. et al. (2017). “The Gaia-ESO Survey: Galactic evolution of sulphur and zinc”. *Astronomy and Astrophysics* 604, A128.
- Eggen, O. J., D. Lynden-Bell, and A. R. Sandage (1962). “Evidence from the motions of old stars that the Galaxy collapsed.” *The Astrophysical Journal* 136, p. 748.
- Eichler, D., M. Livio, T. Piran, and D. N. Schramm (1989). “Nucleosynthesis, neutrino bursts and gamma-rays from coalescing neutron stars”. *Nature* 340, pp. 126–128.
- Elmegreen, B. G. and J. Scalo (2004). “Interstellar Turbulence I: Observations and Processes”. *Annual Review of Astronomy and Astrophysics* 42, pp. 211–273.
- Feng, Y. and M. R. Krumholz (2014). “Early turbulent mixing as the origin of chemical homogeneity in open star clusters”. *Nature* 513, pp. 523–525.
- Ferland, G. J., K. T. Korista, D. A. Verner, J. W. Ferguson, J. B. Kingdon, and E. M. Verner (1998). “CLOUDY 90: Numerical Simulation of Plasmas and Their Spectra”. *Publications of the Astronomical Society of the Pacific* 110, pp. 761–778.

- Ferland, G. J., R. L. Porter, P. A. M. van Hoof, R. J. R. Williams, N. P. Abel, M. L. Lykins, G. Shaw, W. J. Henney, and P. C. Stancil (2013). “The 2013 Release of Cloudy”. *Revista Mexicana de Astronomía y Astrofísica* 49, pp. 137–163.
- Fernández, R. and B. D. Metzger (2016). “Electromagnetic Signatures of Neutron Star Mergers in the Advanced LIGO Era”. *Annual Review of Nuclear and Particle Science* 66, pp. 23–45.
- Fioc, M. and B. Rocca-Volmerange (1997). “PEGASE: a UV to NIR spectral evolution model of galaxies. Application to the calibration of bright galaxy counts.” *Astronomy and Astrophysics* 326, pp. 950–962.
- François, P., F. Matteucci, R. Cayrel, M. Spite, F. Spite, and C. Chiappini (2004). “The evolution of the Milky Way from its earliest phases: Constraints on stellar nucleosynthesis”. *Astronomy and Astrophysics* 421, pp. 613–621.
- François, P., E. Depagne, V. Hill, M. Spite, F. Spite, B. Plez, T. C. Beers, J. Andersen, G. James, B. Barbuy, R. Cayrel, P. Bonifacio, P. Molaro, B. Nordström, and F. Primas (2007). “First stars. VIII. Enrichment of the neutron-capture elements in the early Galaxy”. *Astronomy and Astrophysics* 476, pp. 935–950.
- Frebel, A., E. N. Kirby, and J. D. Simon (2010). “Linking dwarf galaxies to halo building blocks with the most metal-poor star in Sculptor”. *Nature* 464, pp. 72–75.
- Frebel, A. and J. E. Norris (2015). “Near-Field Cosmology with Extremely Metal-Poor Stars”. *Annual Review of Astronomy and Astrophysics* 53, pp. 631–688.
- Frebel, A., J. D. Simon, and E. N. Kirby (2014). “Segue 1: An Unevolved Fossil Galaxy from the Early Universe”. *The Astrophysical Journal* 786, 74.
- Frebel, A., J. D. Simon, M. Geha, and B. Willman (2010). “High-Resolution Spectroscopy of Extremely Metal-Poor Stars in the Least Evolved Galaxies: Ursa Major II and Coma Berenices”. *The Astrophysical Journal* 708, pp. 560–583.
- Freiburghaus, C., S. Rosswog, and F.-K. Thielemann (1999). “R-Process in Neutron Star Mergers”. *The Astrophysical Journal Letters* 525, pp. L121–L124.
- Fulbright, J. P. (2000). “Abundances and Kinematics of Field Halo and Disk Stars. I. Observational Data and Abundance Analysis”. *The Astronomical Journal* 120, pp. 1841–1852.
- Gaia Collaboration, A. G. A. Brown, A. Vallenari, T. Prusti, J. H. J. de Bruijne, F. Mignard, R. Drimmel, C. Babusiaux, C. A. L. Bailer-Jones, U. Bastian, and et al. (2016a). “Gaia Data Release 1. Summary of the astrometric, photometric, and survey properties”. *Astronomy and Astrophysics* 595, A2.
- Gaia Collaboration, T. Prusti, J. H. J. de Bruijne, A. G. A. Brown, A. Vallenari, C. Babusiaux, C. A. L. Bailer-Jones, U. Bastian, M. Biermann, D. W. Evans, and et al. (2016b). “The Gaia mission”. *Astronomy and Astrophysics* 595, A1.
- Geisler, D., V. V. Smith, G. Wallerstein, G. Gonzalez, and C. Charbonnel (2005). ““Sculptor-ing” the Galaxy? The Chemical Compositions of Red Giants in the Sculptor Dwarf Spheroidal Galaxy”. *The Astronomical Journal* 129, pp. 1428–1442.
- Gill, S. P. D., A. Knebe, and B. K. Gibson (2004). “The evolution of substructure - I. A new identification method”. *Monthly Notices of the Royal Astronomical Society* 351, pp. 399–409.

- Gilmore, G., J. E. Norris, L. Monaco, D. Yong, R. F. G. Wyse, and D. Geisler (2013). “Elemental Abundances and their Implications for the Chemical Enrichment of the Boötes I Ultrafaint Galaxy”. *The Astrophysical Journal* 763, 61.
- Gingold, R. A. and J. J. Monaghan (1977). “Smoothed particle hydrodynamics - Theory and application to non-spherical stars”. *Monthly Notices of the Royal Astronomical Society* 181, pp. 375–389.
- Goldstein, A., P. Veres, E. Burns, M. S. Briggs, R. Hamburg, D. Kocevski, C. A. Wilson-Hodge, R. D. Preece, S. Poolakkil, O. J. Roberts, C. M. Hui, V. Connaughton, J. Racusin, A. von Kienlin, T. Dal Canton, N. Christensen, T. Littenberg, K. Siellez, L. Blackburn, J. Broida, E. Bissaldi, W. H. Cleveland, M. H. Gibby, M. M. Giles, R. M. Kippen, S. McBreen, J. McEnery, C. A. Meegan, W. S. Paciesas, and M. Stanbro (2017). “An Ordinary Short Gamma-Ray Burst with Extraordinary Implications: Fermi-GBM Detection of GRB 170817A”. *The Astrophysical Journal Letters* 848, L14.
- Goriely, S., A. Bauswein, and H.-T. Janka (2011). “r-process Nucleosynthesis in Dynamically Ejected Matter of Neutron Star Mergers”. *The Astrophysical Journal Letters* 738, L32.
- Goswami, A. and N. Prantzos (2000). “Abundance evolution of intermediate mass elements (C to Zn) in the Milky Way halo and disk”. *Astronomy and Astrophysics* 359, pp. 191–212.
- Governato, F., C. Brook, L. Mayer, A. Brooks, G. Rhee, J. Wadsley, P. Jonsson, B. Willman, G. Stinson, T. Quinn, and P. Madau (2010). “Bulgeless dwarf galaxies and dark matter cores from supernova-driven outflows”. *Nature* 463, pp. 203–206.
- Greif, T. H., S. C. O. Glover, V. Bromm, and R. S. Klessen (2009). “Chemical mixing in smoothed particle hydrodynamics simulations”. *Monthly Notices of the Royal Astronomical Society* 392, pp. 1381–1387.
- Guetta, D. and M. Della Valle (2007). “On the Rates of Gamma-Ray Bursts and Type Ib/c Supernovae”. *The Astrophysical Journal Letters* 657, pp. L73–L76.
- Haardt, F. and P. Madau (2012). “Radiative Transfer in a Clumpy Universe. IV. New Synthesis Models of the Cosmic UV/X-Ray Background”. *The Astrophysical Journal* 746, 125.
- Haggard, D., M. Nynka, J. J. Ruan, V. Kalogera, S. B. Cenko, P. Evans, and J. A. Kennea (2017). “A Deep Chandra X-Ray Study of Neutron Star Coalescence GW170817”. *The Astrophysical Journal Letters* 848, L25.
- Hahn, O. and T. Abel (2011). “Multi-scale initial conditions for cosmological simulations”. *Monthly Notices of the Royal Astronomical Society* 415, pp. 2101–2121.
- Hansen, C. J., A. C. Andersen, and N. Christlieb (2014). “Stellar abundances and presolar grains trace the nucleosynthetic origin of molybdenum and ruthenium”. *Astronomy and Astrophysics* 568, A47.
- Helmi, A., M. J. Irwin, E. Tolstoy, G. Battaglia, V. Hill, P. Jablonka, K. Venn, M. Shetrone, B. Letarte, N. Arimoto, T. Abel, P. Francois, A. Kaufer, F. Primas, K. Sadakane, and T. Szeifert (2006). “A New View of the Dwarf Spheroidal Satellites of the Milky Way from VLT FLAMES: Where Are the Very Metal-poor Stars?” *The Astrophysical Journal Letters* 651, pp. L121–L124.
- Hernquist, L. (1993). “N-body realizations of compound galaxies”. *The Astrophysical Journals* 86, pp. 389–400.

- Heyer, M., C. Krawczyk, J. Duval, and J. M. Jackson (2009). “Re-Examining Larson’s Scaling Relationships in Galactic Molecular Clouds”. *The Astrophysical Journal* 699, pp. 1092–1103.
- Hill, V. and DART Collaboration (2012). “Abundance Patterns and the Chemical Enrichment of Nearby Dwarf Galaxies”. *Galactic Archaeology: Near-Field Cosmology and the Formation of the Milky Way*. Ed. by W. Aoki, M. Ishigaki, T. Suda, T. Tsujimoto, and N. Arimoto. Vol. 458. Astronomical Society of the Pacific Conference Series, p. 297.
- Hill, V., B. Plez, R. Cayrel, T. C. Beers, B. Nordström, J. Andersen, M. Spite, F. Spite, B. Barbuy, P. Bonifacio, E. Depagne, P. François, and F. Primas (2002). “First stars. I. The extreme r-element rich, iron-poor halo giant CS 31082-001. Implications for the r-process site(s) and radioactive cosmochronology”. *Astronomy and Astrophysics* 387, pp. 560–579.
- Hillebrandt, W., K. Nomoto, and R. G. Wolff (1984). “Supernova explosions of massive stars - The mass range 8 to 10 solar masses”. *Astronomy and Astrophysics* 133, pp. 175–184.
- Hirai, Y. and T. R. Saitoh (2017). “Efficiency of Metal Mixing in Dwarf Galaxies”. *The Astrophysical Journal Letters* 838, L23.
- Hirai, Y., Y. Ishimaru, T. R. Saitoh, M. S. Fujii, J. Hidaka, and T. Kajino (2015). “Enrichment of r-process Elements in Dwarf Spheroidal Galaxies in Chemo-dynamical Evolution Model”. *The Astrophysical Journal* 814, 41.
- (2017). “Early chemo-dynamical evolution of dwarf galaxies deduced from enrichment of r-process elements”. *Monthly Notices of the Royal Astronomical Society* 466, pp. 2474–2487.
- Hirai, Y., T. R. Saitoh, Y. Ishimaru, and S. Wanajo (2018). “Enrichment of Zinc in galactic chemodynamical evolution models”. *The Astrophysical Journal in press* (*arXiv: 1801.08141*).
- Hitomi Collaboration et al. (2017). “Solar abundance ratios of the iron-peak elements in the Perseus cluster”. *Nature* 551, pp. 478–480.
- Homma, H., T. Murayama, M. A. R. Kobayashi, and Y. Taniguchi (2015). “A New Chemical Evolution Model for Dwarf Spheroidal Galaxies Based on Observed Long Star Formation Histories”. *The Astrophysical Journal* 799, 230.
- Honda, S., W. Aoki, T. Kajino, H. Ando, T. C. Beers, H. Izumiura, K. Sadakane, and M. Takada-Hidai (2004). “Spectroscopic Studies of Extremely Metal-Poor Stars with the Subaru High Dispersion Spectrograph. II. The r-Process Elements, Including Thorium”. *The Astrophysical Journal* 607, pp. 474–498.
- Honda, S., W. Aoki, N. Arimoto, and K. Sadakane (2011). “Enrichment of Heavy Elements in the Red Giant S 15-19 in the Sextans Dwarf Spheroidal Galaxy”. *Publications of the Astronomical Society of Japan* 63, pp. 523–529.
- Hopkins, P. F. (2013). “A general class of Lagrangian smoothed particle hydrodynamics methods and implications for fluid mixing problems”. *Monthly Notices of the Royal Astronomical Society* 428, pp. 2840–2856.
- Hopkins, P. F., E. Quataert, and N. Murray (2011). “Self-regulated star formation in galaxies via momentum input from massive stars”. *Monthly Notices of the Royal Astronomical Society* 417, pp. 950–973.

- Hopkins, P. F., D. Kereš, J. Oñorbe, C.-A. Faucher-Giguère, E. Quataert, N. Murray, and J. S. Bullock (2014). “Galaxies on FIRE (Feedback In Realistic Environments): stellar feedback explains cosmologically inefficient star formation”. *Monthly Notices of the Royal Astronomical Society* 445, pp. 581–603.
- Horiuti, K. (1987). “Comparison of Conservative and Rotational Forms in Large Eddy Simulation of Turbulent Channel Flow”. *Journal of Computational Physics* 71, pp. 343–370.
- Horowitz, C. J., G. Shen, E. O’Connor, and C. D. Ott (2012). “Charged-current neutrino interactions in core-collapse supernovae in a virial expansion”. *Physical Review C* 86.6, 065806.
- Hotokezaka, K., K. Kiuchi, K. Kyutoku, H. Okawa, Y.-i. Sekiguchi, M. Shibata, and K. Taniguchi (2013). “Mass Ejection from the merger of binary neutron stars”. *Physical Review D* 87.2, 024001.
- Irwin, M. and D. Hatzidimitriou (1995). “Structural parameters for the Galactic dwarf spheroidals”. *Monthly Notices of the Royal Astronomical Society* 277, pp. 1354–1378.
- Ishigaki, M. N., W. Aoki, and M. Chiba (2013). “Chemical Abundances of the Milky Way Thick Disk and Stellar Halo. II. Sodium, Iron-peak, and Neutron-capture Elements”. *The Astrophysical Journal* 771, 67.
- Ishimaru, Y. and S. Wanajo (1999). “Enrichment of the R-Process Element Europium in the Galactic Halo”. *The Astrophysical Journal Letters* 511, pp. L33–L36.
- Ishimaru, Y., S. Wanajo, and N. Prantzos (2006). “Chemical evolution of C-Zn and r-process elements produced by the first generation stars”. *International Symposium on Nuclear Astrophysics - Nuclei in the Cosmos*, p. 37.1.
- (2015). “Neutron Star Mergers as the Origin of r-process Elements in the Galactic Halo Based on the Sub-halo Clustering Scenario”. *The Astrophysical Journal Letters* 804, L35.
- Ishimaru, Y., S. Wanajo, W. Aoki, and S. G. Ryan (2004). “The Detection of Low Eu Abundances in Extremely Metal-poor Stars and the Origin of r-Process Elements”. *The Astrophysical Journal Letters* 600, pp. L47–L50.
- Janka, H.-T., T. Melson, and A. Summa (2016). “Physics of Core-Collapse Supernovae in Three Dimensions: A Sneak Preview”. *Annual Review of Nuclear and Particle Science* 66, pp. 341–375.
- Janka, H.-T., B. Müller, F. S. Kitaura, and R. Buras (2008). “Dynamics of shock propagation and nucleosynthesis conditions in O-Ne-Mg core supernovae”. *Astronomy and Astrophysics* 485, pp. 199–208.
- Janka, H.-T., F. Hanke, L. Hüdepohl, A. Marek, B. Müller, and M. Obergaulinger (2012). “Core-collapse supernovae: Reflections and directions”. *Progress of Theoretical and Experimental Physics* 2012.1, 01A309, 01A309.
- Jeon, M., G. Besla, and V. Bromm (2017). “Connecting the First Galaxies with Ultrafaint Dwarfs in the Local Group: Chemical Signatures of Population III Stars”. *The Astrophysical Journal* 848, 85, p. 85.
- Ji, A. P., A. Frebel, and V. Bromm (2015). “Preserving chemical signatures of primordial star formation in the first low-mass stars”. *Monthly Notices of the Royal Astronomical Society* 454, pp. 659–674.

- Ji, A. P., A. Frebel, J. D. Simon, and A. Chiti (2016a). “Complete Element Abundances of Nine Stars in the r-process Galaxy Reticulum II”. *The Astrophysical Journal* 830, 93.
- Ji, A. P., A. Frebel, A. Chiti, and J. D. Simon (2016b). “R-process enrichment from a single event in an ancient dwarf galaxy”. *Nature* 531, pp. 610–613.
- Johnson, J. A. (2002). “Abundances of 30 Elements in 23 Metal-Poor Stars”. *The Astrophysical Journals* 139, pp. 219–247.
- Jones, S., R. Hirschi, and K. Nomoto (2014). “The Final Fate of Stars that Ignite Neon and Oxygen Off-center: Electron Capture or Iron Core-collapse Supernova?” *The Astrophysical Journal* 797, 83.
- Jones, S., R. Hirschi, K. Nomoto, T. Fischer, F. X. Timmes, F. Herwig, B. Paxton, H. Toki, T. Suzuki, G. Martínez-Pinedo, Y. H. Lam, and M. G. Bertolli (2013). “Advanced Burning Stages and Fate of 8-10 M \odot Stars”. *The Astrophysical Journal* 772, 150.
- Karlsson, T., V. Bromm, and J. Bland-Hawthorn (2013). “Pregalactic metal enrichment: The chemical signatures of the first stars”. *Reviews of Modern Physics* 85, pp. 809–848.
- Katz, N. (1992). “Dissipational galaxy formation. II - Effects of star formation”. *The Astrophysical Journal* 391, pp. 502–517.
- Katz, N. and J. E. Gunn (1991). “Dissipational galaxy formation. I - Effects of gasdynamics”. *The Astrophysical Journal* 377, pp. 365–381.
- Katz, N., D. H. Weinberg, and L. Hernquist (1996). “Cosmological Simulations with TreeSPH”. *The Astrophysical Journals* 105, p. 19.
- Kawata, D. (2001). “Effects of Type II and Type Ia Supernovae Feedback on the Chemodynamical Evolution of Elliptical Galaxies”. *The Astrophysical Journal* 558, pp. 598–614.
- Kawata, D. and B. K. Gibson (2003). “GCD+: a new chemodynamical approach to modelling supernovae and chemical enrichment in elliptical galaxies”. *Monthly Notices of the Royal Astronomical Society* 340, pp. 908–922.
- Kim, S. et al. (2017). “ALMA and GMRT Constraints on the Off-axis Gamma-Ray Burst 170817A from the Binary Neutron Star Merger GW170817”. *The Astrophysical Journal Letters* 850, L21.
- Kinugawa, T., K. Inayoshi, K. Hotokezaka, D. Nakauchi, and T. Nakamura (2014). “Possible indirect confirmation of the existence of Pop III massive stars by gravitational wave”. *Monthly Notices of the Royal Astronomical Society* 442, pp. 2963–2992.
- Kirby, E. N. and J. G. Cohen (2012). “Detailed Abundances of Two Very Metal-poor Stars in Dwarf Galaxies”. *The Astronomical Journal* 144, 168.
- Kirby, E. N., J. D. Simon, M. Geha, P. Guhathakurta, and A. Frebel (2008). “Uncovering Extremely Metal-Poor Stars in the Milky Way’s Ultrafaint Dwarf Spheroidal Satellite Galaxies”. *The Astrophysical Journal Letters* 685, L43, p. L43.
- Kirby, E. N., P. Guhathakurta, M. Bolte, C. Sneden, and M. C. Geha (2009). “Multi-element Abundance Measurements from Medium-resolution Spectra. I. The Sculptor Dwarf Spheroidal Galaxy”. *The Astrophysical Journal* 705, pp. 328–346.
- Kirby, E. N., P. Guhathakurta, J. D. Simon, M. C. Geha, C. M. Rockosi, C. Sneden, J. G. Cohen, S. T. Sohn, S. R. Majewski, and M. Siegel (2010). “Multi-element

- Abundance Measurements from Medium-resolution Spectra. II. Catalog of Stars in Milky Way Dwarf Satellite Galaxies”. *The Astrophysical Journal Supplement Series* 191, pp. 352–375.
- Kirby, E. N., J. G. Cohen, P. Guhathakurta, L. Cheng, J. S. Bullock, and A. Galazzi (2013). “The Universal Stellar Mass-Stellar Metallicity Relation for Dwarf Galaxies”. *The Astrophysical Journal* 779, 102.
- Kitaura, F. S., H.-T. Janka, and W. Hillebrandt (2006). “Explosions of O-Ne-Mg cores, the Crab supernova, and subluminal type II-P supernovae”. *Astronomy and Astrophysics* 450, pp. 345–350.
- Knollmann, S. R. and A. Knebe (2009). “AHF: Amiga’s Halo Finder”. *The Astrophysical Journals* 182, pp. 608–624.
- Kobayashi, C. (2004). “GRAPE-SPH chemodynamical simulation of elliptical galaxies - I. Evolution of metallicity gradients”. *Monthly Notices of Royal Astronomical Society* 347, pp. 740–758.
- Kobayashi, C., A. I. Karakas, and H. Umeda (2011). “The evolution of isotope ratios in the Milky Way Galaxy”. *Monthly Notices of the Royal Astronomical Society* 414, pp. 3231–3250.
- Kobayashi, C. and N. Nakasato (2011). “Chemodynamical Simulations of the Milky Way Galaxy”. *The Astrophysical Journal* 729, 16.
- Kobayashi, C. and K. Nomoto (2009). “The Role of Type Ia Supernovae in Chemical Evolution. I. Lifetime of Type Ia Supernovae and Metallicity Effect”. *The Astrophysical Journal* 707, pp. 1466–1484.
- Kobayashi, C., H. Umeda, K. Nomoto, N. Tominaga, and T. Ohkubo (2006). “Galactic Chemical Evolution: Carbon through Zinc”. *The Astrophysical Journal* 653, pp. 1145–1171.
- Koch, A., E. K. Grebel, G. F. Gilmore, R. F. G. Wyse, J. T. Kleyna, D. R. Harbeck, M. I. Wilkinson, and N. Wyn Evans (2008). “Complexity on Small Scales. III. Iron and α Element Abundances in the Carina Dwarf Spheroidal Galaxy”. *The Astronomical Journal* 135, pp. 1580–1597.
- Komiya, Y. and T. Shigeyama (2016). “Contribution of Neutron Star Mergers to the r-Process Chemical Evolution in the Hierarchical Galaxy Formation”. *The Astrophysical Journal* 830, 76.
- Komiya, Y., S. Yamada, T. Suda, and M. Y. Fujimoto (2014). “The New Model of Chemical Evolution of r-process Elements Based on the Hierarchical Galaxy Formation. I. Ba and Eu”. *The Astrophysical Journal* 783, 132.
- Korobkin, O., S. Rosswog, A. Arcones, and C. Winteler (2012). “On the astrophysical robustness of the neutron star merger r-process”. *Monthly Notices of the Royal Astronomical Society* 426, pp. 1940–1949.
- Kratz, K.-L., J.-P. Bitouzet, F.-K. Thielemann, P. Moeller, and B. Pfeiffer (1993). “Isotopic r-process abundances and nuclear structure far from stability - Implications for the r-process mechanism”. *The Astrophysical Journal* 403, pp. 216–238.
- Kroupa, P. (2001). “On the variation of the initial mass function”. *Monthly Notices of the Royal Astronomical Society* 322, pp. 231–246.
- Krumholz, M. R. and J. C. Tan (2007). “Slow Star Formation in Dense Gas: Evidence and Implications”. *The Astrophysical Journal* 654, pp. 304–315.

- Kuroda, K. and LCGT Collaboration (2010). “Status of LCGT”. *Classical and Quantum Gravity* 27.8, 084004.
- Lada, C. J. and E. A. Lada (2003). “Embedded Clusters in Molecular Clouds”. *Annual Review of Astronomy and Astrophysics* 41, pp. 57–115.
- Larson, R. B. (1981). “Turbulence and star formation in molecular clouds”. *Monthly Notices of the Royal Astronomical Society* 194, pp. 809–826.
- Lattimer, J. M. and D. N. Schramm (1974). “Black-hole-neutron-star collisions”. *The Astrophysical Journal Letters* 192, pp. L145–L147.
- (1976). “The tidal disruption of neutron stars by black holes in close binaries”. *The Astrophysical Journal* 210, pp. 549–567.
- Lattimer, J. M., F. Mackie, D. G. Ravenhall, and D. N. Schramm (1977). “The decomposition of cold neutron star matter”. *The Astrophysical Journal* 213, pp. 225–233.
- Lee, D. M., K. V. Johnston, J. Tumlinson, B. Sen, and J. D. Simon (2013). “A Mass-dependent Yield Origin of Neutron-Capture Element Abundance Distributions in Ultra-faint Dwarfs”. *The Astrophysical Journal* 774, 103.
- Lee, D. M., K. V. Johnston, B. Sen, and W. Jessop (2015). “Reconstructing the Accretion History of the Galactic Stellar Halo from Chemical Abundance Ratio Distributions”. *The Astrophysical Journal* 802, 48.
- Lemasle, B., V. Hill, E. Tolstoy, K. A. Venn, M. D. Shetrone, M. J. Irwin, T. J. L. de Boer, E. Starkenburg, and S. Salvadori (2012). “VLT/FLAMES spectroscopy of red giant branch stars in the Carina dwarf spheroidal galaxy”. *Astronomy and Astrophysics* 538, A100.
- Letarte, B. (2007). “Chemical Analysis of the Fornax Dwarf Galaxy”. PhD thesis. University of Groningen.
- Letarte, B., V. Hill, E. Tolstoy, P. Jablonka, M. Shetrone, K. A. Venn, M. Spite, M. J. Irwin, G. Battaglia, A. Helmi, F. Primas, P. François, A. Kaufer, T. Szeifert, N. Arimoto, and K. Sadakane (2010). “A high-resolution VLT/FLAMES study of individual stars in the centre of the Fornax dwarf spheroidal galaxy”. *Astronomy and Astrophysics* 523, A17.
- Li, T. et al. (2018). “Insight-HXMT observations of the first binary neutron star merger GW170817”. *Science China Physics, Mechanics, and Astronomy* 61.3, 31011.
- Limongi, M. and A. Chieffi (2012). “Presupernova Evolution and Explosive Nucleosynthesis of Zero Metal Massive Stars”. *The Astrophysical Journal Supplement* 199, 38.
- Lipunov, V. M. et al. (2017). “MASTER Optical Detection of the First LIGO/Virgo Neutron Star Binary Merger GW170817”. *The Astrophysical Journal Letters* 850, L1.
- Liszt, H. S., X. Delin, and W. B. Burton (1981). “Properties of the galactic molecular cloud ensemble from observations of $^{13}\text{C}/^{18}\text{O}$ ”. *The Astrophysical Journal* 249, pp. 532–549.
- Lodders, K. (2003). “Solar System Abundances and Condensation Temperatures of the Elements”. *The Astrophysical Journal* 591, pp. 1220–1247.
- Lorimer, D. R. (2008). “Binary and Millisecond Pulsars”. *Living Reviews in Relativity* 11, p. 8.

- Lu, Y., R. H. Wechsler, R. S. Somerville, D. Croton, L. Porter, J. Primack, P. S. Behroozi, H. C. Ferguson, D. C. Koo, Y. Guo, M. Safarzadeh, K. Finlator, M. Castellano, C. E. White, V. Sommariva, and C. Moody (2014). “Semi-analytic Models for the CANDELS Survey: Comparison of Predictions for Intrinsic Galaxy Properties”. *The Astrophysical Journal* 795, 123.
- Lucy, L. B. (1977). “A numerical approach to the testing of the fission hypothesis”. *The Astronomical Journal* 82, pp. 1013–1024.
- Ma, X., P. F. Hopkins, C.-A. Faucher-Giguère, N. Zolman, A. L. Muratov, D. Kereš, and E. Quataert (2016). “The origin and evolution of the galaxy mass-metallicity relation”. *Monthly Notices of the Royal Astronomical Society* 456, pp. 2140–2156.
- Makino, J. (1991). “A Modified Aarseth Code for GRAPE and Vector Processors”. *Publications of the Astronomical Society of Japan* 43, pp. 859–876.
- (2004). “A Fast Parallel Treecode with GRAPE”. *Publications of the Astronomical Society of Japan* 56, pp. 521–531.
- Maoz, D. and F. Mannucci (2012). “Type-Ia Supernova Rates and the Progenitor Problem: A Review”. *Publication of the Astronomical Society of Australia* 29, pp. 447–465.
- Maoz, D., F. Mannucci, and G. Nelemans (2014). “Observational Clues to the Progenitors of Type Ia Supernovae”. *Annual Review of Astronomy and Astrophysics* 52, pp. 107–170.
- Margutti, R., E. Berger, W. Fong, C. Guidorzi, K. D. Alexander, B. D. Metzger, P. K. Blanchard, P. S. Cowperthwaite, R. Chornock, T. Eftekhari, M. Nicholl, V. A. Villar, P. K. G. Williams, J. Annis, D. A. Brown, H. Chen, Z. Doctor, J. A. Frieman, D. E. Holz, M. Sako, and M. Soares-Santos (2017). “The Electromagnetic Counterpart of the Binary Neutron Star Merger LIGO/Virgo GW170817. V. Rising X-Ray Emission from an Off-axis Jet”. *The Astrophysical Journal* 848, L20.
- Martínez-Pinedo, G., T. Fischer, A. Lohs, and L. Huther (2012). “Charged-Current Weak Interaction Processes in Hot and Dense Matter and its Impact on the Spectra of Neutrinos Emitted from Protoneutron Star Cooling”. *Physical Review Letters* 109.25, 251104.
- Mathews, G. J., G. Bazan, and J. J. Cowan (1992). “Evolution of heavy-element abundances as a constraint on sites for neutron-capture nucleosynthesis”. *The Astrophysical Journal* 391, pp. 719–735.
- Mathews, G. J. and J. J. Cowan (1990). “New insights into the astrophysical r-process”. *Nature* 345, pp. 491–494.
- Matteucci, F., ed. (2001). *The chemical evolution of the Galaxy*. Vol. 253. Astrophysics and Space Science Library.
- Matteucci, F. and E. Brocato (1990). “Metallicity distribution and abundance ratios in the stars of the Galactic bulge”. *The Astrophysical Journal* 365, pp. 539–543.
- Matteucci, F., C. M. Raiteri, M. Busson, R. Gallino, and R. Gratton (1993). “Constraints on the nucleosynthesis of Cu and Zn from models of chemical evolution of the Galaxy”. *Astronomy and Astrophysics* 272, p. 421.
- Matteucci, F., D. Romano, A. Arcones, O. Korobkin, and S. Rosswog (2014). “Europium production: neutron star mergers versus core-collapse supernovae”. *Monthly Notices of the Royal Astronomical Society* 438, pp. 2177–2185.

- Mayer, L., C. Mastropietro, J. Wadsley, J. Stadel, and B. Moore (2006). “Simultaneous ram pressure and tidal stripping; how dwarf spheroidals lost their gas”. *Monthly Notices of the Royal Astronomical Society* 369, pp. 1021–1038.
- McConnachie, A. W. (2012). “The Observed Properties of Dwarf Galaxies in and around the Local Group”. *The Astronomical Journal* 144, 4.
- McCully, C., D. Hiramatsu, D. A. Howell, G. Hosseinzadeh, I. Arcavi, D. Kasen, J. Barnes, M. M. Shara, T. B. Williams, P. Väisänen, S. B. Potter, E. Romero-Colmenero, S. M. Crawford, D. A. H. Buckley, J. Cooke, I. Andreoni, T. A. Pritchard, J. Mao, M. Gromadzki, and J. Burke (2017). “The Rapid Reddening and Featureless Optical Spectra of the Optical Counterpart of GW170817, AT 2017gfo, during the First Four Days”. *The Astrophysical Journal Letters* 848, L32.
- McMillan, S. L. W. (1986). “The Vectorization of Small-N Integrators”. *The Use of Supercomputers in Stellar Dynamics*. Ed. by P. Hut and S. L. W. McMillan. Vol. 267. Lecture Notes in Physics, Berlin Springer Verlag, p. 156.
- McWilliam, A. and T. A. Smecker-Hane (2005). “The Composition of the Sagittarius Dwarf Spheroidal Galaxy, and Implications for Nucleosynthesis and Chemical Evolution”. *Cosmic Abundances as Records of Stellar Evolution and Nucleosynthesis*. Ed. by T. G. Barnes III and F. N. Bash. Vol. 336. Astronomical Society of the Pacific Conference Series, p. 221.
- McWilliam, A., G. W. Preston, C. Sneden, and L. Searle (1995). “Spectroscopic Analysis of 33 of the Most Metal Poor Stars. II.” *The Astronomical Journal* 109, p. 2757.
- Meneveau, C. and J. Katz (2000). “Scale-Invariance and Turbulence Models for Large-Eddy Simulation”. *Annual Review of Fluid Mechanics* 32, pp. 1–32.
- Mennekens, N. and D. Vanbeveren (2014). “Massive double compact object mergers: gravitational wave sources and r-process element production sites”. *Astronomy and Astrophysics* 564, A134.
- Meyer, B. S. (1989). “Decompression of initially cold neutron star matter - A mechanism for the r-process?” *The Astrophysical Journal* 343, pp. 254–276.
- Meyer, B. S., G. J. Mathews, W. M. Howard, S. E. Woosley, and R. D. Hoffman (1992). “R-process nucleosynthesis in the high-entropy supernova bubble”. *The Astrophysical Journal* 399, pp. 656–664.
- Miyaji, S. and K. Nomoto (1987). “On the collapse of 8-10 solar mass stars due to electron capture”. *The Astrophysical Journal* 318, pp. 307–315.
- Miyaji, S., K. Nomoto, K. Yokoi, and D. Sugimoto (1980). “Supernova Triggered by Electron Captures”. *Publications of the Astronomical Society of Japan* 32, p. 303.
- Monaco, L., M. Bellazzini, P. Bonifacio, F. R. Ferraro, G. Marconi, E. Pancino, L. Sbordone, and S. Zaggia (2005). “The Ital-FLAMES survey of the Sagittarius dwarf spheroidal galaxy. I. Chemical abundances of bright RGB stars”. *Astronomy and Astrophysics* 441, pp. 141–151.
- Monaghan, J. J. (1992). “Smoothed particle hydrodynamics”. *Annual Review of Astronomy and Astrophysics* 30, pp. 543–574.
- Monaghan, J. J. and J. C. Lattanzio (1985). “A refined particle method for astrophysical problems”. *Astronomy and Astrophysics* 149, pp. 135–143.
- Montes, G., E. Ramirez-Ruiz, J. Naiman, S. Shen, and W. H. Lee (2016). “Transport and Mixing of r-process Elements in Neutron Star Binary Merger Blast Waves”. *The Astrophysical Journal* 830, 12.

- Moriya, T. J. and J. J. Eldridge (2016). “Rapidly evolving faint transients from stripped-envelope electron-capture supernovae”. *Monthly Notices of the Royal Astronomical Society* 461, pp. 2155–2161.
- Moriya, T. J., N. Tominaga, N. Langer, K. Nomoto, S. I. Blinnikov, and E. I. Sorokina (2014). “Electron-Capture supernovae exploding within their progenitor wind”. *Astronomy and Astrophysics* 569, A57.
- Navarro, J. F. and S. D. M. White (1993). “Simulations of Dissipative Galaxy Formation in Hierarchically Clustering Universes - Part One - Tests of the Code”. *Monthly Notices of the Royal Astronomical Society* 265, p. 271.
- Nicholl, M. et al. (2017). “The Electromagnetic Counterpart of the Binary Neutron Star Merger LIGO/Virgo GW170817. III. Optical and UV Spectra of a Blue Kilonova from Fast Polar Ejecta”. *The Astrophysical Journal Letters* 848, L18.
- Nichols, M., Y. Revaz, and P. Jablonka (2014). “Gravitational tides and dwarf spheroidal galaxies”. *Astronomy and Astrophysics* 564, A112.
- Nishimura, N., T. Takiwaki, and F.-K. Thielemann (2015). “The r-process Nucleosynthesis in the Various Jet-like Explosions of Magnetorotational Core-collapse Supernovae”. *The Astrophysical Journal* 810, 109.
- Nissen, P. E., Y. Q. Chen, M. Asplund, and M. Pettini (2004). “Sulphur and zinc abundances in Galactic stars and damped Ly α systems”. *Astronomy and Astrophysics* 415, pp. 993–1007.
- Nissen, P. E., C. Akerman, M. Asplund, D. Fabbian, F. Kerber, H. U. Kaufl, and M. Pettini (2007). “Sulphur and zinc abundances in Galactic halo stars revisited”. *Astronomy and Astrophysics* 469, pp. 319–330.
- Nomoto, K. (1984). “Evolution of 8-10 solar mass stars toward electron capture supernovae. I - Formation of electron-degenerate O + Ne + Mg cores”. *The Astrophysical Journal* 277, pp. 791–805.
- (1987). “Evolution of 8-10 solar mass stars toward electron capture supernovae. II - Collapse of an O + Ne + Mg core”. *The Astrophysical Journal* 322, pp. 206–214.
- Nomoto, K., C. Kobayashi, and N. Tominaga (2013). “Nucleosynthesis in Stars and the Chemical Enrichment of Galaxies”. *Annual Review of Astronomy and Astrophysics* 51, 457 (N13)–509.
- Nomoto, K., D. Sugimoto, W. M. Sparks, R. A. Fesen, T. R. Gull, and S. Miyaji (1982). “The Crab Nebula’s progenitor”. *Nature* 299, pp. 803–805.
- Nomoto, K., M. Hashimoto, T. Tsujimoto, F.-K. Thielemann, N. Kishimoto, Y. Kubo, and N. Nakasato (1997). “Nucleosynthesis in type II supernovae”. *Nuclear Physics A* 616, pp. 79–90.
- Nomoto, K., N. Tominaga, H. Umeda, C. Kobayashi, and K. Maeda (2006). “Nucleosynthesis yields of core-collapse supernovae and hypernovae, and galactic chemical evolution”. *Nuclear Physics A* 777, pp. 424–458.
- Norris, J., M. S. Bessell, and A. J. Pickles (1985). “Population studies. I - The Bidelman-MacConnell ‘weak-metal’ stars”. *Astrophysical Journal Supplement Series* 58, pp. 463–492.
- Norris, J. E., G. Gilmore, R. F. G. Wyse, M. I. Wilkinson, V. Belokurov, N. W. Evans, and D. B. Zucker (2008). “The Abundance Spread in the Boötes I Dwarf Spheroidal Galaxy”. *The Astrophysical Journal Letters* 689, L113.

- Oh, S.-H., W. J. G. de Blok, E. Brinks, F. Walter, and R. C. Kennicutt Jr. (2011). “Dark and Luminous Matter in THINGS Dwarf Galaxies”. *The Astronomical Journal* 141, 193.
- Oh, S.-H., D. A. Hunter, E. Brinks, B. G. Elmegreen, A. Schruba, F. Walter, M. P. Rupen, L. M. Young, C. E. Simpson, M. C. Johnson, K. A. Herrmann, D. Ficut-Vicas, P. Cigan, V. Heesen, T. Ashley, and H.-X. Zhang (2015). “High-resolution Mass Models of Dwarf Galaxies from LITTLE THINGS”. *The Astronomical Journal* 149, 180.
- Ojima, T., Y. Ishimaru, S. Wanajo, and N. Prantzos (2017). “Stochastic Chemical Evolution of Sub-Halos and the Origin of r-Process Elements”. *14th International Symposium on Nuclei in the Cosmos (NIC2016)*. Ed. by S. Kubono, T. Kajino, S. Nishimura, T. Isobe, S. Nagataki, T. Shima, and Y. Takeda.
- Okamoto, T., R. S. Nemmen, and R. G. Bower (2008). “The impact of radio feedback from active galactic nuclei in cosmological simulations: formation of disc galaxies”. *Monthly Notices of the Royal Astronomical Society* 385, pp. 161–180.
- Okamoto, T., I. Shimizu, and N. Yoshida (2014). “Reproducing cosmic evolution of galaxy population from $z = 4$ to 0”. *Publications of the Astronomical Society of Japan* 66, 70.
- Okamoto, T., A. Jenkins, V. R. Eke, V. Quilis, and C. S. Frenk (2003). “Momentum transfer across shear flows in smoothed particle hydrodynamic simulations of galaxy formation”. *Monthly Notices of the Royal Astronomical Society* 345, pp. 429–446.
- Okamoto, T., V. R. Eke, C. S. Frenk, and A. Jenkins (2005). “Effects of feedback on the morphology of galaxy discs”. *Monthly Notices of the Royal Astronomical Society* 363, pp. 1299–1314.
- Okamoto, T., C. S. Frenk, A. Jenkins, and T. Theuns (2010). “The properties of satellite galaxies in simulations of galaxy formation”. *Monthly Notices of the Royal Astronomical Society* 406, pp. 208–222.
- Oort, J. H. (1922). “Some peculiarities in the motion of stars of high velocity”. *Bulletin of the Astronomical Institutes of the Netherlands* 1, p. 133.
- (1926). “The Stars of High Velocity”. PhD thesis. Publications of the Kapteyn Astronomical Laboratory Groningen, vol. 40, pp.1-75.
- Otsuki, K., S. Honda, W. Aoki, T. Kajino, and G. J. Mathews (2006). “Neutron-Capture Elements in the Metal-poor Globular Cluster M15”. *The Astrophysical Journal Letters* 641, pp. L117–L120.
- Pancino, E., R. Carrera, E. Rossetti, and C. Gallart (2010). “Chemical abundance analysis of the open clusters Cr 110, NGC 2099 (M 37), NGC 2420, NGC 7789, and M 67 (NGC 2682)”. *Astronomy and Astrophysics* 511, A56.
- Pian, E. et al. (2017). “Spectroscopic identification of r-process nucleosynthesis in a double neutron-star merger”. *Nature* 551, pp. 67–70.
- Piatek, S., C. Pryor, E. W. Olszewski, H. C. Harris, M. Mateo, D. Minniti, and C. G. Tinney (2003). “Proper Motions of Dwarf Spheroidal Galaxies from Hubble Space Telescope Imaging. II. Measurement for Carina”. *The Astronomical Journal* 126, pp. 2346–2361.
- Planck Collaboration, P. A. R. Ade, N. Aghanim, C. Armitage-Caplan, M. Arnaud, M. Ashdown, F. Atrio-Barandela, J. Aumont, C. Baccigalupi, A. J. Banday, and

- et al. (2014). “Planck 2013 results. XVI. Cosmological parameters”. *Astronomy and Astrophysics* 571, A16.
- Planck Collaboration, P. A. R. Ade, N. Aghanim, M. Arnaud, M. Ashdown, J. Aumont, C. Baccigalupi, A. J. Banday, R. B. Barreiro, J. G. Bartlett, and et al. (2016). “Planck 2015 results. XIII. Cosmological parameters”. *Astronomy and Astrophysics* 594, A13.
- Podsiadlowski, P., N. Langer, A. J. T. Poelarends, S. Rappaport, A. Heger, and E. Pfahl (2004a). “The Effects of Binary Evolution on the Dynamics of Core Collapse and Neutron Star Kicks”. *The Astrophysical Journal* 612, pp. 1044–1051.
- Podsiadlowski, P., P. A. Mazzali, K. Nomoto, D. Lazzati, and E. Cappellaro (2004b). “The Rates of Hypernovae and Gamma-Ray Bursts: Implications for Their Progenitors”. *The Astrophysical Journal Letters* 607, pp. L17–L20.
- Poelarends, A. J. T. (2007). “Stellar evolution on the borderline of white dwarf and neutron star formation”. PhD thesis. Utrecht University.
- Poelarends, A. J. T., F. Herwig, N. Langer, and A. Heger (2008). “The Supernova Channel of Super-AGB Stars”. *The Astrophysical Journal* 675, 614–625, pp. 614–625.
- Poelarends, A. J. T., S. Wurtz, J. Tarka, L. Cole Adams, and S. T. Hills (2017). “Electron Capture Supernovae from Close Binary Systems”. *The Astrophysical Journal* 850, 197.
- Portegies Zwart, S. F. and L. R. Yungelson (1998). “Formation and evolution of binary neutron stars”. *Astronomy and Astrophysics* 332, pp. 173–188.
- Prantzos, N. (2008). “The metallicity distribution of the halo and the satellites of the Milky Way in the hierarchical merging paradigm”. *Astronomy and Astrophysics* 489, pp. 525–532.
- Rahmati, A., A. H. Pawlik, M. Raičević, and J. Schaye (2013). “On the evolution of the H I column density distribution in cosmological simulations”. *Monthly Notices of the Royal Astronomical Society* 430, pp. 2427–2445.
- Raiteri, C. M., M. Villata, R. Gallino, M. Busso, and A. Cravanzola (1999). “Simulations of Galactic Chemical Evolution: BA Enrichment”. *The Astrophysical Journal Letters* 518, pp. L91–L94.
- Reddy, A. B. S., S. Giridhar, and D. L. Lambert (2012). “Comprehensive abundance analysis of red giants in the open clusters NGC 752, 1817, 2360 and 2506”. *Monthly Notices of the Royal Astronomical Society* 419, pp. 1350–1361.
- (2013). “Comprehensive abundance analysis of red giants in the open clusters NGC 2527, 2682, 2482, 2539, 2335, 2251 and 2266”. *Monthly Notices of the Royal Astronomical Society* 431, pp. 3338–3348.
- Reddy, S., M. Prakash, and J. M. Lattimer (1998). “Neutrino interactions in hot and dense matter”. *Physical Review D* 58.1, 013009.
- Revaz, Y. and P. Jablonka (2012). “The dynamical and chemical evolution of dwarf spheroidal galaxies with GEAR”. *Astronomy and Astrophysics* 538, A82.
- Revaz, Y., P. Jablonka, T. Sawala, V. Hill, B. Letarte, M. Irwin, G. Battaglia, A. Helmi, M. D. Shetrone, E. Tolstoy, and K. A. Venn (2009). “The dynamical and chemical evolution of dwarf spheroidal galaxies”. *Astronomy and Astrophysics* 501, pp. 189–206.

- Revaz, Y., A. Arnaudon, M. Nichols, V. Bonvin, and P. Jablonka (2016). “Computational issues in chemo-dynamical modelling of the formation and evolution of galaxies”. *Astronomy and Astrophysics* 588, A21.
- Roberts, L. F., S. Reddy, and G. Shen (2012). “Medium modification of the charged-current neutrino opacity and its implications”. *Physical Review C* 86.6, 065803.
- Roederer, I. U., G. W. Preston, I. B. Thompson, S. A. Shectman, C. Sneden, G. S. Burley, and D. D. Kelson (2014). “A Search for Stars of Very Low Metal Abundance. VI. Detailed Abundances of 313 Metal-poor Stars”. *The Astronomical Journal* 147, 136.
- Roederer, I. U., M. Mateo, J. I. Bailey III, Y. Song, E. F. Bell, J. D. Crane, S. Loebman, D. L. Nidever, E. W. Olszewski, S. A. Shectman, I. B. Thompson, M. Valluri, and M. G. Walker (2016). “Detailed Chemical Abundances in the r-process-rich Ultra-faint Dwarf Galaxy Reticulum 2”. *The Astronomical Journal* 151, 82.
- Roman, N. G. (1955). “A Catalogue of High-Velocity Stars.” *Astrophysical Journal Supplement* 2, p. 195.
- Rosswog, S., O. Korobkin, A. Arcones, F.-K. Thielemann, and T. Piran (2014). “The long-term evolution of neutron star merger remnants - I. The impact of r-process nucleosynthesis”. *Monthly Notices of the Royal Astronomical Society* 439, pp. 744–756.
- Roy, J.-R. and D. Kunth (1995). “Dispersal and mixing of oxygen in the interstellar medium of gas-rich galaxies”. *Astronomy and Astrophysics* 294, pp. 432–442.
- Ryan, S. G. and J. E. Norris (1991). “Subdwarf Studies. III. The Halo Metallicity Distribution”. *The Astronomical Journal* 101, pp. 1865–1878.
- Sadakane, K., N. Arimoto, C. Ikuta, W. Aoki, P. Jablonka, and A. Tajitsu (2004). “Subaru/HDS Abundances in Three Giant Stars in the Ursa Minor Dwarf Spheroidal Galaxy”. *Publications of the Astronomical Society of Japan* 56, pp. 1041–1058.
- Safarzadeh, M. and B. Côté (2017). “On the impact of neutron star binaries’ natal-kick distribution on the Galactic r-process enrichment”. *Monthly Notices of the Royal Astronomical Society* 471, pp. 4488–4493.
- Saito, Y.-J., M. Takada-Hidai, S. Honda, and Y. Takeda (2009). “Chemical Evolution of Zinc in the Galaxy”. *Publications of the Astronomical Society of Japan* 61, pp. 549–561.
- Saitoh, T. R. (2016). *CELib: Software library for simulations of chemical evolution*. Astrophysics Source Code Library.
- (2017). “Chemical Evolution Library for Galaxy Formation Simulation”. *The Astronomical Journal* 153, 85.
- Saitoh, T. R. and J. Makino (2009). “A Necessary Condition for Individual Time Steps in SPH Simulations”. *The Astrophysical Journal Letters* 697, pp. L99–L102.
- (2010). “FAST: A Fully Asynchronous Split Time-Integrator for a Self-Gravitating Fluid”. *Publications of the Astronomical Society of Japan* 62, pp. 301–314.
- (2012). “A natural symmetrization for the plummer potential”. *New Astronomy* 17, pp. 76–81.
- (2013). “A Density-independent Formulation of Smoothed Particle Hydrodynamics”. *The Astrophysical Journal* 768, 44.
- (2016). “Santa Barbara Cluster Comparison Test with DISPH”. *The Astrophysical Journal* 823, 144.

- Saitoh, T. R., H. Daisaka, E. Kokubo, J. Makino, T. Okamoto, K. Tomisaka, K. Wada, and N. Yoshida (2008). “Toward First-Principle Simulations of Galaxy Formation: I. How Should We Choose Star-Formation Criteria in High-Resolution Simulations of Disk Galaxies?” *Publications of the Astronomical Society of Japan* 60, pp. 667–681.
- (2009). “Toward First-Principle Simulations of Galaxy Formation: II. Shock-Induced Starburst at a Collision Interface during the First Encounter of Interacting Galaxies”. *Publications of the Astronomical Society of Japan* 61, pp. 481–486.
- Salpeter, E. E. (1955). “The Luminosity Function and Stellar Evolution.” *The Astrophysical Journal* 121, p. 161.
- Sanders, D. B., N. Z. Scoville, and P. M. Solomon (1985). “Giant molecular clouds in the Galaxy. II - Characteristics of discrete features”. *The Astrophysical Journal* 289, pp. 373–387.
- Savchenko, V., C. Ferrigno, E. Kuulkers, A. Bazzano, E. Bozzo, S. Brandt, J. Chenevez, T. J.-L. Courvoisier, R. Diehl, A. Domingo, L. Hanlon, E. Jourdain, A. von Kienlin, P. Laurent, F. Lebrun, A. Lutovinov, A. Martin-Carrillo, S. Mereghetti, L. Natalucci, J. Rodi, J.-P. Roques, R. Sunyaev, and P. Ubertini (2017). “INTEGRAL Detection of the First Prompt Gamma-Ray Signal Coincident with the Gravitational-wave Event GW170817”. *The Astrophysical Journal Letters* 848, L15.
- Sawala, T., C. S. Frenk, A. Fattahi, J. F. Navarro, R. G. Bower, R. A. Crain, C. Dalla Vecchia, M. Furlong, J. C. Helly, A. Jenkins, K. A. Oman, M. Schaller, J. Schaye, T. Theuns, J. Trayford, and S. D. M. White (2016). “The APOSTLE simulations: solutions to the Local Group’s cosmic puzzles”. *Monthly Notices of the Royal Astronomical Society* 457, pp. 1931–1943.
- Sbordone, L., P. Bonifacio, R. Buonanno, G. Marconi, L. Monaco, and S. Zaggia (2007). “The exotic chemical composition of the Sagittarius dwarf spheroidal galaxy”. *Astronomy and Astrophysics* 465, pp. 815–824.
- Schaye, J., R. A. Crain, R. G. Bower, M. Furlong, M. Schaller, T. Theuns, C. Dalla Vecchia, C. S. Frenk, I. G. McCarthy, J. C. Helly, A. Jenkins, Y. M. Rosas-Guevara, S. D. M. White, M. Baes, C. M. Booth, P. Camps, J. F. Navarro, Y. Qu, A. Rahmati, T. Sawala, P. A. Thomas, and J. Trayford (2015). “The EAGLE project: simulating the evolution and assembly of galaxies and their environments”. *Monthly Notices of the Royal Astronomical Society* 446, pp. 521–554.
- Searle, L. and R. Zinn (1978). “Compositions of halo clusters and the formation of the galactic halo”. *The Astrophysical Journal* 225, pp. 357–379.
- Seitenzahl, I. R., F. Ciaraldi-Schoolmann, F. K. Röpke, M. Fink, W. Hillebrandt, M. Kromer, R. Pakmor, A. J. Ruiter, S. A. Sim, and S. Taubenberger (2013). “Three-dimensional delayed-detonation models with nucleosynthesis for Type Ia supernovae”. *Monthly Notices of the Royal Astronomical Society* 429, pp. 1156–1172.
- Shen, S., J. Wadsley, and G. Stinson (2010). “The enrichment of the intergalactic medium with adiabatic feedback - I. Metal cooling and metal diffusion”. *Monthly Notices of the Royal Astronomical Society* 407, pp. 1581–1596.
- Shen, S., R. J. Cooke, E. Ramirez-Ruiz, P. Madau, L. Mayer, and J. Guedes (2015). “The History of R-Process Enrichment in the Milky Way”. *The Astrophysical Journal* 807, 115.

- Shetrone, M., K. A. Venn, E. Tolstoy, F. Primas, V. Hill, and A. Kaufer (2003). “VLT/UVES Abundances in Four Nearby Dwarf Spheroidal Galaxies. I. Nucleosynthesis and Abundance Ratios”. *The Astronomical Journal* 125, pp. 684–706.
- Shetrone, M. D., P. Côté, and W. L. W. Sargent (2001). “Abundance Patterns in the Draco, Sextans, and Ursa Minor Dwarf Spheroidal Galaxies”. *The Astrophysical Journal* 548, pp. 592–608.
- Shibagaki, S., T. Kajino, G. J. Mathews, S. Chiba, S. Nishimura, and G. Lorusso (2016). “Relative Contributions of the Weak, Main, and Fission-recycling r-process”. *The Astrophysical Journal* 816, 79.
- Siess, L. (2007). “Evolution of massive AGB stars. II. model properties at non-solar metallicity and the fate of Super-AGB stars”. *Astronomy and Astrophysics* 476, pp. 893–909.
- Simionescu, A., N. Werner, O. Urban, S. W. Allen, Y. Ichinohe, and I. Zhuravleva (2015). “A Uniform Contribution of Core-collapse and Type Ia Supernovae to the Chemical Enrichment Pattern in the Outskirts of the Virgo Cluster”. *The Astrophysical Journal Letters* 811, L25.
- Simmerer, J., C. Sneden, J. J. Cowan, J. Collier, V. M. Woolf, and J. E. Lawler (2004). “The Rise of the s-Process in the Galaxy”. *The Astrophysical Journal* 617, pp. 1091–1114.
- Simon, J. D. and M. Geha (2007). “The Kinematics of the Ultra-faint Milky Way Satellites: Solving the Missing Satellite Problem”. *The Astrophysical Journal* 670, pp. 313–331.
- Simon, J. D., H. R. Jacobson, A. Frebel, I. B. Thompson, J. J. Adams, and S. A. Shectman (2015). “Chemical Signatures of the First Supernovae in the Sculptor Dwarf Spheroidal Galaxy”. *The Astrophysical Journal* 802, 93.
- Simpson, C. M., G. L. Bryan, K. V. Johnston, B. D. Smith, M.-M. Mac Low, S. Sharma, and J. Tumlinson (2013). “The effect of feedback and reionization on star formation in low-mass dwarf galaxy haloes”. *Monthly Notices of the Royal Astronomical Society* 432, pp. 1989–2011.
- Skúladóttir, Á., E. Tolstoy, S. Salvadori, V. Hill, M. Pettini, M. D. Shetrone, and E. Starkenburg (2015). “The first carbon-enhanced metal-poor star found in the Sculptor dwarf spheroidal”. *Astronomy and Astrophysics* 574, A129.
- Skúladóttir, Á., E. Tolstoy, S. Salvadori, V. Hill, and M. Pettini (2017). “Zinc abundances in the Sculptor dwarf spheroidal galaxy”. *Astronomy and Astrophysics* 606, A71.
- Smagorinsky, J. (1963). “General Circulation Experiments with the Primitive Equations”. *Monthly Weather Review* 91, p. 99.
- Smartt, S. J. et al. (2017). “A kilonova as the electromagnetic counterpart to a gravitational-wave source”. *Nature* 551, pp. 75–79.
- Smith, N. (2013). “The Crab nebula and the class of Type II_n-P supernovae caused by sub-energetic electron-capture explosions”. *Monthly Notices of the Royal Astronomical Society* 434, pp. 102–113.
- Sneden, C., J. J. Cowan, and R. Gallino (2008). “Neutron-Capture Elements in the Early Galaxy”. *Annual Review of Astronomy and Astrophysics* 46, pp. 241–288.
- Sneden, C., R. P. Kraft, M. D. Shetrone, G. H. Smith, G. E. Langer, and C. F. Prosser (1997). “Star-To-Star Abundance Variations Among Bright Giants in the Metal-Poor Globular Cluster M15”. *The Astronomical Journal* 114, p. 1964.

- Soares-Santos, M. et al. (2017). “The Electromagnetic Counterpart of the Binary Neutron Star Merger LIGO/Virgo GW170817. I. Discovery of the Optical Counterpart Using the Dark Energy Camera”. *The Astrophysical Journal Letters* 848, L16.
- Solomon, P. M., A. R. Rivolo, J. Barrett, and A. Yahil (1987). “Mass, luminosity, and line width relations of Galactic molecular clouds”. *The Astrophysical Journal* 319, pp. 730–741.
- Somerville, R. S. and R. Davé (2015). “Physical Models of Galaxy Formation in a Cosmological Framework”. *Annual Review of Astronomy and Astrophysics* 53, pp. 51–113.
- Springel, V. (2005). “The cosmological simulation code GADGET-2”. *Monthly Notices of the Royal Astronomical Society* 364, pp. 1105–1134.
- Springel, V., J. Wang, M. Vogelsberger, A. Ludlow, A. Jenkins, A. Helmi, J. F. Navarro, C. S. Frenk, and S. D. M. White (2008). “The Aquarius Project: the subhaloes of galactic haloes”. *Monthly Notices of the Royal Astronomical Society* 391, pp. 1685–1711.
- Starkenburg, E., V. Hill, E. Tolstoy, J. I. González Hernández, M. Irwin, A. Helmi, G. Battaglia, P. Jablonka, M. Tafelmeyer, M. Shetrone, K. Venn, and T. de Boer (2010). “The NIR Ca ii triplet at low metallicity. Searching for extremely low-metallicity stars in classical dwarf galaxies”. *Astronomy and Astrophysics* 513, A34.
- Starkenburg, E., V. Hill, E. Tolstoy, P. François, M. J. Irwin, L. Boschman, K. A. Venn, T. J. L. de Boer, B. Lemasle, P. Jablonka, G. Battaglia, P. Groot, and L. Kaper (2013). “The extremely low-metallicity tail of the Sculptor dwarf spheroidal galaxy”. *Astronomy and Astrophysics* 549, A88.
- Steinmetz, M. and E. Müller (1994). “The formation of disk galaxies in a cosmological context: Populations, metallicities and metallicity gradients”. *Astronomy and Astrophysics* 281, pp. L97–L100.
- Stinson, G., A. Seth, N. Katz, J. Wadsley, F. Governato, and T. Quinn (2006). “Star formation and feedback in smoothed particle hydrodynamic simulations - I. Isolated galaxies”. *Monthly Notices of the Royal Astronomical Society* 373, pp. 1074–1090.
- Suda, T., Y. Katsuta, S. Yamada, T. Suwa, C. Ishizuka, Y. Komiya, K. Sorai, M. Aikawa, and M. Y. Fujimoto (2008). “Stellar Abundances for the Galactic Archeology (SAGA) Database — Compilation of the Characteristics of Known Extremely Metal-Poor Stars”. *Publications of the Astronomical Society of Japan* 60, pp. 1159–1171.
- Suda, T., S. Yamada, Y. Katsuta, Y. Komiya, C. Ishizuka, W. Aoki, and M. Y. Fujimoto (2011). “The Stellar Abundances for Galactic Archaeology (SAGA) data base - II. Implications for mixing and nucleosynthesis in extremely metal-poor stars and chemical enrichment of the Galaxy”. *Monthly Notices of the Royal Astronomical Society* 412, pp. 843–874.
- Suda, T., J. Hidaka, M. Ishigaki, Y. Katsuta, S. Yamada, Y. Komiya, M. Y. Fujimoto, and W. Aoki (2014). “Stellar Abundances for Galactic Archaeology database for stars in dwarf galaxies”. *memsai* 85, p. 600.
- Suda, T., J. Hidaka, W. Aoki, Y. Katsuta, S. Yamada, M. Y. Fujimoto, Y. Ohtani, M. Masuyama, K. Noda, and K. Wada (2017). “Stellar Abundances for Galactic

- Archaeology Database. IV. Compilation of stars in dwarf galaxies”. *Publications of the Astronomical Society of Japan* 69, 76.
- Sukhbold, T., T. Ertl, S. E. Woosley, J. M. Brown, and H.-T. Janka (2016). “Core-collapse Supernovae from 9 to 120 Solar Masses Based on Neutrino-powered Explosions”. *The Astrophysical Journal* 821, 38, p. 38.
- Sumiyoshi, K., M. Terasawa, G. J. Mathews, T. Kajino, S. Yamada, and H. Suzuki (2001). “r-Process in Prompt Supernova Explosions Revisited”. *The Astrophysical Journal* 562, pp. 880–886.
- Symbolist, E. and D. N. Schramm (1982). “Neutron star collisions and the r-process”. *Astrophysics Letters* 22, pp. 143–145.
- Tafelmeyer, M., P. Jablonka, V. Hill, M. Shetrone, E. Tolstoy, M. J. Irwin, G. Battaglia, A. Helmi, E. Starkenburg, K. A. Venn, T. Abel, P. Francois, A. Kaufer, P. North, F. Primas, and T. Szeifert (2010). “Extremely metal-poor stars in classical dwarf spheroidal galaxies: Fornax, Sculptor, and Sextans”. *Astronomy and Astrophysics* 524, A58.
- Takada, M., R. S. Ellis, M. Chiba, J. E. Greene, H. Aihara, N. Arimoto, K. Bundy, J. Cohen, O. Doré, G. Graves, J. E. Gunn, T. Heckman, C. M. Hirata, P. Ho, J.-P. Kneib, O. Le Fèvre, L. Lin, S. More, H. Murayama, T. Nagao, M. Ouchi, M. Seiffert, J. D. Silverman, L. Sodré, D. N. Spergel, M. A. Strauss, H. Sugai, Y. Suto, H. Takami, and R. Wyse (2014). “Extragalactic science, cosmology, and Galactic archaeology with the Subaru Prime Focus Spectrograph”. *Publications of the Astronomical Society of Japan* 66, R1.
- Takahashi, K., T. Yoshida, and H. Umeda (2013). “Evolution of Progenitors for Electron Capture Supernovae”. *The Astrophysical Journal* 771, 28.
- Tanaka, M. and K. Hotokezaka (2013). “Radiative Transfer Simulations of Neutron Star Merger Ejecta”. *The Astrophysical Journal* 775, 113.
- Tanaka, M., N. Tominaga, K. Nomoto, S. Valenti, D. K. Sahu, T. Minezaki, Y. Yoshii, M. Yoshida, G. C. Anupama, S. Benetti, G. Chincarini, M. Della Valle, P. A. Mazzali, and E. Pian (2009). “Type Ib Supernova 2008D Associated With the Luminous X-Ray Transient 080109: An Energetic Explosion of a Massive Helium Star”. *The Astrophysical Journal* 692, pp. 1131–1142.
- Tanaka, M. et al. (2017). “Kilonova from post-merger ejecta as an optical and near-Infrared counterpart of GW170817”. *Publications of the Astronomical Society of Japan* 69, 102.
- Tanikawa, A., K. Yoshikawa, T. Okamoto, and K. Nitadori (2012). “N-body simulation for self-gravitating collisional systems with a new SIMD instruction set extension to the x86 architecture, Advanced Vector eXtensions”. *New Astronomy* 17, pp. 82–92.
- Tanvir, N. R., A. J. Levan, A. S. Fruchter, J. Hjorth, R. A. Hounsell, K. Wiersema, and R. L. Tunnicliffe (2013). “A ‘kilonova’ associated with the short-duration γ -ray burst GRB 130603B”. *Nature* 500, pp. 547–549.
- Tanvir, N. R. et al. (2017). “The Emergence of a Lanthanide-rich Kilonova Following the Merger of Two Neutron Stars”. *The Astrophysical Journal Letters* 848, L27.
- Tauris, T. M., N. Langer, and P. Podsiadlowski (2015). “Ultra-stripped supernovae: progenitors and fate”. *Monthly Notices of the Royal Astronomical Society* 451, pp. 2123–2144.

- Tauris, T. M., N. Langer, T. J. Moriya, P. Podsiadlowski, S.-C. Yoon, and S. I. Blinnikov (2013). “Ultra-stripped Type Ic Supernovae from Close Binary Evolution”. *The Astrophysical Journal Letters* 778, L23.
- Thielemann, F.-K., M. Eichler, I. V. Panov, and B. Wehmeyer (2017). “Neutron Star Mergers and Nucleosynthesis of Heavy Elements”. *Annual Review of Nuclear and Particle Science* 67, pp. 253–274.
- Timmes, F. X., S. E. Woosley, and T. A. Weaver (1995). “Galactic chemical evolution: Hydrogen through zinc”. *The Astrophysical Journals* 98, pp. 617–658.
- Ting, Y.-S., G. M. De Silva, K. C. Freeman, and S. J. Parker (2012). “High-resolution elemental abundance analysis of the open cluster IC 4756”. *Monthly Notices of the Royal Astronomical Society* 427, pp. 882–892.
- Tinsley, B. M. (1979). “Stellar lifetimes and abundance ratios in chemical evolution”. *The Astrophysical Journal* 229, pp. 1046–1056.
- (1980). “Evolution of the Stars and Gas in Galaxies”. *Fundamentals of Cosmic Physics* 5, pp. 287–388.
- Tolstoy, E., V. Hill, and M. Tosi (2009). “Star-Formation Histories, Abundances, and Kinematics of Dwarf Galaxies in the Local Group”. *Annual Review of Astronomy and Astrophysics* 47, pp. 371–425.
- Tominaga, N., S. I. Blinnikov, and K. Nomoto (2013). “Supernova Explosions of Super-asymptotic Giant Branch Stars: Multicolor Light Curves of Electron-Capture Supernovae”. *The Astrophysical Journal Letters* 771, L12.
- Tominaga, N., H. Umeda, and K. Nomoto (2007). “Supernova Nucleosynthesis in Population III 13–50 M_{solar} Stars and Abundance Patterns of Extremely Metal-poor Stars”. *The Astrophysical Journal* 660, pp. 516–540.
- Torrey, P., M. Vogelsberger, S. Genel, D. Sijacki, V. Springel, and L. Hernquist (2014). “A model for cosmological simulations of galaxy formation physics: multi-epoch validation”. *Monthly Notices of the Royal Astronomical Society* 438, pp. 1985–2004.
- Totani, T., T. Morokuma, T. Oda, M. Doi, and N. Yasuda (2008). “Delay Time Distribution Measurement of Type Ia Supernovae by the Subaru/XMM-Newton Deep Survey and Implications for the Progenitor”. *Publications of the Astronomical Society of Japan* 60, pp. 1327–1346.
- Travaglio, C., D. Galli, and A. Burkert (2001). “Inhomogeneous Chemical Evolution of the Galactic Halo: Abundance of r-Process Elements”. *The Astrophysical Journal* 547, pp. 217–230.
- Travaglio, C., D. Galli, R. Gallino, M. Busso, F. Ferrini, and O. Straniero (1999). “Galactic Chemical Evolution of Heavy Elements: From Barium to Europium”. *The Astrophysical Journal* 521, pp. 691–702.
- Troja, E. et al. (2017). “The X-ray counterpart to the gravitational-wave event GW170817”. *Nature* 551, pp. 71–74.
- Tsujimoto, T. and T. Shigeyama (2014). “Enrichment history of r-process elements shaped by a merger of neutron star pairs”. *Astronomy and Astrophysics* 565, L5.
- Tsujimoto, T., T. Shigeyama, and Y. Yoshii (2000). “Probing the Site for R-Process Nucleosynthesis with Abundances of Barium and Magnesium in Extremely Metal-poor Stars”. *The Astrophysical Journal Letters* 531, pp. L33–L36.

- Tsujimoto, T., T. Yokoyama, and K. Bekki (2017). “Chemical evolution of ^{244}Pu in the solar vicinity and its implications for the properties of r-process production”. *The Astrophysical Journal Letters* 835, L3.
- Umeda, H. and K. Nomoto (2002). “Nucleosynthesis of Zinc and Iron Peak Elements in Population III Type II Supernovae: Comparison with Abundances of Very Metal Poor Halo Stars”. *The Astrophysical Journal* 565, pp. 385–404.
- (2005). “Variations in the Abundance Pattern of Extremely Metal-Poor Stars and Nucleosynthesis in Population III Supernovae”. *The Astrophysical Journal* 619, pp. 427–445.
- Utsumi, Y. et al. (2017). “J-GEM observations of an electromagnetic counterpart to the neutron star merger GW170817”. *Publications of the Astronomical Society of Japan* 69, 101.
- Valcke, S., S. de Rijcke, and H. Dejonghe (2008). “Simulations of the formation and evolution of isolated dwarf galaxies”. *Monthly Notices of the Royal Astronomical Society* 389, pp. 1111–1126.
- Valenti, S., David, J. Sand, S. Yang, E. Cappellaro, L. Tartaglia, A. Corsi, S. W. Jha, D. E. Reichart, J. Haislip, and V. Kouprianov (2017). “The Discovery of the Electromagnetic Counterpart of GW170817: Kilonova AT 2017gfo/DLT17ck”. *The Astrophysical Journal Letters* 848, L24.
- van de Voort, F., E. Quataert, P. F. Hopkins, D. Kereš, and C.-A. Faucher-Giguère (2015). “Galactic r-process enrichment by neutron star mergers in cosmological simulations of a Milky Way-mass galaxy”. *Monthly Notices of the Royal Astronomical Society* 447, pp. 140–148.
- Venn, K. A., M. Irwin, M. D. Shetrone, C. A. Tout, V. Hill, and E. Tolstoy (2004). “Stellar Chemical Signatures and Hierarchical Galaxy Formation”. *The Astrophysical Journal* 128, pp. 1177–1195.
- Venn, K. A., M. D. Shetrone, M. J. Irwin, V. Hill, P. Jablonka, E. Tolstoy, B. Lemasle, M. Divell, E. Starkenburg, B. Letarte, C. Baldner, G. Battaglia, A. Helmi, A. Kaufer, and F. Primas (2012). “Nucleosynthesis and the Inhomogeneous Chemical Evolution of the Carina Dwarf Galaxy”. *The Astrophysical Journal* 751, 102.
- Vladilo, G., C. Abate, J. Yin, G. Cescutti, and F. Matteucci (2011). “Silicon depletion in damped Ly α systems. The S/Zn method”. *Astronomy and Astrophysics* 530, A33.
- Vogelsberger, M., S. Genel, D. Sijacki, P. Torrey, V. Springel, and L. Hernquist (2013). “A model for cosmological simulations of galaxy formation physics”. *Monthly Notices of the Royal Astronomical Society* 436, pp. 3031–3067.
- Walker, M. G., M. Mateo, E. W. Olszewski, O. Y. Gnedin, X. Wang, B. Sen, and M. Woodroffe (2007). “Velocity Dispersion Profiles of Seven Dwarf Spheroidal Galaxies”. *The Astrophysical Journal Letters* 667, pp. L53–L56.
- Walker, M. G., M. Mateo, E. W. Olszewski, J. Peñarrubia, N. Wyn Evans, and G. Gilmore (2009). “A Universal Mass Profile for Dwarf Spheroidal Galaxies?” *The Astrophysical Journal* 704, pp. 1274–1287.
- Wanajo, S. (2013). “The r-process in Proto-neutron-star Wind Revisited”. *The Astrophysical Journal Letters* 770, L22.
- Wanajo, S., H.-T. Janka, and B. Müller (2011). “Electron-Capture Supernovae as The Origin of Elements Beyond Iron”. *The Astrophysical Journal Letters* 726, L15.

- (2013a). “Electron-Capture Supernovae as Origin of ^{48}Ca ”. *The Astrophysical Journal Letters* 767, L26.
- (2013b). “Electron-Capture Supernovae as Sources of ^{60}Fe ”. *The Astrophysical Journal Letters* 774, L6.
- Wanajo, S., T. Kajino, G. J. Mathews, and K. Otsuki (2001). “The r-Process in Neutrino-driven Winds from Nascent, “Compact” Neutron Stars of Core-Collapse Supernovae”. *The Astrophysical Journal* 554, pp. 578–586.
- Wanajo, S., M. Tamamura, N. Itoh, K. Nomoto, Y. Ishimaru, T. C. Beers, and S. Nozawa (2003). “The r-Process in Supernova Explosions from the Collapse of O-Ne-Mg Cores”. *The Astrophysical Journal* 593, pp. 968–979.
- Wanajo, S., K. Nomoto, H.-T. Janka, F. S. Kitaura, and B. Müller (2009). “Nucleosynthesis in Electron Capture Supernovae of Asymptotic Giant Branch Stars”. *The Astrophysical Journal* 695, pp. 208–220.
- Wanajo, S., Y. Sekiguchi, N. Nishimura, K. Kiuchi, K. Kyutoku, and M. Shibata (2014). “Production of All the r-process Nuclides in the Dynamical Ejecta of Neutron Star Mergers”. *The Astrophysical Journal Letters* 789, L39.
- Wanajo, S., B. Müller, H.-T. Janka, and A. Heger (2018). “Nucleosynthesis in the Innermost Ejecta of Neutrino-driven Supernova Explosions in Two Dimensions”. *The Astrophysical Journal* 852, 40.
- Wehmeyer, B., M. Pignatari, and F.-K. Thielemann (2015). “Galactic evolution of rapid neutron capture process abundances: the inhomogeneous approach”. *Monthly Notices of the Royal Astronomical Society* 452, pp. 1970–1981.
- Weisz, D. R., A. E. Dolphin, E. D. Skillman, J. Holtzman, K. M. Gilbert, J. J. Dalcanton, and B. F. Williams (2014). “The Star Formation Histories of Local Group Dwarf Galaxies. I. Hubble Space Telescope/Wide Field Planetary Camera 2 Observations”. *The Astrophysical Journal* 789, 147.
- Wendland, Holger (1995). “Piecewise polynomial, positive definite and compactly supported radial functions of minimal degree”. *Advances in Computational Mathematics* 4.1, pp. 389–396. ISSN: 1572-9044.
- Werner, N., O. Urban, A. Simionescu, and S. W. Allen (2013). “A uniform metal distribution in the intergalactic medium of the Perseus cluster of galaxies”. *Nature* 502, pp. 656–658.
- Westin, J., C. Sneden, B. Gustafsson, and J. J. Cowan (2000). “The r-Process-enriched Low-Metallicity Giant HD 115444”. *The Astrophysical Journal* 530, pp. 783–799.
- White, S. D. M. and M. J. Rees (1978). “Core condensation in heavy halos - A two-stage theory for galaxy formation and clustering”. *Monthly Notices of the Royal Astronomical Society* 183, pp. 341–358.
- Wiersma, R. P. C., J. Schaye, T. Theuns, C. Dalla Vecchia, and L. Tornatore (2009). “Chemical enrichment in cosmological, smoothed particle hydrodynamics simulations”. *Monthly Notices of the Royal Astronomical Society* 399, pp. 574–600.
- Williamson, D., H. Martel, and D. Kawata (2016). “Metal Diffusion in Smoothed Particle Hydrodynamics Simulations of Dwarf Galaxies”. *The Astrophysical Journal* 822, 91.
- Winteler, C., R. Käppeli, A. Perego, A. Arcones, N. Vassetz, N. Nishimura, M. Liebendörfer, and F.-K. Thielemann (2012). “Magnetorotationally Driven Supernovae as the Origin of Early Galaxy r-process Elements?” *The Astrophysical Journal Letters* 750, L22.

- Wolfe, A. M., E. Gawiser, and J. X. Prochaska (2005). “Damped Ly α Systems”. *Annual Review of Astronomy and Astrophysics* 43, pp. 861–918.
- Woosley, S. E. and A. Heger (2007). “Nucleosynthesis and remnants in massive stars of solar metallicity”. *Physics Reports* 442, pp. 269–283.
- (2015). “The Remarkable Deaths of 9-11 Solar Mass Stars”. *The Astrophysical Journal* 810, 34.
- Woosley, S. E. and T. A. Weaver (1995). “The Evolution and Explosion of Massive Stars. II. Explosive Hydrodynamics and Nucleosynthesis”. *The Astrophysical Journals* 101, p. 181.
- Woosley, S. E., J. R. Wilson, G. J. Mathews, R. D. Hoffman, and B. S. Meyer (1994). “The r-process and neutrino-heated supernova Ejecta”. *The Astrophysical Journal* 433, pp. 229–246.
- Yamada, S., T. Suda, Y. Komiya, W. Aoki, and M. Y. Fujimoto (2013). “The Stellar Abundances for Galactic Archaeology (SAGA) Database - III. Analysis of enrichment histories for elements and two modes of star formation during the early evolution of the Milky Way”. *Monthly Notices of the Royal Astronomical Society* 436, pp. 1362–1380.
- Yamamoto, S., T. R. Saitoh, and J. Makino (2015). “Smoothed particle hydrodynamics with smoothed pseudo-density”. *Publications of the Astronomical Society of Japan* 67, 37.
- Yoshida, T., Y. Suwa, H. Umeda, M. Shibata, and K. Takahashi (2017). “Explosive nucleosynthesis of ultra-stripped Type Ic supernovae: application to light trans-iron elements”. *Monthly Notices of the Royal Astronomical Society* 471, pp. 4275–4285.
- Yoshii, Y. and H. Saio (1979). “Kinematics of the Old Stars and Initial Contraction of the Galaxy”. *Publications of the Astronomical Society of Japan* 31, pp. 339–368.
- Zuckerman, B. and N. J. Evans II (1974). “Models of massive molecular clouds”. *The Astrophysical Journal Letters* 192, pp. L149–L152.